2005

Carbon Monoxide Oxidation on Nanoparticle Catalysts and Gas Phase Reactions of Small Molecules and Volatile Organics with Metal Cations

Khaled Mohammad Eqab Saoud
Virginia Commonwealth University

College of Humanities and Science
Virginia Commonwealth University

This is to certify that the dissertation prepared by Khaled Mohammad Saoud entitled CARBON MONOXIDE OXIDATION ON NANOPARTICLE CATALYSTS AND GAS PHASE REACTIONS OF SMALL MOLECULES AND VOLATILE ORGANICS WITH METAL CATIONS has been approved by his committee as satisfactory completion of the thesis or dissertation requirement for the degree of Doctor of Philosophy.

M. Samy El-Shall, Ph.D., Professor, Department of Chemistry, Research Adviser

---

James Terner, Ph.D., Professor, Department of Chemistry

Alison Baski, Ph.D., Associate Professor, Department of Physics

---

Shiv N. Khanna, Ph.D., Professor, Department of Physics

Mohammad Hajaligol, Ph.D., Senior Scientist, RD&E, Phillip Morris USA

Nicholas P. Farrell, Ph.D., Professor, Chairman Department of Chemistry

---

Robert D. Holsworth, Ph.D., Interim Dean of Humanities and Science

---

F. Douglas Boudinot, Dean of the School of Graduate Studies

CARBON MONOXIDE OXIDATION ON NANOPARTICLE CATALYSTS AND GAS PHASE REACTIONS OF SMALL MOLECULES AND VOLATILE ORGANICS WITH METAL CATIONS

A Dissertation submitted in partial fulfillment of the requirements for the degree of Doctor of Philosophy at Virginia Commonwealth University

by

KHALED MOHAMMAD SAOUD
B.Sc., Yarmouk University, Jordan, 1990
M.Sc., Virginia Commonwealth University, USA, 2000

Director: M. SAMY EL-SHALL
PROFESSOR, DEPARTMENT OF CHEMISTRY

Virginia Commonwealth University
Richmond, Virginia
December 2004

Acknowledgement

There are many people that I would like to thank for supporting me during the course of my work and for making this thesis possible. I would like to dedicate this dissertation to my family: my parents Mohammad Saoud and Alia Maa'dleh who don't have a chance to go to school but they gave me the support and encouragement to achieve the highest level of education, and my wife Rola and my son Sahl who bring joy to my life and scarified there time to help carry out this work, and I don't forget my brothers and sisters for their endless support especially Riyadh Saoud for all his support through the hard and good times we have together.

I want to express a special thanks to my adviser Dr. M. Samy El-Shall for giving me the opportunity to carry out the work for my PhD and to discover the fascinating field of Nanotechnology. His wealth of ideas and constructive advice, his unique way to always find the right words of encouragement as well as his constant good humor and optimism gave me enormous energy and motivation.

I want to thank Dr. Garry Glaspell for those laborious hours in correcting my grammatical and spelling errors. A Special thanks to Dr. Mohammad Hajaligol who initiated my PhD project and supported me throughout my research and career at Philip Morris USA. I also would like to thank Dr. Firooz Rasouli, Dr. Sorajini Deevi, Dr. Alsion

Baski, Dr. Khanna, Dr. James Terner, Dr. Yehia Ibrahim, Dr. Hatem Mahmoud, Ahmed Elzatahry and Dr. Victor Abdelsayed for many discussions that benefited me greatly.

Finally I would like to thank the department of Chemistry and Philip Morris USA for the financial support during my graduate study at Virginia Commonwealth University.

Table of Contents

Page

List of Tables

Page

List of Figures

Page

Abstract

Carbon Monoxide Oxidation on Nanoparticle Catalysts and Gas Phase Reactions of Small Molecules and Volatile Organics with Metal Cations

By: Khaled Mohammad Saoud

A dissertation submitted in partial fulfillment of the requirements for the degree of Doctor of Philosophy at Virginia Commonwealth University.

Virginia Commonwealth University, 2004

Major Director: M. Samy El-Shall
Professor, Department of Chemistry

This dissertation demonstrates the application of a vapor phase method to synthesize supported and unsupported nanoparticle catalysts for CO oxidation. The method is based on the Laser Vaporization/Controlled Condensation (LVCC) technique. The first part of this dissertation presents the vapor phase synthesis and characterization of gold nanoparticles supported on a variety of oxide supports such as CeO_2, TiO_2, CuO and MgO. The results indicate that Au nanoparticles supported on CeO_2 exhibit higher catalytic activity than Au supported on other oxides. The high activity of the Au/CeO_2 catalyst is

attributed to the strong interaction of Au with CeO_2. The results also indicate that 5 % Au loading on CeO_2 has higher activity than 2% Au or 10% Au. When comparing the catalytic activity of Au/CeO_2 prepared by physical (LVCC) and chemical (deposition-precipitation) methods, it was found that the catalytic activity is higher for Au/CeO_2 prepared by the deposition-precipitation method.

The effect of alloying Au and Cu nanoparticles on the catalytic activity for low temperature CO oxidation was also investigated. The unsupported Au-Cu alloy nanoparticle catalyst exhibits higher catalytic activity than the activities of the individual components and their physical mixtures. The XRD data of Au-Cu alloy taken after the catalysis test indicates the formation of CuO within the bimetallic nanoparticles, which improves the catalytic activity of Au-Cu alloy nanoparticle.

The second part of this dissertation investigates the gas phase reactions of Au^+ and Cu^+ with CO, O_2 and H_2O molecules using the Laser Vaporization ionization, High-Pressure Mass Spectrometry (LVI-HPMS) technique. The gas phase reactions resulting from the interactions of Au^+ with CO and O_2 molecules are investigated. Although multiple additions of CO and O_2 molecules on Au^+ have been observed at room temperature, no evidence was found of the production of CO_2. This is attributed to the presence of water molecules which effectively replace the oxygen molecules on Au^+ at room temperature

Finally, the role of the metal cations Au^+ and Cu^+ in initiating the gas phase polymerization of butadiene and isoprene vapors was investigated.

1 : Introduction

Carbon monoxide and volatile organic compounds (VOC), such as butadiene and isoprene, are air pollutants emitted by many industrial sources, such as burning of wood and fuel with poor ventilation, and by natural sources including forest fires or volcanic eruptions [1-4]. CO and VOC are also significantly abundant in cigarette smoke.

The health effects associated with CO depends on its concentration and duration of exposure [5,6]. CO Concentrations of 10 to 100 ppm in ambient air can have many health effects on the general population [7]. The health effects associated with exposure to CO are due to its strong bond with the hemoglobin molecule, forming carboxyhemoglobin (COHb). COHb impairs the oxygen-carrying capacity of the blood by putting a strain on tissues with high oxygen demand, such as the heart and the brain. CO also binds to Cytochrome oxidase, which reduces the cells' ability to utilize oxygen [8].

Catalytic oxidation is one effective method of removing CO. Nanophase metal and metal oxide catalysts, with controlled particle size, high surface area, and more densely populated unsaturated surface coordination sites, could potentially provide significantly improved catalytic performance over conventional catalysts [9-13]. The large numbers of surface and edge atoms provide active sites for catalyzing surface reactions as shown in Figure 1. Highly non-stoichiometric oxide nanoparticles, such as CeO_{2-x}, provide a high oxygen vacancy concentration and active superoxide surface species. These nanoparticle oxides enable catalytic activation at significantly lower temperatures for the reduction of

sulfur dioxide and the oxidation of carbon monoxide [11,12]. Research in this area is motivated by the possibility of designing nanostructured catalysts that possess novel catalytic properties such as low temperature activity, selectivity, stability, and resistance to poisoning and degradation effects [9-13]. Such catalysts are essential for technological advances in environmental protection, improving indoor air quality, and in chemical synthesis and processing.

Since the catalytic properties of platinum were discovered by Faraday in 1835, transition metal oxide catalysts have been used as CO oxidation catalysts. Although CO has a small dipole moment and is only a weak donor, CO strongly bonds with transition metals and their oxides due to the electron donation from the 5σ carbon monoxide orbital to the metal, and the subsequent transfer of two electrons from the d metal atomic orbitals to the antibonding $2\pi^*$ CO orbital. This electron transfer is known as back-donation [14,15]. The CO adsorption on metal oxide surfaces under ambient conditions favored the site that contains a cation with low oxidation state. However, CO bonding to metal oxide via σ-donation to Lewis acid sites required very low temperatures [16]. CO reacts with pre-adsorbed or lattice oxygen to give CO_2. The molecular oxygen (O_2) is a powerful electron acceptor and can be molecularly or atomically adsorbed. Molecular adsorption occurs on n-type semi-conductive oxides, while atomic adsorption occurs on the defects such as oxygen vacancies on reduced transition and none-transition metal oxides[17-19]. However, these catalysts are less active and unstable in the presence of moisture and sulfur compounds than noble metal catalysts [20,21]. Precious metals such as (Pt, Pd) are well

known oxidation catalysts with high activity and stability, even in the presence of moisture and sulfur compounds, and they are usually used in gas exhaust emissions control [22].

Nanoparticles play important roles in many technological areas due to their unusual properties. These materials are characterized by small particle size and high surface area.

Depending on their size, shape, and preparation conditions, nanoparticles can exhibit unique properties (electrical, optical, magnetic, and catalytic) which are different from their bulk material properties [23-27]. The high surface area of the nanoparticles is associated with their surface structure and morphology. The surface of the nanoparticles contains a large number of defects. These defects have high surface energy sites as shown in Figure 1 and described by a model proposed by Somorjai [28]. The presence of structurally heterogeneous sites on the nanoparticles can greatly reduced the activation energy of CO oxidation reaction by the adsorption of CO molecules on these high energy sites.

Controlling the size and morphology in the synthesis of nanoparticles is crucial in achieving high surface area and small particle size. Many nanoparticle catalysts preparation methods are involved in the chemical and the physical techniques. However, the synthesis of nanoparticles of controlled size and composition have been achieved using laser vaporization controlled condensation (LVCC) method [26,29,30]. This technique (LVCC) uses laser vaporization of bulk materials, under controlled condensation conditions, to prepare a wide variety of metallic and semiconductor nanoparticles [26,29,30]

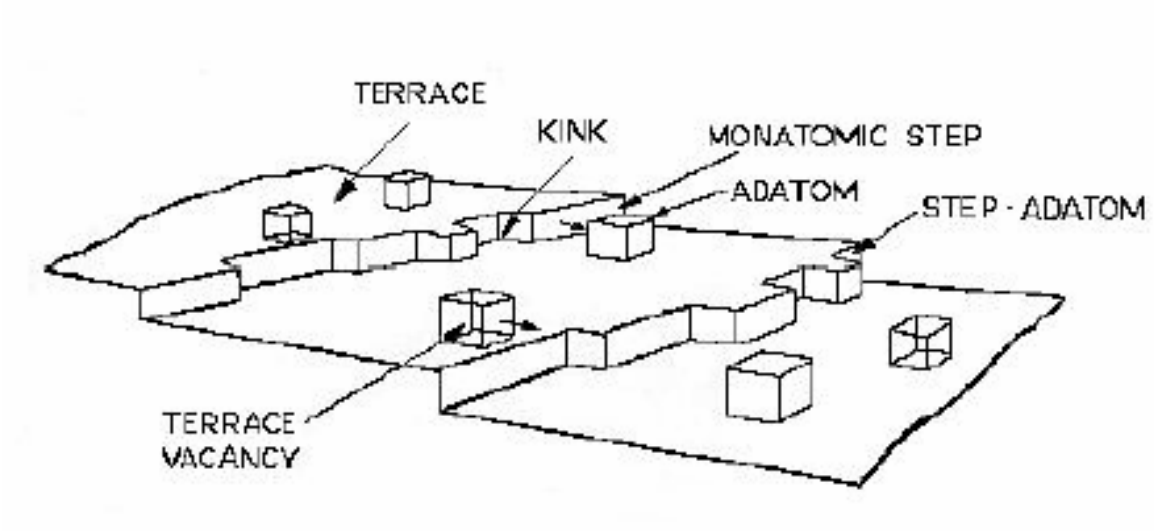

Figure 1: Model of heterogeneous solid surface of a nanoparticle having different surface sites defined by the number of the nearest neighbors [28].

2 : Experimental Techniques and Methods

This chapter describes the experimental techniques used in the synthesis and characterization of nanoparticle catalysts.

2.1 Catalyst Preparation

There are many techniques used to produce nanoparticles using both chemical and physical methods. In this work, laser vaporization controlled condensation (LVCC) was used as an example of a physical method and deposition precipitation (DP) was used as an example of a chemical method.

2.1.1 Physical method (Laser Vaporization Controlled Condensation (LVCC)

There are different physical methods used to produce nanoparticles from the vapor phase, such as sputtering, chemical vapor deposition, exploding wire, and laser vaporization controlled condensation[31]. These methods are based on the condensation of supersaturated metal vapors.

The LVCC has an advantage over typical thermal vaporization methods due to the production of a high density vapor of any metal or metal oxide targets. The advantages of the vapor phase synthesis are the contamination-free products (as compared to chemical reductions in solutions), the elimination of chemical precursors and solvents, and, in most cases, the production of highly crystalline nanoparticles [9,32-39]. The LVCC can be used to produce a wide variety of metals and supported metal nanoparticles with controlled size and composition [26,29,30]. El-Shall et al. introduced the LVCC method and demonstrated its use in producing nanoparticles of Si, Ge, MoO_3, and WO_3 with unique surface oxidation,

photochromic, and photoluminescence properties [39,40]. A schematic diagram and relevant components of the LVCC method are shown in Figure 2. In the LVCC method, a pulsed beam of the second harmonic (532 nm) Nd-YAG laser operated at 30 Hz (50-200 mJ/pulse laser power, 5 ns pulse duration) is focused on a target of interest. The target is placed in a chamber with well-defined temperature and pressure. The chamber consists of two horizontal, circular stainless-steel plates separated by a class ring. The chamber is usually filled with a pure carrier gas such as He or Ar or a mixture containing a known concentration of reactant gas such as O_2. The target is placed on the bottom plate where the temperature is maintained higher than the top plate and controlled by circulating water. The top plate can be cooled to 150 K using liquid N_2. The advantage of the temperature gradient between the two plates is to create a convection current; this current is further enhanced by using a heavy carrier gas under high pressure (10^3 torr). The pulsed metal vapor is generated by laser vaporization of the target. To achieve good reproducibility of the amount of vapor produced, the laser beam is moved on the target surface to expose new surface areas. After the laser pulse strikes the target and creates plasma, the ejected pulse of metal atoms interacts with the gas inside the chamber. Nucleation takes place immediately and results in the formation of nanoparticles.

Diffusion and convection currents prevent the particles from growing to larger particle sizes by removing them from the nucleation zone with high density. Temperature gradient, total pressure, and laser power (determined by the number density of the metal atoms in the vapor phase) control the size of the condensing particles. For example, 5 % Au/CeO_2 was prepared by physical mixture of (5%) Au and (95%) CeO_2 powders. The

sample was then pressed with high pressure to form a homogenous target. The laser power was measured using OPHIR optronics LTD., NOVA laser power monitor.

The catalyst samples as prepared by the LVCC method (fresh samples) were tested for activity by heating the samples in (3.60 wt. % of CO and 20.0 wt. % of O_2 balanced with helium) mixture, which is referred to as (run 1), cooled to room temperature, reheated again, and tested for activity (run 2).

2.1.2 Chemical method: (Deposition – Precipitation (DP))

In this method, 0.885 g of Hydrogen tetrachloroaurate (III) hydrate ($HAuCl_4$) was dissolved in water and slowly and homogenously precipitated by hydroxide ion from (NaOH) solution with pH between 6 and 10. CeO_2 powder (4.75 g) was suspended in water with pH between 6 and 10 by adding the NaOH solution drop wise and stirring for one hour, then the HAuCl4 solution was added to the CeO_2 solution drop wise; controlling the pH between 6 and 10 by adding NaOH. As a result, Au $(OH)_3$ precursor is deposited exclusively on CeO_2. Then the solution was washed, dried, and heated at 98 ^{0} C for one hour to produce Au metal on CeO_2 nanoparticles. This method is described in detail by Iizuka *et al* [41].

2.2 Catalyst Activity Measurements

The catalytic activity of each catalyst was carried out by using a flow tube reactor (length 50 cm, i.d. 0.9 cm) coupled to an infrared detector. A schematic diagram of the experimental setup is shown in Figure 3.

The catalyst sample is placed in a fixed bed between two pieces of quartz wool in the middle of a quartz tube. The flow tube is then placed inside a temperature programmer Thermolyne 21100 tube furnace. The sample temperature is monitored using an Omega K-type thermocouple inserted in the middle of the sample. Another thermocouple is built into the furnace to measure the furnace temperature. The temperatures and the concentration data are recorded by a Labview-based program. The sample temperature is always higher than the furnace temperature since the catalytic oxidation reaction of CO is exothermic. Therefore, all the data in this work are plotted as a function of sample temperatures.

The gas mixture flow rate is controlled by MKS digital flow meters. The effluent gases are analyzed using an Automated Custom System infrared gas analyzer. In these experiments, a gas mixture containing 3.60 wt. % of CO and 20.0 wt. % of O_2 balanced with helium was used. The mixture was flowed over the catalyst (100 CC/min) while the catalyst is heated to different temperatures. The effluent gases were introduced to the infrared gas analyzer. CO and CO_2 concentrations are measured based on the absorption of IR radiation. Transmittance is related to gas concentrations through Beer's law:

$$\tau(\nu) = I / I_0 = \exp\left[\left(-\alpha_g \nu\right) L\right] \tag{2.1}$$

I = intensity of radiation transmitted through the sample at a given wave number, ν, I_O = intensity of transmitted radiation with no sample, $\alpha_g(\nu)$ = absorption coefficient of the gas, and L = path length of the IR beam through the sample. The absorption $\alpha_g(\nu)$ is zero outside the gas absorption bands and is proportional to the gas concentration inside the absorption bands. CO has an absorption band at the characteristic wave number of 2200

cm^{-1}, and CO_2 has an absorption band at the characteristic wavenumber of 2350 cm^{-1}. By monitoring the change of the CO and CO_2 concentrations and plotting the normalized ratio (([CO] / [CO] + [CO_2]) * 100 %)) as a function of catalyst temperature, the catalyst activity can be measured.

The surface area of the catalyst was measured using five points N_2 physisorption using Brunauer, Emmett, Teller technique (BET) (Quantachrome Autosorb Automated Gas Sorption Unit). The crystallographic structure of the catalyst was analyzed using X-ray diffraction (XRD) (Philips X'Pert Pro Theta-Theta system operated at 45 kV and tube current of 40 mA). Scanning Electron Microscopy (SEM) was done using a Quantum DS-130S electron microscope. The Energy Dispersed X-ray (EDS) and the transmission electron microscope (TEM) images were obtained using a JOEL JEM-FXII TEM operated at 200kV. High-resolution TEM (HRTEM) images were obtained using a JOEL 4000EX operated at 400 kV. Typically, a drop of methanol-dispersed nanoparticles was placed on a carbon-coated copper grid, and left to dry. X-ray Photon Electron Spectroscopy (XPS) spectra were obtained using Physical Electronics Model 5700LSci ESCA spectrometer. Temperature Programmed Reduction (TPR) profiles where obtained using EPA Cincinnati AutoChem II 2920 V2.

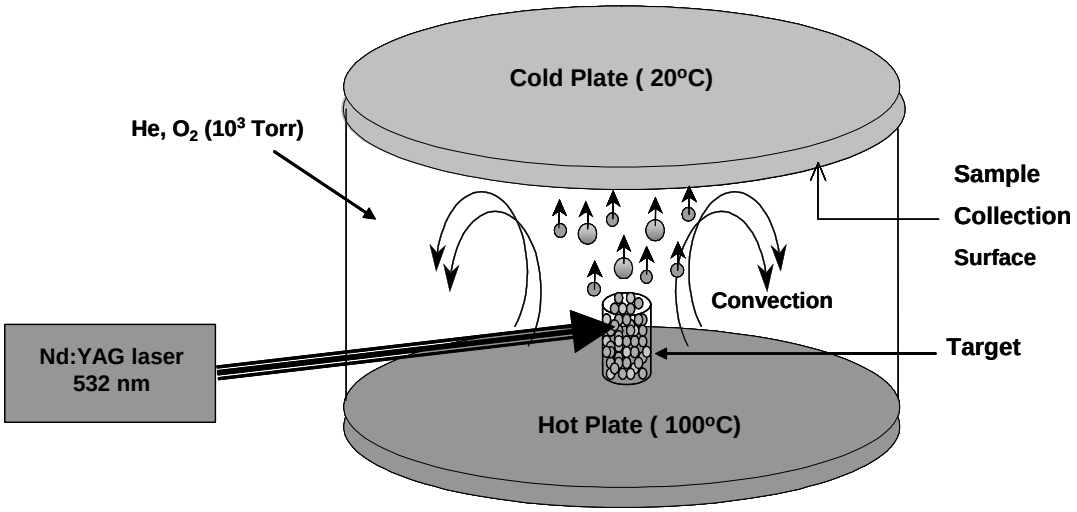

Figure 2: Experimental setup of Laser Vaporization Controlled Condensation (LVCC) method.

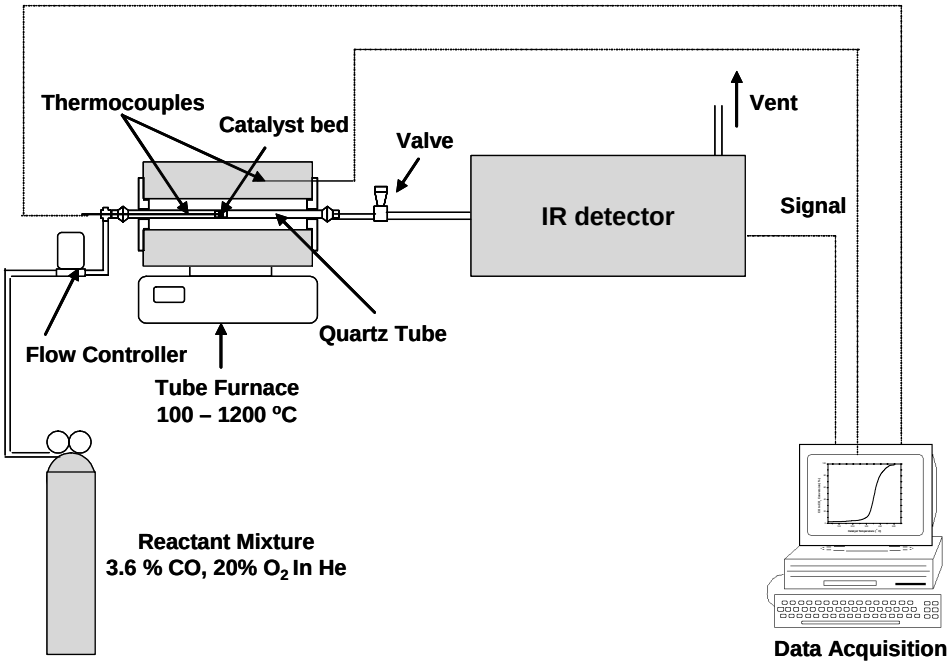

Figure 3: Experimental setup for catalysis experiment with relative components.

Part. I

3 : Low temperature CO oxidation on Au nanoparticle catalyst

3.1 Introduction

Gold is regarded as being catalytically inert [42,43]. However, Au catalyst, when dispersed on metal oxide support, are found to be 1000 times more active than Pt based catalysts in electrochemical and catalytic CO oxidation under a basic environment [44-48]. Metal oxide or activated carbon supported Au also promote many other reactions [42,49,50].

The low catalytic activity of Au is due to the filled 5d shells (i.e. [Xe] $4f^{14}$ $5d^{10}$ $6s^{1}$) as well as its high value of first ionization potential (i.e. 888 kJ/mole). For bulk gold, the formation enthalpy for Au_2O_3 is positive (ΔH_f = + 19.3 kJ/mol)[43], and therefore this oxide is instable. Based on the assumption that the initial chemisorption's enthalpies are linearly related to the formation enthalpies of stable metal oxides (the Tanaka-Tamaru rule), oxygen chemisorption on gold is impossible [51].

A number of studies have shown how nanoparticles of gold lose their metallic nature as their size decreases, the transition occurring at a size dependent on the chemical environment but, as mentioned previously, certainly somewhere between 1 and 3 nm, corresponding to a hemispherical cluster with somewhere between about 14 and 140 atoms [44-48]. The special electronic configuration of very small nanoparticles results from their physical dimensions being smaller than the characteristic dimension of the electron wave function of the bulk material. An Au cluster diameter of 3 nm size range is associated with the presence of a band gap, in contrast to bulk gold which has no band gap. The oxygen

affinity of Au to form stable metallic nanoclusters is increased, while other metals will normally be oxidized in this size range [52].

The catalytic activity of gold has been investigated by many researchers throughout the 20th century [53]. The hydrogen oxidation on Au was first observed in 1906 by W. A. Bone and R. V. Wheeler. In 1925, Bone and G. W Andrew were the first to report Au catalyzed CO oxidation. During the 50s and 60s, Au was mainly used as a hydrogenation catalyst. In the 70s, G. C. Bond, P. A. Sermon, and G. Paravano prepared small-dispersed Au particles on different metal oxide supports (MgO, Al_2O_3, and SiO_2). They found that some of the samples exhibited catalytic activity toward hydrogenation of alkenes at very low temperatures (e.g. 373 K) [54]. In the mid 70s, Ozin and McIntosh reported the first evidence of CO oxidation on Au neutral atoms; they proposed a gold complex containing a maximum of two Carbon monoxide ligands reacts with O_2 at very low temperatures (30-40 K) to form CO_2. These results were later used to develop a model for the mechanism of heterogeneously catalyzed CO oxidation [55,56]. In 1985 G. J. Hutching reported that Au is the most active catalyst for hydrochlorination of acetylene to vinyl chloride [57].

The initial evidence that supported Au, prepared by co-precipitation or deposition precipitation, being used for ambient temperatures CO oxidation was reported by Haruta in 1987 [46]. These results were the basis of Au catalysis research in the scientific world today.

The discovery of a highly active Au catalyst was based on a volcano-curve between the catalytic activity of metal oxides and the heat of metal oxide formation per one oxygen atom which corresponds to metal–oxygen (M-O) bonding strength [58,59]. They predicted that a combination of metals on the opposite side of the volcano Curve, Au and Ag have

weaker M-O bonds than PtO_2 with Mn, Fe, Co, Ni which have stronger bonding, can produce a complex oxide that is as active as PtO_2, which has the highest bonding strength. In fact, Au supported on transition metal oxides is found to be more active than PtO_2 for CO oxidation. Volcano plots of transition metals and there intermetallic synergetic effect has been studied thoroughly by Jaksic [60-62].

When gold is dispersed on a support with a high surface area, however, its catalytic activity has been found to increase significantly [63]. Since gold nanoparticles are thought to have negative surface charge, strong electrostatic interactions may be expected with metal oxides positively charged on the surface. For highly dispersed gold, oxidation states different from the metallic state might be stabilized under certain conditions, partially covalent bonds between gold and oxide lattices might be of importance for the observed increase in the catalytic activity of finely dispersed gold [49,64].

CO oxidation on Au nanoparticle catalyst is structure sensitive. Therefore, the catalyst preparation is very important for catalysis by Au nanoparticles. There are three major factors defining the selectivity and the rate of the reaction on the Au catalyst: the size of the Au particle, the selection of the support, and (most importantly), the contact structure of Au with the support (the length of perimeter interface) [65].

It was reported that active Au particles in the nanoscale size between [2 and 15 nm] stabilized by metal oxide. The crucial diameter of 2 nm, which corresponds to 3 or 4 atoms thick hemispherical shape Au particle setting on the support [49]. However, the particle size is very sensitive to pre-treatment conditions. The low temperature heat treatment of the catalyst is needed to convert the precursor to catalytically active species [66]. High

temperatures can cause Au particles to grow to larger sizes since the melting point of Au nanoparticle is less than the bulk [67-69]. Most active samples can be obtained without temperature heat treatment (calcinations) or calcinations at low temperatures.

The active site for CO oxidation on a Au nanoparticle catalyst is still unknown. Some studies suggest that the active site is the metallic Au^0 surfaces or Au^+ or both [70]. X-ray absorption fine structure (XAFS) studies of impregnated Au/γ-$Al2O_3$ and Au/MgO catalysts showed two phases of Au. A part structurally similar to Au^0; the rest is present in the form of two-dimensional or atomically dispersed Au structure carrying a formal charge of + 1 [71,72].

CO oxidation appears to occur with high reaction rates if CO, adsorbed on a gold particle, interacts with oxygen adsorbed on a highly reducible metal oxide support, with subsequent dissociation at the metal–support interface. Earlier studies suggested that Au supported on reducible oxides, such as iron oxide, cerium oxide and titanium oxide, has higher activity than Au supported on non-reducible oxides [42,73-75]. However, it has been reported recently that Au supported on non-reducible oxides such as magnesium oxide MgO has extremely high catalytic activity [76]. A strong (metal-support) interaction plays a very important role in enhancing the catalytic activity [77]. Many studies show that the metal–support interaction affects the electronic properties of supported noble metal catalysts, and changes the catalytic activity [78,79]. When the alkalinity of the support increases, there is a decrease in the metal ionization potential, (shift to lower binding energy) due to the electrostatic Coulomb interaction between the support material and the metal particle. A decrease in the ionization potential of the metal valence orbitals changes

the energy of the metal valence orbitals which alters the chemisorption energy. These changes in the chemisorption energy between the metal and adsorbate will affect the catalytic activity [78,79].

Among the metal oxides used as support for gold, ceria has not been widely investigated; on the other hand, ceria-containing materials have been widely studied for a number of heterogeneous catalytic reactions such as the treatment of exhaust gases from automobiles [80]. Ceria (CeO_2) is used as a promoter in the three-way catalyst (TWC) in the automotive emission control system and it can be used as a support for many oxidation catalysts [80,81]. The promoting role of cerium oxide is proposed to involve multiple processes, such as the enhancement of the noble metal dispersion and the stabilization of the support toward thermal sintering, as well as its direct participation in chemical processes like the water–gas shift reaction or the decomposition of nitrogen oxides, and in general, processes involving incorporation/removal of structural oxygen, which are denoted as the oxygen storage capacity (OSC) of the system. CeO_2 is a better support for noble metals than other catalysts such as Al_2O_3 because it prevents the sintering and improves the low temperature activity for CO oxidation[82]. CeO_2 has a high oxygen storage capacity, taking up oxygen under oxidizing conditions and releasing it under reducing conditions [22,83]. The ability of oxygen storage capacity results from the fact that CeO_2 can deviate from a stoichiometric formula to give a continuum of oxygen deficient non stoichiometric oxides CeO_{2-x} under the changing oxidizing or reducing conditions. The change of the oxidation state of cerium from +4 to +3 improves the oxidation of CO by providing oxygen or taking oxygen [84]. Noble metal catalysts such as Pt, Pd, and Rh,

supported on cerium oxide supports have been studied [85]. The results show that these catalysts exhibit high catalytic activities for CO oxidation and water gas shift reaction since they have higher oxygen storage capacity and reducibility as compared to pure ceria [86].

The Au/CeO_2 catalyst is a very active catalyst for CO oxidation and for redox reactions as reported by Flytzani-Stephanopoulos and coworkers [87] and by Luengnaruemitchai et al. [88]. Gardner et al. [89] reported high catalytic activity in CO oxidation at 75 ^oC for co-precipitated 20% Au/CeO_x; with negligible activity decay over 160 h. Lyn and Flytzani-Stephanopoulos [90] demonstrated the complete CO oxidation in air at room temperature on a 5 % $Au/Ce(La)O_x$ catalyst calcined in air at 500–600 ◦C. Dekkers et al. [91] showed an increased catalytic activity in CO oxidation on silica- and alumina-supported Au samples when a 10% CeO_x was subsequently impregnated on the parent catalysts. More recently, Bera and Hegde [92] reported complete CO oxidation below 200 ◦C over thermally treated Au/CeO_x prepared by the solution-combustion method. Moreover, the activity and selectivity of Au/CeO_x for low temperature (40–80 ◦C) CO oxidation in hydrogen-rich reformer gas were found by Han et al. [93] to be higher than those of conventional Pt/Al_2O_3 catalysts. Au/CeO_2 shows enhanced catalytic activity towards the oxidation of selected volatile organic compounds (VOC), which is related to the capacity of gold nanoparticles to weaken the Ce-O bond, therefore increasing the mobility and the reactivity of the surface lattice oxygen which leads to oxidation of VOC's through the Mars-Van Krevelen reaction [94].

3.2 Experimental results

3.2.1 Low temperature CO oxidation on Au nanoparticle catalyst

Gold has a face-centered cubic (FCC) crystal structure with a lattice constant of 0.408 nm [95,96]. Figure 4 compares the X-ray diffraction pattern of Au bulk material with the Au nanoparticles prepared by LVCC. The typical characteristic planes (111), (200), (220), (311) of FCC crystal lattice are retained in Au nanoparticles, which is similar to Au bulk structure. However, the diffraction peaks of Au nanoparticles are broader compared to the bulk Au. This broadening is due to their small particle size.

A Transmission Electron Microscopy (TEM) micrograph of Au nanoparticles as prepared by LVCC method is shown in Figure 5. The micrograph shows two different structures, spheres and web-like structure.

Figure 6 compares the x-ray diffraction patterns of Au nanoparticles before and after heat treatment in CO/O_2 mixture. The diffraction patterns indicate that Au nanoparticles don't oxidize.

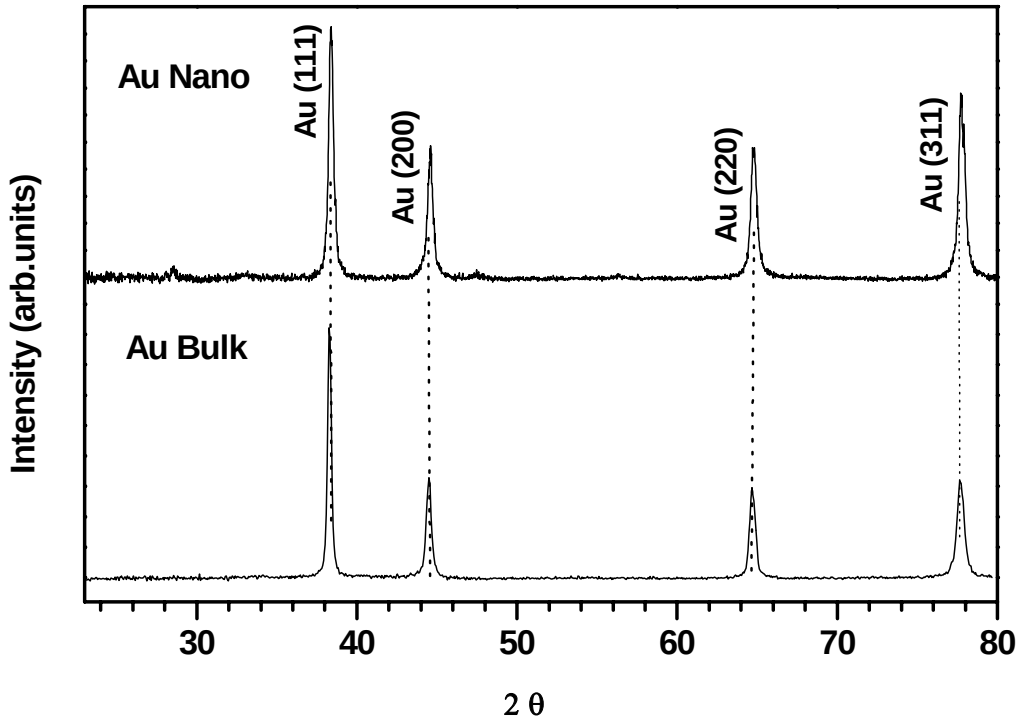

Figure 4: Comparison between X-ray diffraction pattern of Au bulk material and Au nanoparticles prepared by LVCC.

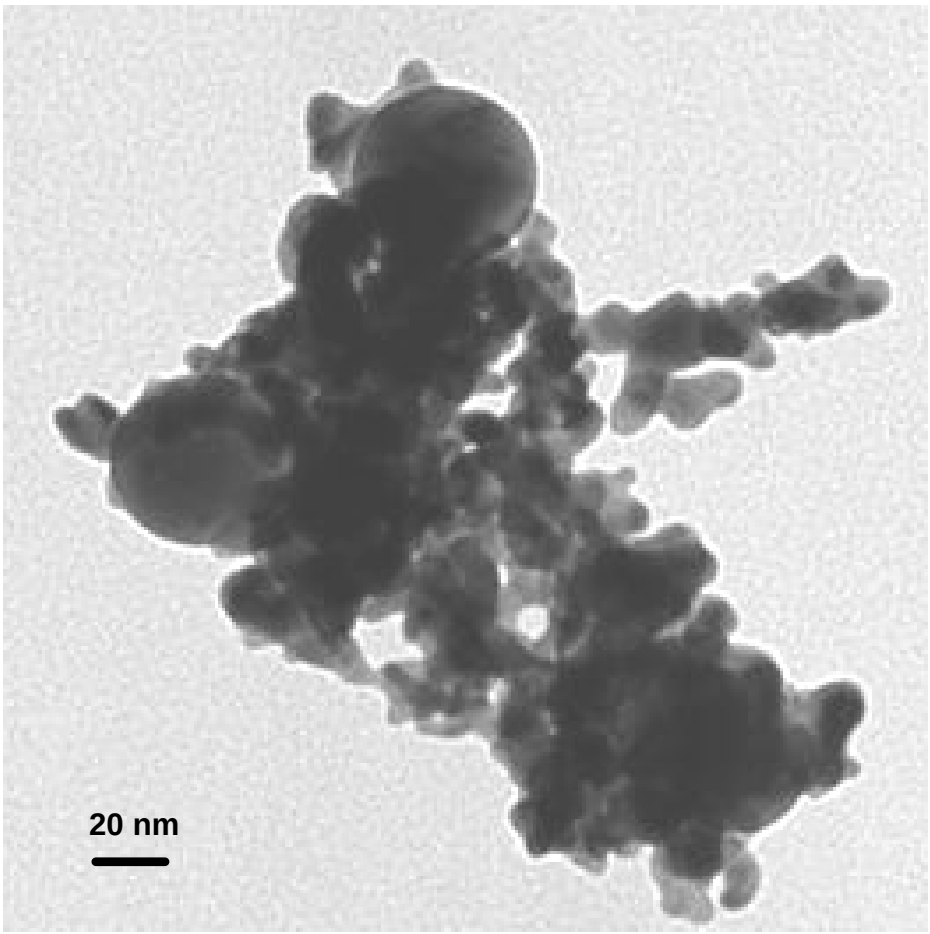

Figure 5: TEM of Au nanoparticles as prepared by LVCC method.

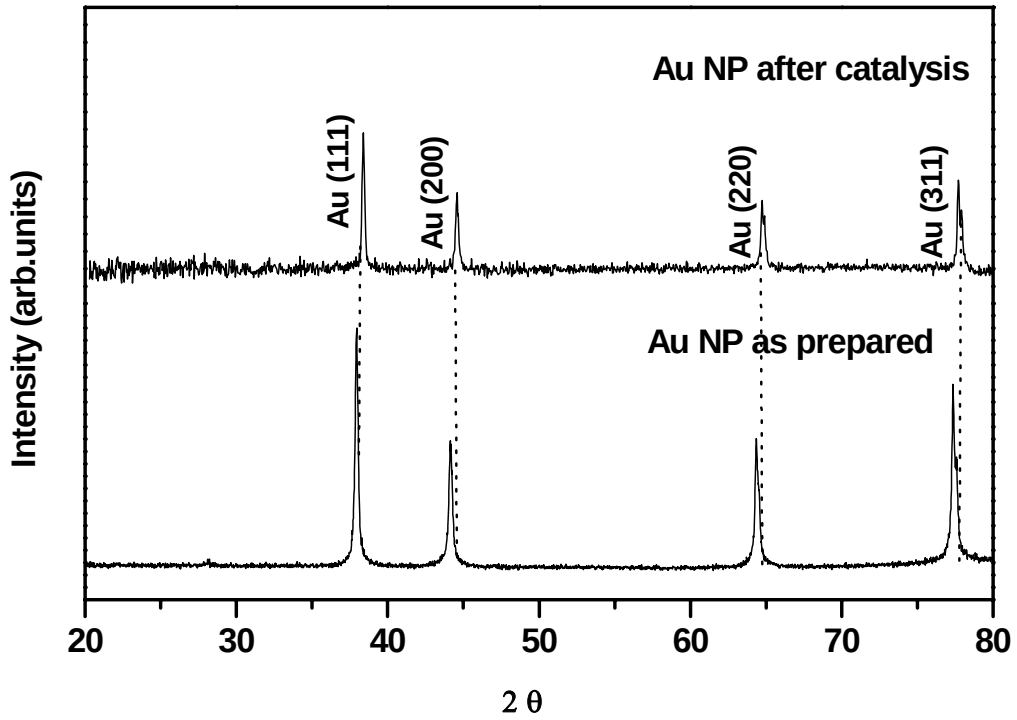

Figure 6: Comparison between X-ray diffraction patterns of Au nanoparticles before and after catalysis (after heat treatment in CO/O_2 mixture).

3.2.2 CO oxidation on supported Au nanoparticle catalyst

A wide range of supported gold catalysts on different metal oxide supports have been studied for CO oxidation [75,76,97,98]. By varying the support for the gold, a high range of control over the reactions is available. Another interesting property of the support is the ability to disperse Au particles. To examine the effect of support, the catalytic activities of Au supported on different metal oxide nanoparticle catalysts will be measured using the flow reactor Infrared spectrometry system shown in Figure 3. Metal loading is also important in the catalytic performance of the catalyst. The effect of Au loading will be examined by varying the percentage of Au supported on the metal oxide that exhibits the highest catalytic activity.

Depending on the interaction between the Au nanoparticles and the support material, Au nanoparticle catalyst can exhibit a variety of conversion percentages. To examine the effect of the Au-support interaction, the catalytic activity of Au supported on the metal oxide that exhibits the highest catalytic activity will be compared to the catalytic activities of unsupported Au and support nanoparticles.

After optimizing the support and metal loading, we will evaluate the catalytic performance of the best catalyst in the presence of volatile organic compounds such as butadiene and isoprene will be evaluated.

The initial work in this dissertation was carried out using flow tube mass spectrometry reactor as shown in Appendix A.

3.2.3 Effect of Support

The effects of the oxide support on the catalytic activity of Au nanoparticles prepared by the LVCC method have been investigated. The X-ray diffraction patterns of 5 wt. % Au supported on different metal oxides as prepared by LVCC method at 200 Torr of Ar are shown in Figure 7. It is clear that Au peaks can be distinguished beside the support peaks. The peak intensities for Au supported on ZrO_2, Al_2O_3, and SiO_2 are higher than Au supported on CeO_2 , where Au peaks are almost not observable. These results indicate that Au nanoparticles are well dispersed in CeO_2 and less dispersed in other supports. Also this is indicates that depending on the support, Au particles can have different sizes as reported in the literature [75,76].

Figure 8 describes the catalytic activities of nanoparticle catalysts containing 5% Au on different metal oxide supports (run 1) as prepared by LVCC method in 200 Torr Ar using the flow reactor IR spectrometry system. Table 1 summarizes the catalytic activities of nanoparticle catalysts containing 5% Au on different metal oxide supports (run 1) as prepared by the LVCC method. The Au/CeO_2 catalyst has the highest activity, followed by Au/Al_2O_3, Au/ZrO_2, and finally Au/SiO_2. The light-off temperature of 5% Au/CeO_2 nanoparticles is 214 ^{0}C, reaches 50% conversion at 243 ^{0}C, and a 99% conversion at 358 ^{0}C. In the second run, the conversion curves are different. As shown in Figure 9 the Au/CeO_2 catalyst has the highest activity followed by Au/ZrO_2, Au/Al_2O_3 and finally Au/SiO_2. The light-off temperatures in the cases of Au/CeO_2, and Au/ZrO_2 systems are shifted downward to the lower temperature region while in case of Au/Al_2O_3, and Au/SiO_2 they are shifted to a higher temperature region. The maximum conversion percentage

increases by 1 % for the Au/CeO2 system while it increases by 10 % for the Au / ZrO_2 system and decreases sharply in case of Au / Al_2O_3 and Au / SiO_2. For comparison, in the second run, the light-off temperature of 5% Au/CeO_2 nanoparticles shifted downward to a lower temperature region by about 181 ^{0}C to 33.5 ^{0}C and reached 50% conversion at 76 ^{0}C, and 100% conversion at 323 ^{0}C. Table 2 summarizes the catalytic activities of nanoparticle catalysts containing 5% Au on different metal oxide supports (run 2).

The high activity of the Au/CeO_2 nanoparticle catalyst is attributed to the strong interaction between Au and CeO_2 and to the oxygen storage capacity and redox properties of CeO_2 nanoparticles. The interaction between Au and the supports depends on the electronic structure of the support. In the case of a semiconductive metal oxide support, such as CeO_2 and ZrO_2, Au is more stable than in the case of an insulating support, such as Al_2O_3 and SiO_2.

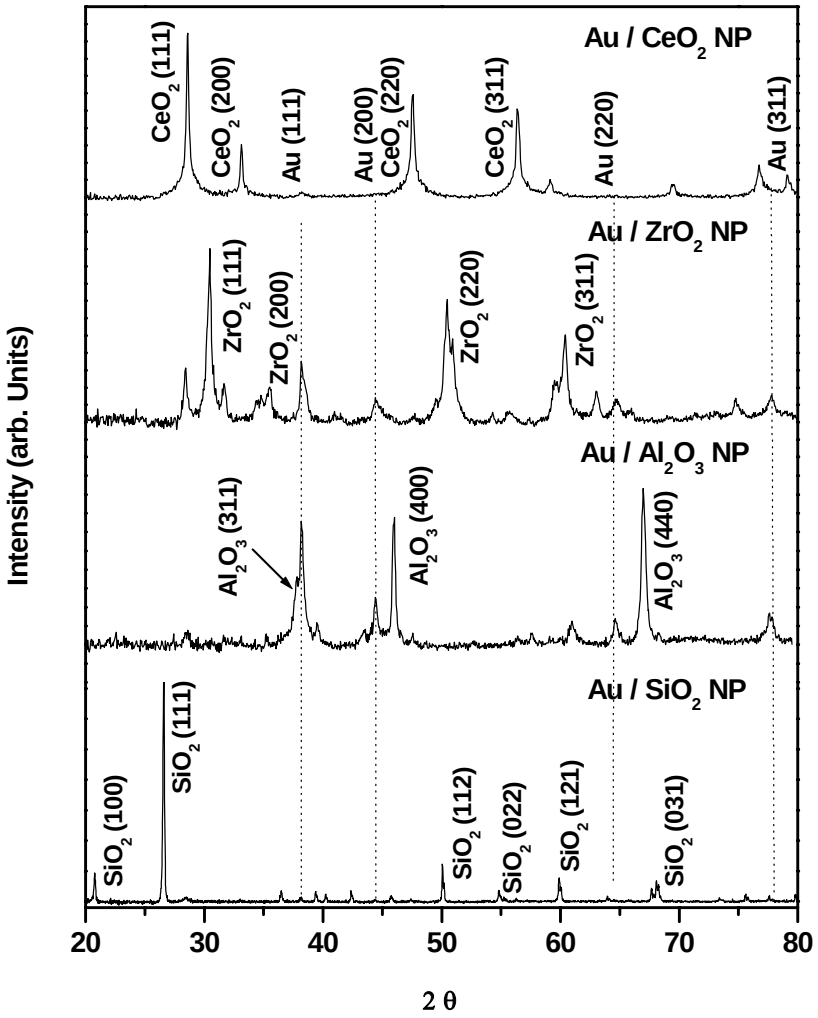

Figure 7: X-ray diffraction patterns of Au nanoparticles supported on different metal oxide supports as prepared by the LVCC method at 200 Torr of Ar.

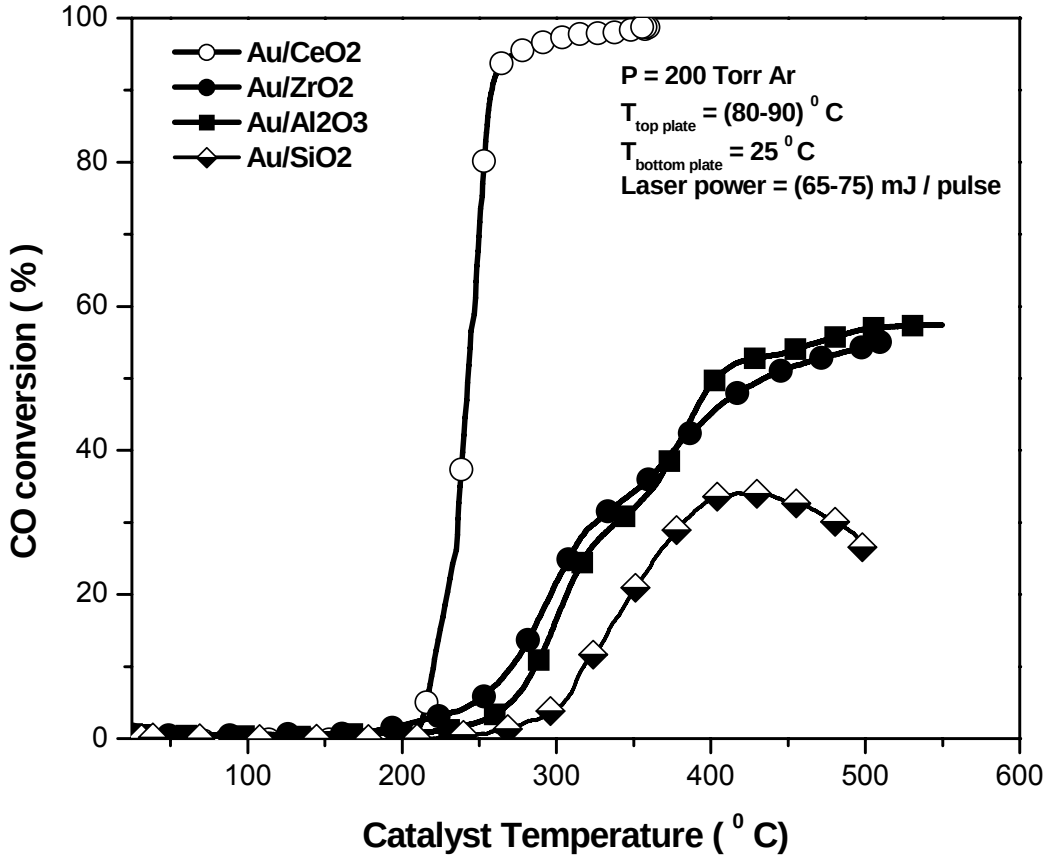

Figure 8: Catalytic activities of nanoparticle catalysts containing 5% Au on different metal oxide supports as prepared by the LVCC method in 200 Torr Ar (run 1).

Table 1 summarizes the catalytic activities of nanoparticle catalysts containing 5% Au on different metal oxide supports as prepared by the LVCC method in 200 Torr Ar (run 1).

Sample	3% Conversion Light-off Temp. (^{o} C)	50 % Conversion Temp. (^{o} C)	Maximum Conversion (%)	
			Temp. (^{o} C)	Conversion
Au/CeO_2	213.7	242.5	357.7	98.9
Au/ZrO_2	222.5	434.8	508.8	54.9
Au/Al_2O_3	256.5	404.0	546.5	57.4
Au/SiO_2	291.3	-	431.4	34.1

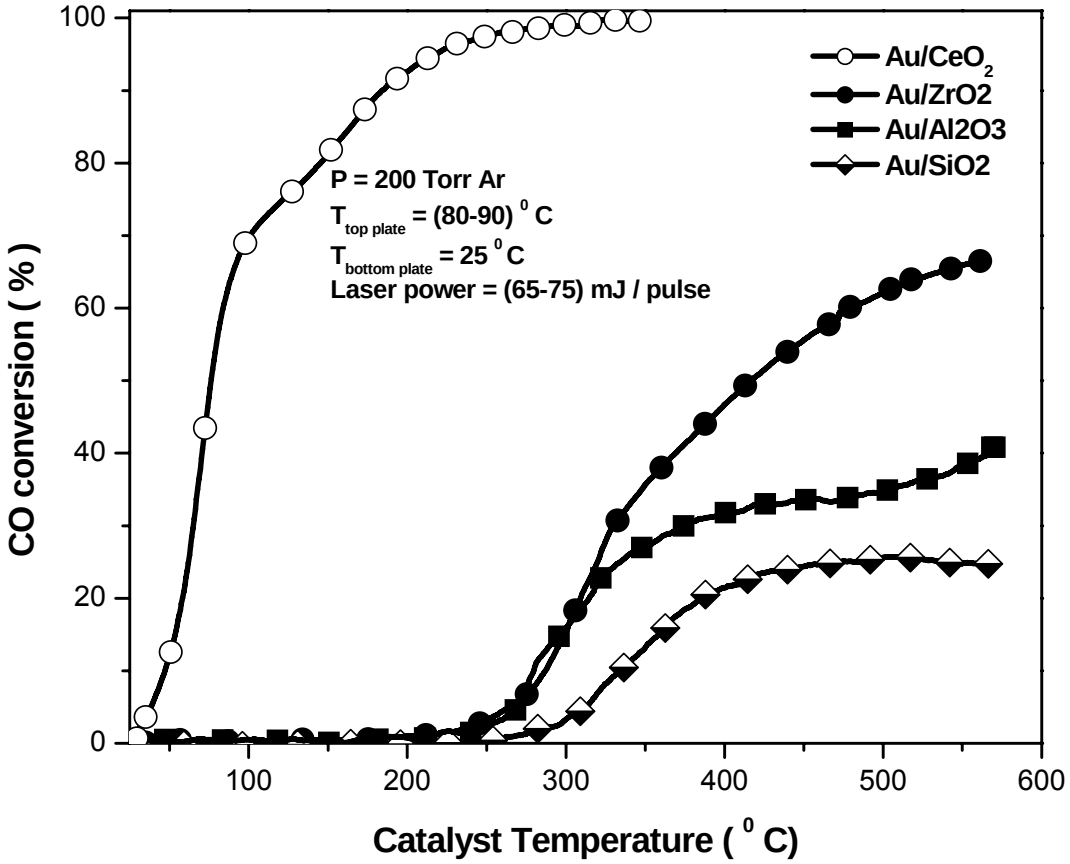

Figure 9: Catalytic activities of nanoparticle catalysts containing 5% Au on different metal oxide supports (run 2) prepared by the LVCC method in 200 Torr Ar using the flow reactor IR spectrometry system.

Table 2 summarizes the catalytic activities of nanoparticle catalysts containing 5% Au on different metal oxide supports by the LVCC method in 200 Torr Ar after heat treatment (run 2).

Sample	**3% Conversion Light-off Temp.(^{o} C)**	**50 % Conversion Temp. (^{o} C)**	**Maximum Conversion (%)**	
			Temp. (^{o} C)	**Conversion**
Au/CeO_2	33.5	76.4	323.2	99.7
Au/ZrO_2	249.0	416.4	561.2	66.5
Au/Al_2O_3	256.8	-	565.9	40.3
Au/SiO_2	298.4	-	494.9	25.6

3.2.4 Effect of Au loading

Since Au supported on CeO_2 exhibits higher catalytic activity than Au supported on other metal oxide supports, it is important to investigate the Au loading that gives the highest activity. Figure 10 shows X-ray diffraction patterns of different Au loading in CeO_2 as prepared by the LVCC method at 200 Torr of Ar. X-ray diffraction patterns show both crystalline CeO_2 peaks and crystalline Au peaks. However, the intensities of Au peaks increases as the Au loading increases, as expected. Also, the peak broadening in both CeO_2 is attributed to their small size. For Au peaks, the broadening decreases as the Au loading increases which is attributed to the nucleation of small Au particles to larger particles. TEM micrographs, shown in Figure 11, support the diffraction data which show that Au particle size increases as the Au loading increases and that it transforms from island growth for 2 % Au to three dimensional growths for 5, 10 % Au loading. However for 10 % Au loading there is excess Au beside the Au setting on spherical CeO_2 that nucleates to form large Au particles which is separated from the spherical particles. For the spherical particles, Au alters new types of morphology where new faces of spherical particles start emerging, which is considered as a precursor for new phase of growth of Au on CeO_2.

The catalytic activities of the Au/CeO_2 system with different Au loading percentages (2, 5, and 10 %) as prepared by the LVCC method in 200 Ar (run 1) are tested using the flow reactor IR spectroscopy, and are shown in Figure 12. The light-off temperature of 5 % Au/CeO_2 is higher than 2 % Au/CeO_2 followed by 10 % Au/CeO2 and

the conversion percentage of 2 % Au/CeO2 is higher than 5 % Au/CeO_2 followed by 10 % Au/CeO_2. The overall activity curve of 5 % Au loading shows a higher conversion than 2% Au and 10 % Au. Table 3 summarizes the catalytic activities of Au/CeO_2 nanoparticle catalyst with (2%, 5%, and 10%) Au loading as prepared by LVCC method in 200 Torr Ar (run 1). These results can be explained based on the X-ray patterns and TEM micrographs where the 2 % Au particles are small islands and the number of these particles are insufficient to fill the entire sites on a CeO_2 surface and are perhaps less active sites for CO oxidation reaction to occur, which is reflected in the conversion curve. For 10 % Au loading, there is excess gold that caused Au particles to grow to larger particle size and separate from the CeO_2 which reduced their activity. 5 % Au is the optimal loading to fill all vacant sites on a CeO_2 surface and form 3-D particles of Au with strong contact with CeO_2. In the second run, as shown in Figure 13, the 5 % Au/CeO_2 system shows higher activity than the 2 % Au/CeO_2 system, followed by the 10 % Au/CeO_2 system. The catalytic activities of different Au loading on CeO_2 prepared by LVCC at 200 Torr Ar (run 2) are summarized in Table 4. The conversion curves of all catalysts are shifted to a lower temperature region. For comparison, the light-off temperature for the 5 % Au/CeO_2 is 33.5 ^{o} C, 53.2 ^{o} C for 2 % / CeO_2, and finally is 117 ^{o} C for 10 % / CeO_2. The maximum conversion is 99.7 % at 323.2 ^{o} C for 5 % Au/CeO2, 99.9 % at 258.2 ^{o} C for 2 % / CeO_2, and finally 94.1% at 361 ^{o} C for the 10 % / CeO_2 system. The temperature shift is due to the reduction of the active component which enhanced the metal-support interaction, and the removal of the contaminants and moisture which improve the active site.

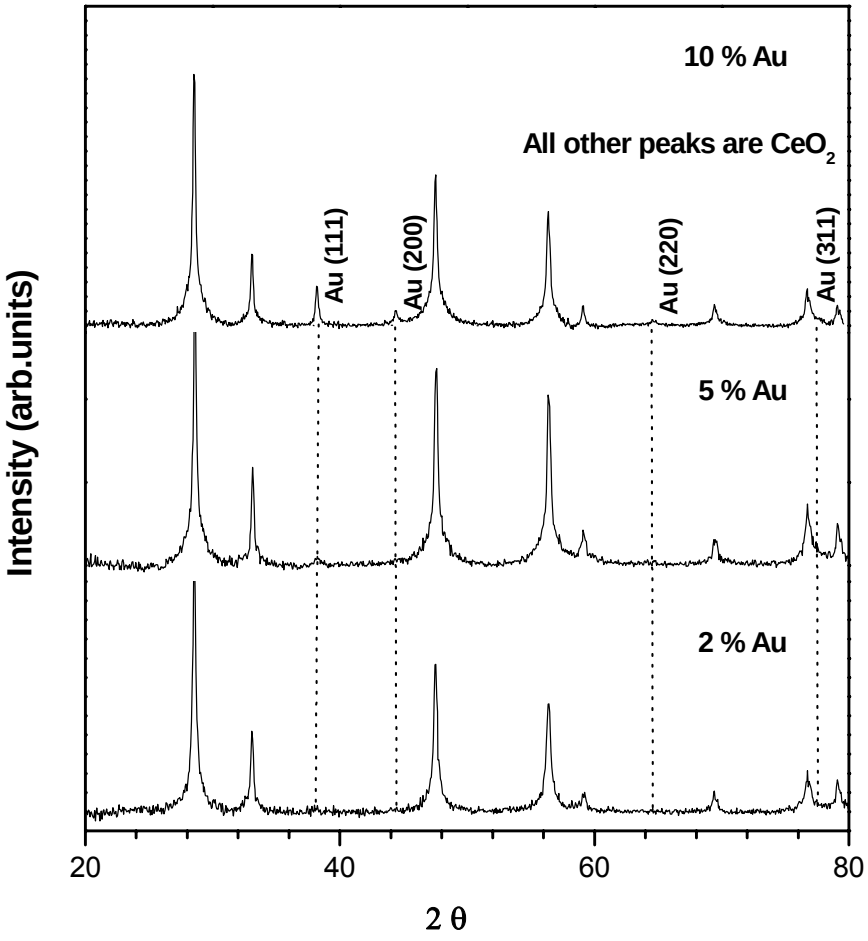

Figure 10: Comparison of X-ray patterns of different Au loading supported on CeO_2 as prepared by the LVCC method at 200 Torr Ar.

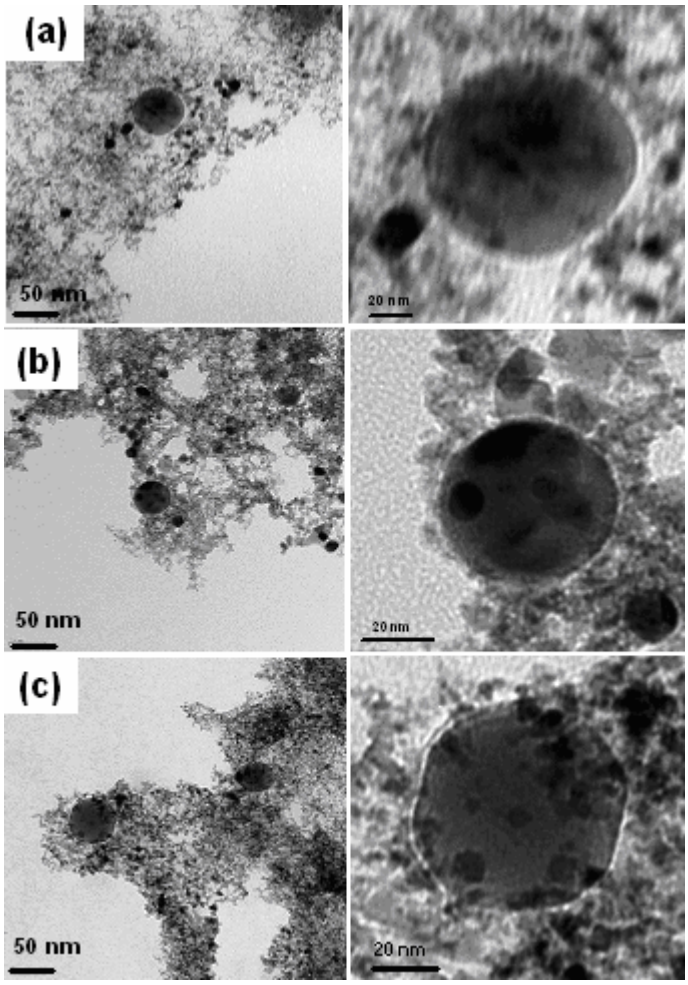

Figure 11: TEM micrographs of different Au loading supported on CeO_2 as prepared by the LVCC method at 200 Torr Ar a) 2 % Au b) 5 % Au c) 10 % Au.

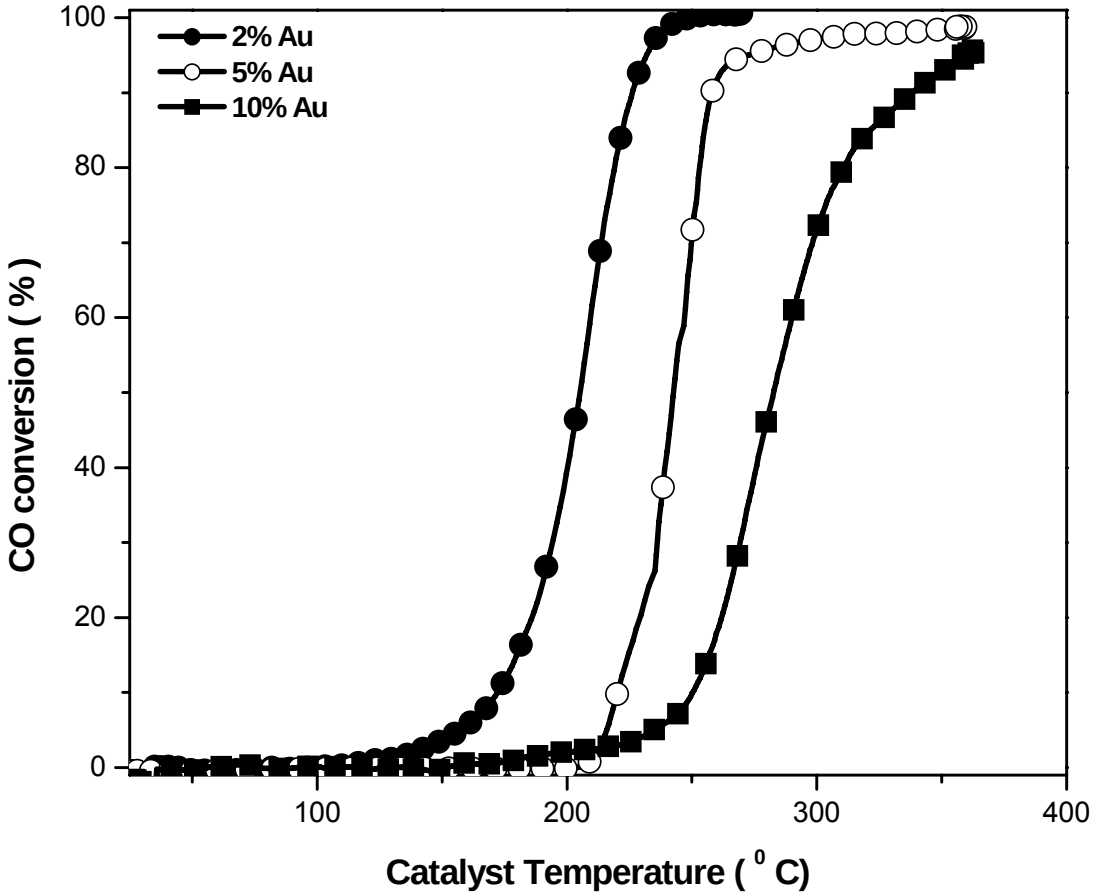

Figure 12: Catalytic activities of Au/CeO_2 nanoparticle catalyst with (2%, 5%, and 10 % Au) as prepared by the LVCC method at 200 Torr Ar (run 1).

Table 3 summarizes the catalytic activities of the Au/CeO_2 nanoparticle catalyst with (2%, 5%, and 10%) Au loading as prepared by the LVCC method in 200 Torr Ar.

Sample	**3% Conversion Light-off Temp. (^{o} C)**	**50 % Conversion Temp. (^{o} C)**	**Maximum Conversion (%)**	
			Temp. (^{o} C)	**Conversion**
2% Au	145.9	204.2	249.8	100
5% Au	213.7	242.5	357.7	98.8
10% Au	220.0	283.0	358.4	95.0

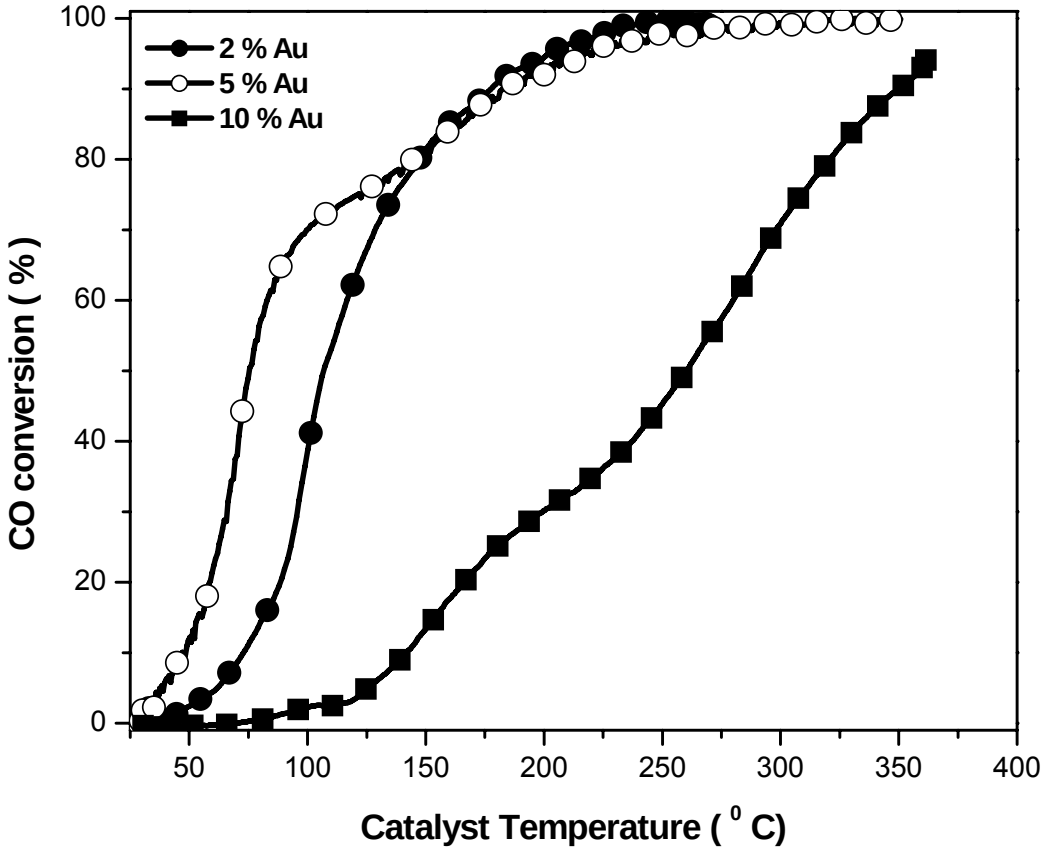

Figure 13: Catalytic activities of the Au/CeO_2 nanoparticle catalyst with (2%. 5%, and 10 % Au) prepared by the LVCC method at 200 Torr Ar (run 2).

Table 4 summarizes the catalytic activities of the Au/CeO_2 nanoparticle catalyst with (2%, 5%, and 10%) Au loading prepared by the LVCC method in 200 Torr Ar after heat treatment in CO/O_2 mixture (run 2).

Sample	**3% Conversion Light-off Temp. (^{o} C)**	**50 % Conversion Temp. (^{o} C)**	**Maximum Conversion (%)**	
			Temp. (^{o} C)	**Conversion**
2% Au	53.2	107.5	258.2	99.9
5% Au	33.5	76.4	323.2	99.7
10% Au	117.6	260.1	361.0	94.1

3.2.5 Effect of Au-support Interaction

Although the individual Au and CeO_2 nanoparticles showed high catalytic activities, the physical mixture of Au nanoparticles with CeO_2 nanoparticles did not exhibit any enhanced activity, as shown in Figure 14 (run 1) and Figure 15 (run2). Table 5 and Table 6 compare the catalytic activity of the supported Au/CeO_2 nanoparticles prepared by the LVCC method (run 1, and 2) with the activities of individual Au nanoparticles, CeO_2 nanoparticles, and the 5% Au nanoparticles in a 95 % CeO_2 nanoparticles mixture. After the heat treatment (run 2), the conversion curve is shifted to lower temperature region for Au/CeO_2 nanoparticles prepared by the LVCC method, while there is no significant shift for the bulk mixture. The very different activity of the physical mixture of a 5% Au and 95% CeO_2 nanoparticles from that of the 5% Au/CeO_2 nanoparticles prepared by the LVCC clearly indicates that laser vaporization of the mixed $Au\text{-}CeO_2$ target under the appropriate LVCC conditions can produce Au nanoparticles supported on CeO_2 nanoparticles with significant metal-support interaction. This effect will be investigated later using the Temperature Programmed Reduction (TPR) experiment.

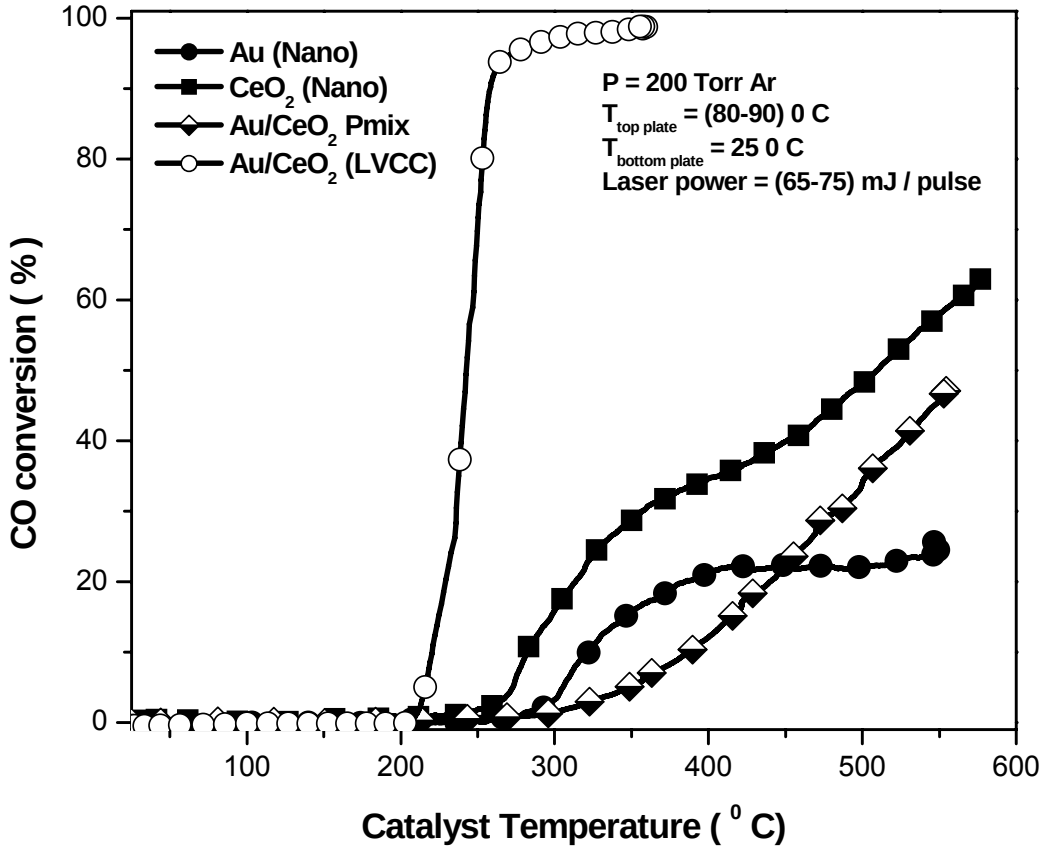

Figure 14: Catalytic activities of the supported Au/CeO_2 nanoparticles prepared by the LVCC method (run 1) and the individual Au nanoparticles, CeO_2 nanoparticles, and the 5% Au nanoparticles in a 95 % CeO_2 nanoparticles mixture.

Table 5 compares the catalytic activities of the supported Au/CeO_2 nanoparticles prepared by the LVCC method (run 1) and the individual Au nanoparticles, CeO_2 nanoparticles, and the 5% Au nanoparticles in a 95 % CeO_2 nanoparticles mixture.

Sample	**3% Conversion Light-off Temp. (^{o} C)**	**50 % Conversion Temp. (^{o} C)**	**Maximum Conversion (%)**	
			Temp. (^{o} C)	**Conversion**
Au (Nano)	298.8	-	546.7	25.7
CeO_2 (Nano)	265.0	509.6	577.2	63.3
Physical Mixture	323.8	-	555.3	47.7
Au/CeO_2 (LVCC)	213.7	242.5	357.7	98.9

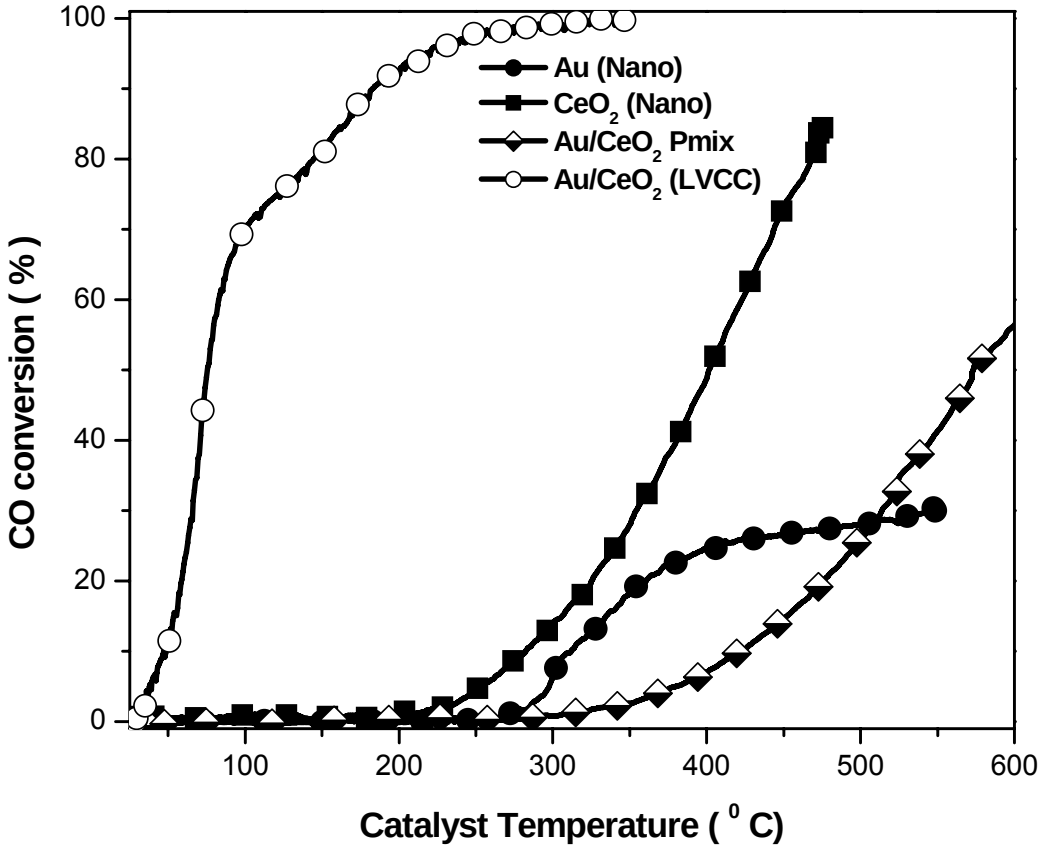

Figure 15: Catalytic activities of the supported Au/CeO_2 nanoparticles prepared by the LVCC method (run 2) and the individual Au nanoparticles, CeO_2 nanoparticles, and the 5% Au nanoparticles in a 95 % CeO_2 nanoparticles mixture.

Table 6 compares the catalytic activities of the supported Au/CeO_2 nanoparticles prepared by the LVCC method (run 2) and the individual Au nanoparticles, CeO_2 nanoparticles, and the 5% Au nanoparticles in a 95 % CeO_2 nanoparticles mixture.

Sample	**3% Conversion Light-off Temp. (^{o} C)**	**50 % Conversion Temp. (^{o} C)**	**Maximum Conversion (%)**	
			Temp. (^{o} C)	**Conversion**
Au (Nano)	289.4	-	549.4	30.0
CeO_2 (Nano)	240.1	402.1	474.8	84.1
Physical Mixture	355.9	573.3	600	56.5
Au/CeO_2 (LVCC)	33.5	76.4	330.2	99.8

3.2.6 Effect of pressure and support at 1500 Torr

Since 5 % Au supported on CeO_2 nanoparticle catalyst shows higher activity than 5 % Au supported on other metal oxide supports, we investigate the effect of pressure on the catalytic activity of this system was investigated using flow reactor IR spectroscopy as shown in Figure 16 and Figure 17. It is clearly indicated that the overall catalytic activity, of 5 % Au supported on CeO_2 nanoparticle catalyst prepared at 1500 is higher in both run 1 and run 2 than the corresponding Au/CeO_2. The light-off temperature in run 1 is 50 ^{o}C for the 1500 Torr sample and 27 ^{o}C in run 2, while light-off temperature in run 1 is 214 ^{o}C for the 200 Torr sample and 33.5 ^{o}C in run 2. These results can be attributed to the possibility of a small leak when the sample is prepared at 200 Torr, which effects the catalyst performance by blocking some of the active sites, while the sample prepared in 1500 Torr eliminated this effect. When comparing the full conversion temperature, the sample prepared at 1500 Torr reached the full conversion at 233 ^{o}C in run 1 and 211 ^{o}C in run 2, while for the sample prepared at the 200 Torr reached the full conversion at 360 ^{o}C in run 1 and 323 ^{o}C in run 2. Table 7 and Table 8 summarize the catalytic activities of 5 % Au/CeO2 prepared by LVCC at 200 and 1500 Ar (run 1 and run 2).

Since 5 % Au supported on CeO_2 nanoparticle catalyst prepared at 1500 Torr shows enhanced activity over the catalyst prepared at 200 Torr, the effect of using a different supports at 1500 Torr than the supports we used previously was explored. Figure 18 shows X-ray diffraction patterns of 5 wt. % Au supported on different metal oxides as prepared by the LVCC method in 1500 Torr Ar. It is obvious that Au peaks are

distinguishable in all patterns except for the Au/CeO_2 and Au/MgO systems which is an indication of a high order of disparity and small particle size. The Au peaks in the Au/TiO_2 system have a high intensity which is indication of large particle size and less dispersion. Figure 19 shows the catalytic activities of 5 % Au supported on CeO_2, CuO, MgO, and TiO_2 as prepared by LVCC in 1500 Torr Ar atmosphere and using flow reactor IR spectroscopy. 5 % Au supported on CeO_2 shows the highest activity followed by 5 % Au supported on CuO, TiO_2, and finally MgO. The catalytic activities of 5 % Au supported on CeO_2, CuO, MgO, and TiO_2 as prepared by the LVCC method (run 1) are summarized in Table 9. These results can be explained based on the nature of the support material where CeO_2, TiO_2, and CuO are active supports, and while MgO is inert. In the second run, the catalytic activities are enhanced as a result of removing the moisture and improving the active site, and the reduction of the active component, except for the Au / MgO system, the catalytic activity is decreased due to the sintering effect, as shown in Figure 20. The catalytic activities of 5 % Au supported on CeO_2, CuO, MgO, and TiO_2 are summarized in Table 10.

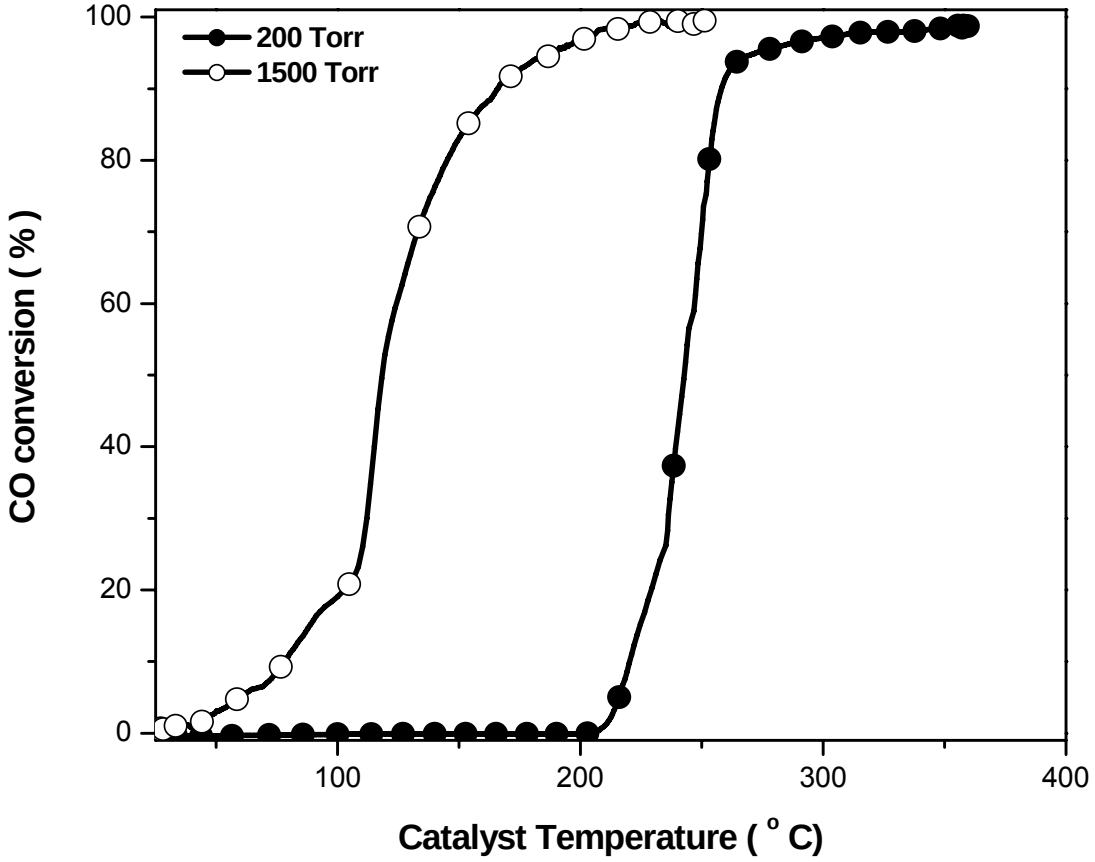

Figure 16: Catalytic activities of 5 % Au/CeO2 as prepared by LVCC in 200 and 1500 Ar (run 1).

Table 7 summarizes the catalytic activities of 5 % Au/CeO2 as prepared by LVCC in 200 and 1500 Ar (run 1).

Sample 5%Au/CeO_2	**3% Conversion Light-off Temp.(^{o} C)**	**50 % Conversion Temp. (^{o} C)**	**Maximum Conversion (%)**	
			Temp. (^{o} C)	**Conversion**
200 Torr	213.7	242.5	357.7	98.8
1500 Torr	50.2	118.2	233.2	99.5

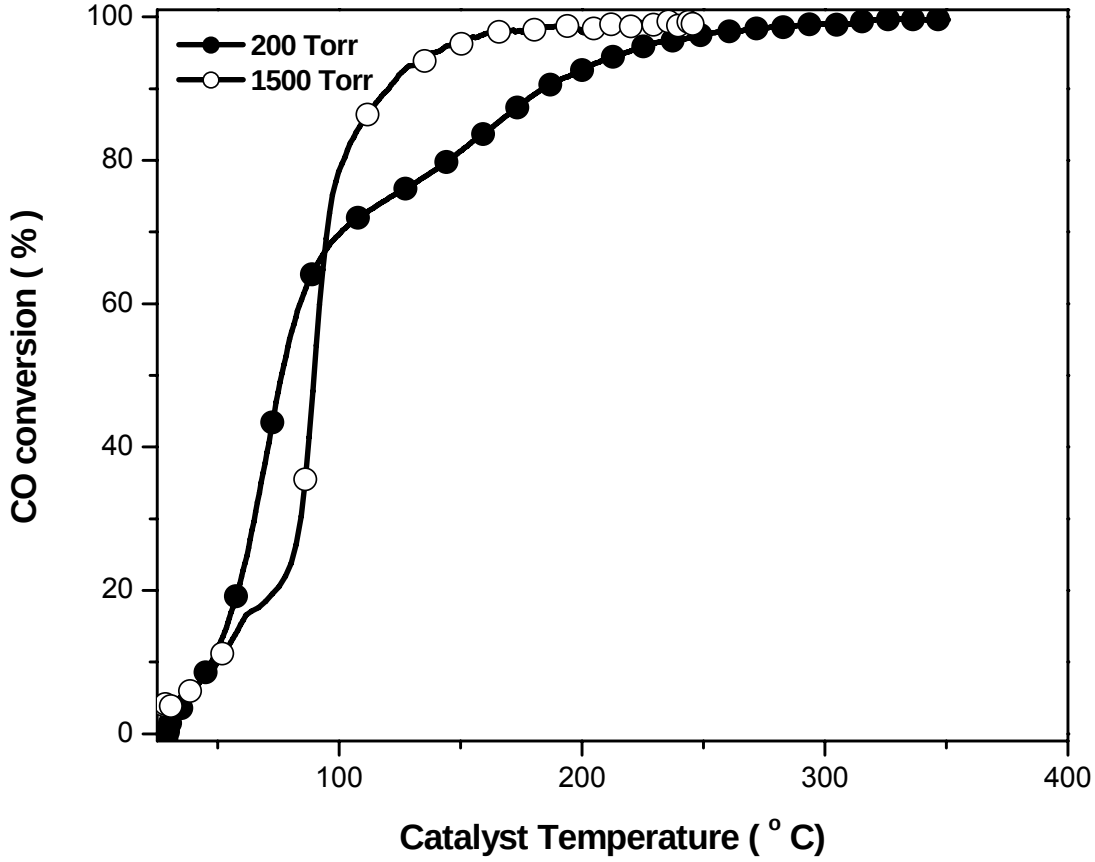

Figure 17: Catalytic activities of 5 % Au/CeO2 prepared by LVCC in 200 and 1500 Ar after heat treatment in CO/O_2 mixture (run 2).

Table 8 summarizes the catalytic activities of 5 % Au/CeO2 prepared by LVCC in 200 and 1500 Ar after heat treatment in CO/O_2 mixture (run 2).

Sample 5%Au/CeO_2	**3% Conversion Light-off Temp.(^{o} C)**	**50 % Conversion Temp. (^{o} C)**	**Maximum Conversion (%)**	
			Temp. (^{o} C)	**Conversion**
200 Torr	33.5	76.4	323.2	99.7
1500 Torr	27.5	89.95	210.9	99.4

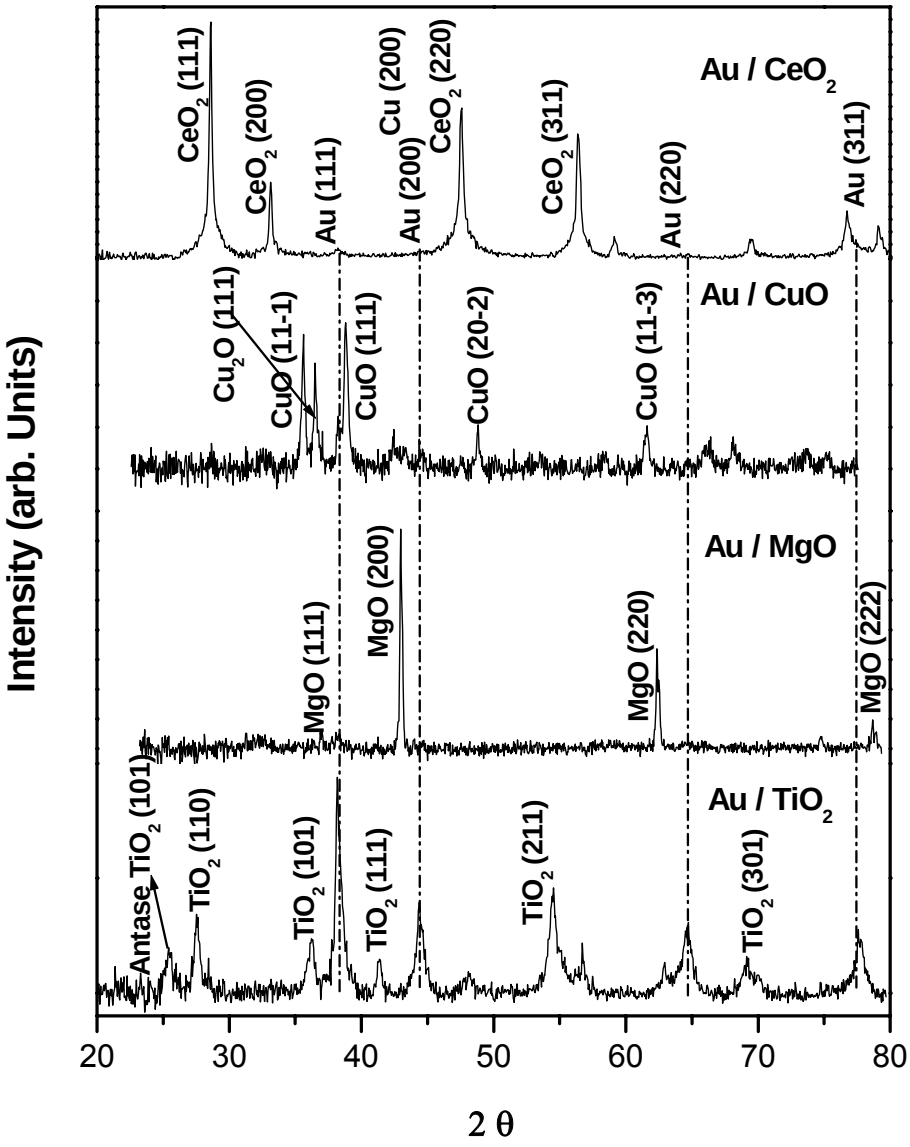

Figure 18: X-ray diffraction patterns of Au nanoparticles supported on different metal oxide supports as prepared by the LVCC method at 1500 Torr of Ar.

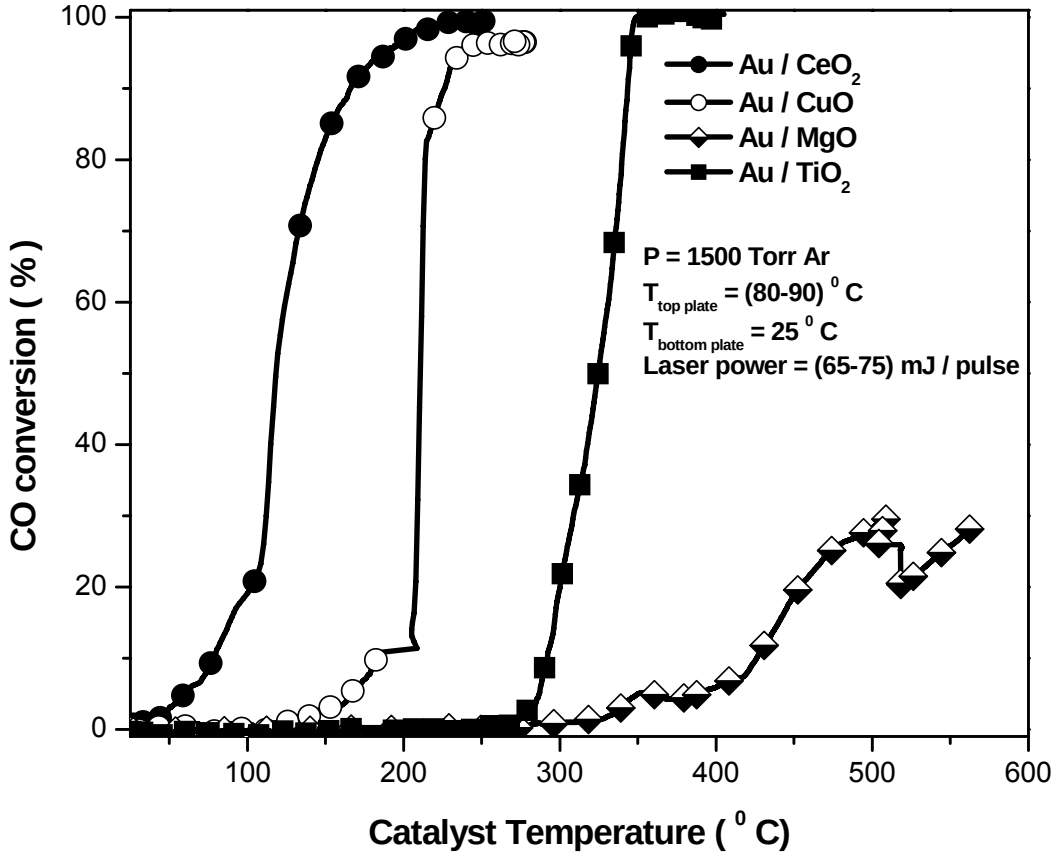

Figure 19: Comparison of the catalytic activities of 5 % Au supported on CeO_2, CuO, MgO, and TiO_2 as prepared (run 1) by LVCC at 1500 Torr in Ar atmosphere and using flow reactor IR spectroscopy.

Table 9 summarizes catalytic activities of 5 % Au supported on CeO_2, CuO, MgO, and TiO_2 as prepared (run 1) by the LVCC method in 1500 Torr Ar.

Sample	**3% Conversion Light-off Temp.(^{o} C)**	**50 % Conversion Temp. (^{o} C)**	**Maximum Conversion (%)**	
			Temp. (^{o} C)	**Conversion**
Au/CeO_2	50.2	118.2	233.2	99.5
Au/CuO	149.0	209.4	263.7	96.5
Au/MgO	339.2	-	563.0	28.1
Au/TiO_2	280.8	324.5	349.2	100

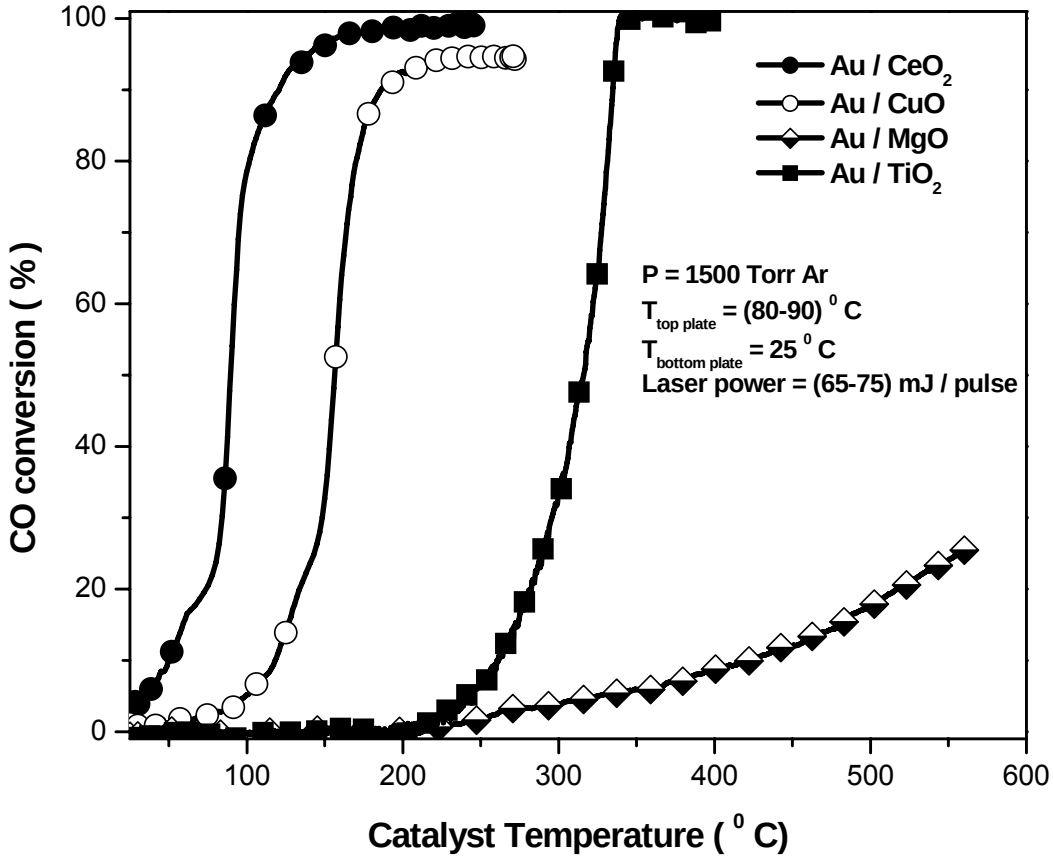

Figure 20: Comparison of the catalytic activities of 5 % Au supported on CeO_2, CuO, MgO, and TiO_2 as prepared (run 2) by the LVCC at 1500 Torr in Ar atmosphere and using flow reactor IR spectroscopy.

Table 10 summarizes the catalytic activities of 5 % Au supported on CeO_2, CuO, MgO, and TiO_2 as prepared (run 2) by the LVCC method in 1500 Torr Ar.

Sample	**3% Conversion Light-off Temp.(^{o} C)**	**50 % Conversion Temp. (^{o} C)**	**Maximum Conversion (%)**	
			Temp. (^{o} C)	**Conversion**
Au/CeO_2	27.5	90.0	210.9	99.4
Au/CuO	88.0	155.5	249.5	94.7
Au/MgO	264.91	-	560.0	25.4
Au/TiO_2	228.54	315.8	339.4	100

3.2.7 CO oxidation on Au/CeO2 prepared by the LVCC method

The Au/CeO_2 system shows great promise for efficient low temperature CO oxidation. To optimize this system, it is crucial to examine many factors that affect the catalytic performance of this catalyst, such as the effect of preparation conditions (pressure; and heat treatment), aging, and stability.

As indicated by Figure 16 and Figure 17, Au/CeO_2 nanoparticles prepared by LVCC at 1500 Torr show higher catalytic activity than the same particles prepared at 200 Torr of Ar. There are other factors that affect the catalytic performance of this catalyst, such as particle size, pretreatment conditions, and the interaction between Au and CeO_2. Furthermore it is important to investigate the reproducibility and the stability of this catalyst.

BET Surface area measurement shows that the Au/CeO_2 catalyst has a surface area of 84.5 m^2 / g. This is a large surface area compared to the surface area of corresponding micron sized powder.

Figure 21 shows X-ray diffraction pattern of 5 % Au/CeO_2 as prepared by the LVCC method at 200 Torr. Both crystalline CeO_2 peaks and crystalline Au peaks can be distinguished. However, the intensities of Au peaks are very small compared to the CeO_2 peaks since this sample contained only 5 % Au. Also, this means that Au is well dispersed within the CeO_2. The Au peak broadening indicates small Au particles.

Laser vaporization from of a 5 % Au/CeO_2 target within an Ar atmosphere resulted in the formation of two types of morphologies; small elongated particles which form

aggregates (web like morphology), and small Au nanoparticles (5-10 nm) deposited on the surface of larger (30-100 nm) support particles, as shown in the SEM micrographs of the Au/CeO_2 nanoparticles in Figure 22. These results can be confirmed using the HRTEM micrographs shown in Figure 23. The HRTEM also show that small particles, which are believed Au, are setting on large spherical particles. In order to confirm these results, EDX spectra from different parts of the sample, were monitored and collected. The peak intensity of both Au and CeO_2 are shown in Figure 24. The intensities of Au peaks in the whole particle are approximately 5 % with 95 % being CeO_2 peaks. However, if we zoom on the spherical particle, the intensities of the Au peaks are decreased and there are mostly CeO_2 peaks, which indicate that the large particles are mostly composed of CeO_2 with a small portion being Au. On the other hand, if we zoom in the small particle that is setting on the surface of the spherical particle, the intensities of the Au peaks increased sharply and only a small signal is coming from CeO_2. These results confirm that the Au particles (5-10 nm) are actually setting on large particles (30-500 nm) of CeO_2. There are Ni peaks detected in EDX spectra that can be attributed to the grid used to hold the sample.

The surface of the 5 % Au/CeO_2 was examined initially by low-resolution survey X-ray photoelectron spectroscopy scan to determine which elements were present, as shown in Figure 25. The sample surface contained various amounts of the following species: cerium as Ce^{+4}, oxygen, carbon in as C-(C, H), C-O, and C=O, O-C=O, and traces of gold as Au°. The concentration of elements detected were 28.2 (Atom %) Ce, 45.4 (Atom %) O, 26.0 (Atom %) Carbon, and 0.3 (Atom %) Au. High-resolution spectra were acquired to determine the binding energy (i.e., chemical state) and concentration of the

elements observed in the survey spectra. The high-resolution Ce 3d spectrum is shown in Figure 26. The high-resolution Ce 3d spectrum was consistent with the Ce^{+4} (including similar shake-up peaks) and a tiny bump at ~885.7eV, which may indicate the presence of a trace Ce^{+3} reported to have a binding energy of ~885.8 eV [99].

Two doublets were used in the curve fit of the Au 4f peak. One doublet at binding energies ~83.9 and ~87.6 eV was used to fit the Au°. The second doublet at ~85.2 and ~88.9 eV was used to curve fit possibly a trace of Au^{+}, as shown in Figure 27. Table 11 summarizes the amount of Au^{0} and Au^{+} in 5 % Au/CeO2 nanoparticle catalyst using curve fitting of Au 4f peak obtained by X-ray photoelectron spectroscopy. Although some studies show that Au^{0} or Au^{+} or both are the active species for the CO oxidation reaction [48,100,101], our results indicate clearly that Au^{0} and Au^{+} are the active species. Figure 28 displays the catalytic activities of the Au/CeO_2 nanoparticle catalyst prepared using the LVCC method in 1500 Torr Ar (run 1, run 2, and run 3). Table 12 summarizes the catalytic activities of the Au/CeO_2 nanoparticle catalyst (run 1, run 2 and run 3). The conversion curve is shifted to a lower temperature region by 23 ^{0}C after the first run and the catalyst becomes very stable, run 2 and run 3 are identical. This shift in temperature could be related to improvement in the active site, which will be investigated thoroughly.

3.2.7.1 Particle size effect

To examine the effect of particle size on the catalytic activity, the catalytic activities of a physical mixture of 5% gold with CeO_2 bulk powder (micron size) and Au/CeO_2 nanoparticle catalyst prepared by the LVCC method after heat treatment (run 2)

were compared, as shown in Figure 29. It is clear that the catalytic activity of the Au/CeO_2 nanoparticle catalyst is higher than that of the bulk Au/CeO_2 under similar conditions. Table 13 summarizes the catalytic activities of a physical mixture consisting of 5% gold with CeO_2 bulk powder (micron size) and Au/CeO_2 nanoparticles prepared by the LVCC method at 1500 Torr Ar. The 5% supported Au/CeO_2 nanoparticles show a 3 % conversion at 28 ^{0}C, a 50% conversion at 90 ^{0}C, and reaches maximum conversion of 99.4 % at 233 ^{0}C compared to the corresponding bulk mixture which reaches a 3 % conversion at 255 ^{0}C, and a maximum conversion of only 60% at temperatures near 600 ^{0}C. Particle size and the high surface area are not the only factors that affect the activity. There are more factors that need to be investigated.

3.2.7.2 Au–CeO_2 interaction

Metal-support interaction plays an important role in the catalytic activity. In the Au/CeO_2 system, Au interacts with CeO_2 and promotes the reduction of Ce^{+4} to Ce^{+3} and thus facilitates charge transfer from Au to Ce, which results in a higher oxidation state of Au and hence increases the oxygen storage capacity of CeO_2. This leads to an increase in the activity of the catalyst. Figure 30 compares the activities of the Au/CeO_2 nanoparticle catalyst prepared by the LVCC method with a physical mixture of 5 %Au and 95 %CeO_2 nanoparticles. Table 14 summarizes the catalytic activities of a physical mixture consisting of 5% gold with CeO_2 nanoparticles and Au/CeO_2 nanoparticles prepared by the LVCC method at 1500 Torr Ar. As expected, the activity of Au/CeO_2 (prepared by the LVCC) is higher than the activity of the physical mixture of Au and CeO_2 nanoparticles due to the

significant metal support interaction between Au and CeO_2 in the Au/CeO_2 nanoparticle catalyst. This effect is also investigated using the Temperature Programmed Reduction (TPR) experiments. Temperature Programmed Reduction (TPR) using H_2 as a probe molecule is a unique technique to study ceria based materials. The results of the TPR study for bulk CeO_2 and 5 % Au supported on a CeO_2 nanoparticle catalyst are shown in Figure 31. The CeO_2 is reduced by H_2 as shown in equation (3.1).

$$CeO_{2(S)} + \delta H_2 \longrightarrow CeO_{2-\delta(S)} + H2O \qquad (3.1)$$

The TPR study of CeO_2 (bulk) showed the reduction of CeO_2 takes place in two temperature regions. The first region is 144-251 ^{0}C with T_{max} around 188 ^{0}C and the second region started at 373 ^{0}C and had a T_{max} around 480 ^{0}C. These reduction regions are characteristics of ceria and are assigned to the surface and the bulk respectively. These peaks correspond to the removing of surface oxygen at low temperatures and bulk oxygen at high temperatures. However, Au plays an important role in the low temperature reduction of CeO_2. In the presence of Au, the reduction of ceria is facilitated by the gold. In a Au/CeO_2 nanoparticle catalyst, there is a somewhat similar behavior as the bulk ceria, but there is a slight shift to a lower temperature region (25-219 ^{0}C) with T_{max} around 151 ^{0}C due to the presence of Au which weekend the CeO_2 surface oxygen bonding. The temperature at which the Au-CeO_2 reaction with H_2 starts up (T_{up}) is 25^{0}C. The high temperature CeO_2 peak is shifted to lower temperature region with T_{max} around 451 ^{0}C. A new feature appears at temperature region (219 -385 ^{0}C), which is believed to be coming from the reduction of Ce-Au-O species. The presence of Ce-Au-O is supported by XPS data which shows the presence of traces of Ce^{+3} and Au^{+}. The reduction Ce-Au-O enhances

the redox activity of Au-CeO_2. These results agree well with the conversion curve of this catalyst. From TPR results, it can be concluded that there is a significant Au-CeO_2 interaction in Au/CeO_2 nanoparticle catalyst prepared by the LVCC method.

3.2.7.3 Effect of pre-treatment

The Au/CeO_2 nanoparticle catalyst shows enhanced activity after the heat treatment in CO/O_2 mixture (run 2and run 3) over the fresh Au/CeO_2 nanoparticle catalyst (run 1), as indicated Figure 28. XRD patterns of Au/CeO_2 before catalysis and Au/CeO_2 catalyst after catalysis (run2 and 3) are shown in Figure 32. Some of the characteristic peaks of CeO_2 appear to have a broad shape which indicates the presence of small crystalline CeO_2 particles. Au peaks are broad peaks with low intensities due to their small particle size and poor crystallinity. The diffraction patterns of Au/CeO_2 after catalysis denotes, beside more crystallinity, the presence of higher intensity peaks related to Au at 2θ = 38.2 , 44.5, 64.7and 77.7 corresponding to the (111), (200), (220), (311) planes. Figure 33 shows TEM micrographs of the Au/CeO_2 nanoparticle catalyst before and after heat treatment. The micrographs show that Au particles are well dispersed in CeO_2. However, Au particles appear more aggregated after catalysis, which appears in the intense dark zones. Although the particle size is hard to be estimated due to the complicated morphology of the sample after catalysis, TEM micrographs before and after catalysis indicates that the particle size is (5-10 nm) as shown in Figure 34. Furthermore, two types of morphologies are observed after catalysis due to heat treatment in oxidizing and reducing atmosphere. In the first morphology Au is dispersed on the surface of an irregular shape of CeO_2, which is denoted

to the precipitation of Au from a solid solution of Au and CeO_2.In the other morphology, the shape of the particles changed from spherical to cubes and unsymmetrical shapes which were altered by the CO oxidation reaction. This change of particle shape has been observed for supported Pt particles on CeO_2 model catalyst reported by Johansson *et.al* [102] and they attributed this change in morphology to faceted behavior of Pt.

Based on these results, it can be concluded that the enhancement of the catalytic activity of Au/CeO_2 nanoparticle catalyst is not only due to the removing of moisture as anticipated earlier; but also as a result of structural change of the catalyst.

The pre-treatment effect on the Au/CeO_2 nanoparticle catalyst was explored by evaluating the catalytic performance of the Au/CeO_2 nanoparticles after heat treatment at 300 ^{o} C in He atmosphere and comparing it to the catalytic performance of untreated Au/CeO_2 nanoparticles, as shown in Figure 35. The activities of untreated Au/CeO_2 catalyst and after heat treatment are summarized in Table 15. Although the activity of the treated sample in run 1 is similar to the activity of run 2 of untreated sample, as expected, run 2 and run 3 of the treated sample show relatively higher conversion at lower temperatures than the untreated sample. The differences in the activities of both samples are related to the gas that is used in the heat treatment. When the sample is treated in a He atmosphere, the catalyst is reduced as result of the heat and becomes very stable. In the case of untreated sample, the catalyst is heated in CO/O_2 mixture where the catalyst is reduced and oxidized at the same time.

3.2.7.4 Stability and aging effect

It is a well known fact that the catalytic activity of a catalyst decreases with time due to the deposition of moisture and hydrocarbons on the surface of the catalyst, as indicated in the XPS results of freshly prepared samples, which block the active site for the CO oxidation reaction. To investigate the effect of aging on the catalytic activity of the Au/CeO_2 catalyst, we prepared 30 mg of Au/CeO_2 using the LVCC method and divided the sample into 3 parts, each part being 10 mg. The catalytic activities of the first part were measured as soon as the particles were prepared, the second part was measured after one week, and the third part after one month. The catalytic activities of untreated (run 1) samples as a function of time are shown in Figure 36. The catalytic activities of the samples after heat treatment are shown in Figure 37. Table 16 summarizes the catalytic activity of the Au/CeO_2 catalyst as prepared and after heat treatment (run1 and run 2) as a function of time. It is clear that the conversion curve of the first run in all samples is shifted to a higher temperature region by 80 ^{o}C after one month of aging while the conversion curve in the second run in all samples is shifted to a higher temperature region by approximately 20 ^{o} C. This shift in temperature could be attributed to the deposition of moisture hydrocarbons from the air. The conversion curve in all the samples is shifted to a lower temperature in the second run as a result of removing these species and improving the active site beside the heat treatment effect on the catalyst.

Although the heat treatment of the Au/CeO_2 results in increasing the catalytic activity and the stabilizing the active site, the stability of treated and untreated samples show different behaviors after one day of aging. First the catalytic activity of the untreated

sample was measured after run 1, run 2 and run 3 on the same day. The sample was then left in the reactor overnight and the catalytic activity was measured after run 1, run 2 and run 3. Figure 38 compares the catalytic activity of Au/CeO_2 as prepared and after one day aging. Table 17 summarizes the catalytic activity of the same untreated sample as prepared and after one day of aging. It is obvious that the activity of the untreated sample is increased after multiple runs in the same day. After one day of aging, the catalytic activity increased for the first, the second, and the third run. These results can be explained by the fact that the heat treatment in CO/O_2 atmosphere results in a reduction of Au and CeO_2. Since Au is hard to oxidize. Meanwhile, CeO_2 can alternate between oxidation and reduction cycles and has high oxygen storage capacity. Furthermore, Au-Ce-O species are reduced and a major part is reoxidized, which leaves part of this species in reduced form. The more the sample is used, the more of these species are reduced. However, the activity of Au/CeO2 on the second day for run 1 is decreased compare to run 3 on first day is due to the absorption of moisture the enhanced activities of run 2 and run 3 on the second day confirm this. For the treated samples, the catalytic activity remains the same after one day of aging; since the catalyst is totally in the reduced form as shown in Figure 39. Table 18 summarizes the catalytic activity multiple of Au/CeO_2 as prepared and treated at 300 ^{o}C in He and after one day of aging.

The heat treatment method and atmosphere can greatly affect the stability of the Au/CeO_2 catalyst. Based on the catalytic activity results of both heating methods (heating in He or CO/O_2 atmospheres), the catalyst shows higher stability after heat treatment in He than in CO/O_2 mixture.

To investigate the long term stability and aging under dynamic conditions, the catalytic activity of the Au/CeO_2 catalyst was measured as a function of time by keeping the temperature constant at 144 ^{o} C, where the conversion is 80%, and 186 ^{o} C, where the conversion is 100%, while flowing CO/O_2 mixture over Au/CeO_2, as shown in Figure 40. It is clear that the Au/CeO_2 nanoparticle catalyst is a very stable catalyst. This stability is demonstrated by the constant conversion percentage of 100 % even after 16 h of continuous use.

3.2.8 Catalytic activity of 5 % Au/CeO_2 in presence of Volatile Organic Compounds (VOC)

In any combustion system, there are significant amounts of other toxic gases, besides CO, such as nitric oxide (NO_x), butadiene, and isoprene. Catalytic activity of the 5 % Au/CeO_2 nanoparticle catalyst is investigated in the presence of 1000 ppm of butadiene and in the presence 1000 ppm of isoprene. Figure 41 compares the mass spectrum at different temperatures of (3.4 % CO, 20 % O_2 in He mixture) in the presence of 1000 ppm butadiene without a catalyst and with the 5 % Au/CeO_2 catalyst. Based on the mass spectrum of the CO/O_2 mixture with butadiene without catalyst as a function of temperature, it is clear that the concentrations of all the gases remain constant. Furthermore, there is no evidence of the formation of carbon dioxide. In the presence of Au/CeO_2 catalyst, it is clear that the CO Concentration is decreased and that CO_2 is formed and at temperatures above 200 ^{o} C, CO is completely converted to CO_2. Also, the concentration of butadiene is decreased as the temperature is increased and at 200 ^{o} C the

butadiene concentration goes to zero and the formation of H_2O is seen. The same behavior is observed for CO oxidation in the presence of isoprene, with exception of a small amount of isoprene present at higher temperatures. Figure 42 compares mass spectrum at different temperatures of (3.4 % CO, 20 % O_2 in He mixture) in the presence of 1000 ppm isoprene without catalyst and with the 5 % Au/CeO_2 catalyst. The catalytic performance of the Au/CeO_2 catalyst in the presence of isoprene and butadiene is measured using flow reactor mass spectrometry as a function of the catalyst temperature. Figure A11 describes the catalytic activity of the 5 % Au/CeO_2 catalyst in presence of 1000 ppm butadiene and in the presence of 1000 ppm isoprene. It clearly indicated that the Au/CeO_2 catalyst loses some of its activity because of the presence of small concentrations of isoprene and butadiene. The conversion curve is shifted upward to a higher temperature region. The light-off temperature is shifted from 72 ^{o}C to 206 ^{o}C in the presence of butadiene and 170 ^{o}C in the presence of isoprene. The 50 % conversion percentage is shifted from 120 ^{o}C to 255 ^{o}C in the presence of butadiene and 327 ^{o}C in the presence of isoprene. The maximum conversion is shifted from 97 % at 183^{o}C to 99 % at 344 ^{o}C in the presence of butadiene, and to 88 % at 466 ^{o}C in the presence of isoprene. Figure A11 compares the catalytic activities of 5 % Au/CeO_2 with and without the presence of 1000 ppm butadiene and 1000 ppm isoprene. These results are attributed to the combustion of butadiene and isoprene to CO_2 and H_2O, as shown in the mass spectrum, however, butadiene is completely combusted at temperatures higher than 206 ^{o}C, which explains the higher conversion percentage of CO to CO_2 where part of CO_2 is a result of butadiene combustion products.

Isoprene is not completely combusted; this can be seen in the conversion curve and the mass spectrum.

Finally, the 5 % Au/CeO_2 nanoparticle catalyst can be an active catalyst for selective CO oxidation at temperatures below 300 ^{o} C even in the presence of VOC. Furthermore, this catalyst shows great promise for the low temperature combustion of VOC such as butadiene and isoprene.

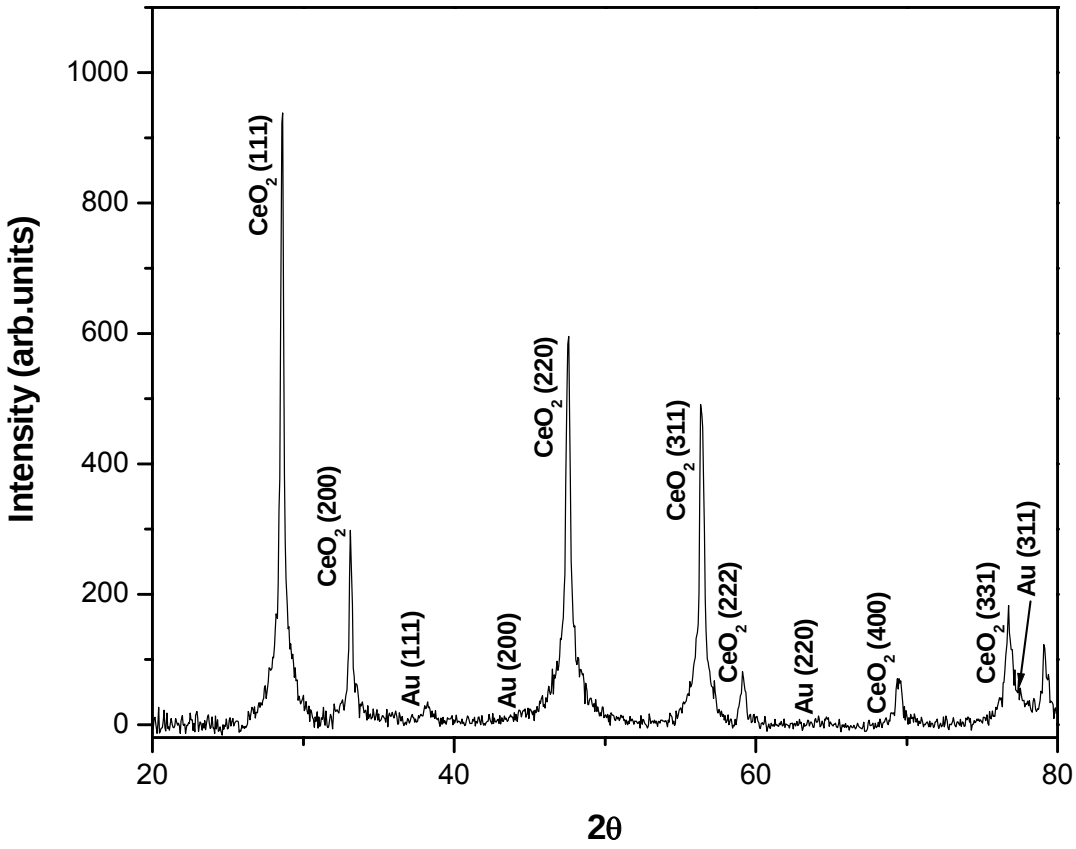

Figure 21: X-ray diffraction pattern of 5 % Au/CeO_2 as prepared by the LVCC method at 200 Torr.

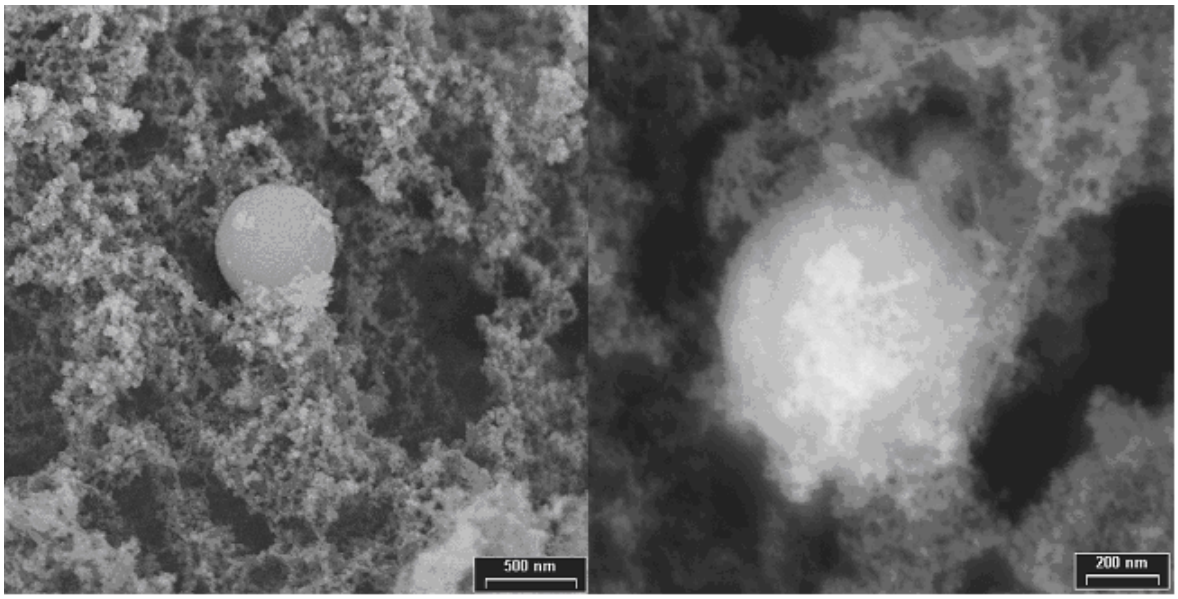

Figure 22: SEM micrograph of Au/CeO_2 nanoparticles containing 5 % Au as prepared by the LVCC method in 200 Torr Ar.

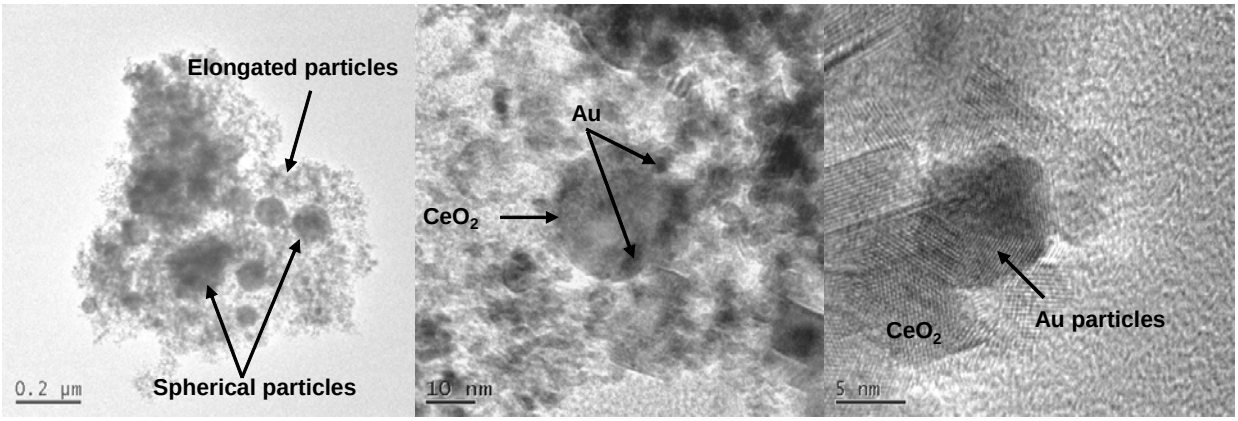

Figure 23: HRTEM micrographs of Au/CeO_2 nanoparticles contain 5 % Au as prepared by the LVCC method in 200 Torr Ar.

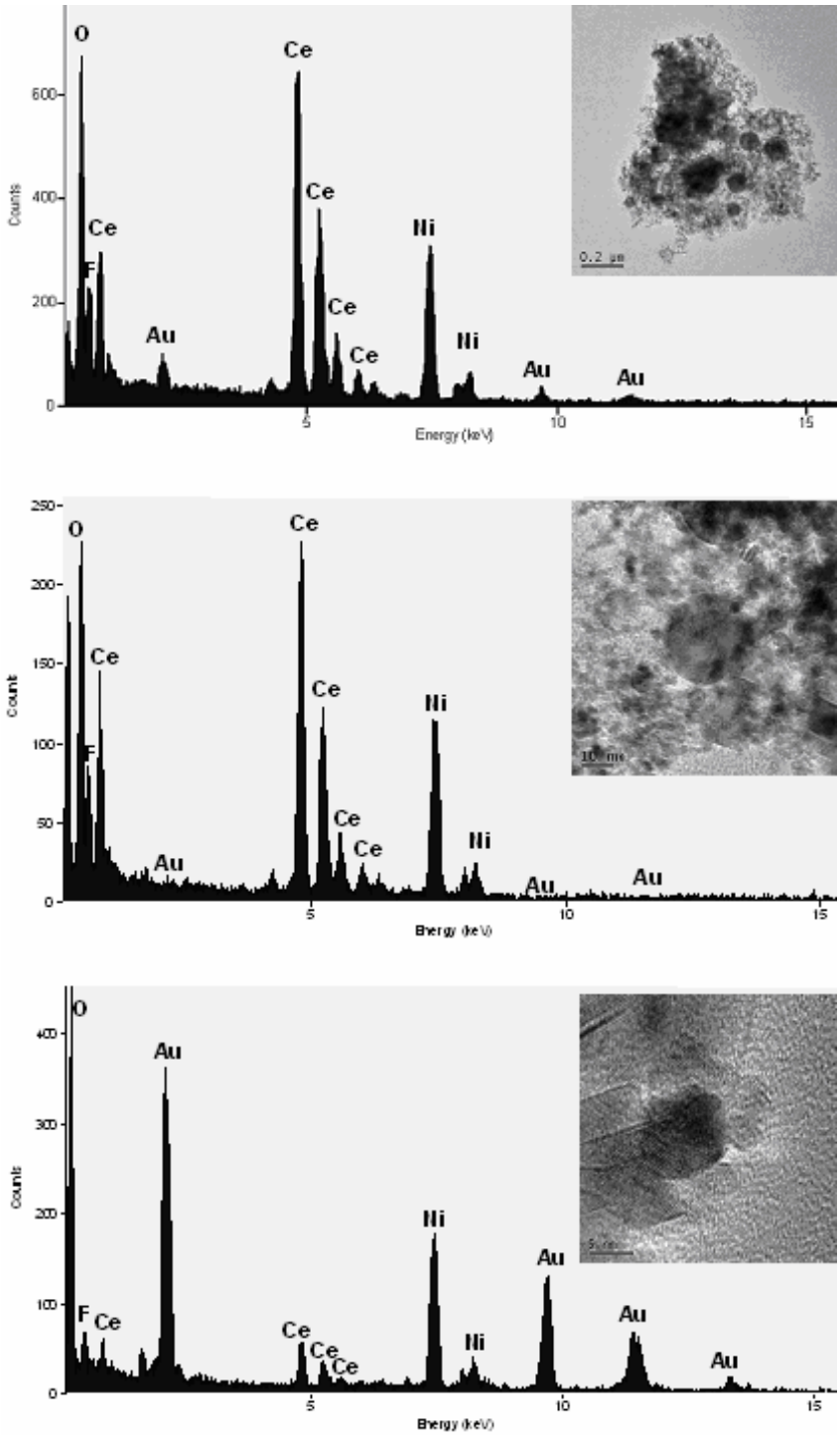

Figure 24: Energy Dispersed X-ray (EDX) of Au/CeO_2 nanoparticles contains 5 % Au as prepared by the LVCC method in 200 Torr Ar.

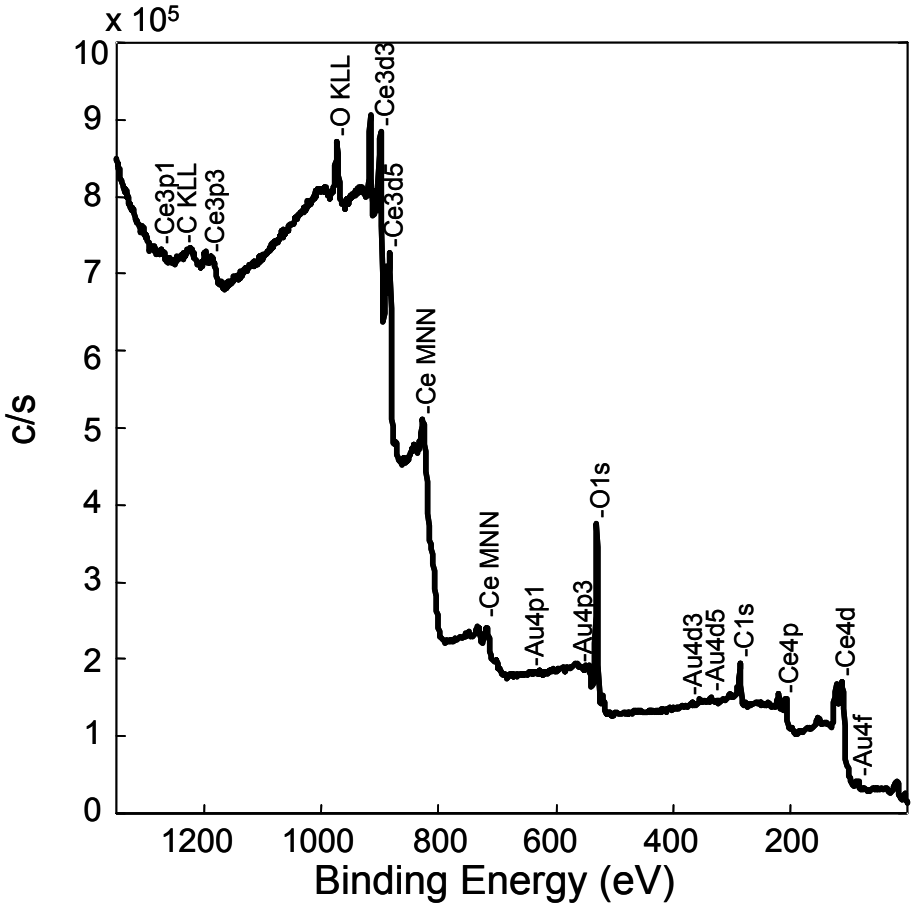

Figure 25: Low-resolution Survey X-ray photoelectron scan of 5 Au/CeO_2 nanoparticles as prepared by the LVCC method.

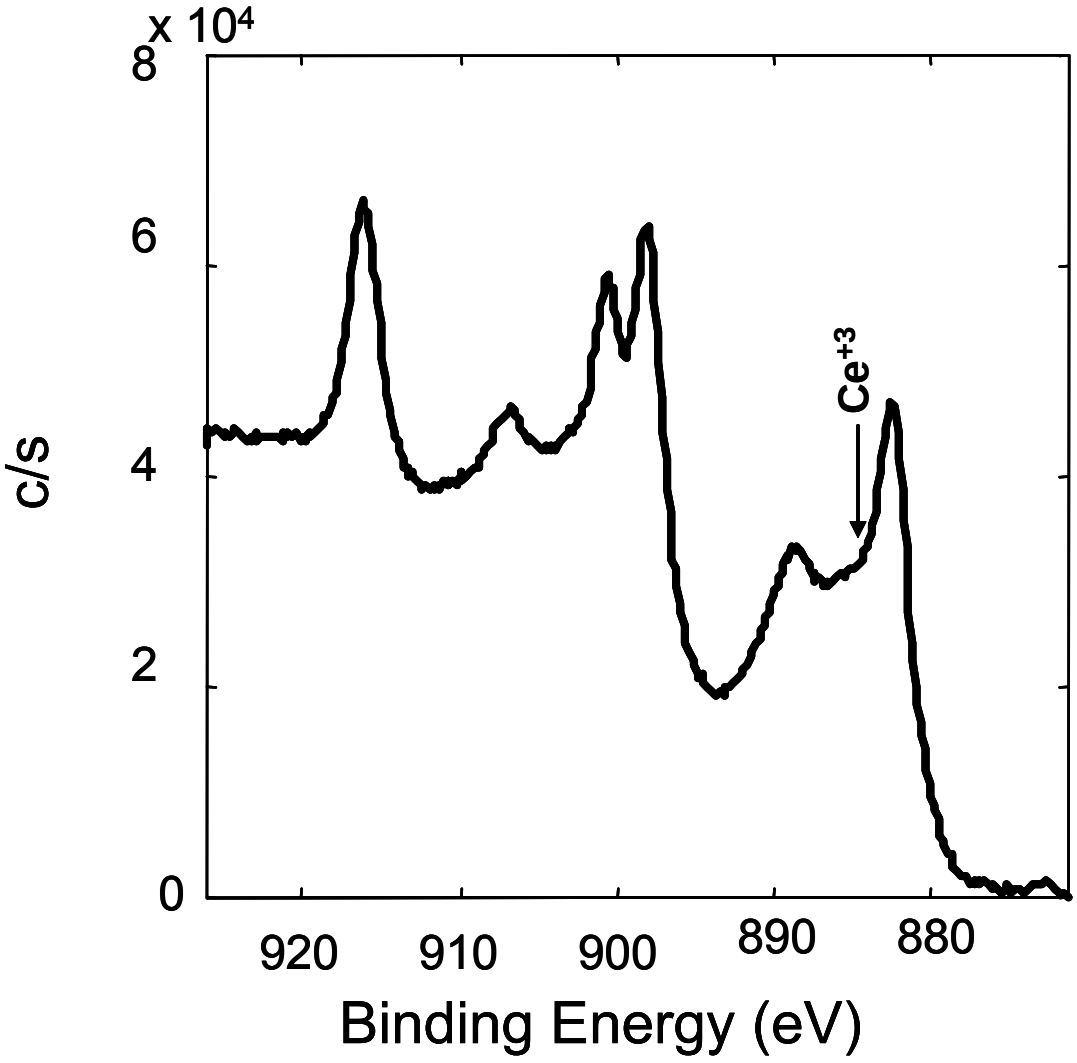

Figure 26: High resolution X-ray photoelectron Ce 3d spectrum of 5 Au/CeO_2 nanoparticles as prepared by the LVCC method.

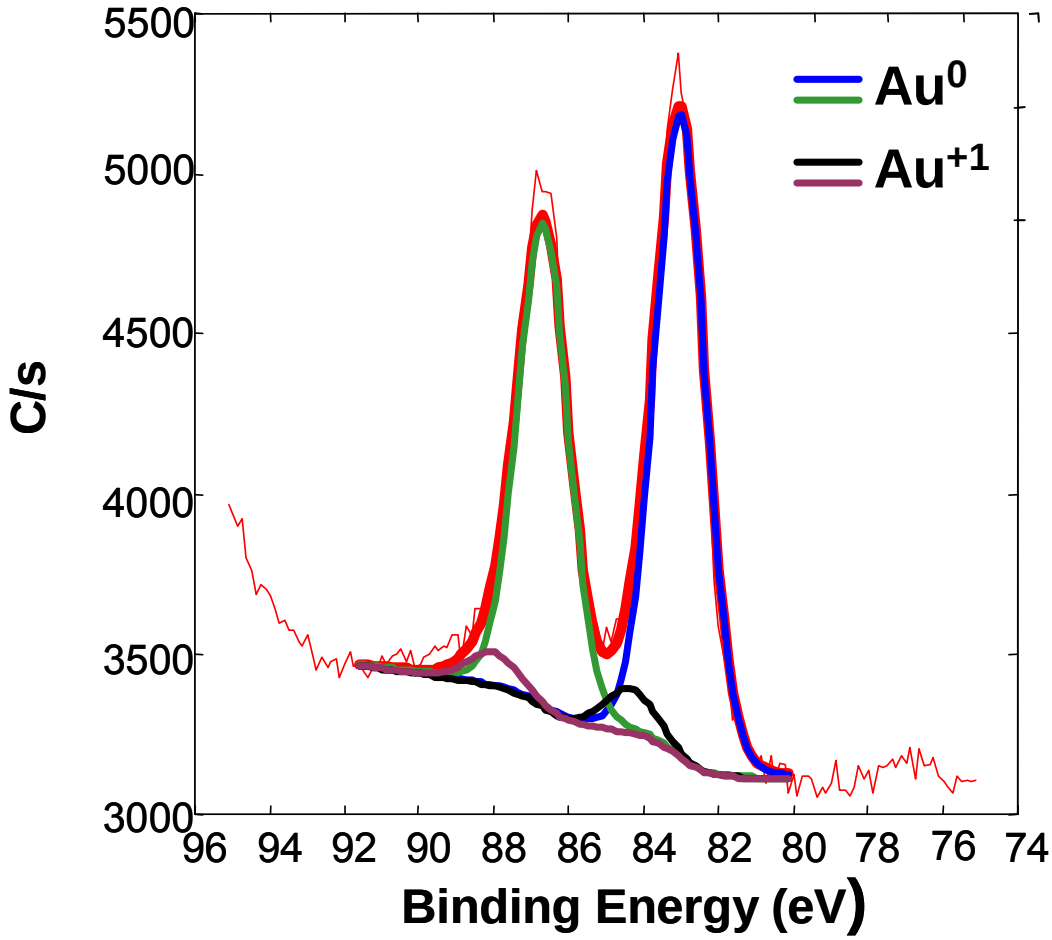

Figure 27: High resolution X-ray photoelectron Au 4f peak spectrum of 5 Au/CeO_2 nanoparticles as prepared by the LVCC method.

Table 11 summarizes the amount of Au^0 and Au^+ in the 5 % Au/CeO_2 nanoparticle catalyst using curve fitting of Au 4f peak obtained by X-ray photoelectron spectroscopy.

Species	% of Au	Atom% Au
Au^0	94	0.282
Au^{+1}	6	0.018

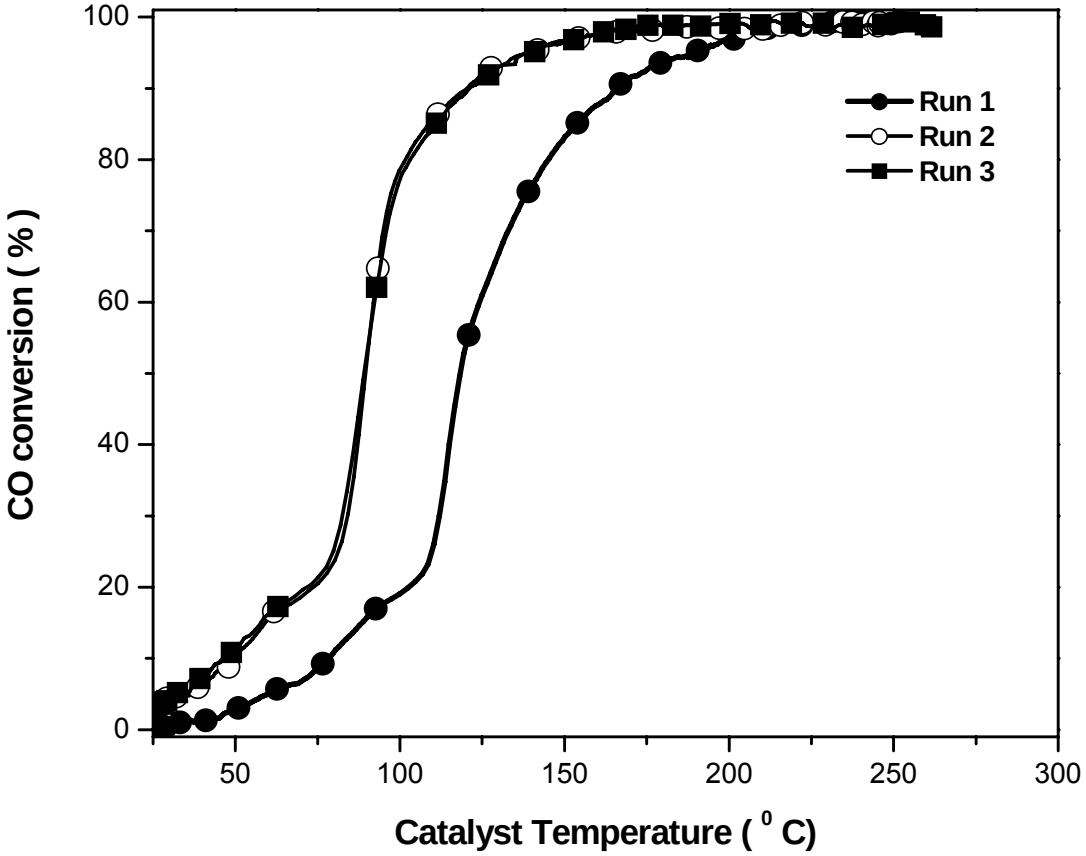

Figure 28: Catalytic activity of Au/CeO_2 nanoparticle catalyst prepared using the LVCC method in 1500 Torr Ar after multiple runs (run 1, run 2, and run 3).

Table 12 summarizes catalytic activities of the Au/CeO_2 nanoparticle catalyst (run 1 , run 2, and run 3).

Sample 5 %Au/CeO2	**3% Conversion Light-off Temp. (^{o} C)**	**50 % Conversion Temp. (^{o} C)**	**Maximum Conversion (%)**	
			Temp. (^{o} C)	**Conversion**
Run 1	50.2	118.2	233.2	99.5
Run 2, and 3	27.5	90.0	210.9	99.4

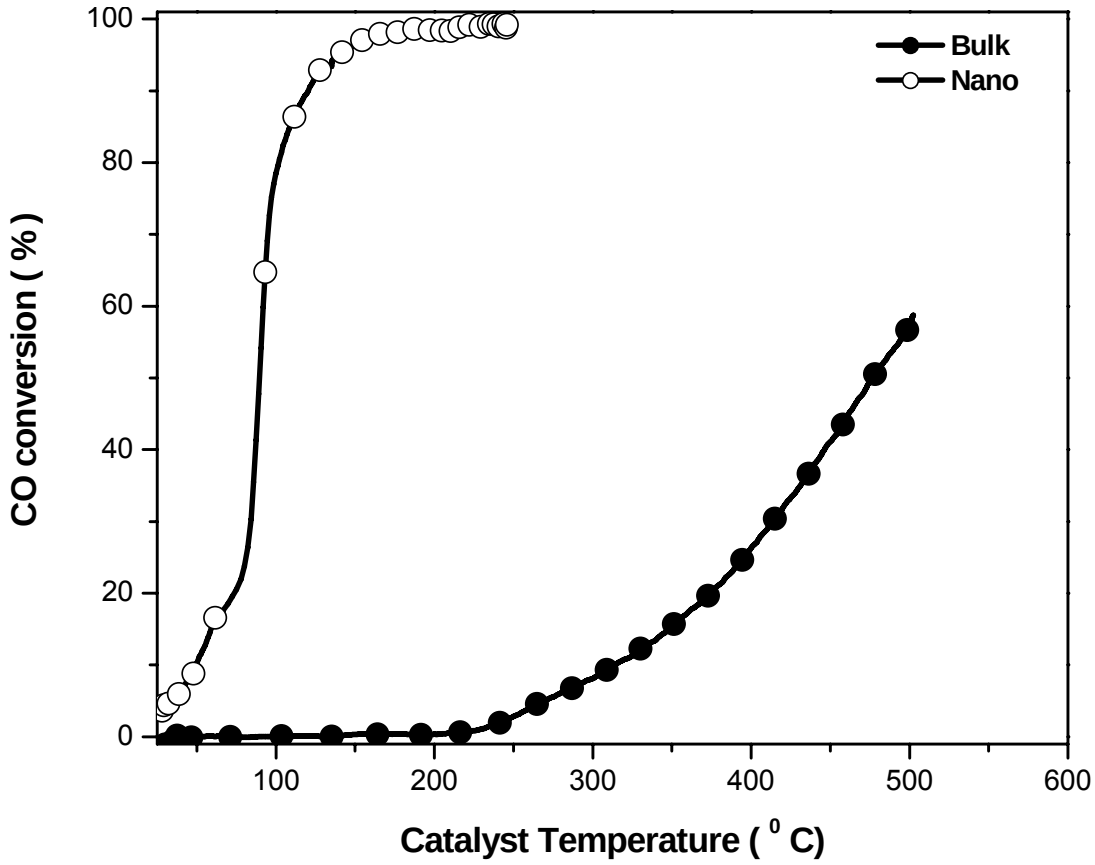

Figure 29: Comparison between the catalytic activities of a physical mixture consisting of 5% gold with CeO_2 bulk powder (micron size) and Au/CeO_2 nanoparticles prepared by the LVCC method at 1500 Torr Ar after heat treatment (run 2).

Table 13 summarizes the catalytic activities of a physical mixture consisting of 5% gold with CeO_2 bulk powder (micron size) verses Au/CeO_2 nanoparticles prepared by the LVCC method at 1500 Torr Ar.

Sample 5 %Au/CeO2	**3% Conversion Light-off Temp. (^{o} C)**	**50 % Conversion Temp. (^{o} C)**	**Maximum Conversion (%)**	
			Temp. (^{o} C)	**Conversion**
Bulk	252.5	476.9	502.4	58.7
Nano	27.5	90.0	210.9	99.4

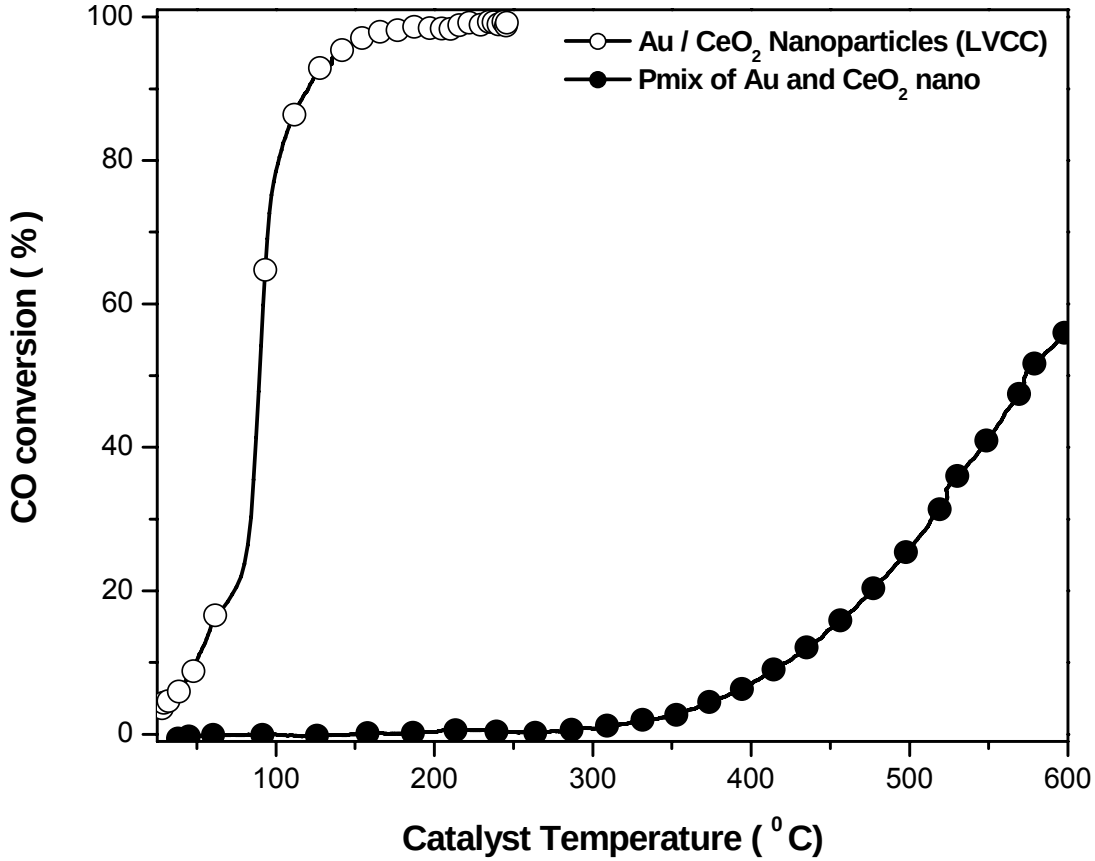

Figure 30: Comparison between the catalytic activities of a physical mixture consisting of 5% gold with CeO_2 nanoparticles verses Au/CeO_2 nanoparticles prepared by the LVCC method at 1500 Torr Ar after heat treatment.

Table 14 summarizes the catalytic activities of a physical mixture consisting of 5% gold with CeO_2 nanoparticles and Au/CeO_2 nanoparticles prepared by the LVCC method at 1500 Torr Ar after heat treatment.

Sample 5 %Au/CeO_2	**3% Conversion Light-off Temp. (^{o}C)**	**50 % Conversion Temp. (^{o}C)**	**Maximum Conversion (%)**	
			Temp. (^{o}C)	**Conversion**
LVCC	27.5	90.0	210.9	99.4
Pmix	356.0	573.3	600	56.5

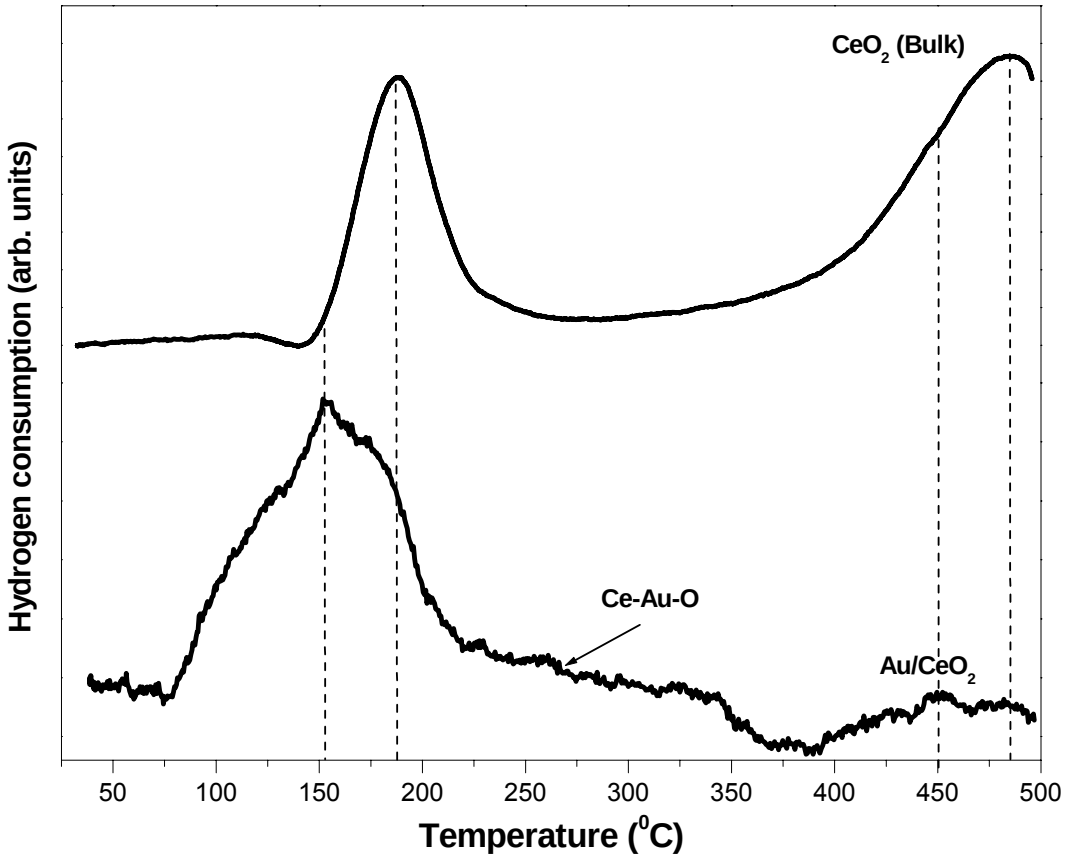

Figure 31: TPR patterns of CeO_2 bulk powder and Au/CeO_2 prepared by the LVCC method.

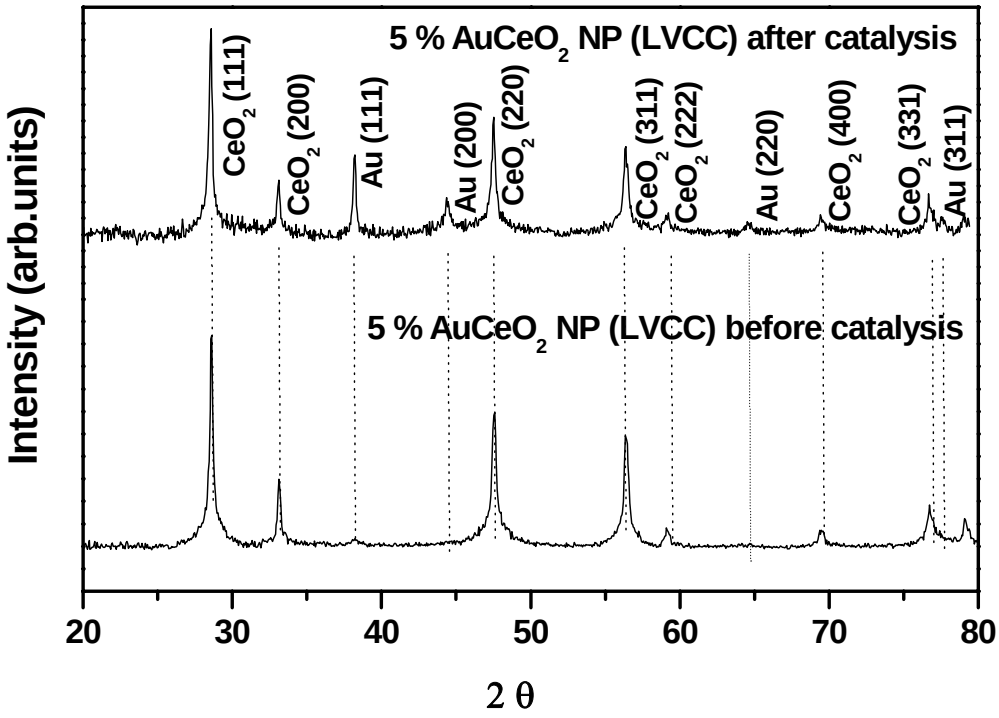

Figure 32: XRD diffraction patterns of Au/CeO_2 nanoparticle catalyst before and after catalysis.

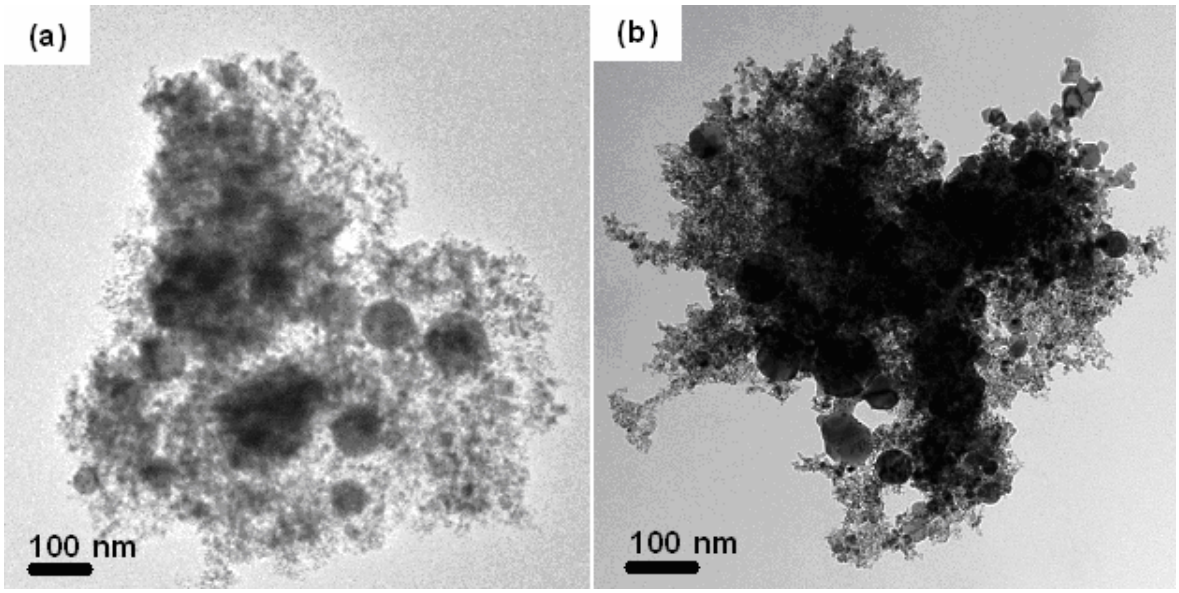

Figure 33: TEM micrographs of Au/CeO_2 catalyst a) before catalysis and b) after catalysis.

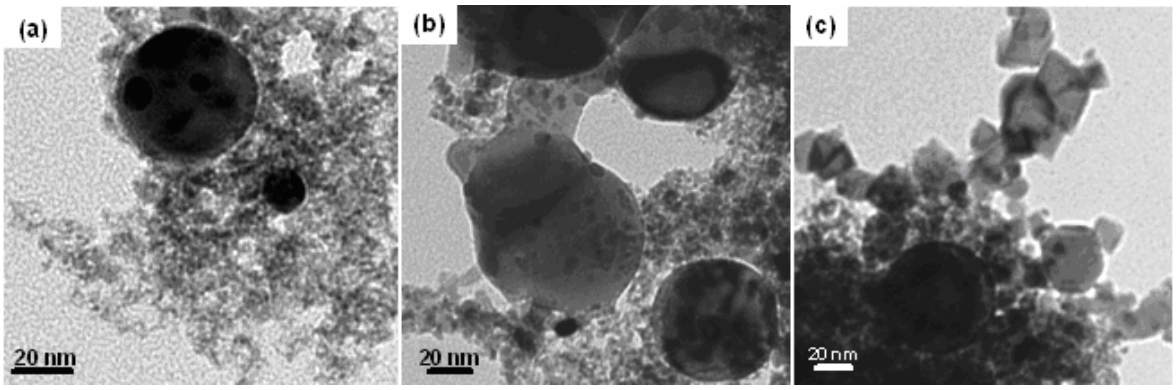

Figure 34: HRTEM of Au/CeO_2 catalyst a) before catalysis b), c) after catalysis.

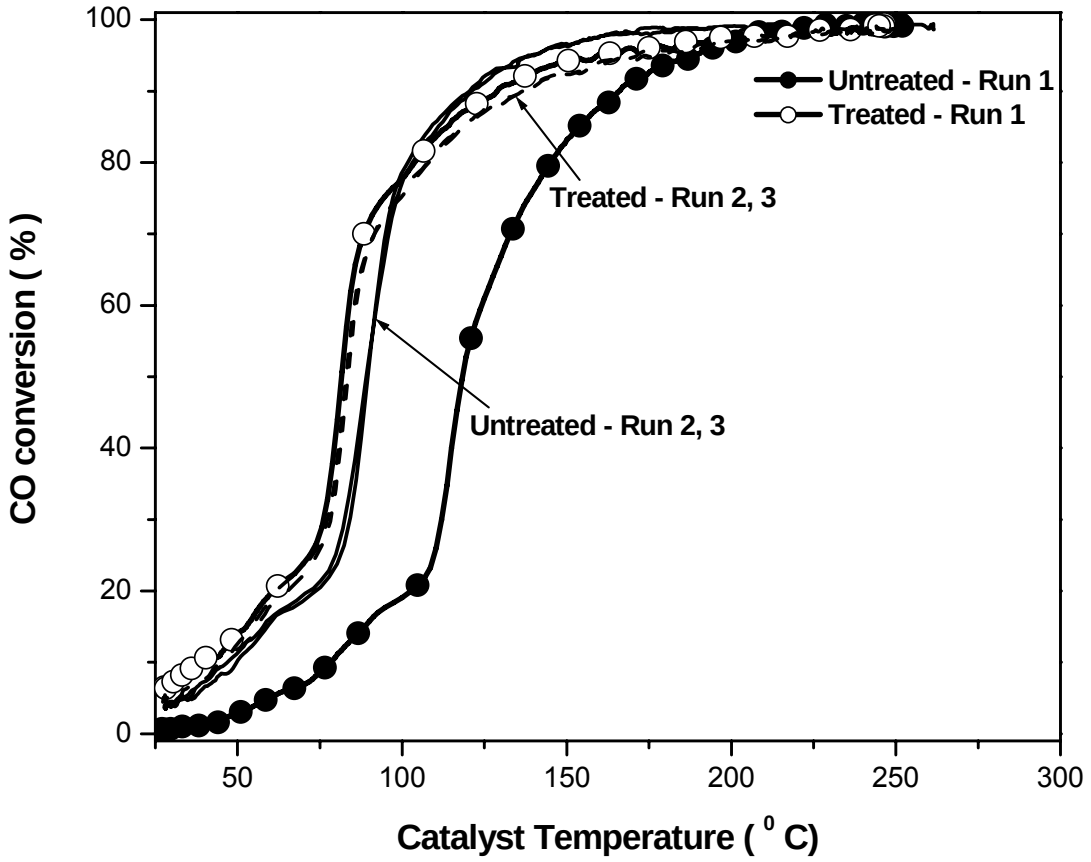

Figure 35: Comparison between activities of treated and untreated Au/CeO_2 nanoparticle catalyst after multiple runs.

Table 15 summarizes the activities of treated and untreated Au/CeO_2 catalyst after multiple runs.

Sample 5%Au/CeO_2	**3% Conversion Light-off Temp.(^{o} C)**	**50 % Conversion Temp. (^{o} C)**	**Maximum Conversion (%)**	
			Temp. (^{o} C)	**Conversion**
Untreated Run 1	50.2	118.2	233.2	99.5
Untreated Run 2, 3	27.5	89.95	210.9	99.4
Treated Run 1	< 25	80.7	170.2	96.3
Treated Run 2, 3	< 25	83.2	210.9	98.9

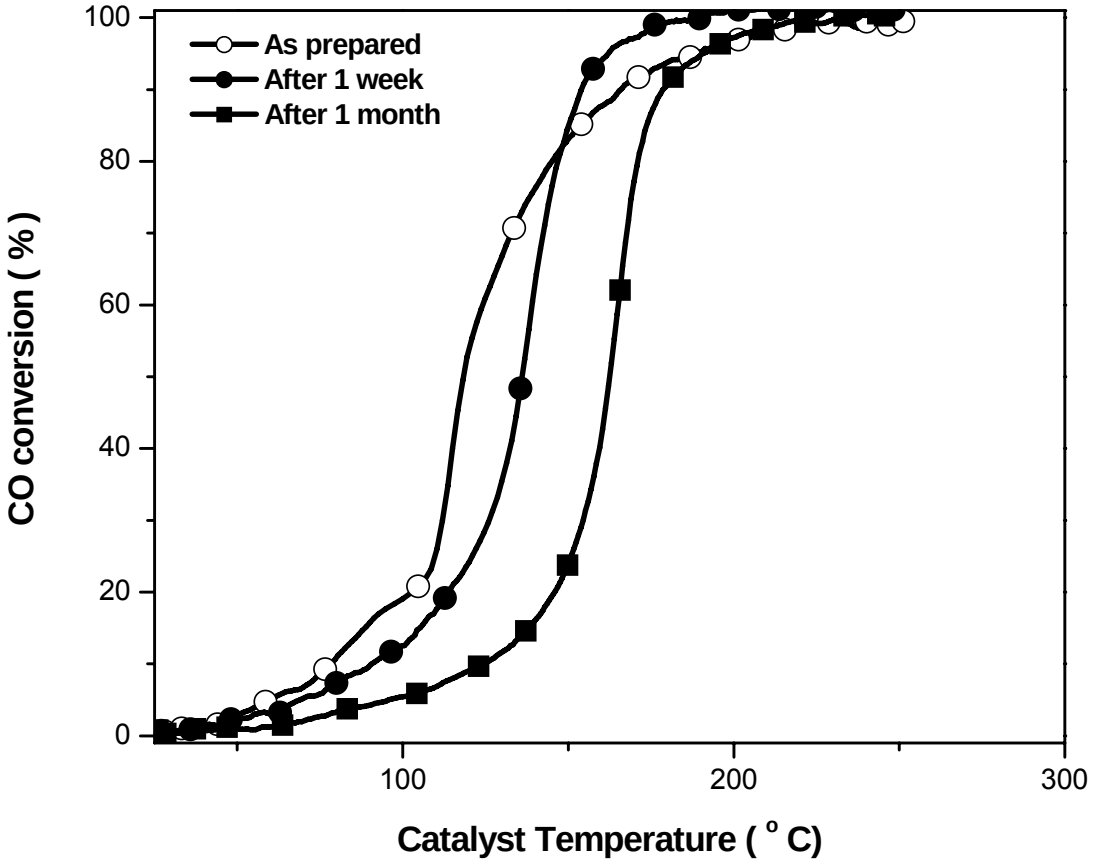

Figure 36: Catalytic activity of Au/CeO_2 as prepared by LVCC (run 1) as a function of time.

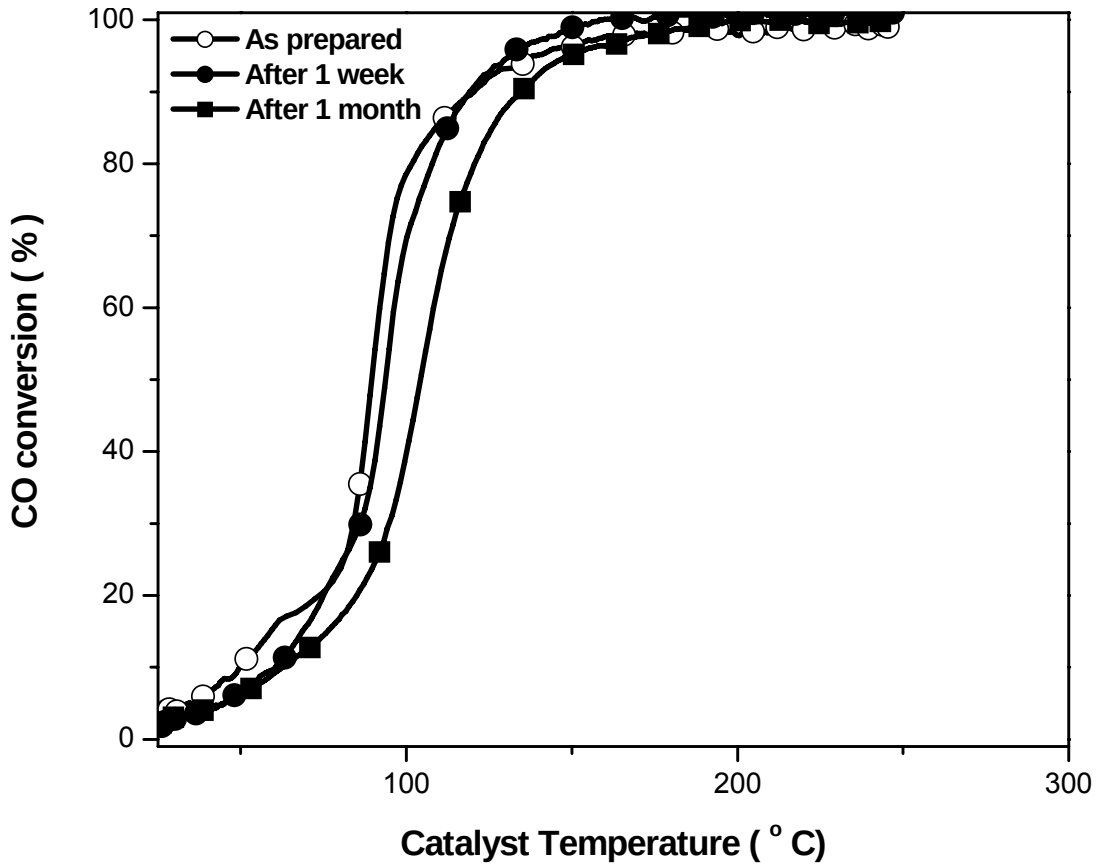

Figure 37: Catalytic activity of Au/CeO_2 prepared by LVCC after heat treatment (run 2) as a function of time.

Table 16 summarizes the catalytic activity of Au/CeO_2 catalyst as a function of time.

Sample 5%Au/CeO_2	**3% Conversion Light-off Temp.(^{o} C)**	**50 % Conversion Temp. (^{o} C)**	**Maximum Conversion (%)**	
			Temp. (^{o} C)	**Conversion**
As prepared Run 1	50.2	118.2	233.2	99.5
As prepared Run 2	27.5	89.95	210.9	99.4
After 1 week Run 1	37.9	93.3	162.9	100.0
After 1 week Run 2	37.9	93.3	188.4	99.6
After 1 month Run 1	77.3	162.2	223.1	100
After 1 month Run 2	32.6	104.5	202.1	100

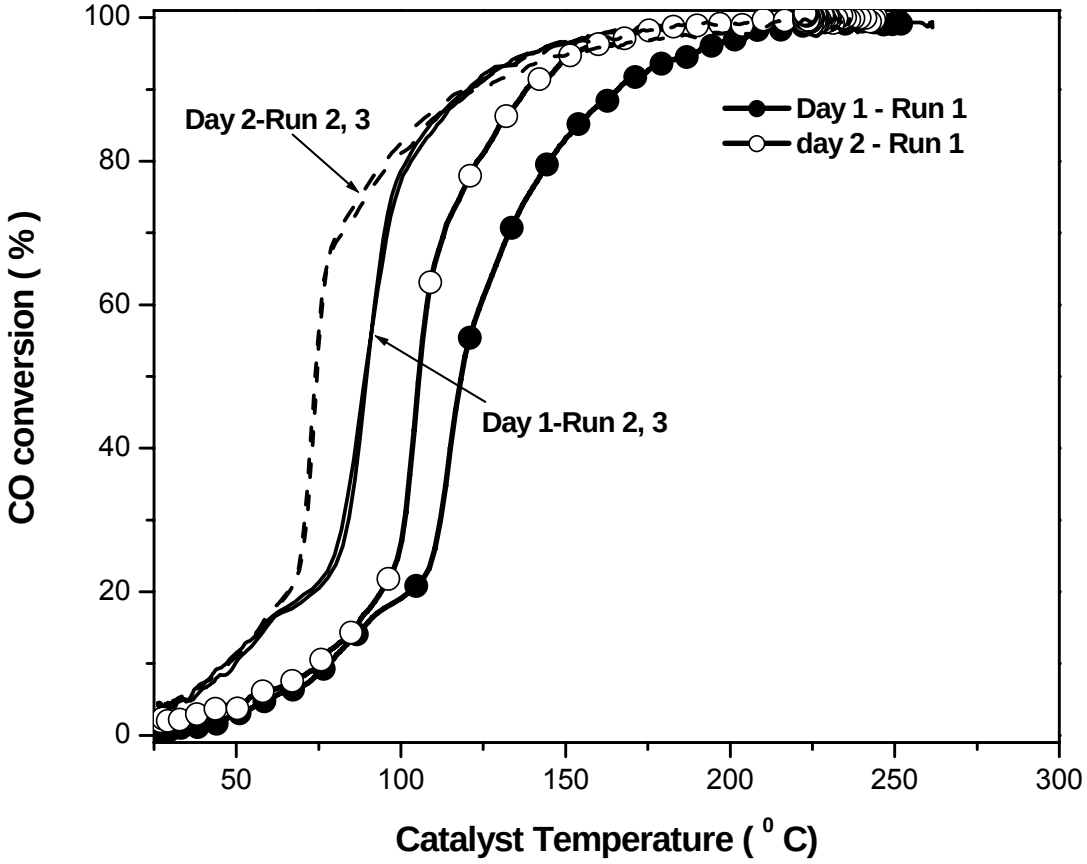

Figure 38: Catalytic activity of same untreated sample as prepared and after one day of aging.

Table 17 summarizes the catalytic activity of the same untreated sample as prepared and after one day of aging.

Sample 5%Au/CeO_2	**3% Conversion Light-off Temp.(^{o} C)**	**50 % Conversion Temp. (^{o} C)**	**Maximum Conversion (%)**	
			Temp. (^{o} C)	**Conversion**
Day 1 Run 1	50.2	118.2	233.2	99.5
Day 1 Run 2, 3	27.5	89.95	210.9	99.4
Day 2 Run 1	38.6	105.8	208.9	100.0
Day2 Run 2, 3	27.5	74.0	227.4	99.2

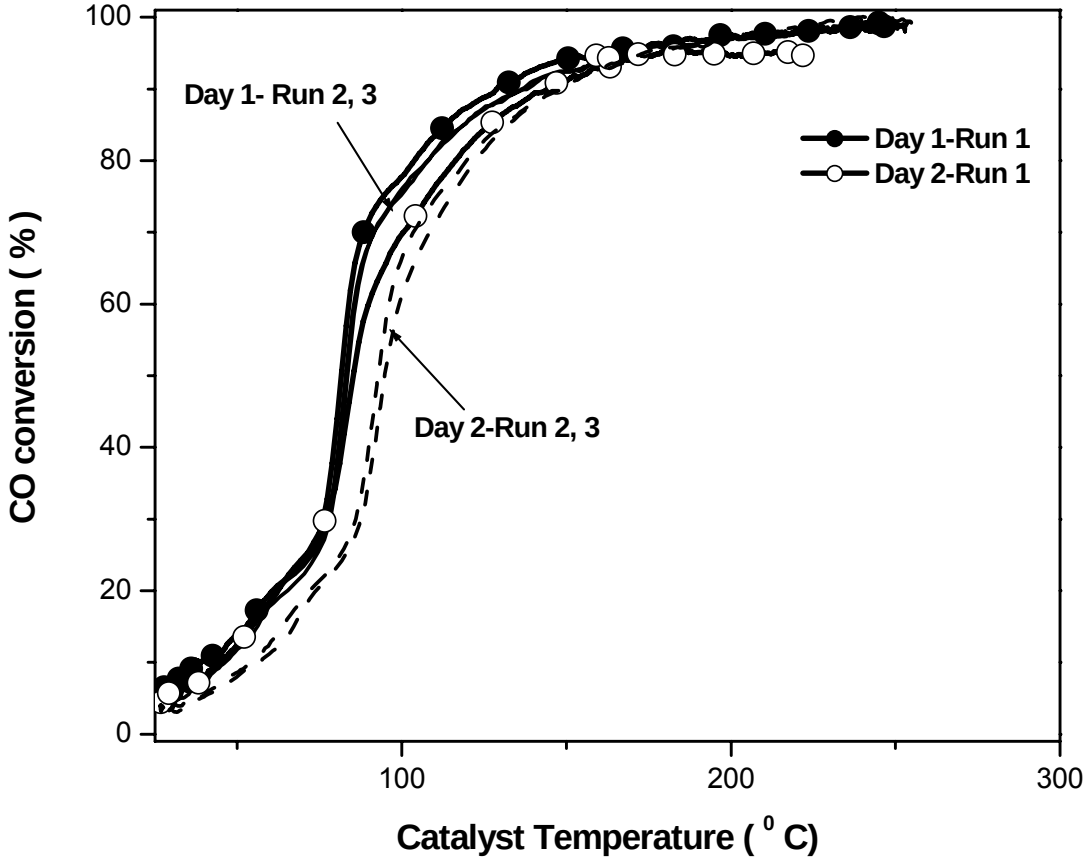

Figure 39: The catalytic activity of multiple runs of the Au/CeO_2 catalyst treated 300 ^{0}C in He as prepared and after one day of aging.

Table 18 summarizes the catalytic activity of multiple runs of the Au/CeO_2 catalyst treated 300 ^{0}C in He as prepared and after one day of aging.

Sample 5%Au/CeO_2	**3% Conversion Light-off Temp.(^{o} C)**	**50 % Conversion Temp. (^{o} C)**	**Maximum Conversion (%)**	
			Temp. (^{o} C)	**Conversion**
Day 1-Run 1	< 25	80.7	170.2	96.3
Day 1-Run 2	< 25	83.2	210.9	98.9
Day 1-Run 3	< 25	83.2	237.7	98.9
After 1day Run 1	< 25	84.9	185.3	95.5
After 1day Run 2	31.6	93.3	253.8	99.4
After 1day Run 3	31.6	94.2	243.1	100.0

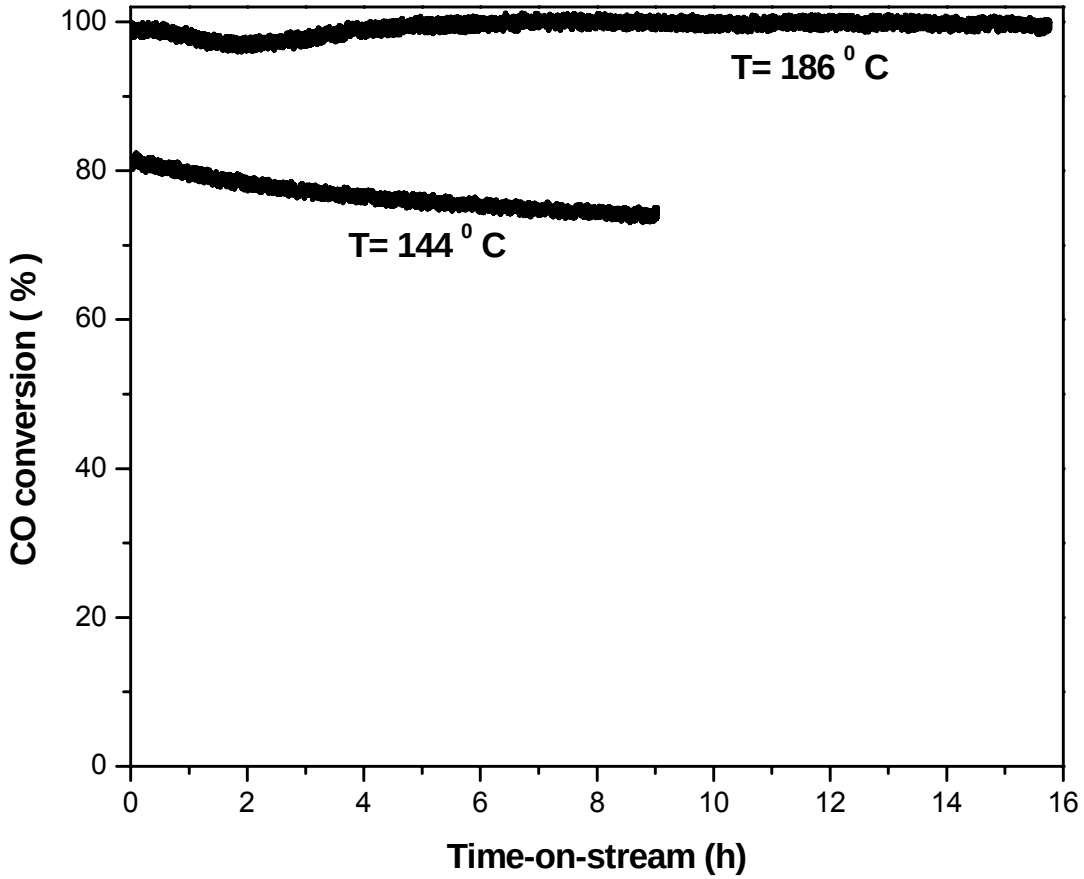

Figure 40: Long term stability of 5 % Au / CeO_2 (1500 Torr Ar) at 80 % and 100 % conversion.

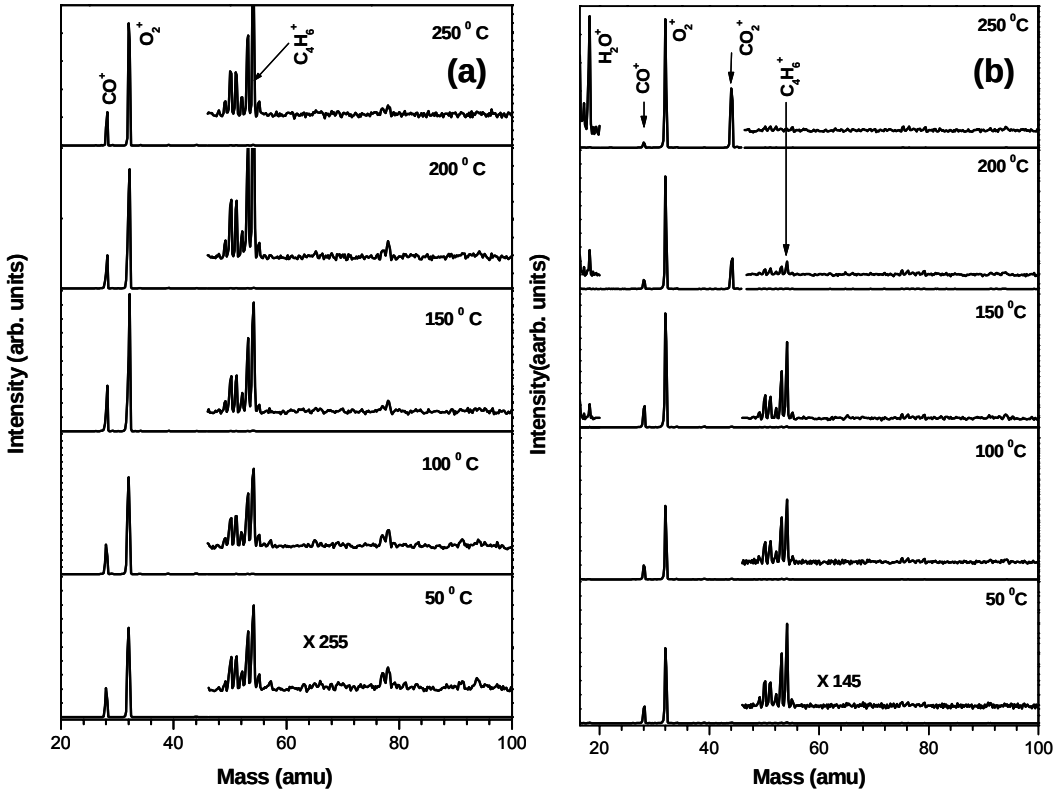

Figure 41: Mass spectrum at different temperatures of (3.4 % CO, 20 % O_2 in He mixture) in presence of 1000 ppm butadiene a**)** Without catalyst. b**)** With 5 % Au/CeO_2 catalyst.

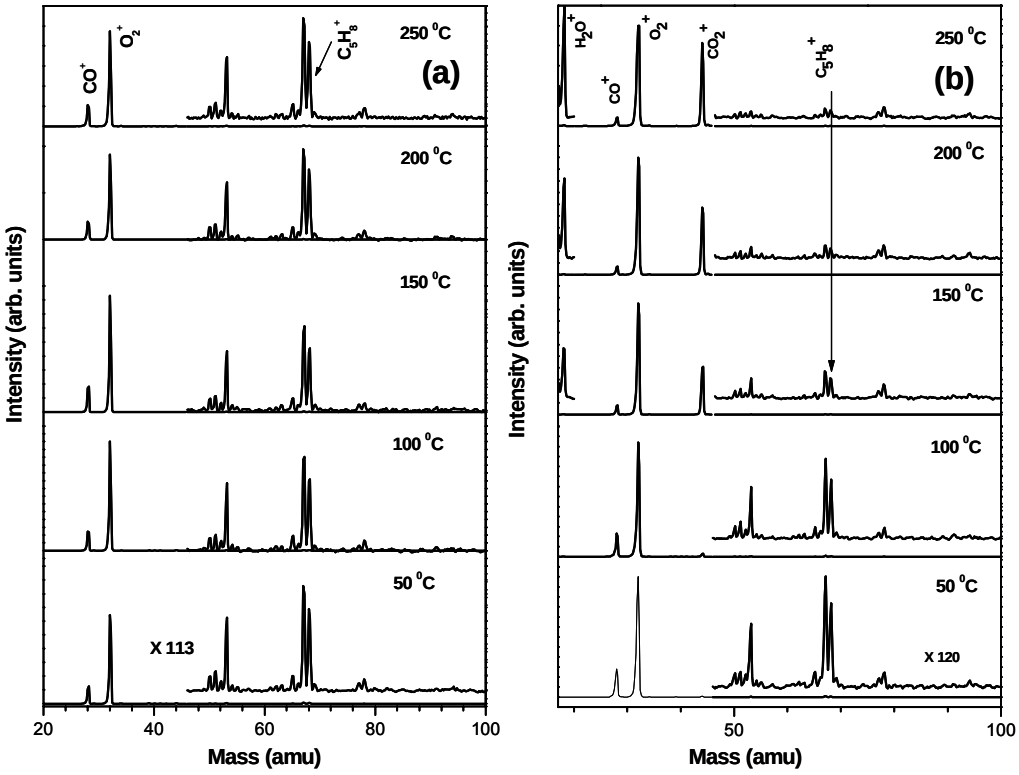

Figure 42: Mass spectrum at different temperatures of (3.4 % CO, 20 % O_2 in He mixture) in presence of 1000 ppm isoprene a**)** without catalyst. b**)** With 5 % Au/CeO_2 catalyst.

4 : Comparison between Au/CeO_2 nanoparticle catalysts prepared by Physical and Chemical Methods

4.1 Introduction

The Au/CeO_2 nanoparticle catalyst has been used in a variety of reactions, such as water-gas reaction [87,103], the catalytic combustion of VOC [94], and low temperature CO oxidation [90,92]. Au/CeO_2 nanoparticle catalysts have been prepared chemically by a variety of methods, the most previous work has been carried out in liquid mixtures or solutions [87-91,93].

Au/CeO_2 catalysts are very sensitive to the preparation method. The preparation method can affect the catalytic activity by determining the Au precursor (metallic or Au ion), as in the case of the classical deposition-precipitation method [104,105], and the method to introduce Au onto the support (e.g., chemical methods [87-91,93] such as impregnation, precipitation, co-precipitation and precipitation-deposition or physical methods such as laser ablation and ion implantation). These factors can affect the particle size and other variables such as the metal support interaction. Pretreatment conditions can also change the stability of catalytic activity, depending on the support nature, increasing the metal-support interaction and the preparation method which determines the oxidation state of the metal the nature of the actives in this catalyst is not yet resolved. Some studies suggest that Au^0 is the active site [94]. Others indicate the role of Au^+ and Au^{+3} species [90,92]. Most active samples can be obtained without temperature heat treatment (calcinations) or calcinations at low temperatures [73,106]. Au nanoparticles can be generated by the mean of physical methods where the vapor resulting from the vaporization of bulk Au result in vapor

consists of Au atoms in the gas phase (which is later condensed under controlled conditions to form nanoparticles [107]) or by chemical methods where Au compounds are used as a starting material, linked with reduction steps.

The advantages of the vapor phase synthesis are the contamination-free products (as compared to Chemical reductions in solutions), the elimination of the chemical precursors and solvents, and in most cases, the production of highly crystalline nanoparticles.

In this chapter, the catalytic activities of Au/CeO_2 prepared from the vapor phase (LVCC) and chemical rout deposition-precipitation technique (DP) will compared.

4.2 Experimental Results

4.2.1 Surface area and particle size

Although the Au/CeO_2 prepared by the LVCC method shows higher catalytic activity than other conventional catalysts, the LVCC method has disadvantages, such as low yield as compared to chemical methods. As an alternative method to produce a large amount of the catalyst, 5% Au/CeO_2 was prepared using chemical methods, in this case Deposition-Precipitation method (DP).

The X-ray diffraction patterns of the Au/CeO_2 nanoparticle catalyst as prepared by the LVCC and deposition-precipitation (DP) methods are shown in Figure 43. Although the X-ray diffraction pattern for Au/CeO2 shows crystalline CeO_2 in both catalysts, the CeO_2 peaks of Au/CeO_2 (DP) catalyst has higher intensity than Au/CeO_2 (LVCC) catalyst. Furthermore, the Au/CeO_2 (LVCC) peaks are more broadened than Au/CeO_2 (DP) peaks.

This result indicates that the Au/CeO_2 (DP) is more crystalline than the Au/CeO_2 (LVCC) and that the particle size of the Au/CeO_2 (LVCC) catalyst is smaller. Owing to the small size of the nanoparticles, the BET (Brunner–Emmett–Teller) surface area of the LVCC catalyst is very high at 84.5 m^2/g, compared to the DP catalyst which has a surface area of 23.93 m^2/g. The X-ray diffraction patterns of the Au/CeO_2 (DP) nanoparticle catalyst does not show Au peaks while the Au/CeO_2 (LVCC) catalyst shows small broad Au peaks were at least Au (111) peak can be distinguished. These results can be attributed to the high disparity of Au particles, the less metallic Au in the Au/CeO_2 (DP) nanoparticles, and the presence of less dispersed crystalline metallic Au particles in the Au/CeO_2 (LVCC) nanoparticles.

Figure 44 shows SEM micrographs of the Au/CeO_2 (LVCC) and Au/CeO_2 (DP) morphologies. There are two types of morphologies that can be distinguished for the LVCC and DP samples. The LVCC has elongated particles with web-like structures where both Au and CeO_2 are in the nanoscale and spherical where metallic Au nanoparticles is dispersed on large CeO_2 particles. The morphology of Au/CeO_2 (DP) is different, though the metallic Au nanoparticles were never observed on the CeO_2 particles. As shown in Figure 45, the Transmission Electron microscope (TEM) of the Au/CeO_2 'as prepared' of both samples confirms the X-ray diffraction results and shows that the LVCC sample has small Au, CeO_2 elongated particles (2-5 nm), and Au particles (5-10 nm) dispersed on large CeO_2 particles (30-500 nm). It is important to note that these results are confirmed by EDS. In the chemical method the phase contrast within the agglomerates is characteristic

of disordered, or semi-crystalline, material where the metallic Au nanoparticles were never observed either by X-ray diffraction patterns or TEM.

4.2.2 Oxidation state of Au and Au-CeO_2 interaction

X-ray and TEM are used to characterize the bulk and do not provide a useful information about the active site for CO oxidation in the catalyst. In order to probe the active site, a surface sensitive technique is needed. X-ray Photoelectron Spectroscopy is a good technique to study the catalyst surface and determine the oxidation state of Au. XPS analysis of 5% Au/CeO2 prepared by physical and chemical methods Ce 3d and Au4f. Figure 46 shows high-resolution Ce 3d spectrum which was consistent with Ce^{+4} (including similar shake-up peaks) for both samples. The LVCC sample has a tiny bump at ~885.7eV which may indication of the presence of Ce^{+3}.

Figure 47 shows a curve fitting of Au4f spectrum of the Au/CeO_2 nanoparticle catalyst prepared by physical and chemical methods. The curve fitting of Au4f spectrum of both samples indicates that both contain mostly Au^0 and small amounts of Au^+ species. Au/CeO_2 prepared by the chemical method has a higher % of Au and contains more Au^+ than Au/CeO_2 prepared by the physical method, as shown in Table 19.

Based on XPS and TEM results, it can be concluded that the Au in both samples is amorphous, most of Au is in the metallic state Au^0, and it forms a solid solution of Au and CeO_2. However, Au obtained by the chemical method is more amorphous and part of the Au exists in the form of AuOH, with an oxidation state of +1 [108].

Oxidation state of the Au is directly related to the interaction between Au and CeO_2. TPR is used to study the interaction between Au and CeO_2 in both samples. Figure 48 is TPR patterns of Au/CeO_2 prepared by physical and chemical methods. The temperature at which $Au\text{-}CeO_2$ reacts with H_2 is 25^0C. The high temperature CeO_2 peak is shifted to a lower temperature region with T_{max} around 451 ^{0}C compared to high temperature CeO_2 peak. A new feature appears at temperature region (219 -385 ^{0}C) is believed to come from the reduction of Ce-Au-O species. The presence of Ce-Au-O is supported by the XPS data which shows the presence of traces of Ce^{+3} and Au^+. The reduction of Ce-Au-O enhances the redox activity of $Au\text{-}CeO_2$. From these results it can be concluded that there is weak metal-support interaction in the Au/CeO_2 (LVCC) method. However, in the case of the Au/CeO_2 (DP) catalyst, all the ceria, including the bulk ceria reduces at 50 ^{o}C and below. The two peaks that characterize the ceria almost disappeared and a new peak formed at approximately room temperature. The high intensity peak at room temperature is attributed to the reduction of Au^+ to Au^o by removing the OH group. This indicates that this catalyst has a strong metal-support interaction (SMSI) compared to the Au/CeO_2 (LVCC) catalyst.

4.2.3 Catalytic activity

The activity of the Au/CeO_2 catalysts prepared by physical and chemical methods is measured as prepared (run 1). Figure 49 is a comparison between Au/CeO_2 activities prepared by the two methods. The light off temperature of Au/CeO_2 (DP) is 0.1^o C and reaches a full conversion at approximately 110^o C compared to Au/CeO_2 (LVCC) which

has a light-off temperature of 50^{o} C and reaches a full conversion at 233^{o} C. Table 20 summarizes the activities of both methods. Heat treatment in the CO/O_2 mixture (run 2) results in a shift in the light-off temperature for both catalysts (from 50^{o} C to 27^{o} C for the LVCC catalyst and from 0.1^{o} C to -28^{o} C for DP catalyst), as shown in Figure 50. Table 21 shows the activities of Au/CeO_2 prepared by physical and chemical methods after heat treatment in CO/O_2 mixture (run 2). The shift in the light-off temperature can be attributed to the removal of the moisture; impurities such as hydrocarbon deposits from the catalyst surface, reduction of the catalyst by CO, and the precipitation of Au in the $Au\text{-}CeO_2$ solid solution to the surface, which increases the metal support interaction. To understand the shift in the catalytic activity curve to the lower temperatures, both catalysts are characterized using X-ray diffraction and HRTEM after catalysis. Figure 51 shows X-ray diffraction patterns of Au/CeO_2 prepared by both methods after the heat treatment in CO/O_2 mixture (run 2). As expected the CeO_2 support becomes crystalline in both catalysts. Strong reflection of crystalline metallic Au can be observed in both catalysts by the presence of Au (111), Au (200), and Au (311) planes. After heat treatment in the CO/O_2 mixture, as shown in Figure 52, both catalysts develop a completely different microstructure, a dispersion of metallic Au nanoparticles having (5-10 nm) in the LVCC catalyst, and (3-7 nm) in the DP catalyst. These particles are supported on highly crystalline CeO_2 particles with sizes ranging from 50-500 nm.

Deposition Precipitation method (DP) shows activity below room temperature similar to Au/TiO_2 catalysts reported by Haruta [47] and Au/Fe_2O_3 catalysts reported by Deevi *et a.l* [109]. Reaction mechanisms of CO oxidation on Au/TiO_2 catalysts are reported

by Haruta *et al.* [47]. He suggests that the reaction take place on Au surfaces at the steps, edges, and corners of Au particles with activation energy of 0 kJ/mol (below 300 K). At temperatures above 300 K, the reaction takes place at the perimeter interfaces, were CO adsorbed on the surfaces of Au nanoparticles and the molecular oxygen adsorbed at the support interface with activation energy of 0 kJ/mol, and it proceeds faster.

In addition to the XPS and TPR results, and based on the results obtained by Haruta [47], The difference in the catalytic activity of Au/CeO_2 catalysts prepared by physical and chemical methods in the way that Au nanoparticles set on the support and the length of the interface between them can be explained. In the physical method, the interface is shorter than in the chemical method. As a result, the interaction is stronger in the chemical method, which results in higher activity. Figure 53 shows the proposed scheme of CO oxidation reactions on Au/CeO_2 prepared by both methods along with the proposed morphologies.

4.2.4 Stability

Finally, the catalytic activity of Au/CeO_2 catalysts prepared by physical and chemical methods was measured as a function of time by keeping the temperature constant at 186 ^{o} C, which corresponds to 100% conversion while CO/O_2 mixture is flowing over Au/CeO_2 as shown in Figure 54. It is clear that Au/CeO_2 nanoparticle catalysts prepared by physical and chemical methods show very good stability for more than 14 h. This stability is demonstrated by the constant conversion percentage of 100 % even after 16 h of continuous conversion.

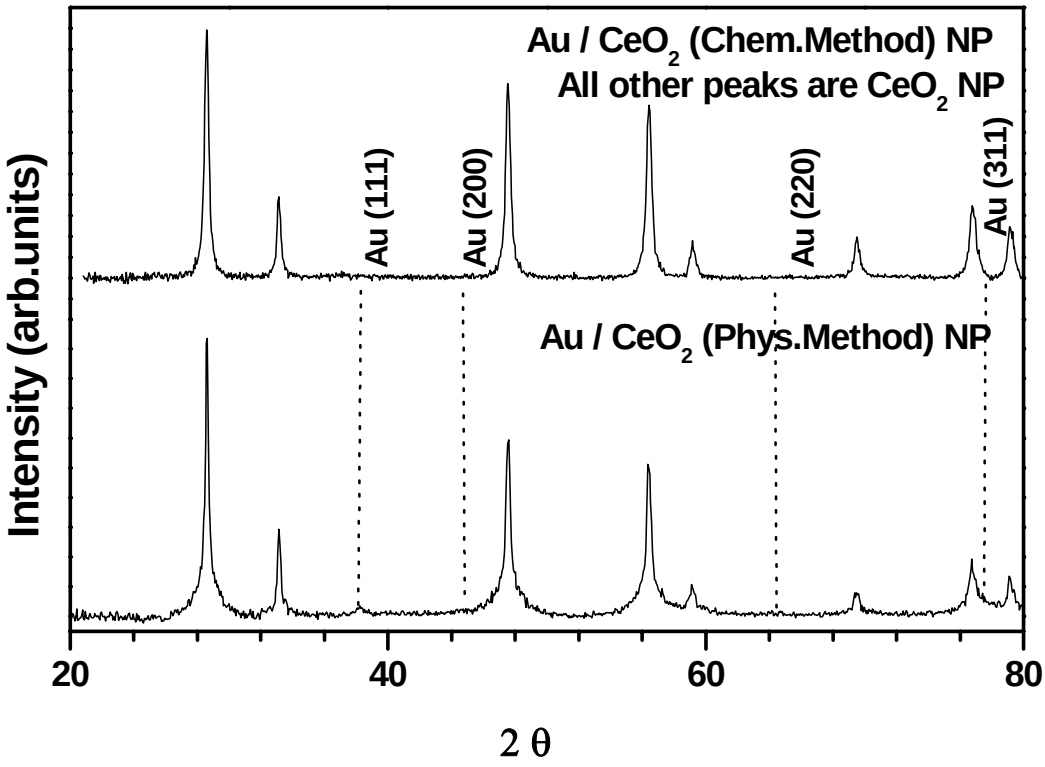

Figure 43: X-ray diffraction patterns of Au/CeO_2 as prepared by the physical method (LVCC) and the chemical method (Deposition-Precipitation (DP).

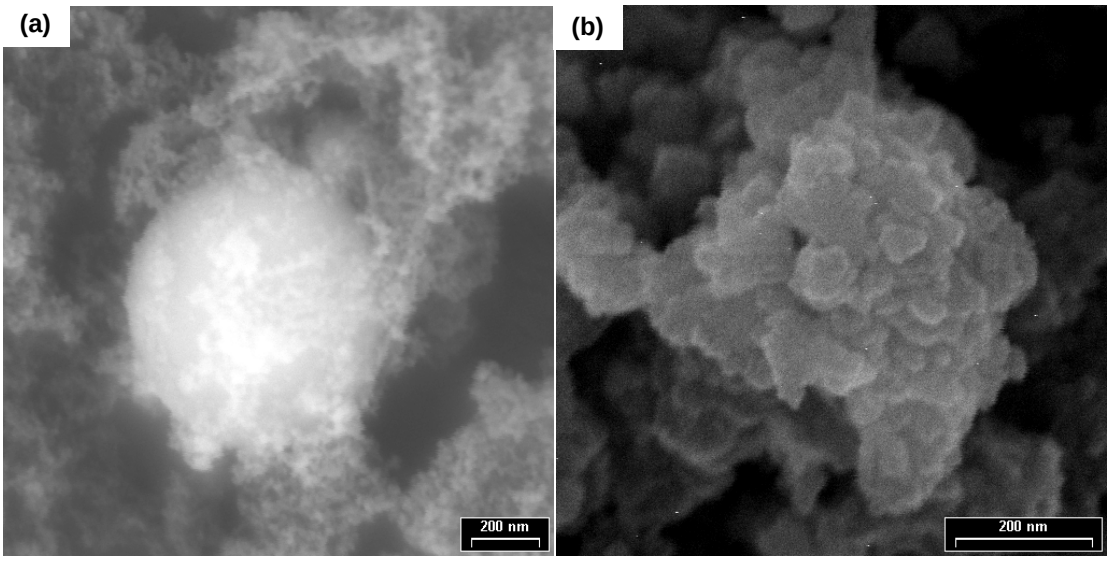

Figure 44: SEM micrographs of Au/CeO_2 nanoparticle catalysts as prepared by the LVCC method and the Deposition-Precipitation method (DP).

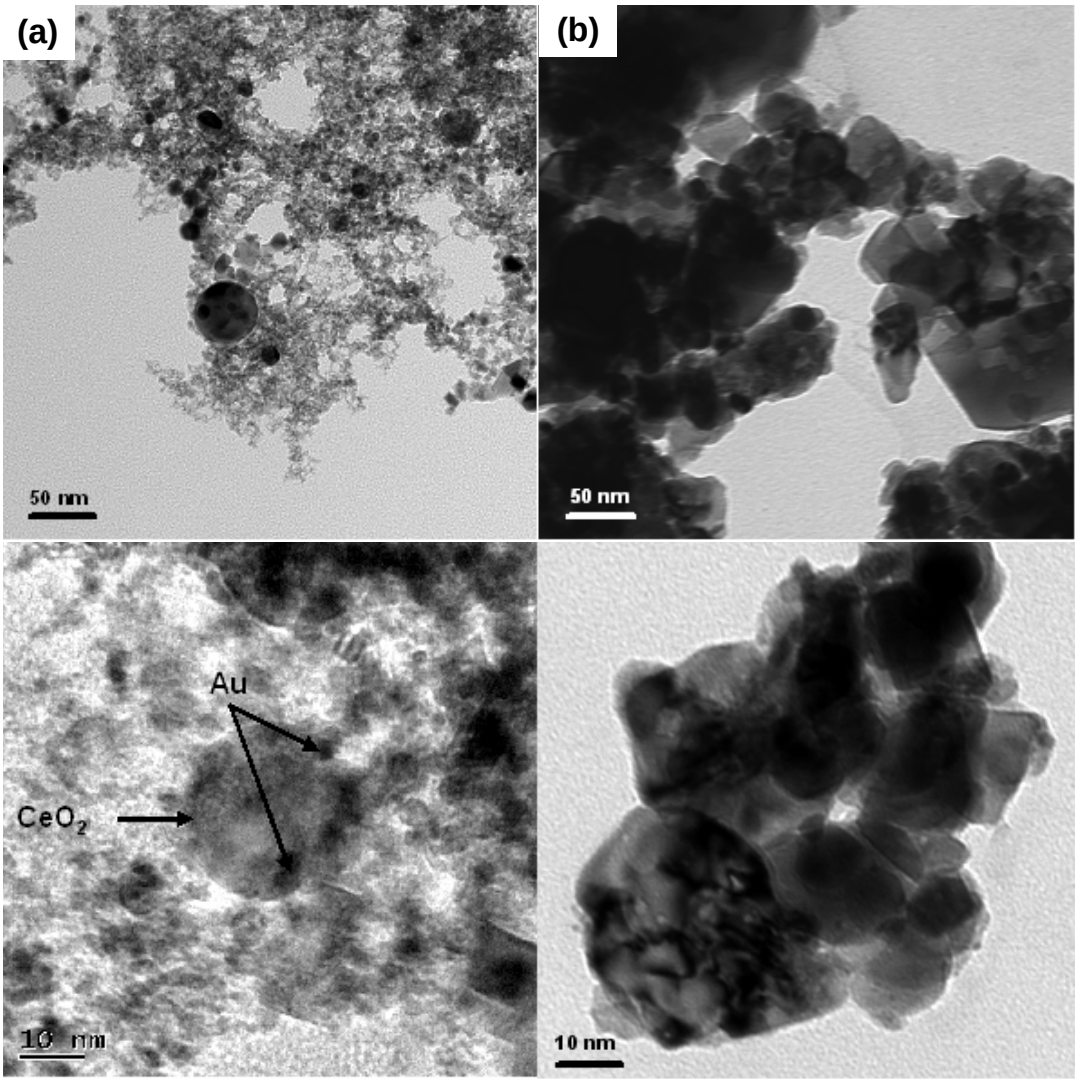

Figure 45: TEM micrographs of Au/CeO_2 as prepared by: a) Physical method (LVCC). b) Chemical method (DP).

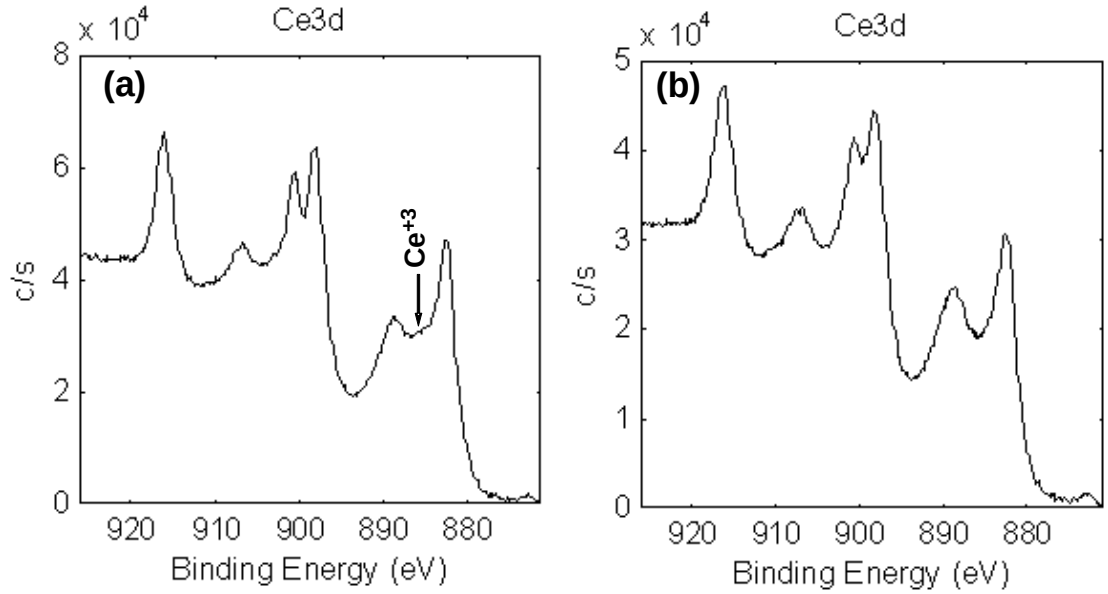

Figure 46: High-resolution Ce 3d spectrum of a) 5% Au/CeO_2 (LVCC) b) 5% Au/CeO_2 (Dp).

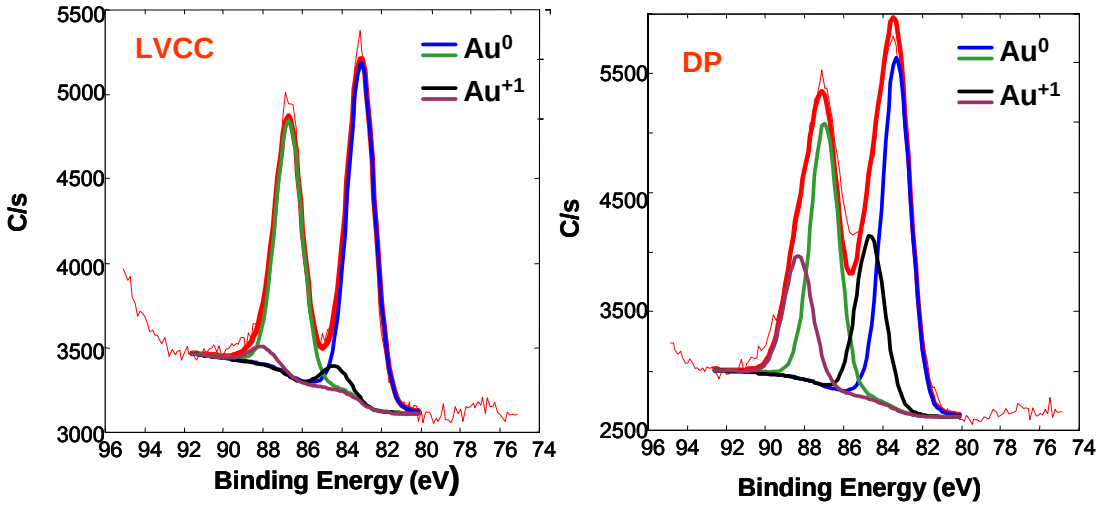

Figure 47: Curve fitting of Au4f spectrum of Au/CeO_2 prepared by a) LVCC method b) DP method.

Table 19 compares the total Atom % of Au (Au^0 and Au^+) at the surface of Au/CeO_2 catalysts prepared by LVCC and DP methods.

Sample	Total Au (Atom %)	Au^0 (Atom %)	Au^+ Atom %
Au/CeO_2 (LVCC)	0.3	0.282	0.018
Au/CeO_2 (DP)	1.2	0.8	0.4

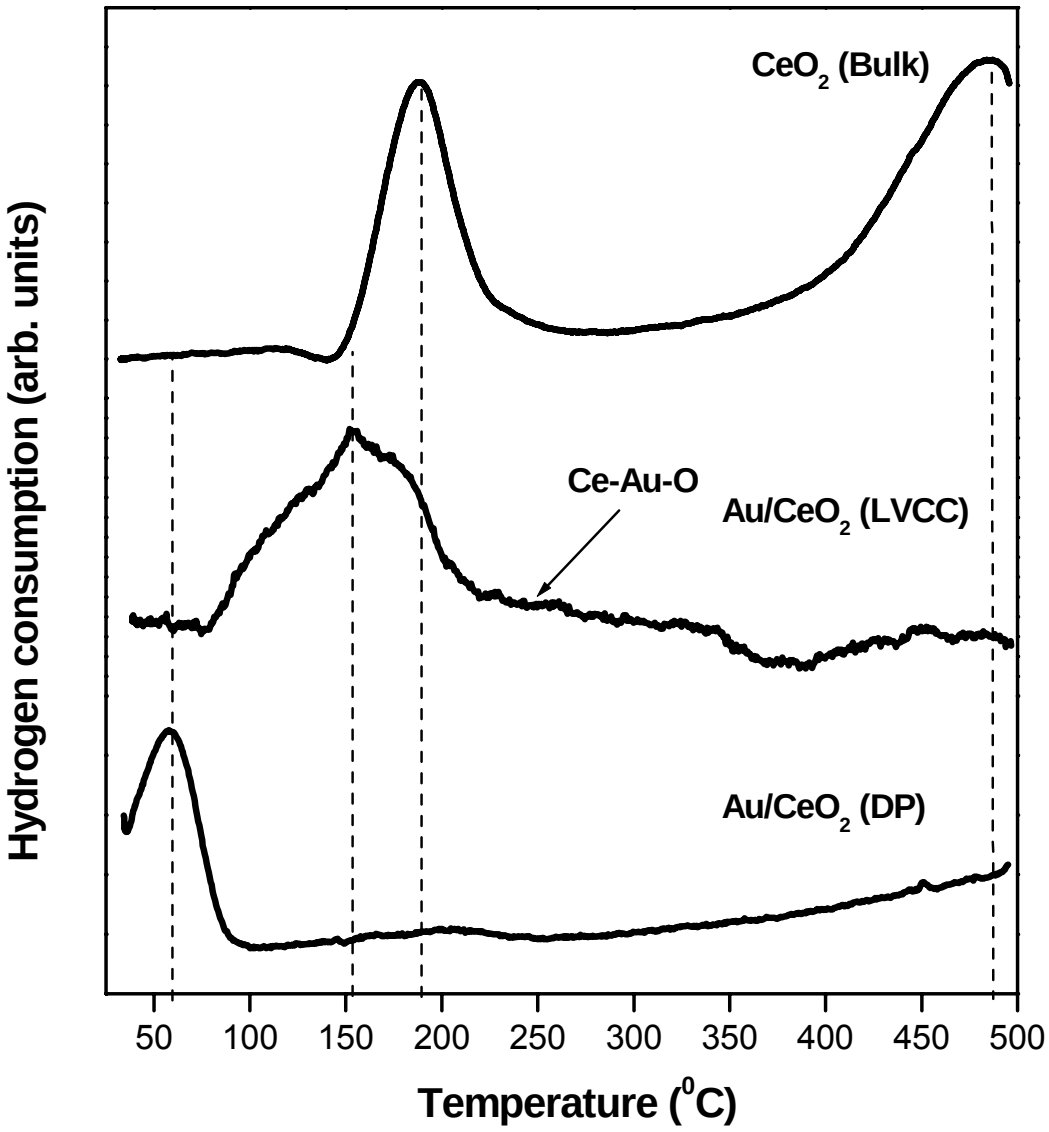

Figure 48: TPR patterns of CeO2 bulk powder and Au/CeO2 prepared by physical and chemical methods.

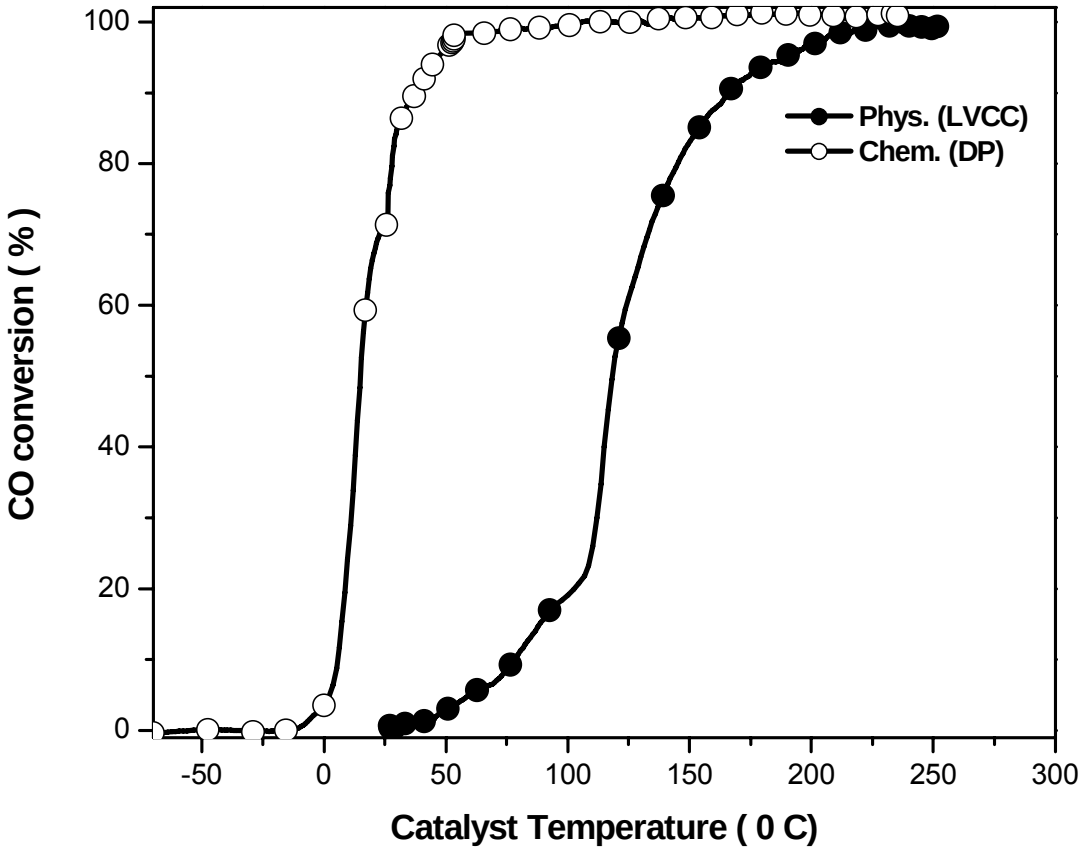

Figure 49: Comparison between Au/CeO_2 activities as prepared (run 1) by chemical and physical methods

Table 20 summarizes the catalytic activities of Au/CeO_2 as prepared (run1) by chemical and physical methods.

Sample 5%Au/CeO_2	**3% Conversion Light-off Temp.(^{o} C)**	**50 % Conversion Temp. (^{o} C)**	**Maximum Conversion (%)**	
			Temp. (^{o} C)	**Conversion**
Physical (LVCC)	50.2	118.2	233.2	99.5
Chemical (DP)	0.1	14.7	110.0	100.0

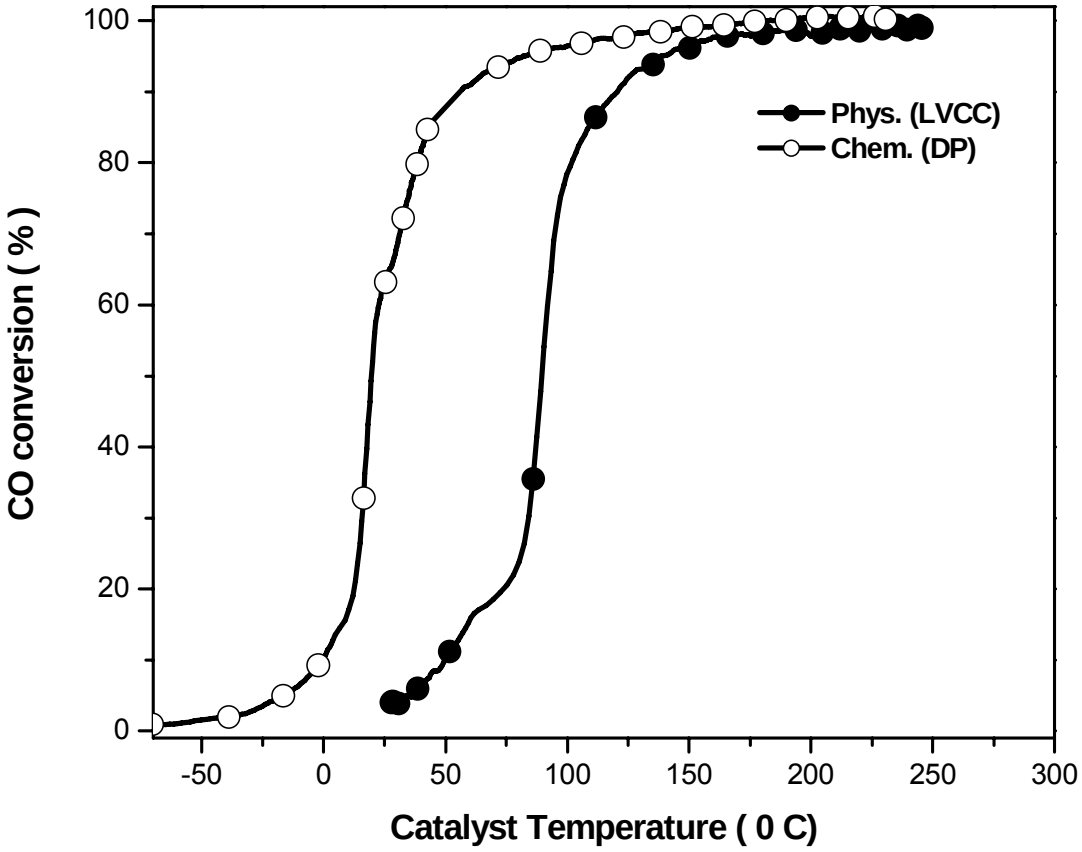

Figure 50: Comparison between Au/CeO_2 activities as prepared (run 2) by chemical and physical methods.

Table 21 summarizes the catalytic activities of Au/CeO_2 as prepared (run2) by chemical and physical methods.

Sample 5%Au/CeO_2	**3% Conversion Light-off Temp.(^{o} C)**	**50 % Conversion Temp. (^{o} C)**	**Maximum Conversion (%)**	
			Temp. (^{o} C)	**Conversion**
Physical (LVCC)	27.5	89.95	210.9	99.4
Chemical (DP)	-28.3	19.2	178.3	100.0

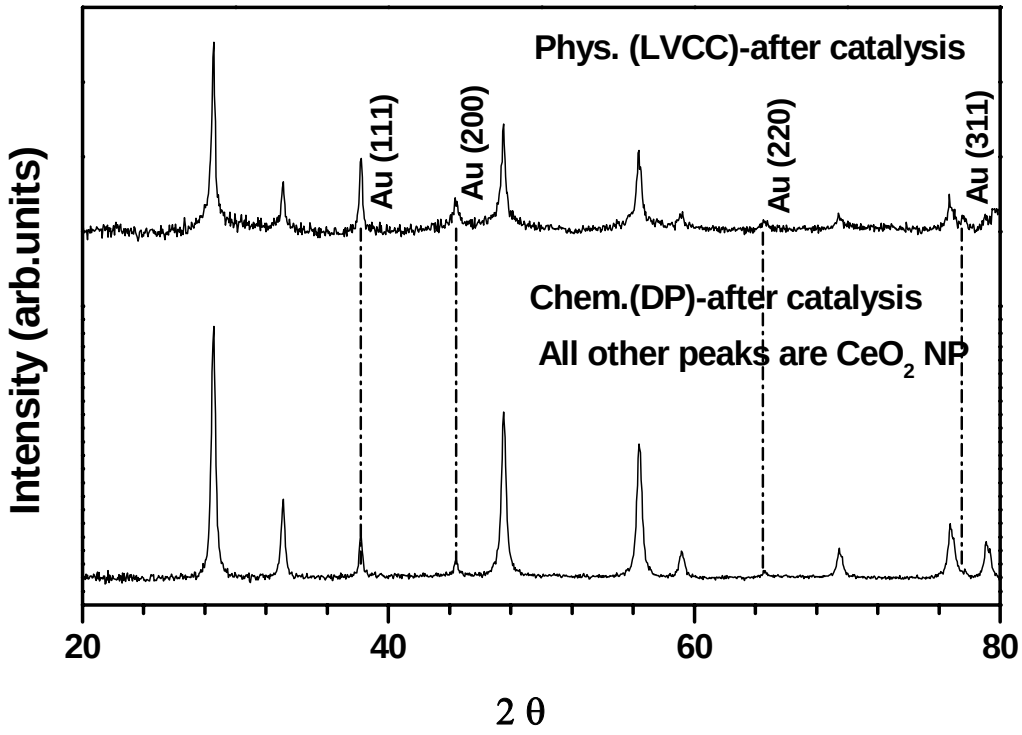

Figure 51: X-ray diffraction patterns of Au/CeO_2 catalysts prepared by physical and chemical methods after heat treatment in CO/O_2 mixture (run 2).

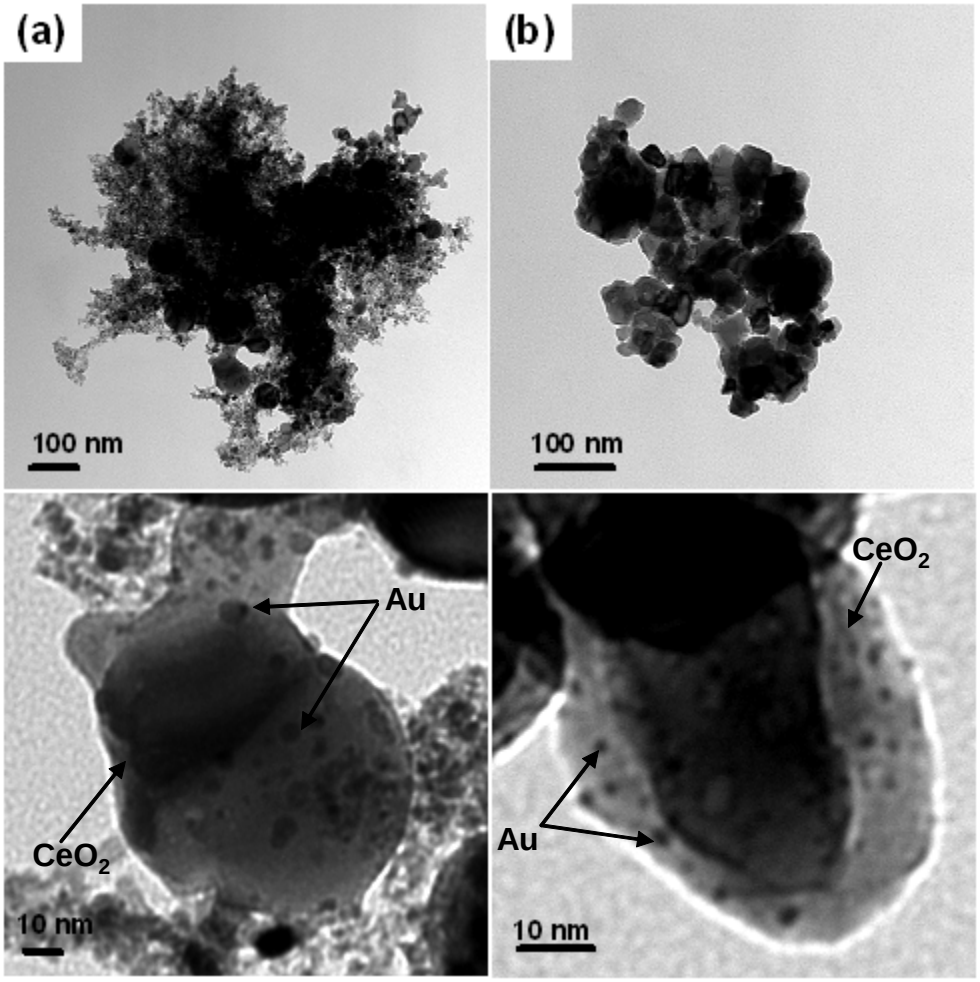

Figure 52: TEM of Au/CeO_2 catalysts prepared by a) Physical method (LVCC) b) chemical method (DP).

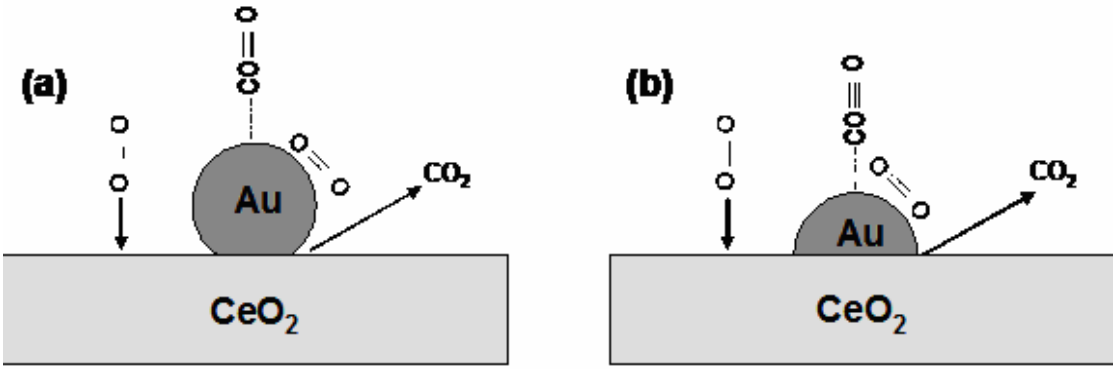

Figure 53: The proposed scheme of CO oxidation reaction on Au/CeO_2 catalyst a) prepared by LVCC method b) deposition-precipitation method proposed by Haruta [47].

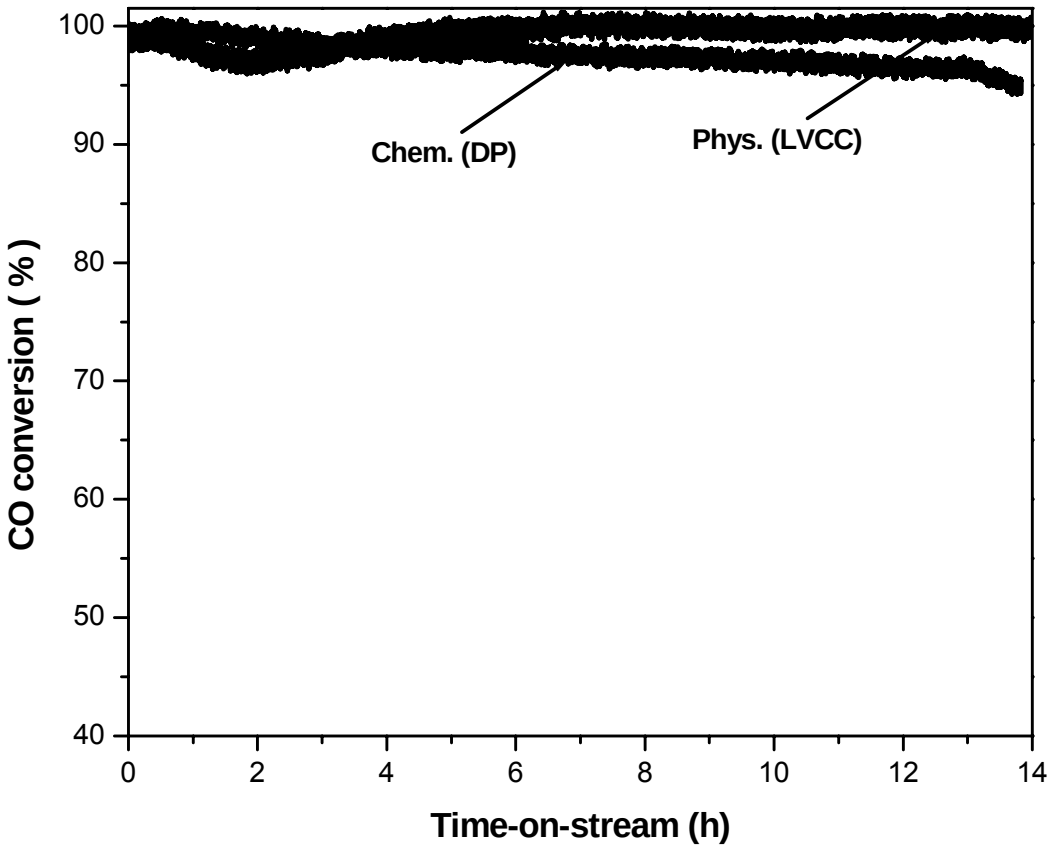

Figure 54: Long term stability of 5 % Au / CeO_2 and 100 % conversion (T= 186 ^{o}C) prepared by physical and chemical methods.

5 : Low temperature CO oxidation Au and Cu and AuCu alloy catalysts.

5.1 Introduction

Oxidation of carbon monoxide has been carried out on various catalysts including precious metals, perovskite-type, and transition metal catalysts[110-114]. However, the high cost of precious metals and their sensitivity to sulfur poisoning motivated researchers to search for new catalysts. The reactivity of adsorbed oxygen on metal surfaces has received considerable interest in relation to heterogeneous catalysis [115]. In contrast to the high reactivity of noble metals, transition metals like Cu are regarded to be much less reactive because stable oxide phases are easily produced due to their large oxygen affinity. The activity of Cu nanoparticle catalysts for CO oxidation is comparable with that of the noble metal Pd catalysts [116]. It was reported that CO oxidation proceeded on metallic Cu films at 473-623 K, with smaller activation energy than those for Pt and Pd [117]. The catalytic CO oxidation on Cu (110) in a mixture of CO and O_2 also proceeds at low temperatures until oxygen coverage increased to cover the surface with the produced -Cu-O- chains as reported by Sasaki *et al* [118]. The catalytic activity of Cu nanoparticles is enhanced after the catalytic reaction due to the oxidation of Cu [116]. The origin of CO oxidation over metallic Cu powders is due to a synergistic effect of rising temperature due to heat generation from Cu oxidation as well as CO oxidation over the partially oxidized copper species. The activity of copper oxide species can be elucidated in terms of species transformation and the change in the number of surface lattice oxygen ions. The non-stoichiometric metastable copper oxide species formed during reduction is active in the course of CO oxidation because of its excellent ability to transport surface lattice oxygen. Consequently, the

metastable cluster of CuO is more active than CuO, and the activity is significantly enhanced when non-stoichiometric copper oxides are formed [119]. Although many studies have reported Cu based catalysts for CO oxidation, most of these studies do not differentiate between the catalytic activity of Cu and CuO since Cu is converted to CuO after the CO oxidation reaction. Supported Cu nanoparticles exhibit higher activity than the unsupported Cu catalysts due to the synergetic interaction with the metal oxide supports [120-126]. Among these supports is CeO_2, which is used as a promoter in the three-way catalyst (TWC) used in automotive emission control systems and can be used as a support for many oxidation catalysts [80,81]. For example, the addition of trace amounts of Ce can increase the Cu activity [116]. The activity of Cu nanoparticle catalysts depends on many factors, other than the supports, such as oxidation atmosphere, and the preparation process. However, many preparation methods focus on the chemical synthesis of these catalysts [127-129] or physical synthesis, such as arc or thermal plasma method [130].

Alloying is a phenomenon that can either improve the catalytic properties of the original single-metal catalysts or create new properties which may not be achieved by either of the individual metal catalysts[131]. Bimetallic systems have long commanded considerable interest in the study of heterogeneous catalysis. The addition of a second dissimilar metal often modifies the catalytic behavior of the first, in many cases enhancing the stability, activity, and/or selectivity beyond that of either catalyst alone [132-134].

Although supported gold catalysts have been extensively investigated for low-temperature CO oxidation [47,73,113,135], an alternative way to modify the gold-based catalysts is to search for a second metal such as Cu that can form an alloy with gold and possess

stronger affinity toward O_2 than gold. When two different metal atoms are in intimate proximity to each other, as in an alloy, the activated O_2 can easily react with the activated CO at a neighboring gold atom to produce CO_2. Häkkinen *et al*. reported that doping Au with Sr significantly changes the bonding and activation of O_2 compared with that in the pure gold, resulting in enhanced activity for CO oxidation [136]. The catalytic activity of AuAg has been investigated by Wang *et al* [137]. Guczi et al. investigated the Au–Pd bimetallic system for CO oxidation [138]. They investigated the effect of the support on the catalytic activity of Au-Pd alloy and found that when supported on SiO_2, the activity of the bimetallic catalyst is higher than the Pd/SiO2 catalyst. When supported on TiO_2, the bimetallic catalyst exhibited a slightly synergistic effect. This may due to the fact that Pd adsorbs O_2 very strongly and weakens the role of gold.

It is known that the electron transfer from metal to O_2 is a key factor in the chemisorption of oxygen on a metal surface [139]. Electron transfer is difficult on the Au (111) surface, since the gold surface has a high work function [140]. When compared to gold, Cu has a larger electron donating ability. It is known that the adsorption of O_2 occurs most easily on Cu, next on Ag, but not on Au. On the other hand, both gold and copper are able to adsorb CO [140,141]. Thus, combining Au with Cu may be an alternative catalyst with a higher activity for CO oxidation. Sra *et al* reported the synthesis of AuCu alloys nanoparticles for electronic applications [142]. Based on the literature, the catalytic activity of AuCu alloys nanoparticles has not been investigated yet.

In this chapter, the catalytic activity of unsupported Cu nanoparticles, and Cu nanoparticles supported on metal oxide supports will be investigated. After determining

the best support with the highest activity, the catalytic activity of the CuO nanoparticles supported on the same support will be compared.

Furthermore, the effect of the addition of Au to the Cu based catalyst on the catalytic activity both supported and unsupported will be examined. Two systems will be thoroughly studied. The first system is the physical mixture of Au and Cu both supported and unsupported. The second system is the alloying of Au and Cu both supported and unsupported. Finally, the catalytic activities of the AuCu physical mixture and the AuCu alloy for Co oxidation will be compared.

5.2 Experimental Results

5.2.1 Low temperature CO oxidation on Cu nanoparticles (unsupported)

Cu has a FCC crystal lattice structure similar to Au. Figure 55 shows the X-ray diffraction pattern of Cu nanoparticles prepared by LVCC. The typical characteristic planes (111), (200), (220) of FCC crystal lattice are retained in Cu nanoparticles, which is similar to Cu bulk structure. However, the diffraction peaks of Cu nanoparticles are broader compared to the bulk Cu, this broadening is due to their small particle size. The Cu nanoparticles have web-like morphology with (5-15 nm) particle size as shown in Transmission Electron Microscope (TEM) micrographs (Figure 56). The catalytic activities of Cu nanoparticles (as prepared by LVCC at 200 Torr Ar (run 1)) and after heat treatment in CO/O_2 mixture (run 2) are shown in Figure 57. It is clear that the catalytic activity is increased after the heat treatment. The catalytic activities of Cu nanoparticles are summarized in Table 22. To investigate these results, the X-ray diffraction patterns were

measured before and after the CO oxidation reaction, as shown in Figure 58. Unlike the X-ray diffraction patterns of Au nanoparticles after heat treatment, Figure 6 shows that Au does not oxidize after the CO oxidation reaction. However, X-ray diffraction patterns of Cu nanoparticles after heat treatment in CO/O_2 mixture show typical characteristic planes of CuO. Based on these results, the enhanced activity was attributed to the oxidation of Cu to form small CuO nanoparticles, which is more active than Cu nanoparticles as reported by Liu et al.[143]. Since Cu is easily oxidized, as demonstrated in the previous results, and to eliminate the possibility of small leaks, the effect of pressure on the catalytic activity of Cu nanoparticles was studied. Figure 59 shows the catalytic activities of Cu nanoparticles as prepared by LVCC in 200 and 1500 Torr Ar. As expected, the catalytic activity of Cu nanoparticles prepared in 1500 Torr is higher than the corresponding Cu nanoparticles prepared in 200 Torr. It is important to point out that there is a phase transition at 212 ^{o}C which corresponds to the oxidation of Cu to CuO. The same behavior is observed in run 2, as shown in Figure 60. Table 23 summarizes the catalytic activities of Cu nanoparticles as prepared by LVCC in 200 and 1500 Torr Ar (run 1 and run 2). The catalytic activities of Cu nanoparticles after heat treatment in CO/O_2 mixture was compared with the commercial nanophase CuO and CuO prepared from the evaporation of CuO target in 1500 Torr using the LVCC method as shown in Figure 61. It is clear that the catalytic activity of Cu nanoparticles after heat treatment in CO/O_2 mixture is identical to nanophase CuO. However, the catalytic activity of CuO prepared by LVCC is less than the catalytic activity of nanophase CuO and Cu nanoparticles after heat treatment in CO/O_2 mixture. These results are attributed to the formation of Cu_2O and a CuO phase during the evaporation of

CuO target in the LVCC method and since Cu_2O has lower oxidation state, it is less active than CuO for CO oxidation.

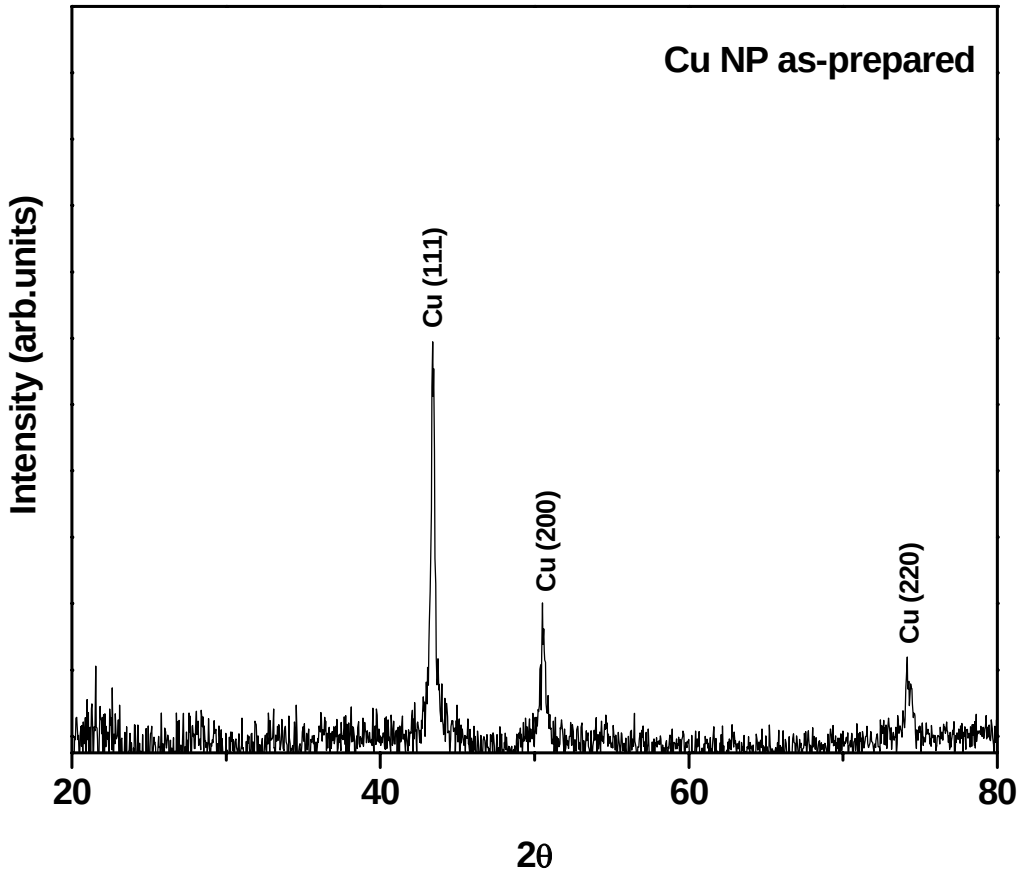

Figure 55: X-ray diffraction patterns of Cu nanoparticle catalysts as prepared by the LVCC method.

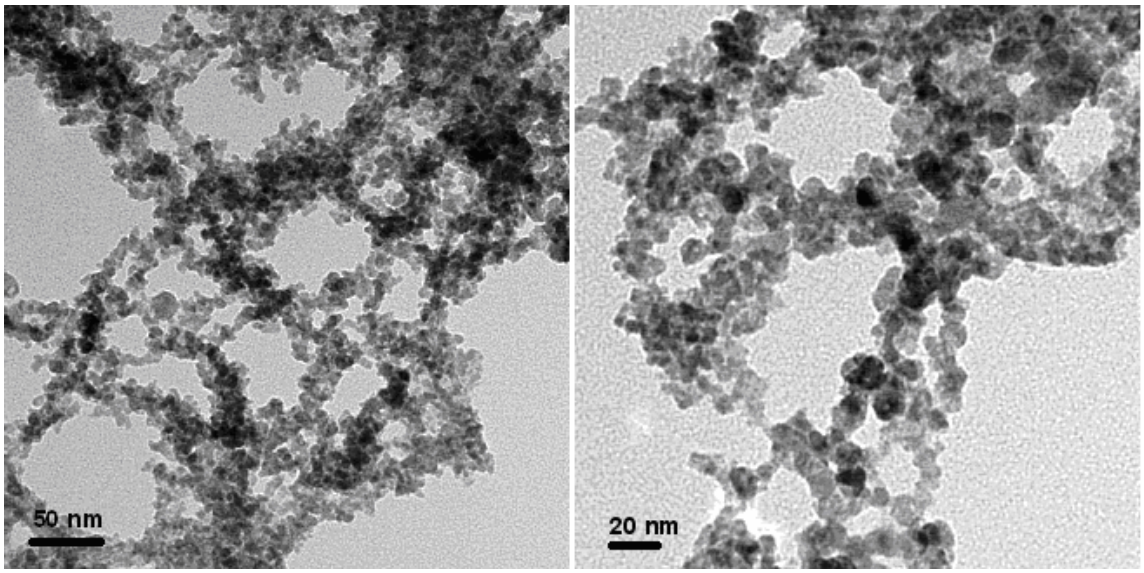

Figure 56: TEM micrographs of Cu nanoparticles as prepared by LVCC.

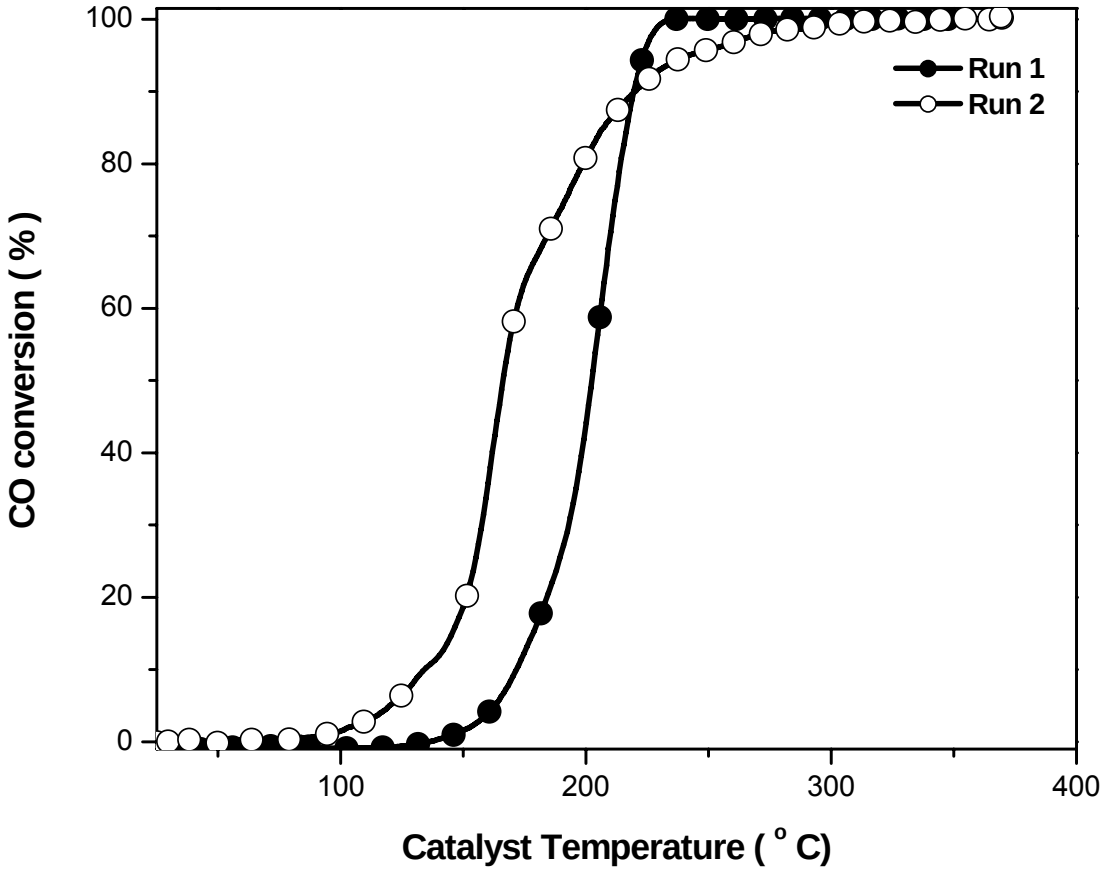

Figure 57: Catalytic activity of Cu nanoparticles as prepared by LVCC (run 1) and after heat treatment in CO/O_2 mixture (run 2).

Table 22 summarizes the catalytic activities of Cu nanoparticles as prepared (run 1) and after heat treatment in CO/O_2 mixture (run 2).

Sample	**3% Conversion Light-off Temp. (^{o} C)**	**50 % Conversion Temp. (^{o} C)**	**Maximum Conversion (%)**	
			Temp. (^{o} C)	**Conversion**
Cu Nano (Run 1)	156.9	202.8	235.6	100.0
Cu Nano (Run 2)	110.7	166.3	351.5	100.0

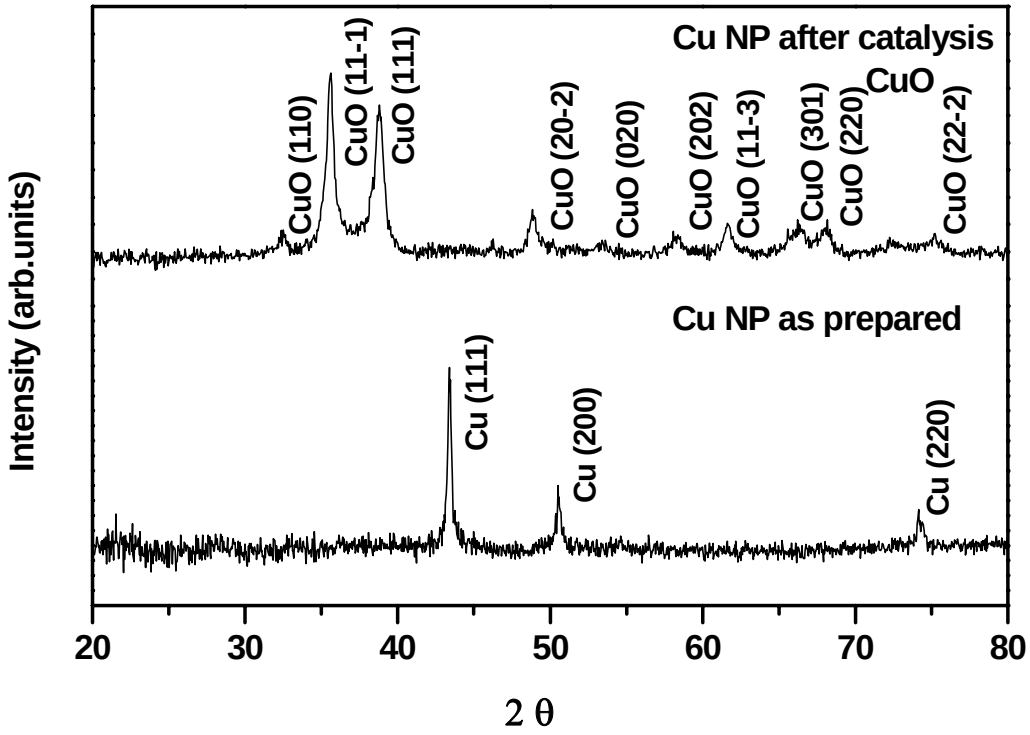

Figure 58: X-ray patterns of Cu nanoparticles before and after catalysis.

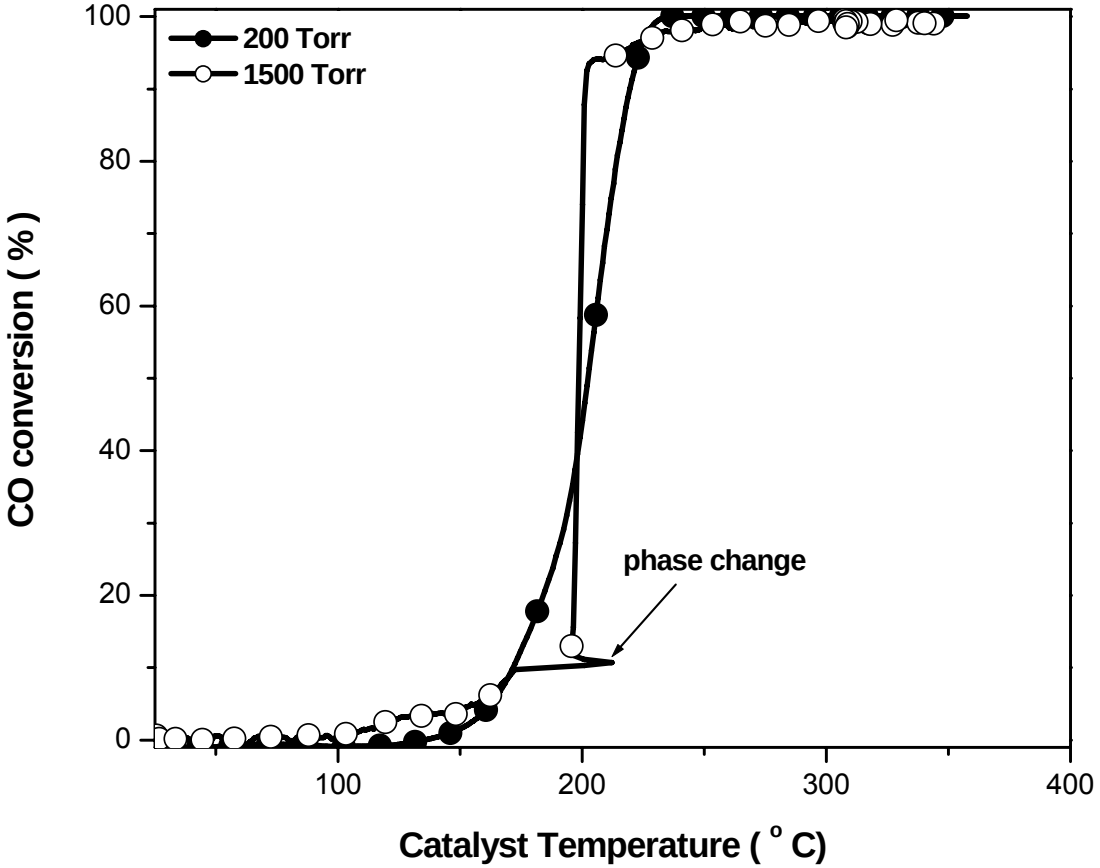

Figure 59: Comparison between the catalytic activities of Cu nanoparticles as prepared by LVCC at 200 and 1500 Torr (run 1).

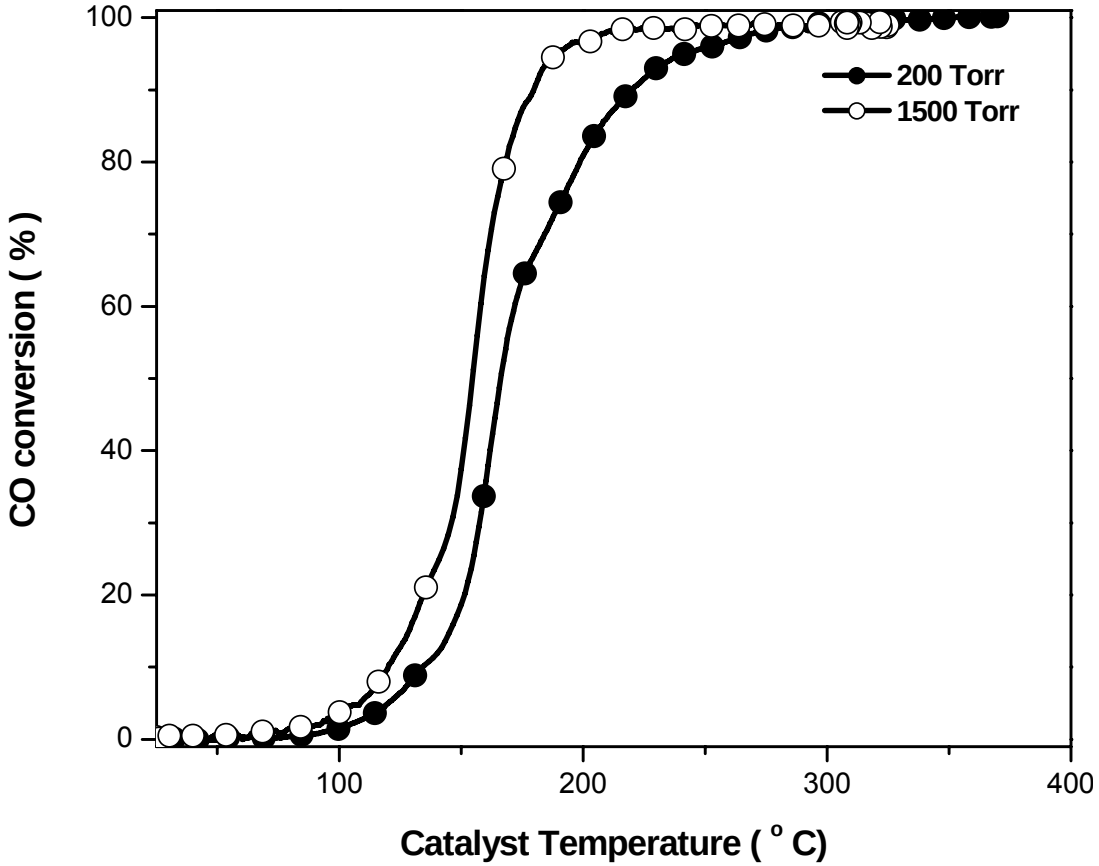

Figure 60: Comparison between the catalytic activities of Cu nanoparticles prepared by LVCC at 200 and 1500 Torr after heat treatment in CO/O_2 mixture (run 2).

Table 23 summarizes the catalytic activities of Cu nanoparticles prepared by LVCC at 200 and 1500 Torr (run 1 and run 2).

Sample Cu	**3% Conversion Light-off Temp. (^{o} C)**	**50 % Conversion Temp. (^{o} C)**	**Maximum Conversion (%)**	
			Temp. (^{o} C)	**Conversion**
200 Torr (Run 1)	156.9	202.8	235.6	100.0
200 Torr (Run 2)	110.7	166.3	351.5	100.0
1500 Torr (Run 1)	124.7	199.3	264.7	99.4
1500 Torr (Run 2)	96.1	153.1	266.0	99.2

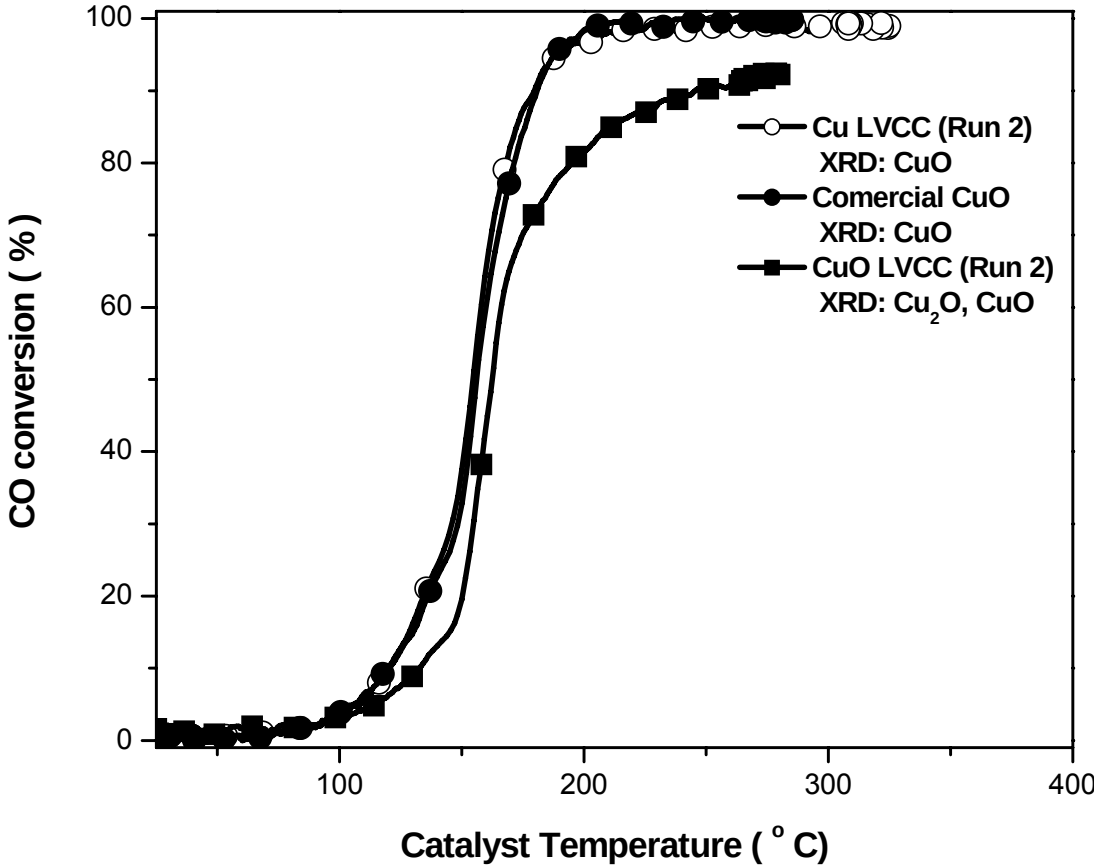

Figure 61: Comparison between the catalytic activities of commercial CuO and Cu and CuO prepared by LVCC in 1500 Torr after heat treatment in CO/O_2 mixture (run 2).

5.2.2 Low temperature CO oxidation on supported Cu nanoparticle catalyst

As reported earlier, the catalytic activity of Au nanoparticles, when dispersed on a reducible metal oxide support, is greatly increased due to the interaction between Au and the support. To examine the effect of the support on the catalytic activity of the Cu nanoparticle catalyst, 5 % Cu loading supported on TiO_2, ZrO_2, and CeO_2 was prepared. Figure 62 compares the catalytic activities of Cu nanoparticles supported on TiO_2, ZrO_2, and CeO_2 as prepared by the LVCC method in 200 Torr Ar (run 1). It clearly indicates that 5% Cu/CeO_2 has the highest activity, followed by 5% Cu/ZrO_2, and finally 5% Cu/TiO_2. However, in run 2 (Figure 63) the catalytic activities of the three catalysts follow the same order. The catalytic activities of 5% Cu/CeO_2 and 5% Cu/ZrO_2 are increased, while in the case of 5% Cu/TiO_2 it decreased. Table 24 summarizes the catalytic activities of 5 % Cu supported on different metal oxide support as prepared by the LVCC method at 200 Torr Ar (run 1) and after heat treatment in the CO/O_2 mixture (run 2). The enhanced catalytic activity of 5% Cu/CeO_2 is attributed to the interaction between Cu and CeO_2. The reducibility and oxygen storage capacity of CeO_2 as observed for 5% Au/CeO_2 system.

Although the catalytic activity of Cu nanoparticles increases as the pressure increases from 200 to 1500 Torr, the catalytic activity of 5% Cu/CeO_2 does not change drastically. However, in run 1 5% Cu/CeO_2 prepared in 1500 Torr shows slightly higher activity (Figure 64), while in run 2, 5% Cu/CeO_2 prepared in 200 Torr has lower light-off temperature, and 5% Cu/CeO_2 prepared in 1500 Torr has a higher CO conversion percentage, as shown in Figure 65. The catalytic activities of 5 % Cu/CeO_2 as prepared by

the LVCC method in 200 and 1500 Torr Ar before (run 1) and after heat treatment in CO/O_2 mixture (run 2) are summarized in Table 25.

Cu supported on a CeO_2 nanoparticle catalyst showed higher activity than Cu supported on other metal oxides. The enhanced catalytic activity of this catalyst is attributed to the strong interaction between Cu and CeO_2, and to the oxygen storage capacity and redox properties of CeO_2 nanoparticles. To characterize 5 % Cu/CeO_2 catalyst, the X-ray diffraction patterns of 5 % Cu/CeO_2 catalyst was measured before and after CO oxidation reaction, as shown in Figure 66. Although the X-ray diffraction patterns before and after catalysis revealed the characteristic diffraction peaks of crystalline CeO_2 (2θ = 28.6, 33.1, 47.5, 56.3, 59.1, and 69.4^o) assigned to the fluorite structure, there is no evidence of Cu (Cu (111) at 2θ = 43) or CuO or Cu_2O diffraction peaks. This is because the Cu nanoparticles in the sample are so small that they can go beyond the detection limit of the instrument sensitivity. TEM micrographs of 5 % Cu/CeO_2 catalyst show web-like aggregates with particle sizes of (2-5 nm) as shown in Figure 67. From the X-ray diffraction patterns and the TEM micrographs, it is clear that Cu nanoparticles are small and well dispersed (X-ray amorphous) with the CeO_2. Since 5 % Cu/CeO_2 only contains a small amount of Cu, it is hard to observe it in the X-ray diffraction patterns, which is in agreement with the results obtained by Liu et al.[143].

The interaction between Cu and CeO_2 has been studied using Hydrogen Temperature Programmed Reduction method (H_2-TPR), as shown in Figure 68. The TPR profile of 5 % Cu/CeO_2 catalyst shows a two-step reduction profile observed for all Cu/CeO_2 and CuO/CeO_2 catalysts, indicating the presence of two types of CuO species.

Luo *et al.* [144] suggested that one of the types is small Cu particles that reduced at low temperatures, and the other type is large CuO particles that reduced at high temperatures. As observed in Au/CeO_2, when compared with bulk CeO_2, there is a slight shift to a lower temperature region (85-190 ^oC) with T_{max} around 165 ^oC due to the presence of Cu which weakened the CeO_2 surface oxygen bonding. The temperature at which $Cu\text{-}CeO_2$ reaction with H_2 starts up (T_{up}) is 85^oC. The high temperature CeO_2 peak is shifted to lower temperature region and starts around 375 ^oC. From the TPR results, it can be concluded that there is a significant $Cu\text{-}CeO_2$ interaction in Cu/CeO_2 or CuO/CeO_2 nanoparticle catalysts prepared by the LVCC method, but not as strong as $Au\text{-}CeO_2$ catalyst.

Figure 69 compares the catalytic activities of 5 % Cu/CeO_2 prepared by the LVCC method 1500 Torr Ar and after heat treatment in CO/O_2 mixture (run 2). The catalytic activity of 5 % Cu/CeO_2 is increased after the heat treatment in CO/O_2 mixture due to the oxidization of Cu nanoparticles to CuO, as observed in the X-ray diffraction pattern, and the reduction of Cu/CeO_2 at lower temperature due to the interaction of Cu with CeO_2, as observed in TPR profiles.

As reported in the previous section, Cu nanoparticles are oxidized after heat treatment in CO/O_2 mixture (run 2). It is important to compare the catalytic activities of 5 % Cu/CeO_2 to 5 % CuO/CeO_2 because the Cu and CuO nanoparticles are so small that they can go beyond the detection limit of the instrument sensitivity, and it is hard to compare their X-diffraction patterns. Figure 70 shows HRTEM micrographs of both 5 % Cu/CeO_2 and 5 % CuO/CeO_2 prepared by the LVCC method in 1500 Torr Ar. The micrographs show that the particle size of 5 % Cu/CeO_2 is smaller than the 5 % CuO/CeO_2

catalyst, and that the 5 % CuO/CeO_2 has large agglomerates compared to the 5 % CuO/CeO_2 catalyst. Although the light-off temperature of 5 % CuO/CeO_2 is less than the light-off temperature of 5 % Cu/CeO_2, the catalytic activity of the 5 % Cu/CeO_2 catalyst is higher, as shown in Figure 71. The catalytic activities of 5 % Cu and 5 % CuO supported on CeO_2 as prepared by the LVCC method in 1500 Torr Ar after heat treatment in CO/O_2 mixture (run 2), are summarized in Table 26.

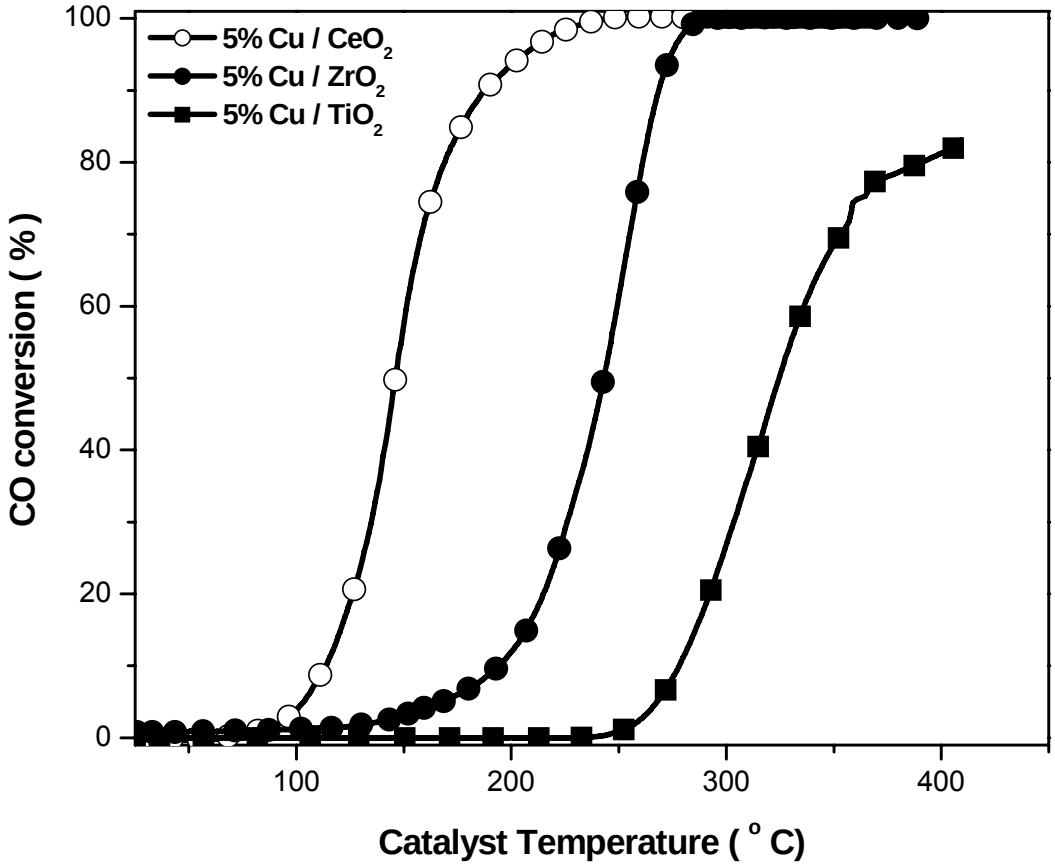

Figure 62: Comparison between the catalytic activities of Cu nanoparticles supported on TiO_2, ZrO_2, and CeO_2 as prepared by the LVCC method in 200 Torr Ar (run 1).

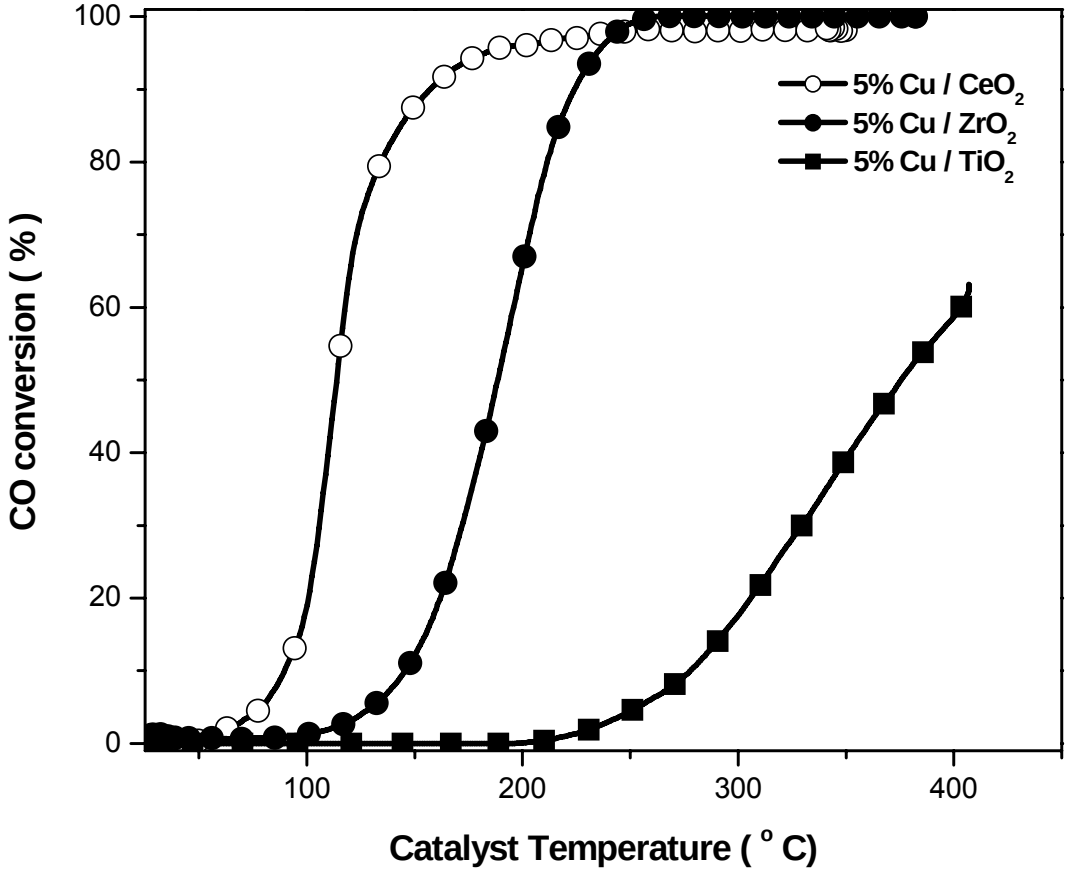

Figure 63: Comparison between the catalytic activities of Cu nanoparticles supported on TiO_2, ZrO_2, and CeO_2 prepared by the LVCC method in 200 Torr Ar (run 2).

Table 24 summarizes the catalytic activities of 5 % Cu supported on different metal oxide support as prepared by the LVCC method at 200 Torr Ar (run 1) and after heat treatment in CO/O_2 mixture (run 2).

Sample	**3% Conversion Light-off Temp. (^{o} C)**	**50 % Conversion Temp. (^{o} C)**	**Maximum Conversion (%)**	
			Temp. (^{o} C)	**Conversion**
Cu / CeO_2 (Run 1)	96.7	145.7	250.2	100.0
Cu / CeO_2 (Run 2)	70.0	113.7	264.4	98.3
Cu / ZrO_2 (Run 1)	148.2	242.6	291.6	87.3
Cu / ZrO_2 (Run 2)	120.0	188.7	262.3	100.0
Cu / TiO_2 (Run 1)	261.9	324.7	409.1	83.1
Cu / TiO_2 (Run 2)	239.7	375.7	406.9	63.2

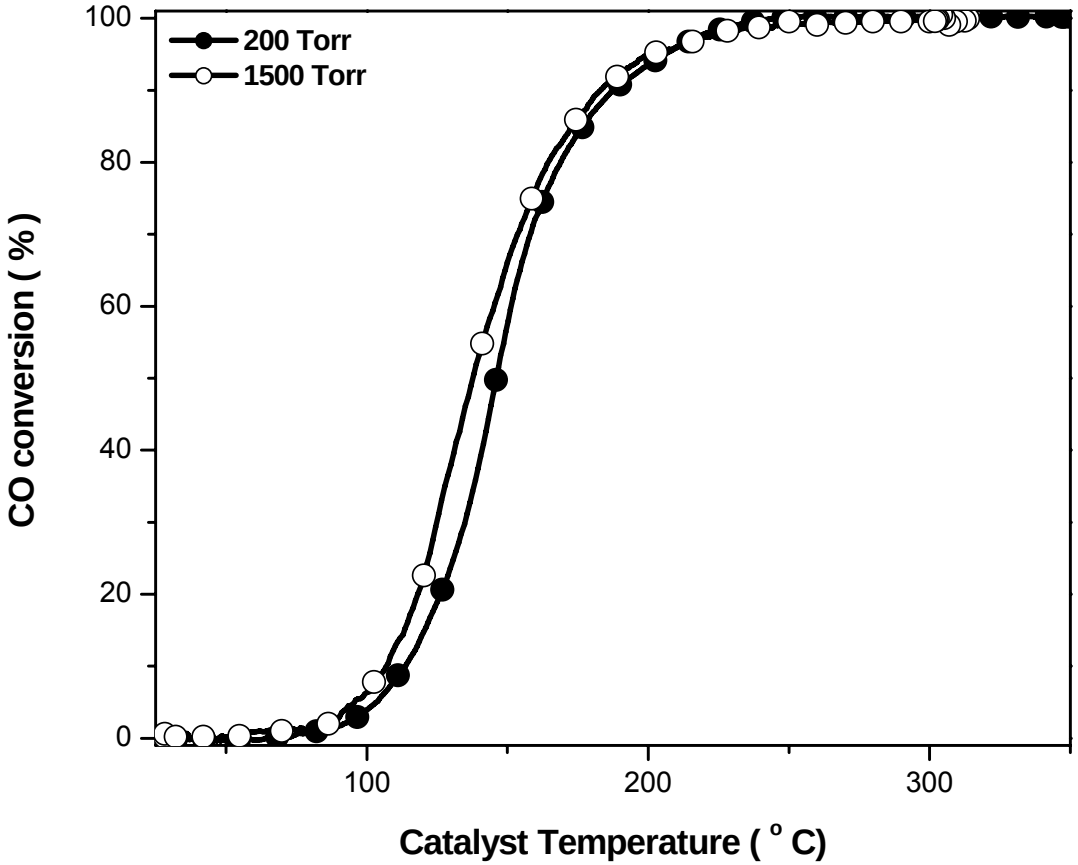

Figure 64: Comparison between the catalytic activities of 5 % Cu/CeO_2 as prepared (run 1) by the LVCC method in 200 and 1500 Torr Ar.

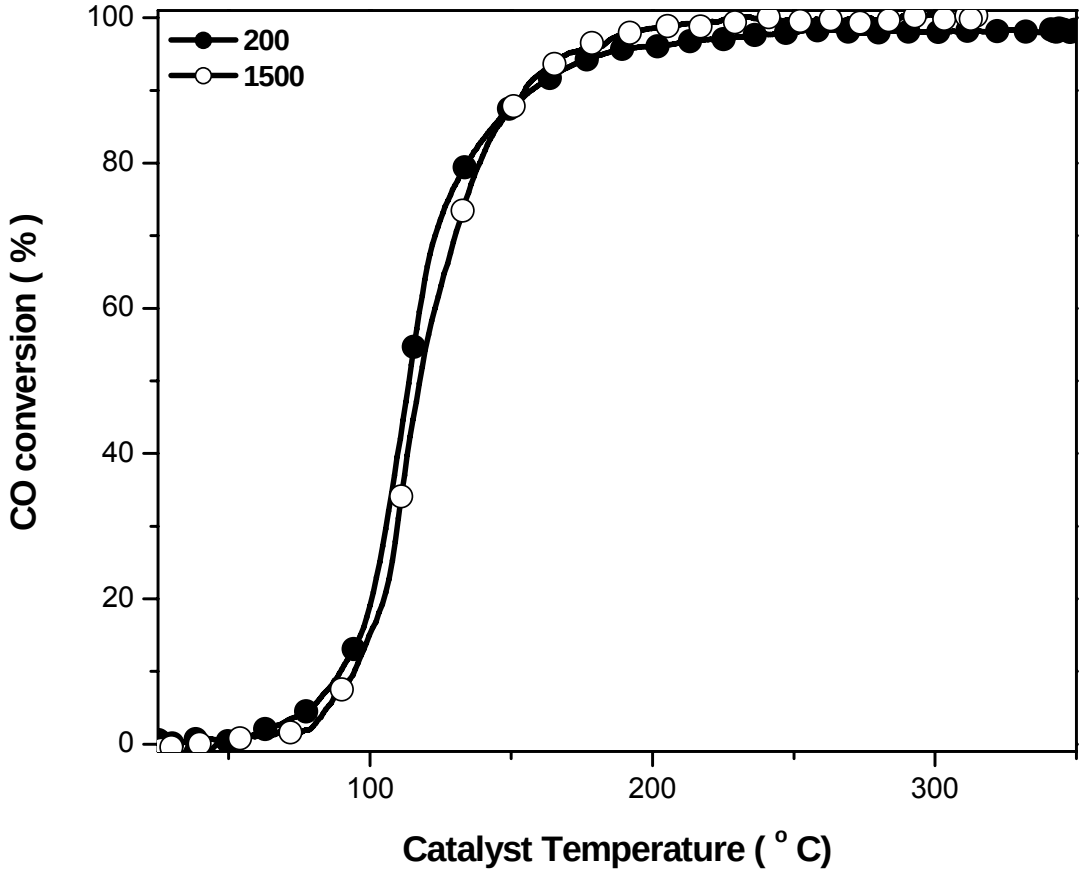

Figure 65: Comparison between the catalytic activities of 5 % Cu/CeO_2 as prepared by the LVCC method in 200 and 1500 Torr Ar after heat treatment in CO/O_2 mixture (run 2).

Table 25 summarizes the catalytic activities of 5 % Cu/CeO_2 as prepared (run 1) by the LVCC method in 200 and 1500 Torr Ar and after heat treatment in CO/O_2 mixture (run 2).

Sample **5 % Cu / CeO_2**	**3% Conversion Light-off Temp. (^{o} C)**	**50 % Conversion Temp. (^{o} C)**	**Maximum Conversion (%)**	
			Temp. (^{o} C)	**Conversion**
200 Torr (Run 1)	96.7	145.7	250.2	100.0
200 Torr (Run 2)	70.0	113.7	264.4	98.3
1500 Torr (Run 1)	88.5	136.4	295.0	99.8
1500 Torr (Run 2)	81.6	117.0	227.8	99.8

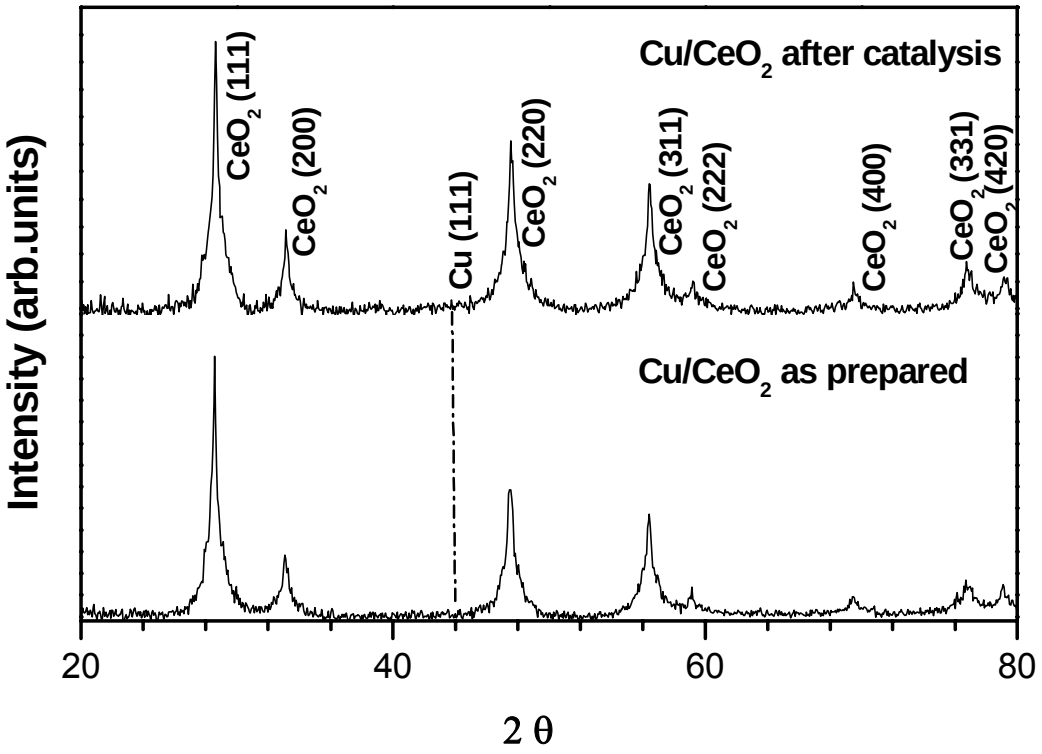

Figure 66: X-ray diffraction patterns of 5 % Cu/CeO_2 before and catalysis.

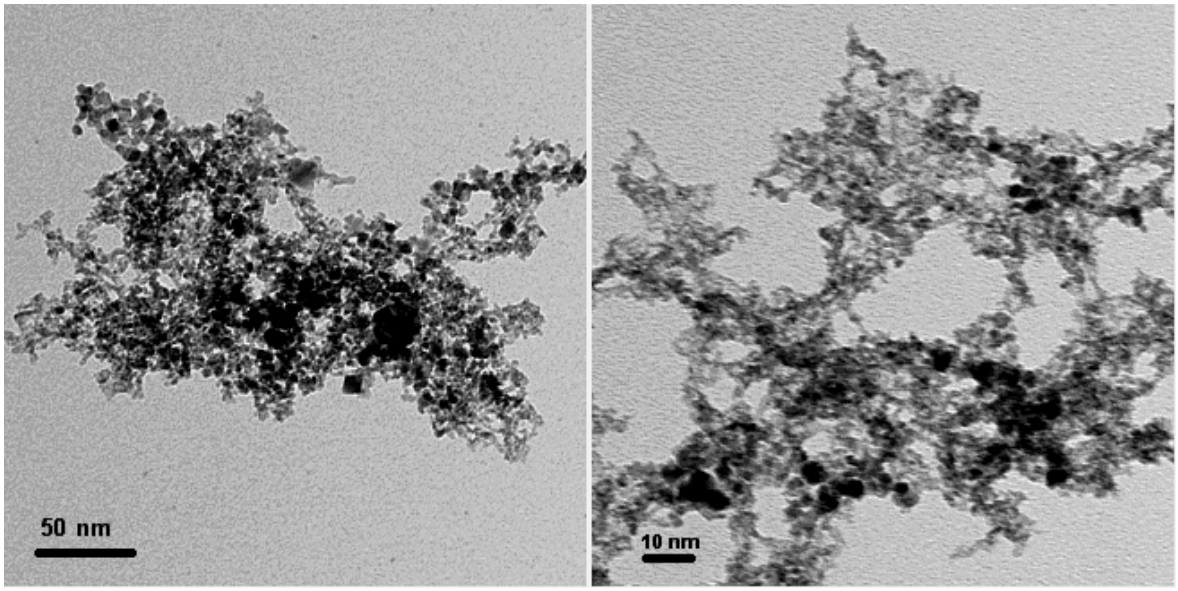

Figure 67: TEM micrographs of 5 % Cu/CeO_2 catalyst as prepared by the LVCC method in 1500 Torr Ar.

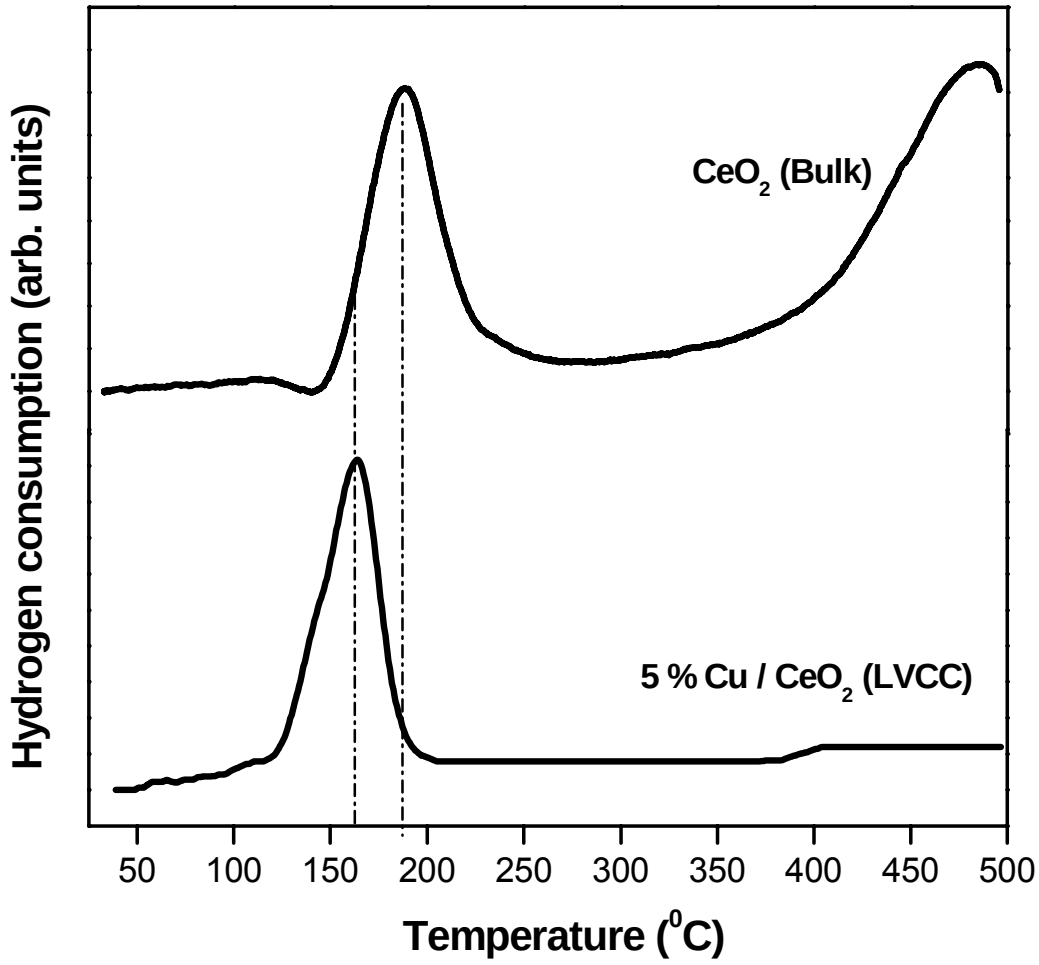

Figure 68: Temperature Programmed Reduction method (H_2-TPR) of 5 % Cu/CeO_2 catalyst prepared by the LVCC method.

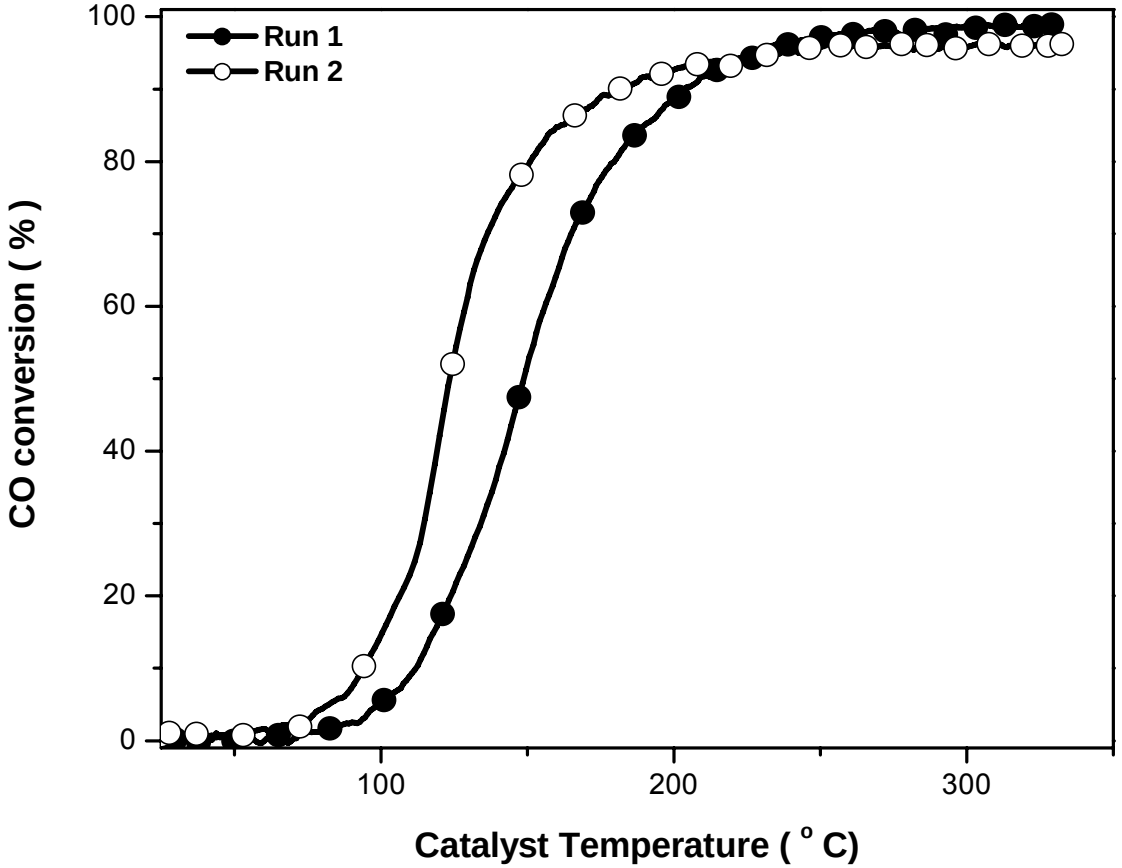

Figure 69: Comparison between the catalytic activities of 5 % Cu/CeO_2 as prepared by the LVCC method in 1500 Torr Ar and after heat treatment in CO/O_2 mixture(run 2).

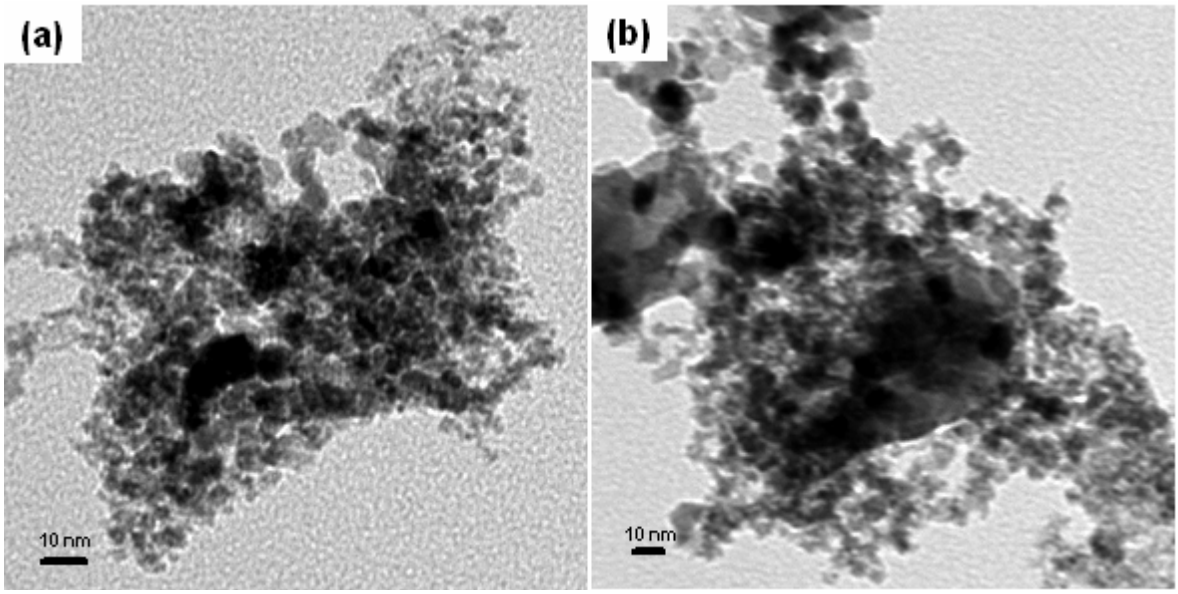

Figure 70: HRTEM of 5% Cu/CeO_2 and 5% CuO/CeO_2 catalysts as prepared by the LVCC method at 1500 Torr Ar.

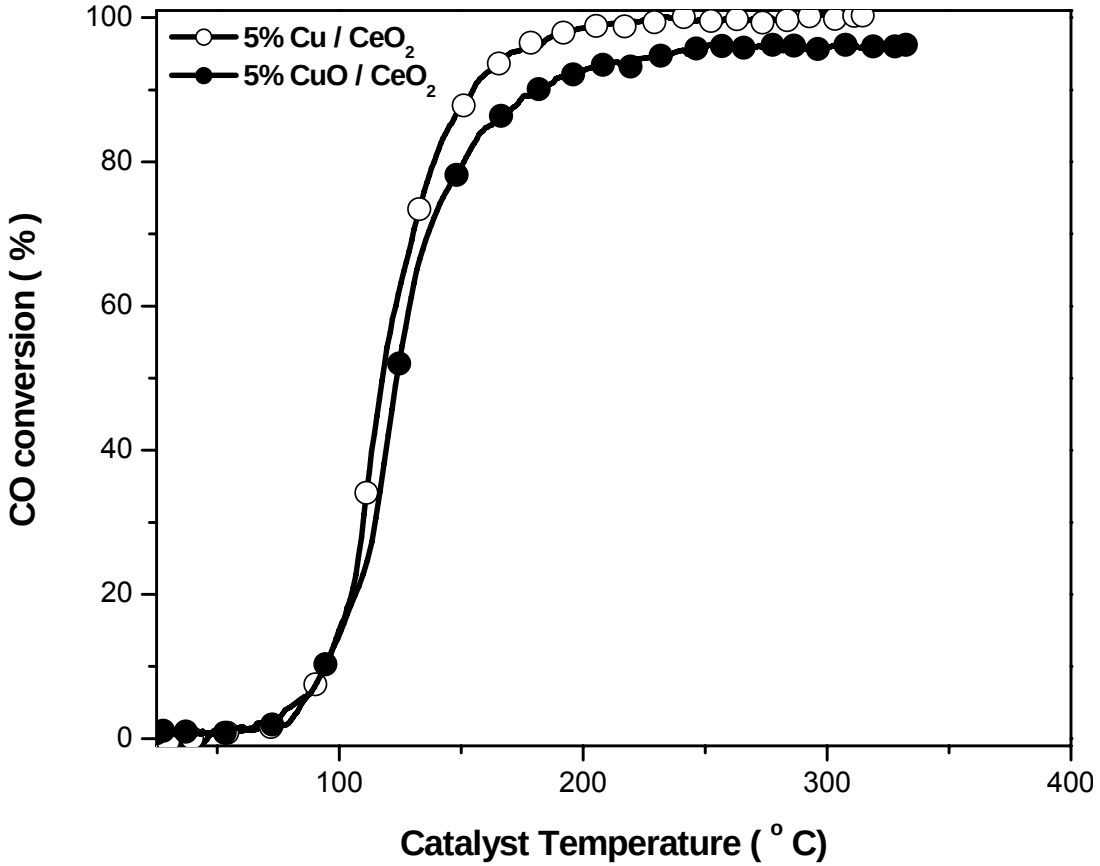

Figure 71: Comparison between the catalytic activities of 5 % Cu/CeO_2 and 5 % CuO/CeO_2 prepared by the LVCC method in 1500 Torr Ar after heat treatment in CO/O_2 mixture (run 2).

Table 26 summarizes the catalytic activities of 5 % Cu/CeO_2 and 5 % CuO/CeO_2 catalysts prepared by the LVCC method in 1500 Torr Ar after heat treatment in CO/O_2 mixture (run 2).

Sample	**3% Conversion Light-off Temp. (^{o} C)**	**50 % Conversion Temp. (^{o} C)**	**Maximum Conversion (%)**	
			Temp. (^{o} C)	**Conversion**
5 % Cu/ CeO_2	81.6	117.0	227.8	99.8
5 % CuO/ CeO_2	75.6	122.7	279.1	96.4

5.2.3 Low temperature CO oxidation on the physical mixtures of Au, Cu nanoparticle catalysts

Both experiment and theory show that the adsorption and activation of O_2 are the key steps in this reaction [145-148]. For active supports, such as TiO_2, the oxygen activation occurred on the support surface and the CO oxidation reaction occurred at the interface between the support and the gold nanoparticles [75,113]. Thus, the need for very small gold nanoparticles may arise mainly from larger contact interface. One way to modify the gold-based catalysts is to mix it with a second metal that can act as promoter for the CO oxidation reaction by adsorbing O_2 and increasing the catalytic activity.

The individual Au, Cu, and CuO nanoparticle catalysts, both unsupported and supported, on CeO_2 show catalytic activities for low temperature CO oxidation as reported in the previous chapters. In this section, the catalytic activities of binary mixture of Au mixed with Cu, and CuO, both unsupported and supported on CeO_2, will be investigated where Cu and CuO act as promoters due to their high affinity toward adsorbing O_2.

5.2.3.1 CO oxidation on physical mixtures of Au, Cu, and CuO nanoparticle catalysts (unsupported)

Since the individual Au and Cu nanoparticle catalysts show high activities towards low temperature CO oxidation, it is important to investigate the catalytic activities of their mixtures and compare it the catalytic activities of individual components. Figure 72 shows the X-ray diffraction patterns of the physical mixture of Au and Cu nanoparticle catalysts (10 % Au, 90 % Cu) as prepared by the LVCC method in 1500 Torr Ar and after heat

treatment in the CO/O_2 mixture. The X-ray diffraction patterns of the fresh sample reveal diffraction peaks which are characteristics of a mixture of Cu and Cu_2O with no evidence of Au diffraction peaks since the amount of Au is small. After the heat treatment however, the diffraction patterns are consistent with the diffraction patterns of CuO with no evidence of Au diffraction peaks. Figure 73 compares the catalytic activities of the physical mixtures of the Au and Cu nanoparticles with Au, Cu, and CuO as prepared by the LVCC method (run 1). It is clear that the catalytic activity of the physical mixture is higher than the activities of the individual components, and similar to the activity of Cu nanoparticles. The same behavior is observed after the heat treatment (run 2), as shown in Figure 74. These results suggest that the activity mainly comes from the Cu nanoparticles since the sample contains 90 % Cu with a small contribution from Au nanoparticles. The catalytic activities of the physical mixture of Au and Cu nanoparticles (10 % Au, 90 % Cu) and the individual components before and after heat treatment in the CO/O_2 mixture (run 1and 2) are summarized in Table 27. The effect of varying percentages of Au and Cu nanoparticles on the catalytic activity of the Au and Cu physical mixture was investigated by increasing the Au percentage and decreasing the Cu percentage. Figure 75 compares the catalytic activities of (10 % Au, 90 % Cu) and (75 % Au, 25 % Cu) physical mixtures after heat treatment (run 2). As indicated in the above figure, the catalytic activity of the physical mixture decreases as the Au percentage increases and shifts towards the catalytic activity of Au nanoparticles, as shown in Table 28. Finally, the catalytic activities of Au and Cu and AuCuO (10% Au, 90 % Cu or CuO) physical mixtures after heat treatment (run 2) was compared, as shown in Figure 76. It is clear that the physical mixture of Au and CuO is

more active than the physical mixture of Au and Cu due to the possible interaction between Au and CuO. The catalytic activities of the physical mixture of Au and CuO are summarized in Table 29.

Based on these results one can conclude that the catalytic activities of the physical mixture is slightly higher than the catalytic activities of the individual components due to weak interaction between Au and Cu or CuO.

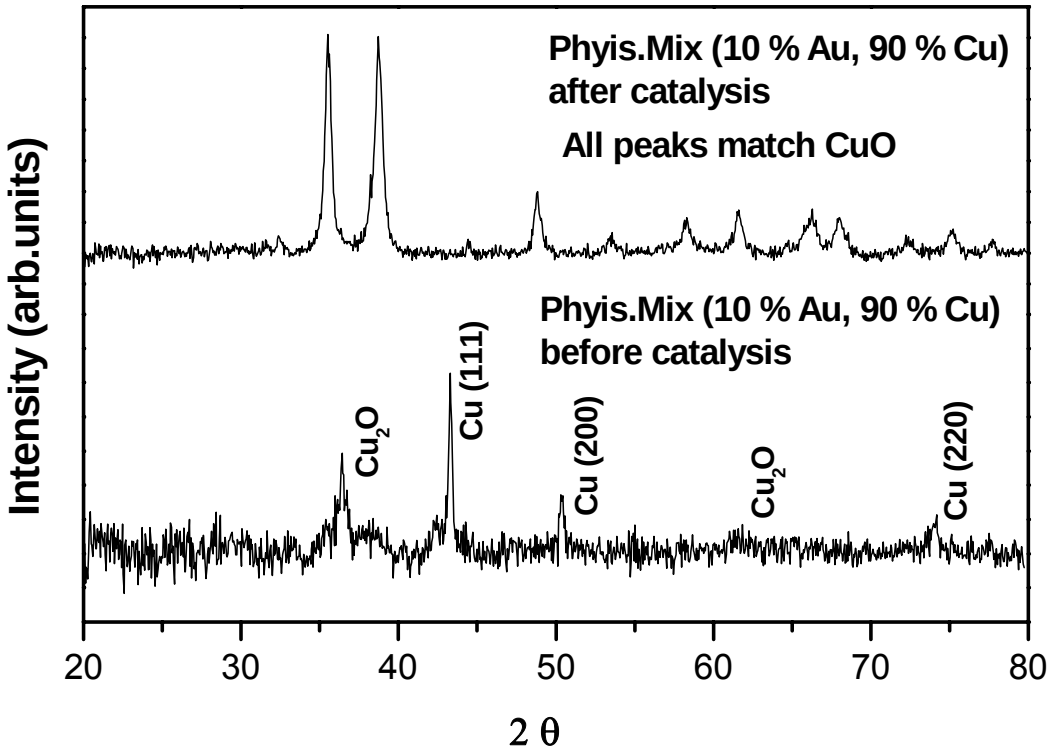

Figure 72: X-ray diffraction patterns of the physical mixture of Au and Cu nanoparticle catalysts (10 % Au, 90 % Cu) as prepared by the LVCC method in 1500 Torr Ar and after catalysis.

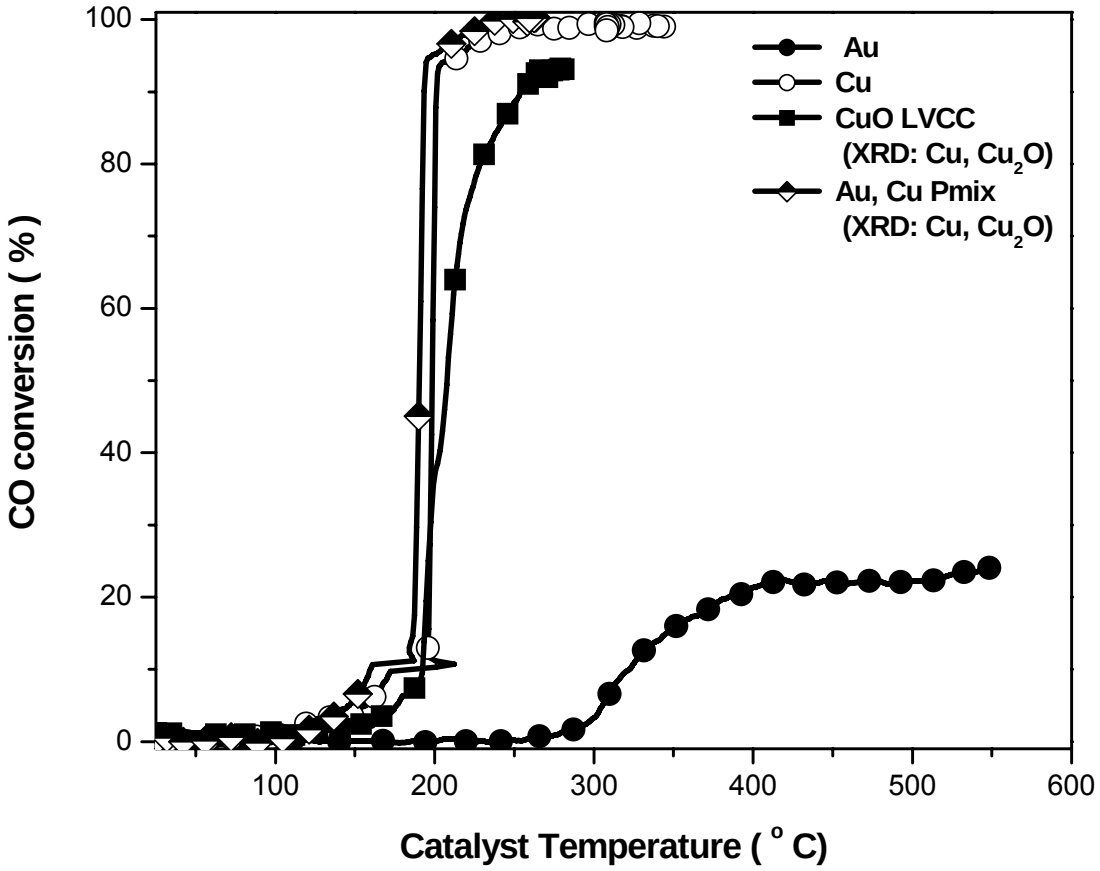

Figure 73: Comparison between the catalytic activities of the physical mixture of Au and Cu nanoparticles (10 % Au, 90 % Cu) and the individual components as prepared by the LVCC method (run 1).

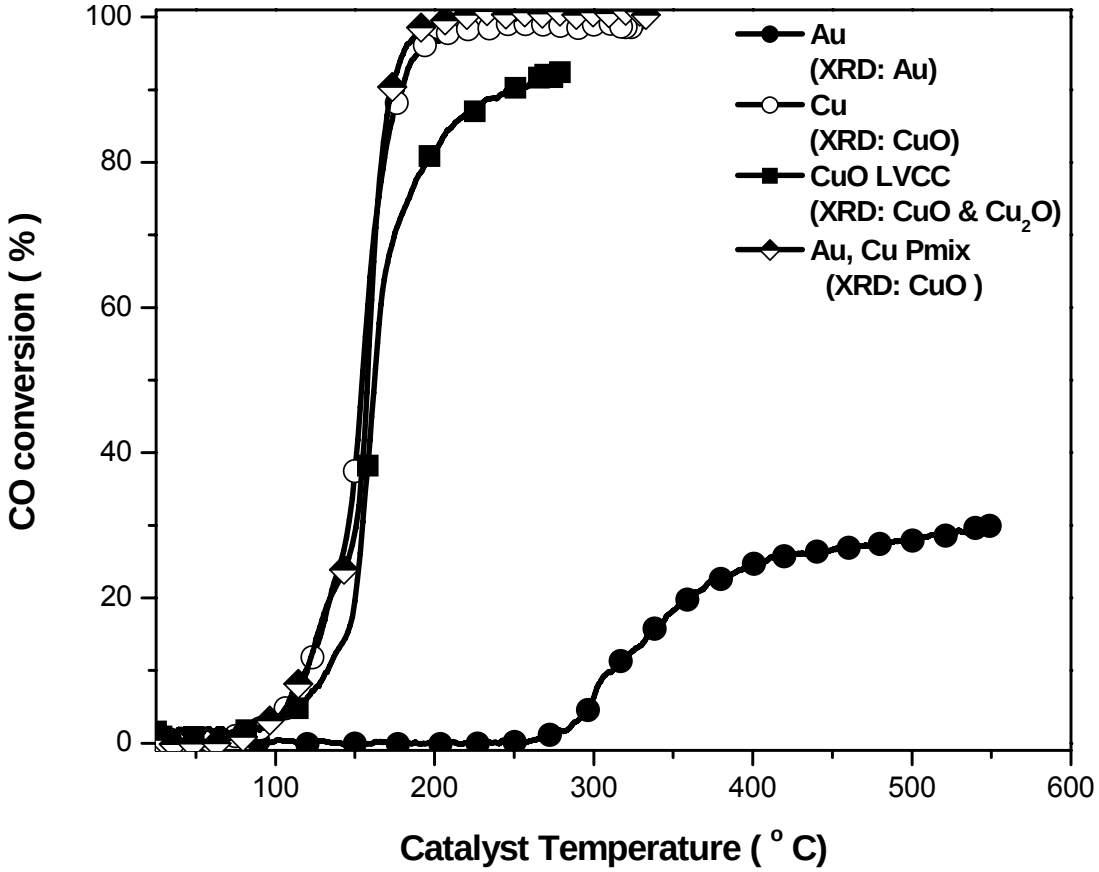

Figure 74: Comparison between the catalytic activities of the physical mixture of Au and Cu nanoparticles (10 % Au, 90 % Cu) and the individual components after heat treatment in CO/O_2 mixture (run 2).

Table 27 summarizes the catalytic activities of the physical mixture of Au and Cu nanoparticles (10 % Au, 90 % Cu) and the individual components before and after heat treatment in CO/O_2 mixture (run 1 and 2).

Sample	**3% Conversion Light-off Temp. (^{o} C)**	**50 % Conversion Temp. (^{o} C)**	**Maximum Conversion (%)**	
			Temp. (^{o} C)	**Conversion**
Au (Run 1)	298.4	-	547.2	25.7
Au (Run 2)	289.4	-	548.9	29.9
Cu (Run 1)	124.7	199.3	264.7	99.4
Cu (Run 2)	96.1	153.1	266.0	99.2
CuO (Run 1)	164.1	207.2	281.1	93.1
CuO (Run 2)	103.4	161.5	277.9	92.5
AuCu Pmix (run 1)	133.0	190.0	257.0	100
AuCu Pmix (run 2)	96.0	158.0	319.0	100

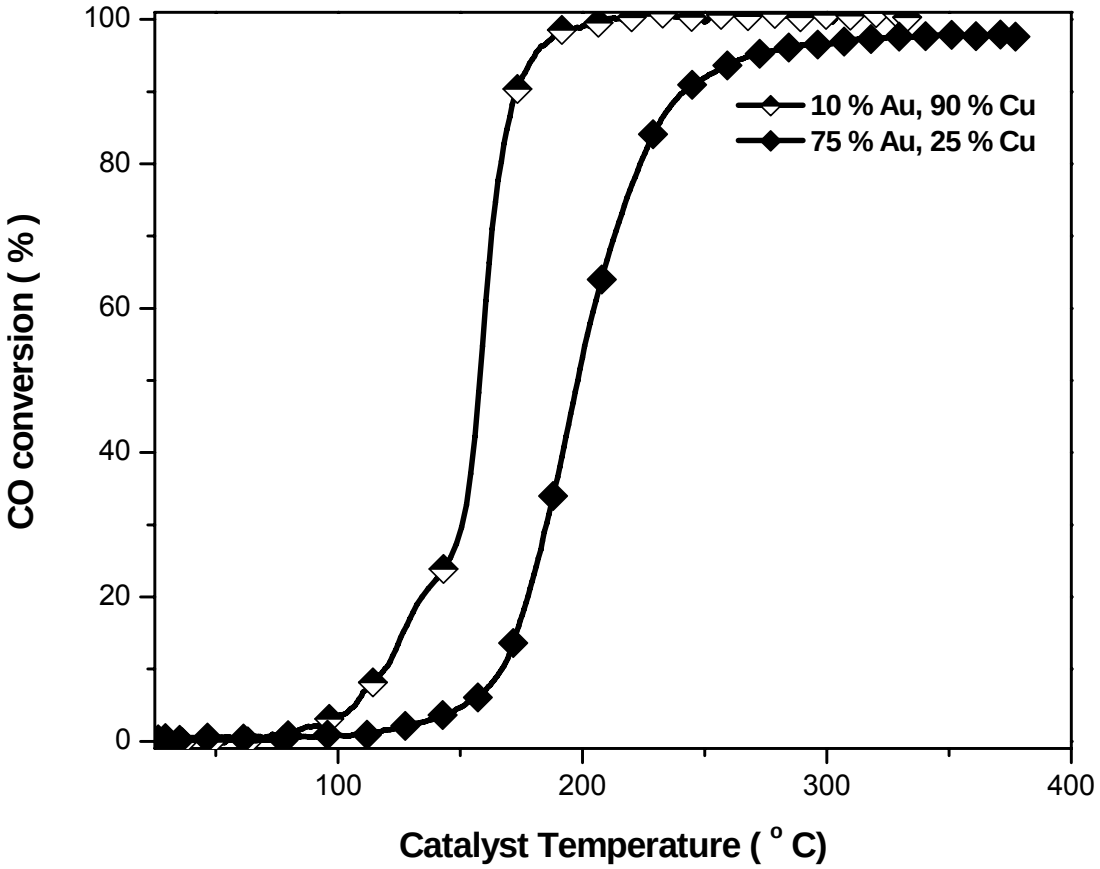

Figure 75: Comparison between the catalytic activities of (10 % Au, 90 % Cu) and (75 % Au, 25 % Cu) physical mixtures after heat treatment (run 2).

Table 28 summarizes the catalytic activities of (10 % Au, 90 % Cu) and (75 % Au, 25 % Cu) physical mixtures after heat treatment (run 2).

Sample	**3% Conversion Light-off Temp. (^{o} C)**	**50 % Conversion Temp. (^{o} C)**	**Maximum Conversion (%)**	
			Temp. (^{o} C)	**Conversion**
10 % Au, 90 % Cu	96.0	158.0	319.0	100
75 % Au, 25 % Cu	138.3	198.0	330.2	97.6

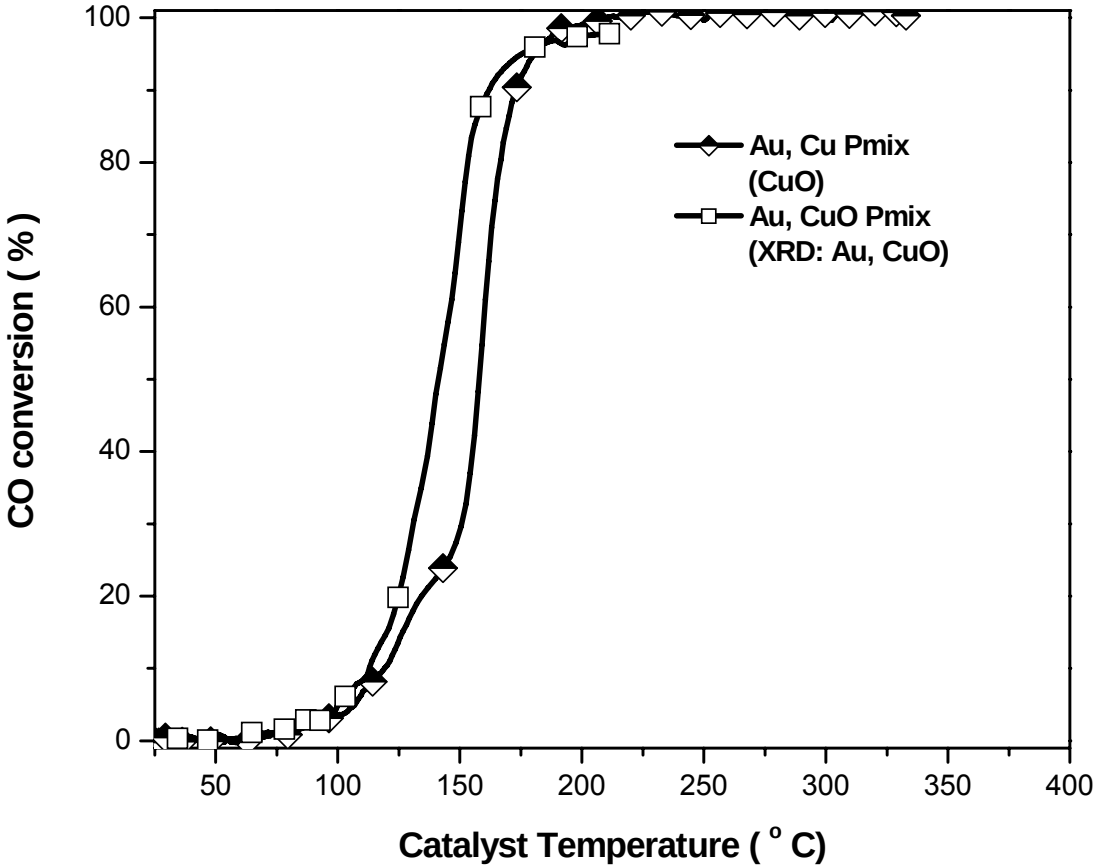

Figure 76: Comparison between catalytic activities of AuCu and AuCuO (10% Au, 90 % Cu or CuO) physical mixtures after heat treatment (run 2).

Table 29 summarizes the catalytic activities of the physical mixtures of Au, Cu (10 % Au, 90 % Cu) and Au, CuO (10 % Au, 90 % CuO).

Sample	**3% Conversion Light-off Temp. (^{o} C)**	**50 % Conversion Temp. (^{o} C)**	**Maximum Conversion (%)**	
			Temp. (^{o} C)	**Conversion**
10 % Au, 90 % Cu	96.0	158.0	319.0	100
10 % Au, 90 % CuO	89.2	140.5	211.4	97.8

5.2.3.2 CO oxidation on of Au, Cu, and CuO nanoparticles and their physical mixtures supported on CeO_2

As reported in the previous sections, the catalytic activities of the unsupported physical mixtures of Au with Cu and CuO are slightly higher than the activities of the individual components, and the Au, Cu, and CuO supported on CeO_2 show high activities for CO oxidation. In this section, the catalytic activities of the physical mixtures of Au with Cu and CuO supported on CeO_2 will be investigated. Figure 77 shows the X-ray diffraction patterns of Au, Cu, and their physical mixtures as prepared by the LVCC method in 1500 Torr Ar. The X-ray diffraction patterns reveal diffraction peaks consistent with the diffraction patterns of crystalline CeO_2 and low intensity diffraction peaks consistent with crystalline Au. The diffraction peaks of Cu are not observed in the diffraction patterns due to its small size, high dispersion, and the small amount of Cu nanoparticles in all the samples, which is below the detection limits of the instrument sensitivity. However, the CeO_2 diffraction peaks are broader in the samples where Cu loading is higher than Au. These results are attributed to the small size of Cu and CeO_2.

As Au loading in the samples increases, the intensities of Au diffraction peaks increases. The intensities of Au diffraction peaks in the 5 % (75 % Au, 25 % Cu)/CeO_2 is higher than the intensities of 5 % pure Au supported on CeO_2. Figure 78 shows TEM micrographs of 5 % Au/CeO_2, 5 % Cu/CeO_2, and 5 % (10 % Au, 90 % Cu)/CeO_2 catalysts as prepared by the LVCC method. Both 5 % Cu/CeO_2 and 5 % Cu/CeO_2 have two types of morphologies. 5 % Cu/CeO_2 has morphology of small elongated particles which form aggregates (web

like morphologies) and a small Cu nanoparticle supported on a large spherical particles (30-100 nm. However, the particle size of 5 % Cu/CeO_2 catalyst is smaller than 5 % Au/CeO_2, and the number of the spherical particles is less in the 5 % Cu/CeO_2. In the physical mixture, the morphology is divided into two regions where one region has morphology similar to the morphology observed in 5 % Au/CeO_2 catalyst and another region is similar to the morphology observed for the 5 % Cu/CeO_2 catalyst. Also, Au is not well-dispersed in the physical mixture of Au, Cu supported on CeO_2. These results agreed well with the X-ray diffraction patterns observed for these systems, which show that the intensities of Au diffraction peaks are higher than pure Au supported on CeO_2.

Figure 79 compares the catalytic activities of 5 % Au/CeO_2, 5 % Cu/CeO_2, and their physical mixtures as prepared by the LVCC method (run 1).Table 30 summarizes the activities of 5 % Au/CeO_2 and 5 % Cu/CeO_2, and their physical mixtures. It is obvious that the 5 % Au/CeO_2 has the highest catalytic activity followed by 5 % Cu/CeO_2, 5 % (10 % Au, 90 % Cu)/CeO_2, and finally 5 % (75 % Au, 25 % Cu)/CeO_2 catalysts are less than the catalytic activities of 5 % Au/CeO_2, 5 % Cu/CeO_2. However, in run 2 the catalytic activities of the physical mixtures are the average of the catalytic activities of 5 % Au/CeO_2 and 5 % Cu/CeO_2, as shown in Figure 80 and summarized in Table 31. Figure 81 show that 5 % (75 % Au, 25 % Cu)/CeO_2 catalyst has higher activity than the 5 % (75 % Au, 25 % CuO)/CeO_2.Table 32 compares the catalytic activities of 5 % (75 % Au, 25 % Cu)/CeO_2 and 5 % (75 % Au, 25 % CuO)/CeO_2 catalysts after heat treatment (run 2). These results can be explained based on the interaction of Au and Cu with the CeO_2 support. Au has a stronger interaction with CeO_2 than Cu, as reported in the previous

chapters, and this interaction increases after the heat treatment. As a result, when the Au loading increases, the activity increases. The activity of 5% Cu/CeO_2 is higher than that of 5% Cu/CeO_2. These results can be explained based on the X-ray diffraction of Cu and CuO before and after catalysis, where if the X-ray diffraction peaks of Cu as prepared by the LVCC method shows pure Cu peaks, and after the reaction, the X-ray diffraction peaks show CuO, and in the case of CuO it shows diffraction peaks of Cu_2O and CuO before and after catalysis. Since Cu_2O is less active than CuO the overall activity is less. The same results apply when Cu and CuO is supported on CeO_2.

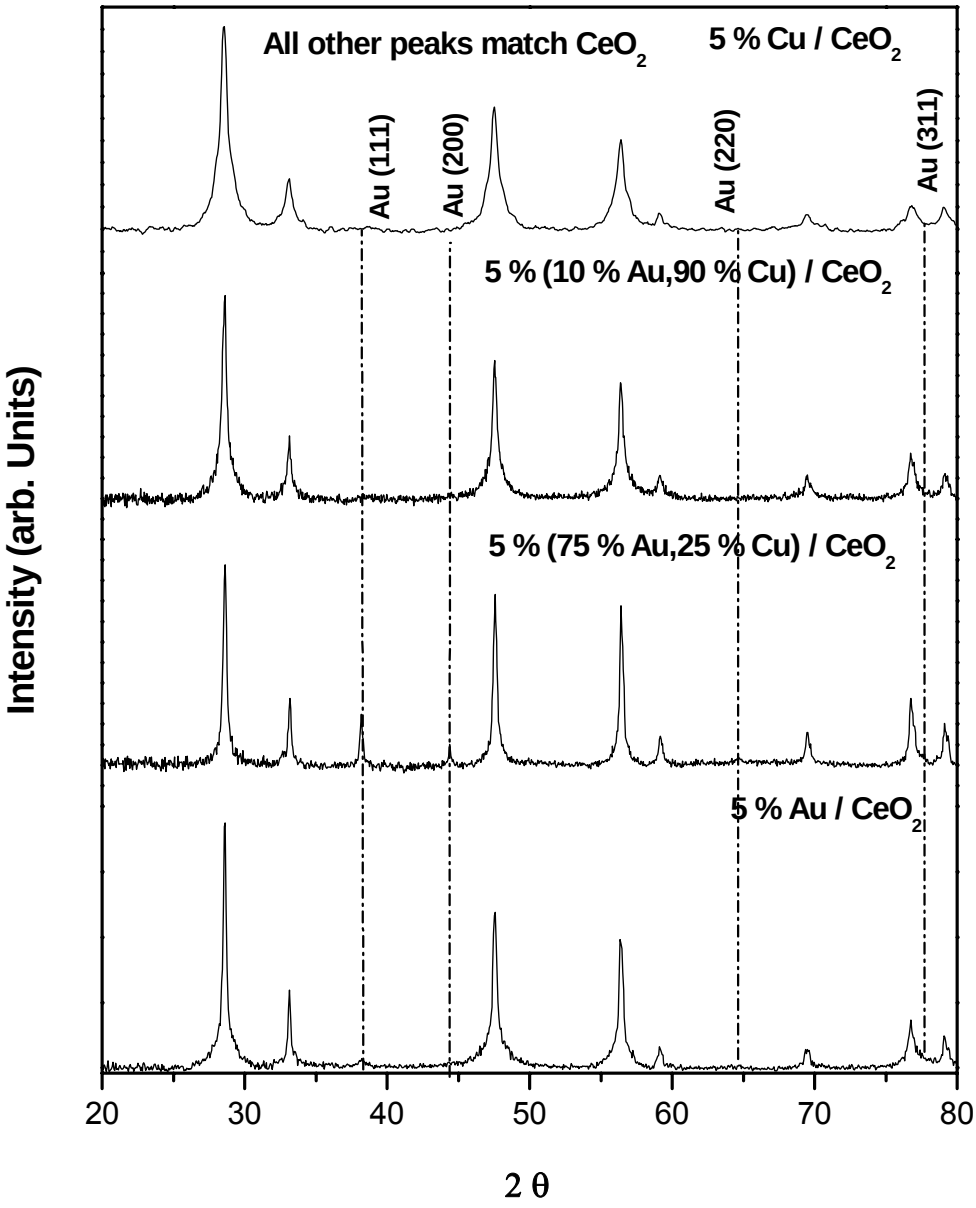

Figure 77: X-ray diffraction patterns of 5 % (Au, Cu, and AuCu physical mixtures) supported on CeO_2 and the individual components as prepared by the LVCC method.

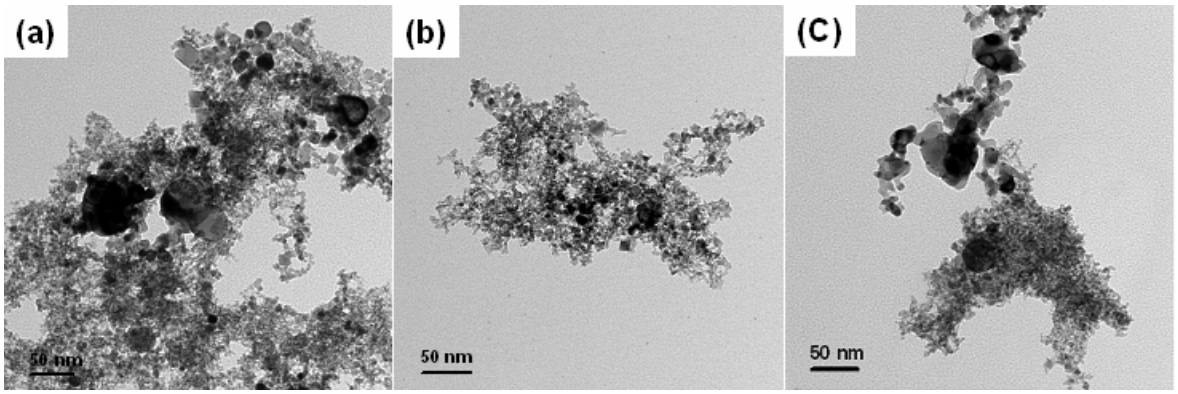

Figure 78: TEM of a). 5 % Au/CeO_2., b). 5 % Cu/CeO_2, and C). 5 % (75 % Au, 25 %)/CeO_2 catalysts as prepared by the LVCC method.

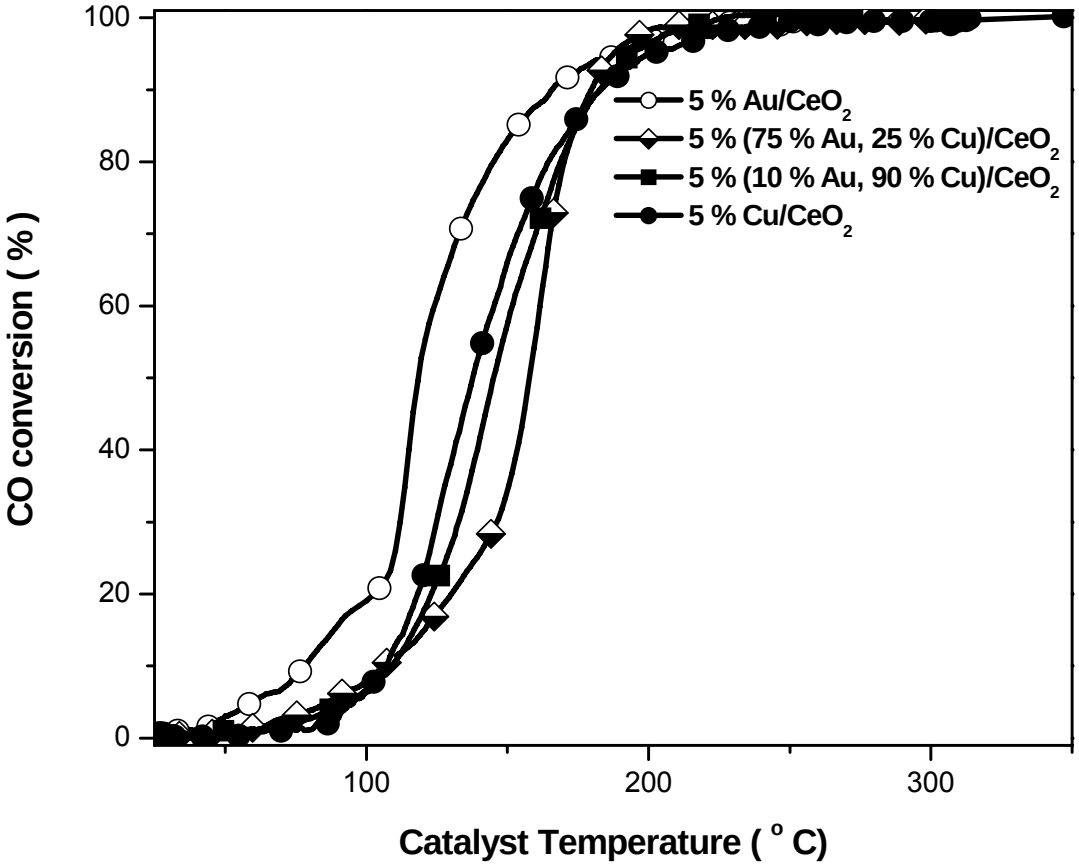

Figure 79: Catalytic activities 5 % Au/CeO_2, 5 % Cu/CeO_2, and their physical mixtures as prepared by the LVCC method (run 1)

Table 30 summarizes the activities of 5 % Au/CeO_2 and 5 % Cu/CeO_2, and their physical mixtures as prepared by the LVCC method (run 1).

Sample 5 % (%Au, %Cu) / CeO_2	**3% Conversion Light-off Temp. (^{o} C)**	**50 % Conversion Temp. (^{o} C)**	**Maximum Conversion (%)**	
			Temp. (^{o} C)	**Conversion**
5 % Au	50.2	118.2	233.2	99.5
75 % Au, 25%Cu	74.5	158.3	224.3	100.0
10 % Au, 90%Cu	82.4	144.8	226.4	100.0
5 % Cu	88.5	136.4	295.0	99.8

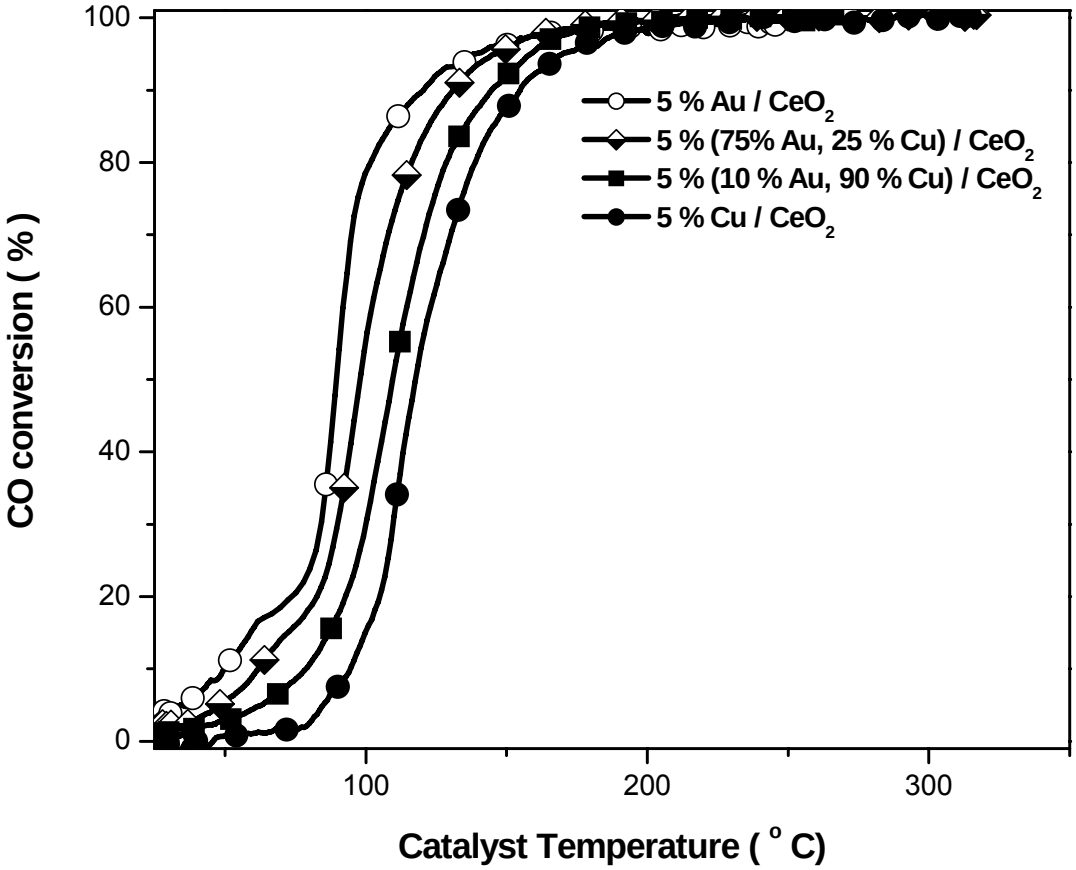

Figure 80: Catalytic activities of 5 % Au/CeO_2, 5 % Cu/CeO_2, and their physical mixtures as prepared by the LVCC method (run 2).

Table 31 summarizes the activities of 5 % Au/CeO_2 and 5 % Cu/CeO_2, and their physical mixtures after heat treatment (run 2).

Sample 5 % (Au, Cu) / CeO_2	**3% Conversion Light-off Temp. (^{o} C)**	**50 % Conversion Temp. (^{o} C)**	**Maximum Conversion (%)**	
			Temp. (^{o} C)	**Conversion**
5 % Au	27.5	89.95	210.9	99.4
75 % Au, 25%Cu	41.1	97.8	192.7	99.6
10 % Au, 90%Cu	51.2	108.6	217.0	100.0
5 % Cu	81.6	117.0	227.8	99.8

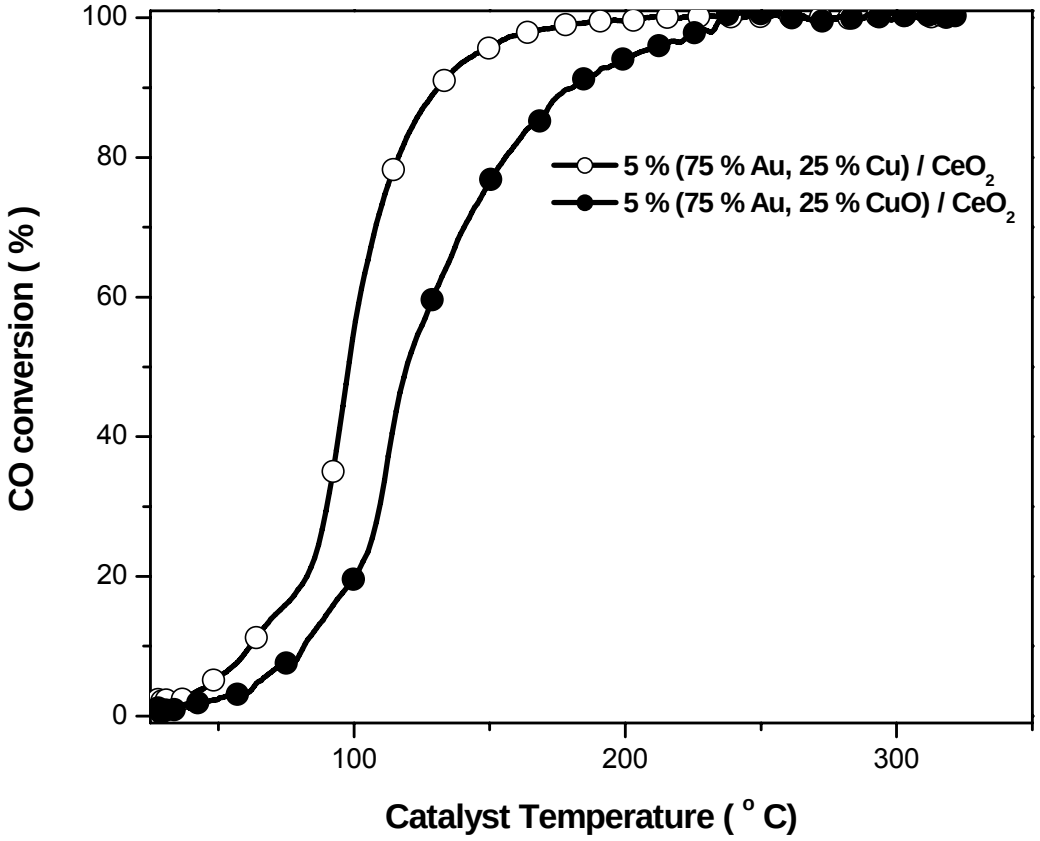

Figure 81: Comparison between the catalytic activities of 5 % (75 % Au, 25 % Cu)/CeO_2 catalyst and 5 % (75 % Au, 25 % CuO)/CeO_2 after heat treatment (run 2).

Table 32 summarizes the catalytic activities of 5 % (75 % Au, 25 % Cu)/CeO_2 catalyst and 5 % (75 % Au, 25 % CuO)/CeO_2 after heat treatment (run 2).

Sample 5 % (Au, Cu) / CeO_2	**3% Conversion Light-off Temp. (^{o} C)**	**50 % Conversion Temp. (^{o} C)**	**Maximum Conversion (%)**	
			Temp. (^{o} C)	**Conversion**
75 % Au, 25%Cu	41.1	97.8	192.7	99.6
75 % Au, 25%CuO	60.5	119.7	235.3	99.0

5.2.4 Low temperature CO oxidation on AuCu Alloy nanoparticle catalyst

Alternative way to modify the gold-based catalysts is to search for a second metal that can form an alloy with gold and that possesses stronger affinity with O_2 than gold. That is, where two different metal atoms are in intimate proximity to each other, as in an alloy, the activated O_2 can easily react with the activated CO in a neighboring gold atom to give the product CO_2.

In this section, will be investigated the alloying effect of Au and Cu on the catalytic activity. Furthermore, will be investigated the catalytic activity of the resultant alloy when it is supported on CeO_2.

5.2.4.1 Low temperature CO oxidation on AuCu Alloy nanoparticle catalyst (unsupported)

Different percentages of Au and Cu were tried to form an alloy and it was discovered that (10 % Au-90 % Cu) is the optimum percentage to form alloys with less Au loading. Figure 82 shows X-ray diffraction patterns of Au, Cu, and (10 % Au-90 % Cu) as prepared by the LVCC method in 1500 Torr Ar. The X-ray diffraction patterns of (10 % Au-90 % Cu) reveal diffraction peaks at 2θ = 36.82, 42.5 (located between the Au (111) and Cu (111)), 49.42 (located between the Au (200) and Cu (200)), 62.38, and 72.5(located between the Au (220) and Cu (200)). These diffraction peaks are broad peaks, which demonstrates the presence of a solid solution of Au and Cu, and is consistent with AuCu diffraction peaks.

The morphology of the AuCu alloy consists of (10-15 nm) are connected by wires to form a web-like structure which is typical in the LVCC method, as shown in Figure 83.

However, the particle size is larger than the particle size of Au and Cu which could be related to the preparation conditions of the alloy nanoparticles.

The H_2 TPR profiles of the AuCu alloy prepared by the LVCC method starts at temperatures below 100^{o}C. However, there are two reduction peaks, one at 183^{o}C and another at 235^{o}C. These peaks could be attributed to the adsorption of O_2 on the alloy, after it is exposed to air to form a Au-O-Cu complex. Upon heating in a H_2/He mixture, this complex is reduced at 183^{o}C to Au^0 and Cu_2O by breaking the Au-O bond in the Au-O-Cu complex followed by the reduction of Cu-O (i.e. CuO) at 235^{o}C to Cu^0. The proposed reduction mechanism of the AuCu alloy can be explained as follow:

$$Au-O-Cu+\delta H_2 \xrightarrow{183^oC} Cu_2O + Au^0 + \delta H_2O \xrightarrow{235^0C+\delta H_2} Cu^0 + Au^0 + \delta H_2O \qquad (5.1)$$

Figure 85 compares the catalytic activities of the AuCu alloy, Au, Cu, and CuO nanoparticles as prepared by the LVCC method (run 1). Although the particle size of the AuCu alloy is larger than the particle size of Au and Cu, AuCu alloy nanoparticles show higher catalytic activity than the catalytic activities of Au, Cu, and CuO nanoparticles. The same behavior is observed in run 2, as shown in Figure 86. The catalytic activities of the AuCu alloy, Au, Cu, and CuO nanoparticles (run 1and run 2) are summarized in Table 33.

To ensure that the AuCu alloy is reproducible, the catalytic activities of two different samples, prepared by the LVCC under the same conditions, were investigated as

shown in Figure 87. The catalytic activities of the two samples are similar before (run 1) and after heat treatment (run 2). The small variation in the activities is due to the variation in the experimental conditions. These results suggest that there is a good reproducibility of AuCu alloy nanoparticle catalysts.

In order to investigate the affect of heat treatment and aging on the catalytic activity of the same AuCu alloy after multiple runs, the X-ray diffraction patterns of AuCu target, as prepared by the LVCC method, after run 1, and after run 5 was measured as shown in Figure 88. The X-ray diffraction patterns of the alloy target show diffraction peaks of the physical mixture of Au and Cu. After the laser evaporation of the AuCu target in Ar atmosphere, the diffraction peaks of the resultant particles are consistent with the formation of the AuCu alloy. Upon the heat treatment of the AuCu alloy in CO/O_2 mixture, the AuCu alloy is oxidized where Cu is converted to CuO and Au remains intact. However, after run 5 the Cu_2O diffraction peaks are observed in the diffraction patterns. Figure 89 compares the catalytic activities of AuCu alloy after multiple runs and after one day of aging. It is clear that the catalytic activity is increased after run 1 and run 3, and decreased after one day of aging. These results are consistent with the X-ray diffraction patterns that show the formation of CuO and Au after run 1, Au, Cu, and Cu_2O after run 5, and the overall activity is decreased due the presence of Cu_2O, which is less active than Au with CuO. Table 34 summarizes the catalytic activities of the same AuCu alloy after multiple runs and one day of aging.

To investigate the effect of aging on the catalytic activity of AuCu alloy further, we measure the catalytic activities of a fresh sample as prepared by LVCC, and after 1 day of

aging before and after the heat treatment was measured as shown in Figure 90. The catalytic activity of the as prepared sample has higher activity than the aged sample. In run 1, the significant decrease in the catalytic activity can be attributed to the absorption of O_2 to form a Au-O-Cu complex as indicated in the TPR results and moisture. In run 2, the change in the catalytic activities is smaller. This is due to the removal of the moisture and the oxidation of Cu to CuO.

The catalytic activities of AuCu alloy nanoparticles with AuCu and AuCuO physical mixtures, as prepared by the LVCC method (run 1) were compared as shown in Figure 91, and after the heat treatment (Figure 92). The light-off temperatures of the AuCu alloy is higher than the AuCu and AuCuO physical mixtures before and after the heat treatment while the AuCuO physical mixture reached the 50% conversion at a lower temperature than the AuCu alloy and the AuCu physical mixture nanoparticles in run 1 and in run 2 however, the AuCu alloy and the AuCuO physical mixture nanoparticles reached 50 % conversion at the same temperature as the AuCu physical mixture nanoparticles. The AuCu physical mixture nanoparticles have a higher conversion percentage at lower temperatures than AuCu alloy and AuCuO physical mixture nanoparticles. These results can be explained based on the X-ray diffraction patterns of all three samples before and after catalysis. In the case of the AuCu alloy, the diffraction peaks show patterns consistent with AuCu alloy, which have lower light-off temperature and high conversion. After run 1, the diffraction patterns of the AuCu alloy reveal the presence of Au, Cu, Cu_2O, and CuO. Since the activity of Cu_2O has a lower activity than CuO, the light-off temperature is shifted to a lower temperature due to the presence of Cu and the maximum conversion is

decreased due to the presence of Cu_2O. The X-ray diffraction peaks of the AuCuO physical mixture nanoparticles after catalysis show diffraction patterns of Au, CuO, and CuO for AuCu physical mixture nanoparticles. The catalytic activities of the AuCu alloy, AuCu physical mixture, and Au, CuO nanoparticles prepared by the LVCC method after heat treatment (run 2) are summarized in Table 35.

Based on these results and the results obtained by Wang *et al* [149] for CO oxidation on AuAg system, the reaction mechanism of CO oxidation on AuCu alloy could be explained as follows the adsorption and activation of oxygen must take place on Cu, and the presence of Au helps the molecular adsorption of oxygen and formation of the O_2^- species on the Cu surface. Meanwhile, the adsorption of CO occurs on Au. For the reaction between O_2^- and adsorbed CO to occur, the Au and Cu must be in proximity to each other so that the two adsorbed species can interact as reported by Kondarides *et al* for the AuAg alloy [150]. The alloy can adsorb CO and O_2 on neighboring sites. Electron transfer from Cu to the antibonding orbital of an oxygen molecule helps weaken its chemical bond. With a neighboring adsorbed CO, the oxygen transfer reaction could then occur easily. The proposed scheme is shown in Figure 93.

5.2.4.2 Low temperature CO oxidation on AuCu alloy nanoparticle catalyst supported on CeO_2

Although, the catalytic activities of the unsupported physical mixtures of Au with Cu and CuO are slightly higher than the activities of the individual components, the AuCu alloy shows higher activity than the physical, the individual component, and their physical

mixture. The Au, Cu, and CuO supported on CeO_2 show high activities for CO oxidation. In this section, the catalytic activities of the AuCu alloy supported on CeO_2 will be investigated.

Figure 94 compares the catalytic activities of 5 % Au/CeO_2, 5 % Cu/CeO_2, and AuCu alloy/CeO_2 nanoparticles as prepared by the LVCC method (run 1). The light-off temperature of the AuCu alloy lower than Au supported on CeO_2 and higher than Cu or CuO supported on CeO_2. the AuCu alloy reaches the maximum conversion percentage at 290^oC, which is higher than Au supported on CeO_2 and lower than Cu or CuO supported on CeO_2. The individual components reach a 50 % conversion at lower temperatures than the AuCu alloy nanoparticles. Table 36 compares the catalytic activities of 5 % Au/CeO_2, 5 % Cu/CeO_2, 5 % CuO/CeO_2, and 5 % AuCu alloy/CeO_2 nanoparticles. In run 2, the catalytic activities of all catalysts is shifted to a lower temperature region due to the synergetic interaction between Au, Cu, CuO, and AuCu alloy with CeO_2 and the reduction of CeO_2 where the light-off temperature follows the same order except for the 5 % CuO/CeO_2 catalyst becomes higher than the 5 % Cu/CeO_2. All catalysts reach a full conversion at lower temperatures than in run 1. 5 % CuO/CeO_2 has less conversion at higher temperatures than the other catalysts, as shown in Figure 95. Table 37 summarizes the catalytic activities of the AuCu alloy catalyst and the individual components after heat treatment (run 2).

The catalytic activity of 5 % AuCu alloy/CeO_2 nanoparticles is enhanced after the heat treatment, as shown in Figure 96. Table 38 summarizes the catalytic activity of 5 % AuCu alloy before and after heat treatment (run 1 and run 2). X-ray diffraction patterns of

5 % AuCu alloy/CeO2 nanoparticles, as prepared by the LVCC method, show a broad diffraction peaks that is consistent with crystalline CeO_2 of small size. After catalysis, the broadening in the diffraction peaks of CeO_2 decreases, which indicates a larger particle size, as shown in Figure 97. There is no evidence of AuCu alloy diffraction peaks in the diffraction patterns before and after catalysis.

In order to investigate these results further, 5 % AuCu alloy/CeO2 and 5 % AuCu physical mixture/CeO2 nanoparticle catalysts were compared Figure 98 shows the morphologies of both catalysts as prepared by the LVCC method. It is clear that in the case of the physical mixture, the morphology is a combination of two regions; one region is similar to Au/CeO_2 with a large particle size and Cu/CeO_2 with a small particle size while in the case of 5 % AuCu alloy/CeO_2, there is only one type of morphology with large particle size.

Although the catalytic activity of the unsupported AuCu alloy nanoparticles is higher than the corresponding unsupported physical mixture of Au and Cu, the catalytic activity of the physical mixture supported on CeO_2 is higher than the catalytic activity of the alloy supported on CeO_2. These results are attributed the decomposition of AuCu alloy after the evaporation in the LVCC process, were the AuCu alloy becomes a mixture of Au and Cu supported on CeO_2, which has less dispersion than the starting physical mixture of Au and Cu supported on CeO_2. Figure 99 shows catalytic activities of 5 % AuCu alloy/CeO_2 and 5 % AuCu physical mixture/CeO_2 nanoparticles as prepared by the LVCC method, and Figure 100 shows the catalytic activities of the same catalysts after heat

treatment. Table 39 summarizes the catalytic activities of both catalysts before and after heat treatment.

These results can be attributed to the fact that the AuCu alloy adsorbs oxygen when it is exposed to air to form Au-O-Cu complex, as reported in the TPR results, when mixed with CeO_2 to form a target. This alloy does not survive after the laser ablation and it decomposes to a mixture of Au with Cu_2O and CuO supported on CeO_2. and Since Au and Cu nanoparticles are close to each other, they are not dispersed well on CeO_2 and they form large particles. The presence of Cu_2O reduces the catalytic activity, as observed earlier. After the heat treatment, the catalytic activity is increased due to the oxidation of Cu_2O to CuO, and there is a synergetic effect of Au and CuO with CeO_2 and between Au and CuO. In the physical mixture, the Au and Cu mixture was supported on CeO_2 where the Au and Cu particles are far from each other and well dispersed on CeO_2 and both catalysts synergetic effect with CeO_2. After the heat treatment in CO/O_2 mixture, Au remains as metallic and Cu is oxidized to CuO. The catalyst then becomes a mixture of Au and CuO supported on CeO_2, where Au and CuO interact separately with CeO_2 and the overall catalytic activity is the average of Au/CeO_2 and CuO/CeO_2. Figure 101 is schematic of the proposed scheme of CO oxidation reaction on the AuCu alloy/CeO_2 and the AuCu physical mixture/CeO_2.

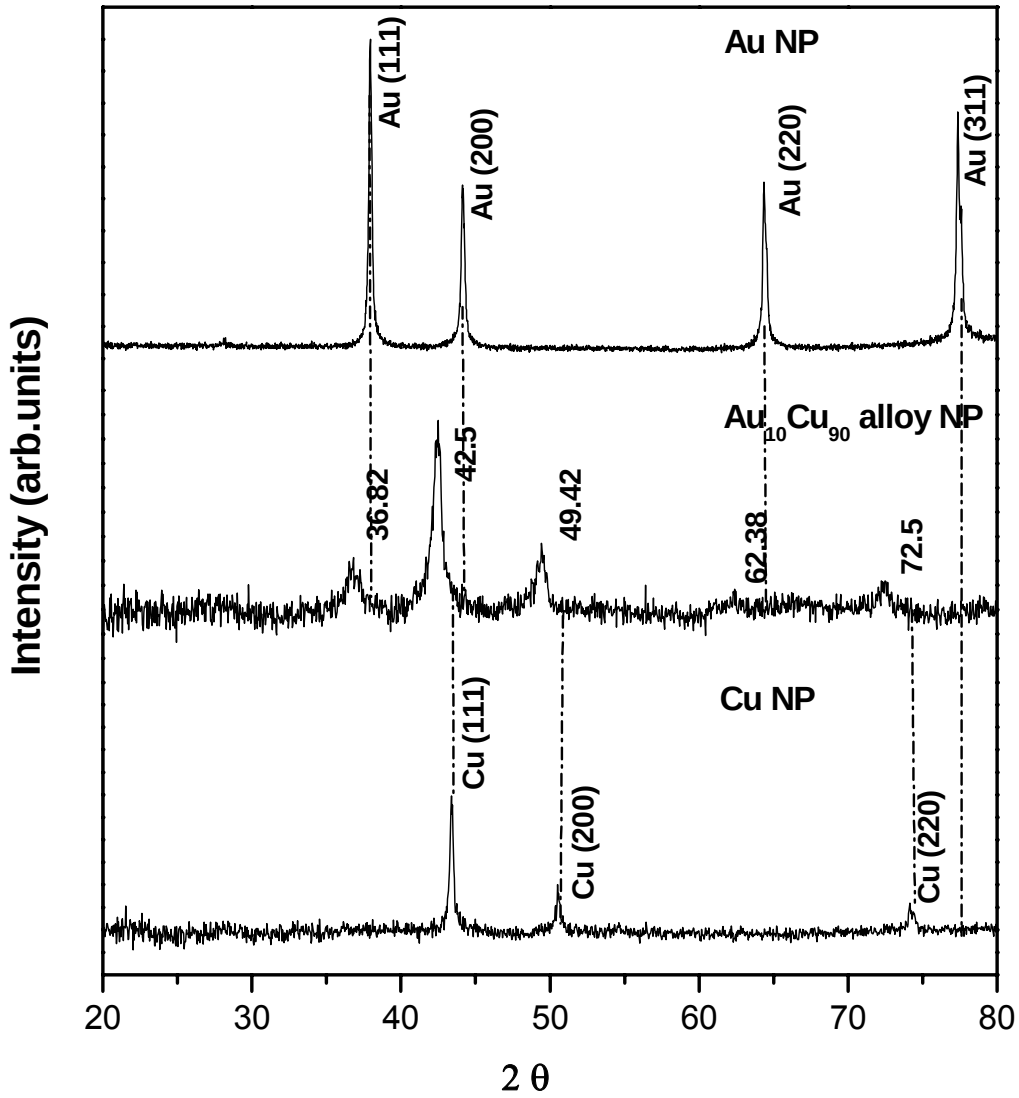

Figure 82: comparison between the X-ray diffraction patterns of Au, Cu, and (10 % Au-90 % Cu) as prepared by the LVCC method in 1500 Torr Ar.

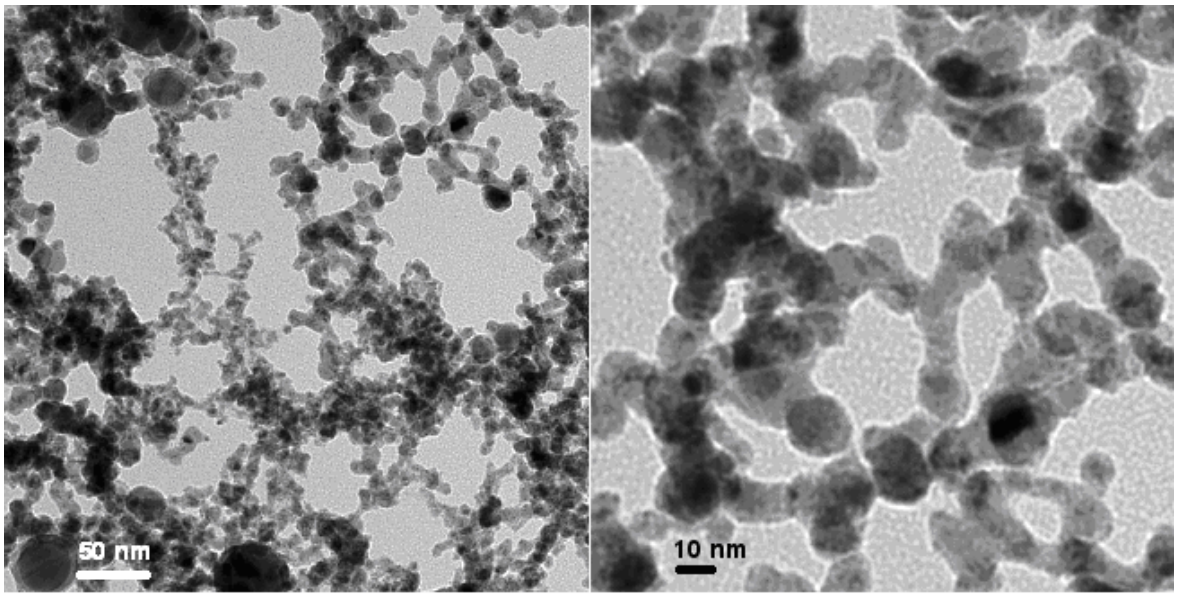

Figure 83: HRTEM micrographs of AuCu alloy prepared by the LVCC method.

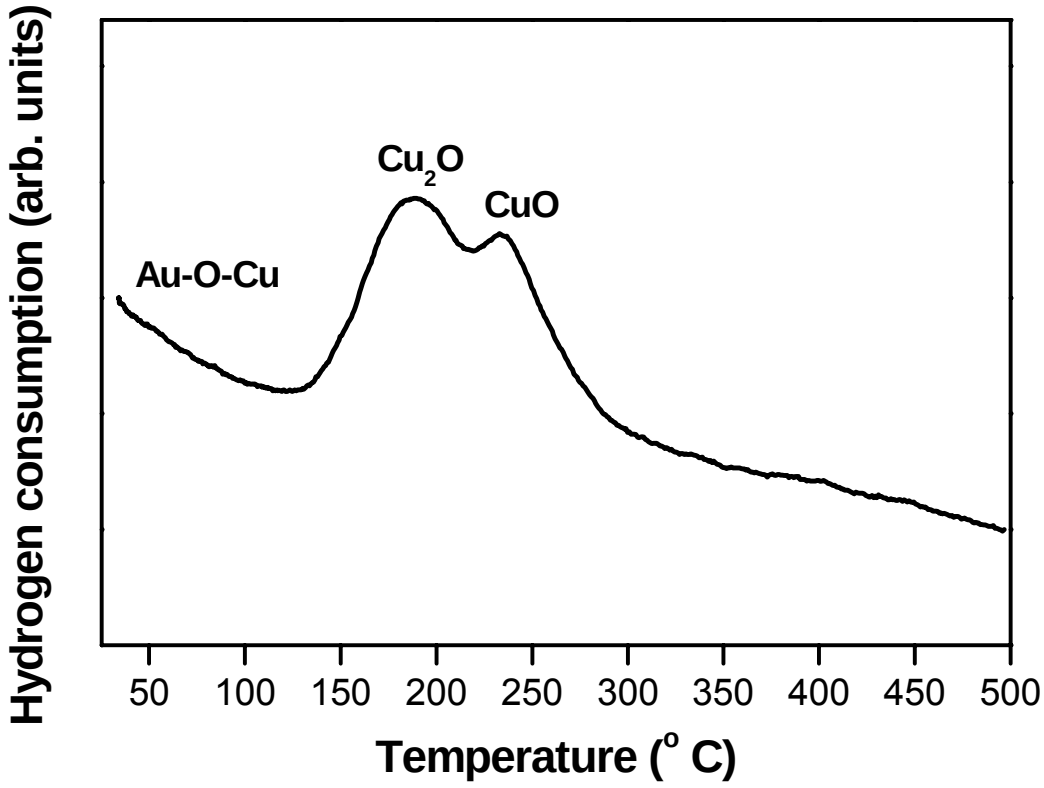

Figure 84: H_2-TPR profile of AuCu alloy nanoparticles.

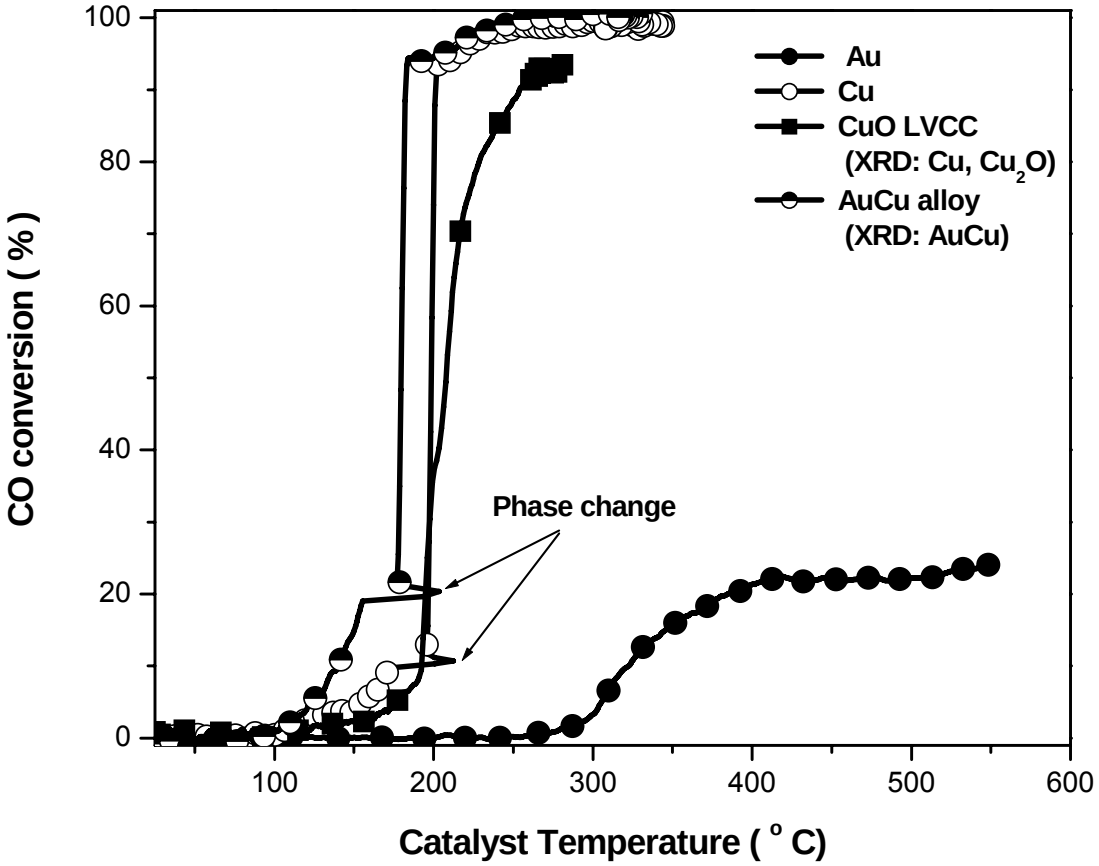

Figure 85: Comparison between catalytic activities of AuCu alloy, Au, Cu, and CuO nanoparticles as prepared by the LVCC method (run 1).

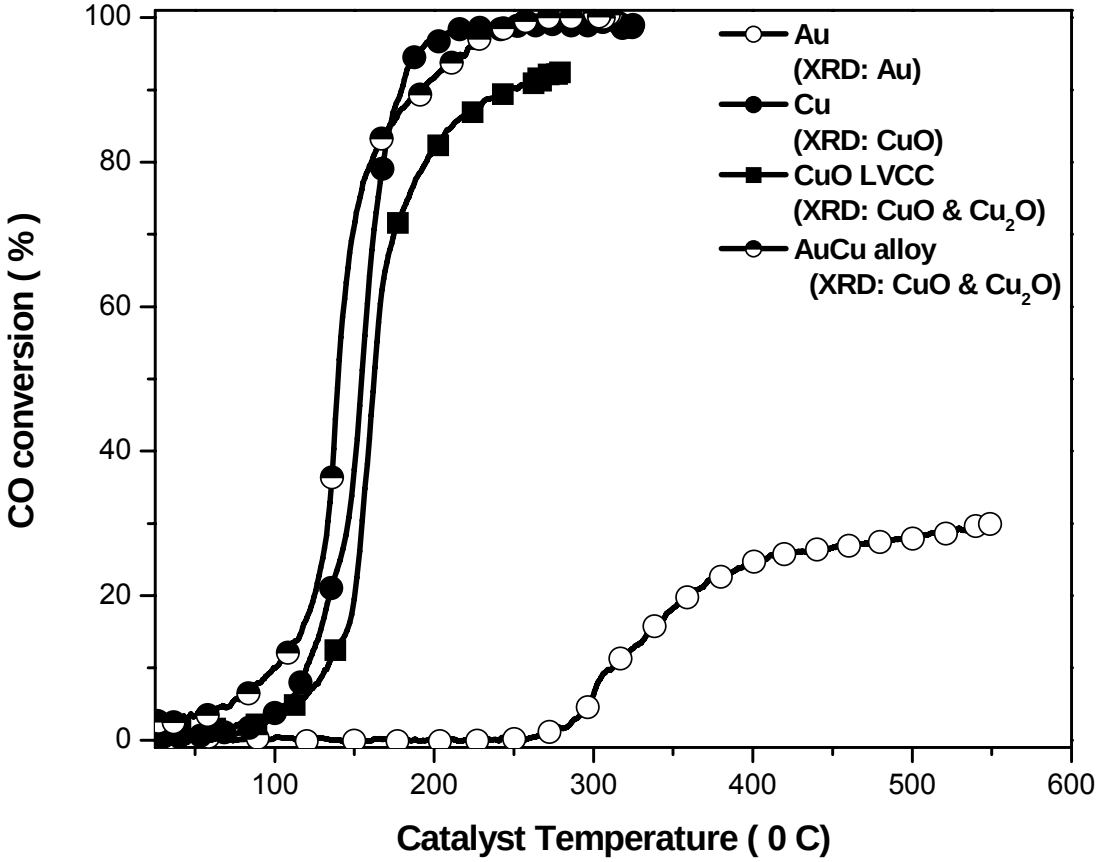

Figure 86: Comparison between catalytic activities of AuCu alloy, Au, Cu, and CuO nanoparticles as prepared by the LVCC method (run 2).

Table 33 summarizes the catalytic activities of AuCu alloy nanoparticles (10 % Au, 90 % Cu) and the individual components before and after heat treatment in CO/O_2 mixture (run 1and 2).

Sample	**3% Conversion Light-off Temp. (^{o} C)**	**50 % Conversion Temp. (^{o} C)**	**Maximum Conversion (%)**	
			Temp. (^{o} C)	**Conversion**
Au (Run 1)	298.4	-	547.2	25.7
Au (Run 2)	289.4	-	548.9	29.9
Cu (Run 1)	124.7	199.3	264.7	99.4
Cu (Run 2)	96.1	153.1	266.0	99.2
CuO (Run 1)	164.1	207.2	281.1	93.1
CuO (Run 2)	103.4	161.5	277.9	92.5
AuCu Alloy (run 1)	114.5	179.0	268.4	100
AuCu Alloy (run 2)	44.8	139.3	264.2	100

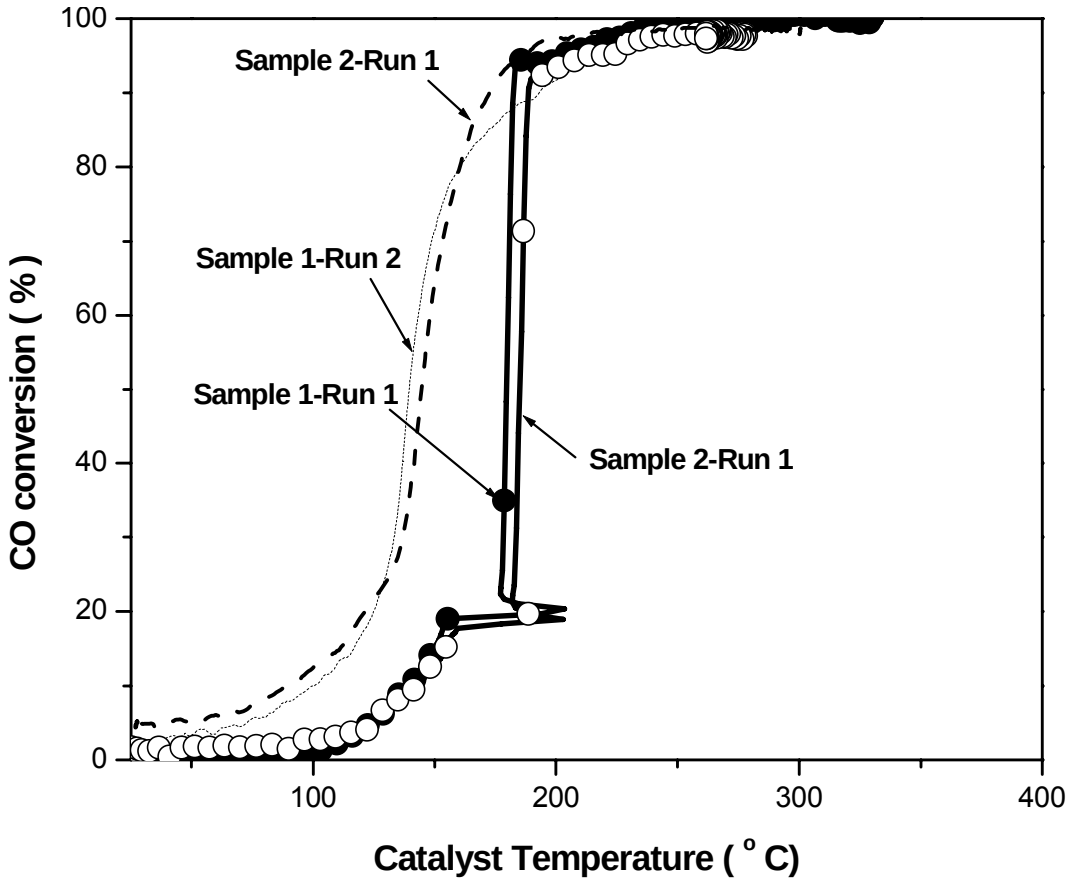

Figure 87: Comparison between the catalytic activities of two AuCu nanoparticles before and after heat treatment (run 1 and run 2).

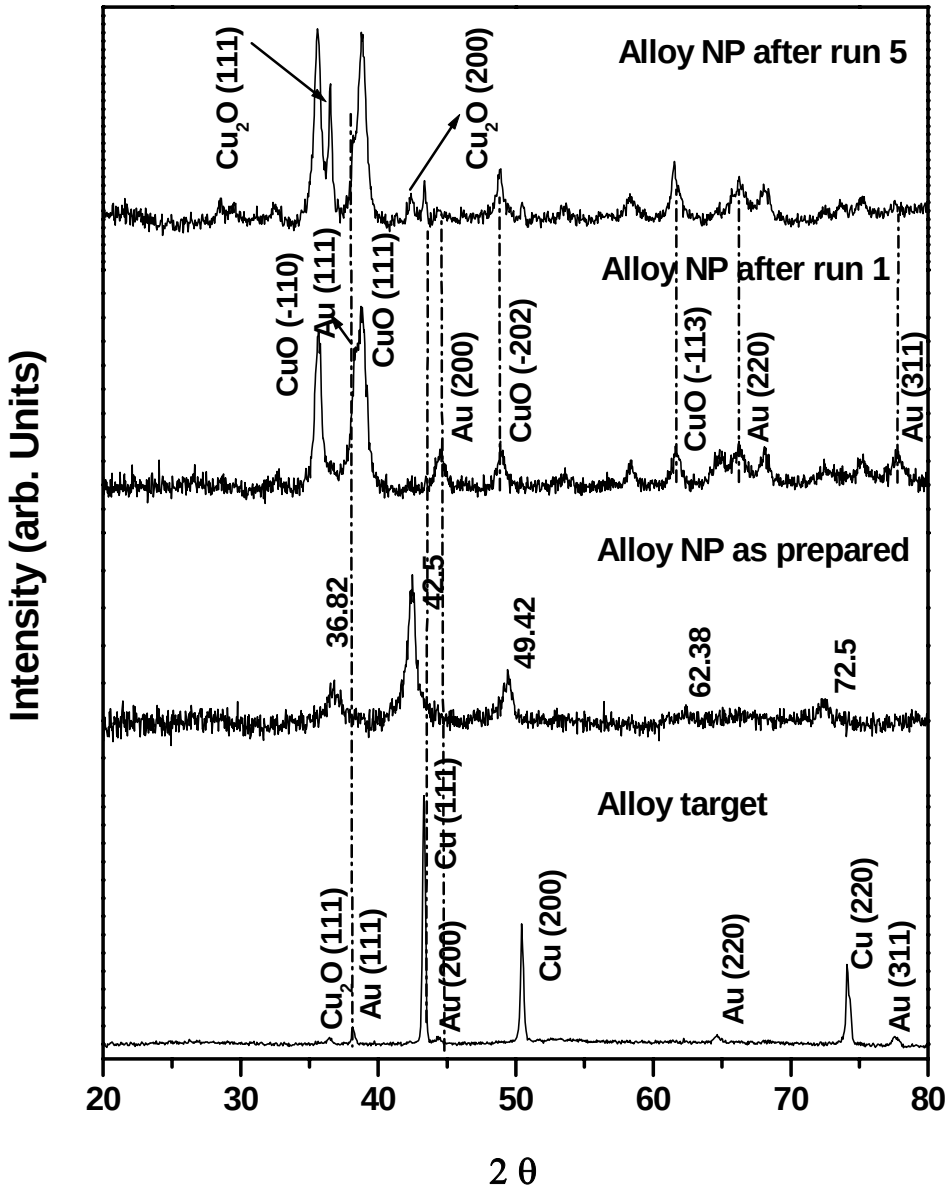

Figure 88: Comparison between X-ray diffraction patterns of AuCu target and the same AuCu alloy after multiple runs and one day of aging.

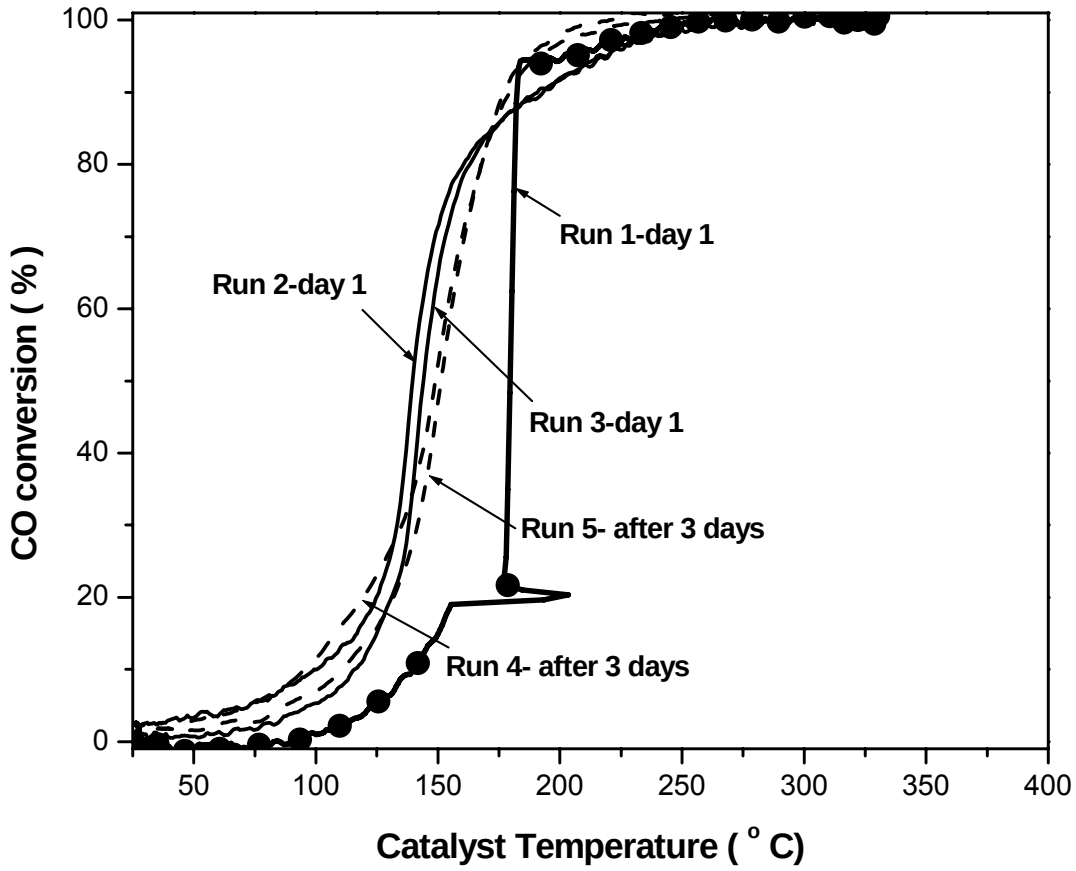

Figure 89: Comparison between the catalytic activities of the same AuCu alloy after multiple runs and one day of aging.

Table 34 summarizes the catalytic activities of the same AuCu alloy after multiple runs and one day of aging.

Sample AuCu alloy	**3% Conversion Light-off Temp. (^{o} C)**	**50 % Conversion Temp. (^{o} C)**	**Maximum Conversion (%)**	
			Temp. (^{o} C)	**Conversion**
(Run 1)	114.5	179.0	268.4	100
(Run 2)	44.8	139.3	264.2	100
(Run 3)	86.2	144.1	256.5	99.5
(Run 5)	78.9	151.4	221.5.0	100

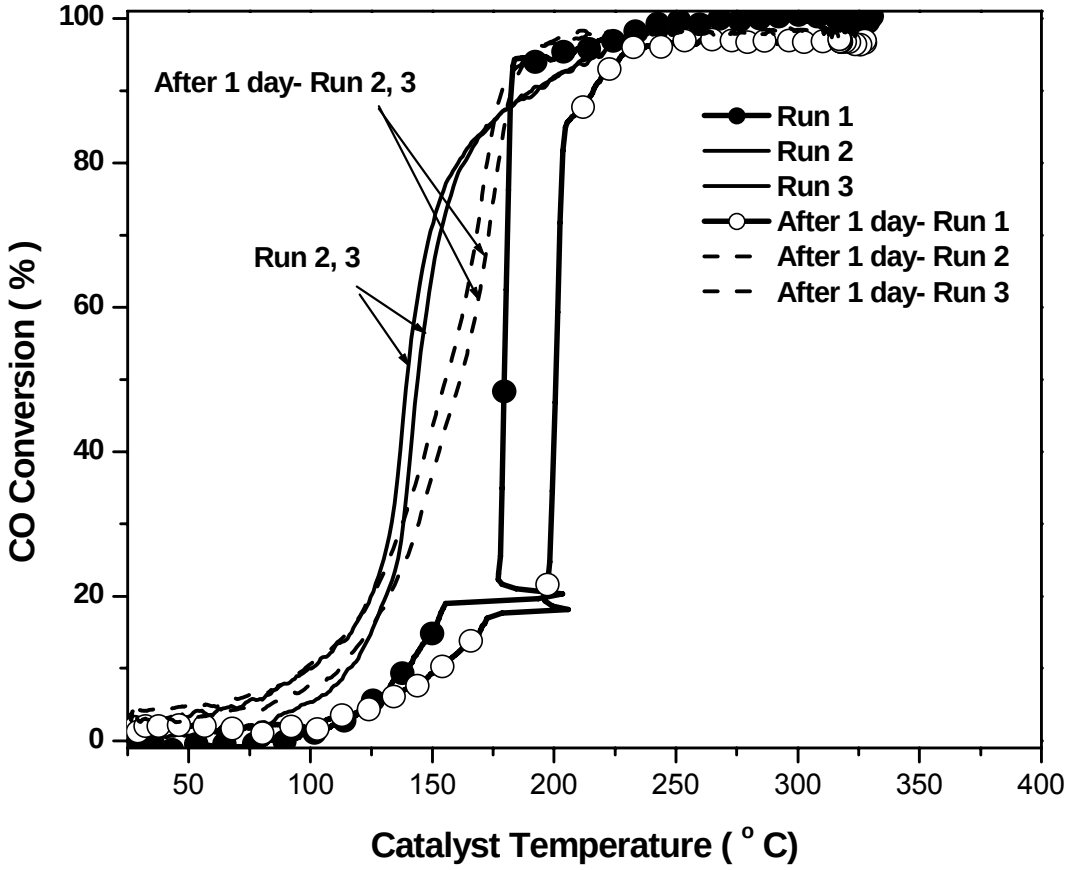

Figure 90: Comparison between the catalytic activity of AuCu nanoparticles as prepared and after one day of aging.

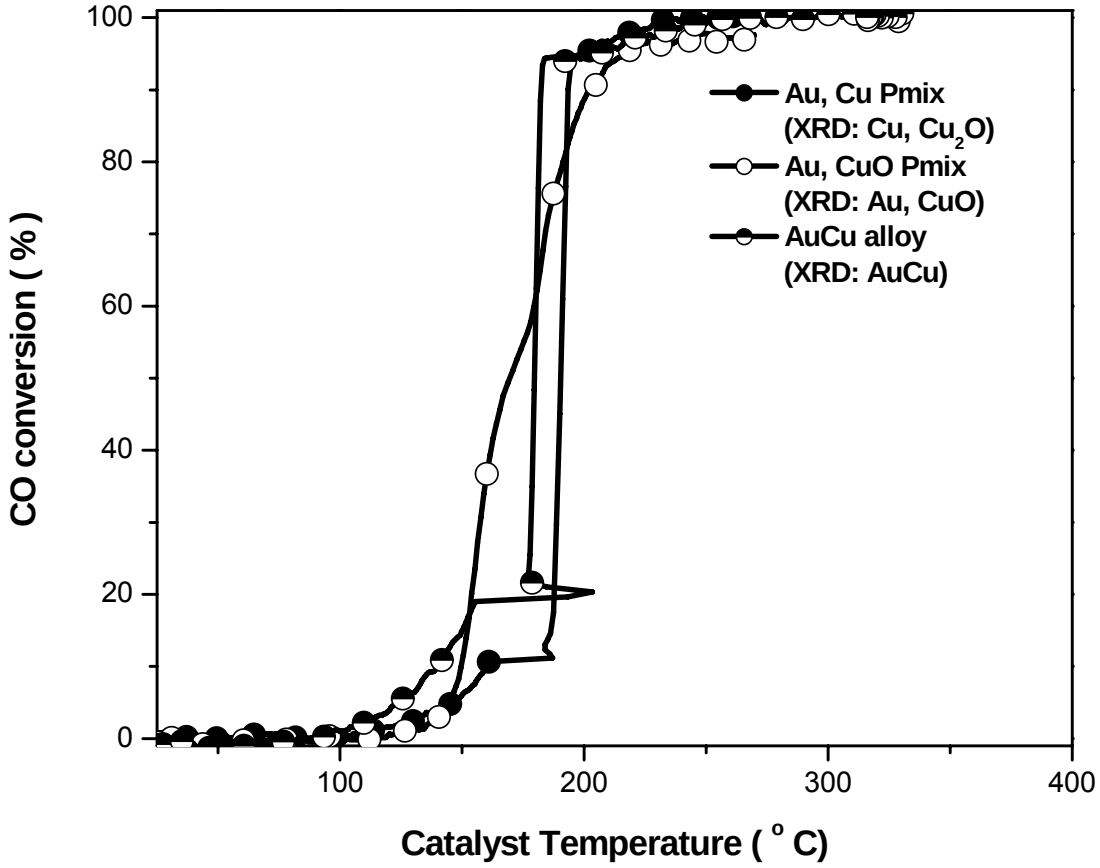

Figure 91: Comparison between the catalytic activities of AuCu alloy, AuCu physical mixture, and Au, CuO nanoparticles as prepared by the LVCC method (run 1).

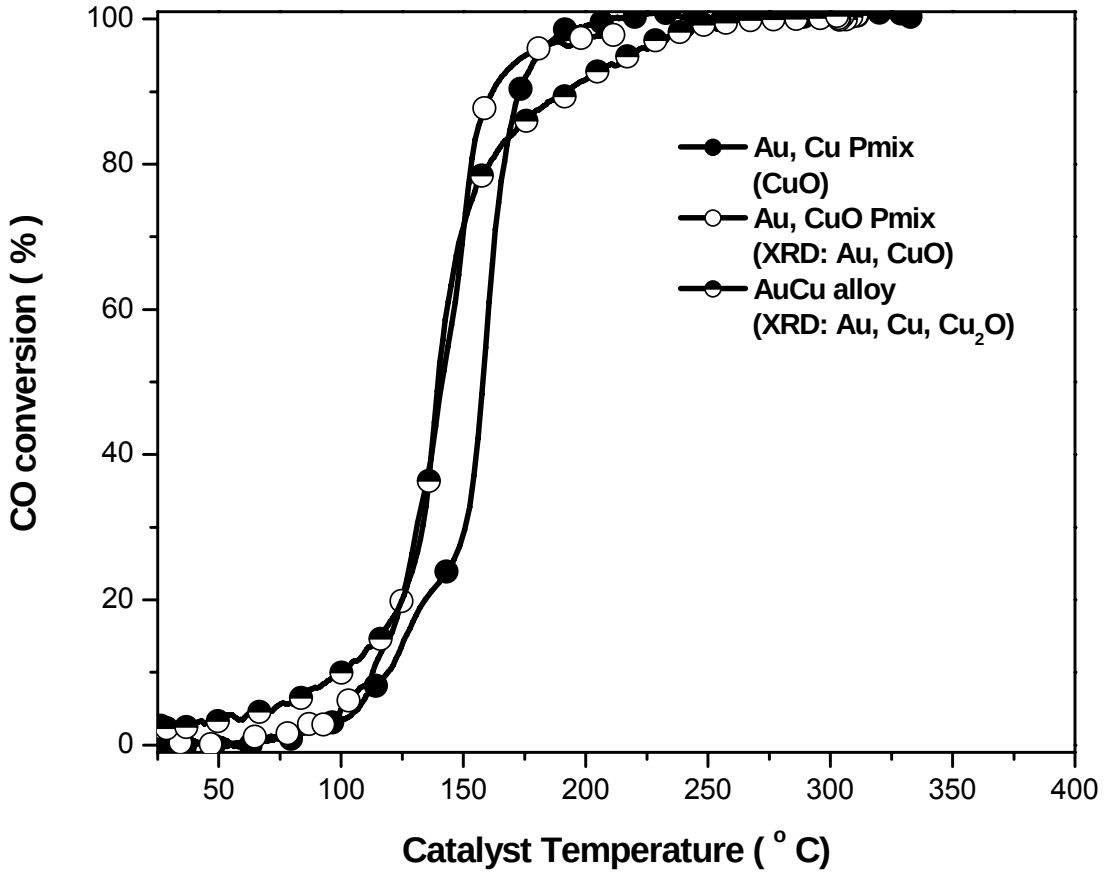

Figure 92: Comparison between the catalytic activities of AuCu alloy, AuCu physical mixture, and Au, CuO nanoparticles prepared by the LVCC method after heat treatment (run 2).

Table 35 summarizes catalytic activities of the AuCu alloy, the AuCu physical mixture, and Au, CuO nanoparticles prepared by the LVCC method after heat treatment (run 2).

Sample	**3% Conversion Light-off Temp. (^{o} C)**	**50 % Conversion Temp. (^{o} C)**	**Maximum Conversion (%)**	
			Temp. (^{o} C)	**Conversion**
AuCu alloy	44.8	139.3	264.2	100
10 % Au, 90 % Cu	96.0	158.0	319.0	100
10 % Au, 90 % CuO	89.2	140.5	211.4	97.8

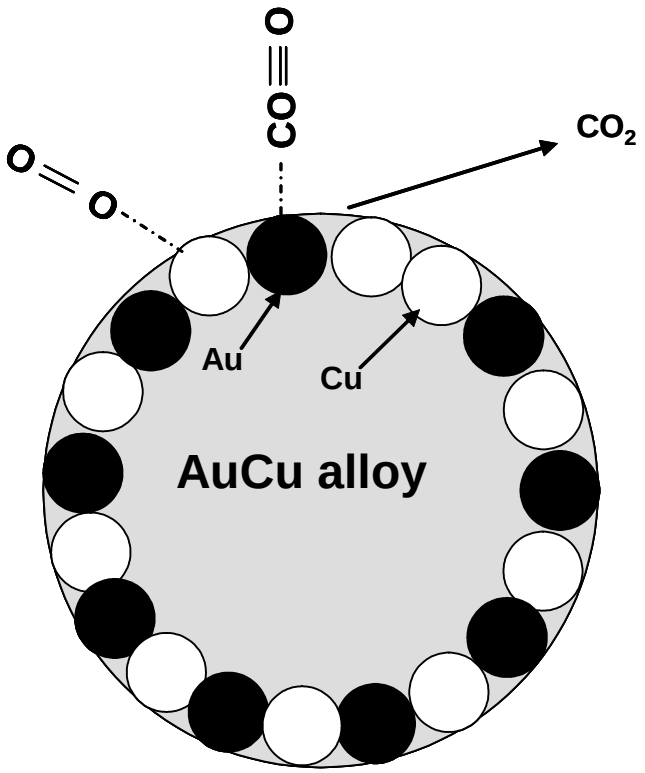

Figure 93: Proposed scheme for CO oxidation reaction on AuCu alloy.

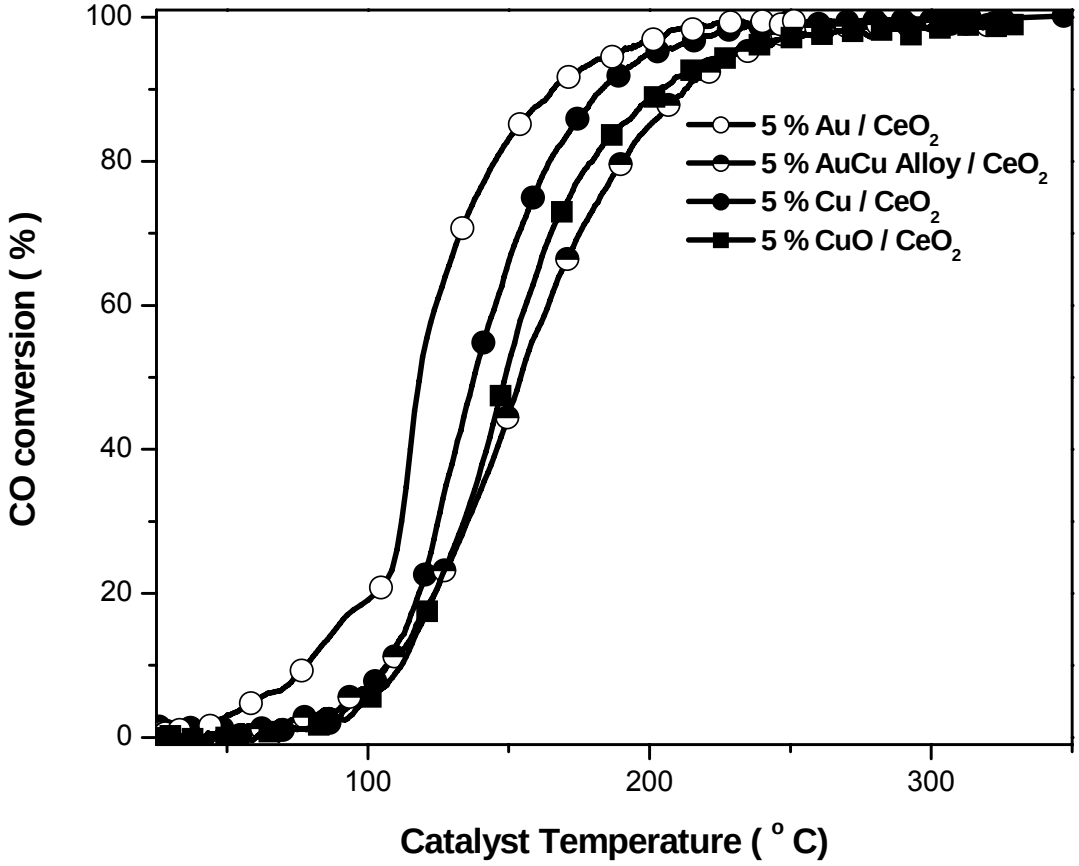

Figure 94: Comparison between the catalytic activities of the AuCu alloy catalyst and the individual components before heat treatment (run 1).

Table 36 summarizes the catalytic activities of the AuCu alloy catalyst and the individual components before heat treatment (run 1).

Sample	**3% Conversion Light-off Temp. (^{o} C)**	**50 % Conversion Temp. (^{o} C)**	**Maximum Conversion (%)**	
			Temp. (^{o} C)	**Conversion**
5 % Au/CeO_2	50.2	118.2	233.2	99.5
AuCu Alloy/CeO_2	82.4	154.0	290.2	99.1
5 % Cu/CeO_2	88.5	136.4	295.0	99.8
5 % CuO/CeO_2	94.2	148.9	298.6	99.0

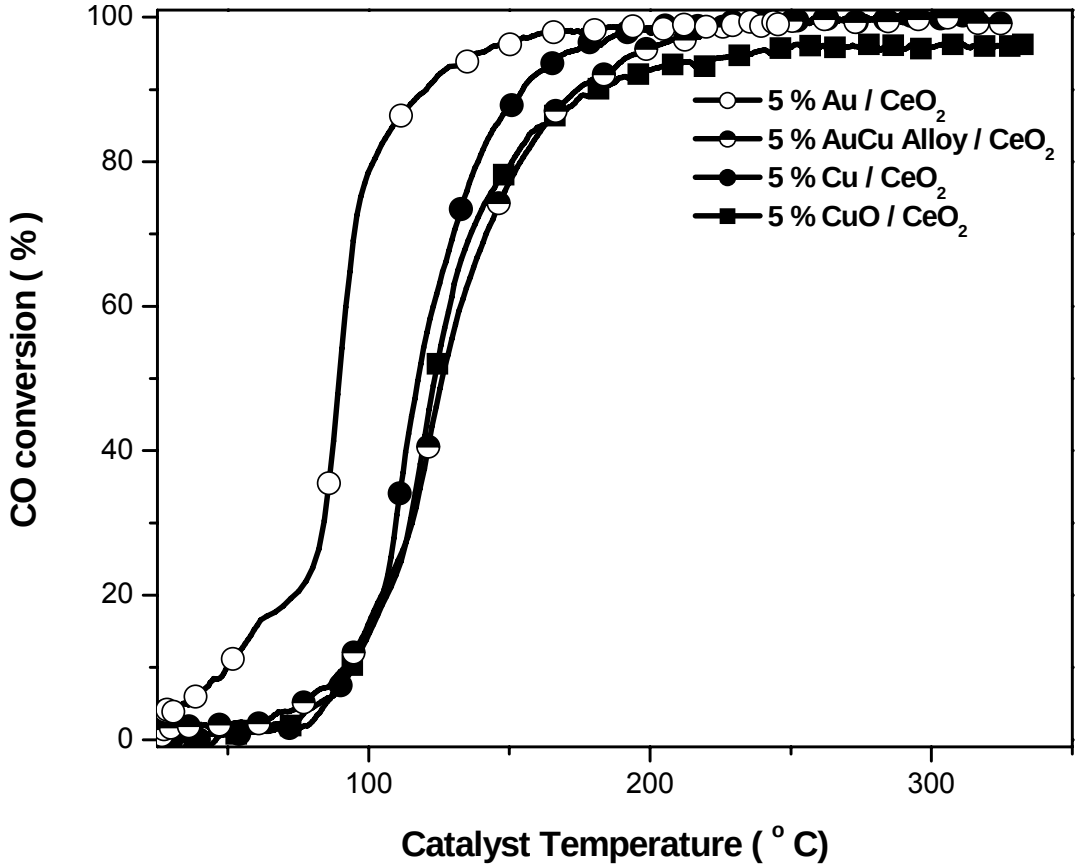

Figure 95: Comparison between the catalytic activities of the AuCu alloy catalyst and the individual components after heat treatment (run 2).

Table 37 summarizes the catalytic activities of the AuCu alloy catalyst and the individual components after heat treatment (run 2).

Sample	**3% Conversion Light-off Temp. (^{o} C)**	**50 % Conversion Temp. (^{o} C)**	**Maximum Conversion (%)**	
			Temp. (^{o} C)	**Conversion**
5 % Au/CeO_2	27.5	89.95	210.9	99.4
AuCu Alloy/CeO_2	65.6	126.1	243.8	99.7
5 % Cu/CeO_2	81.6	117.0	227.8	99.8
5 % CuO/CeO_2	75.6	122.7	279.1	96.4

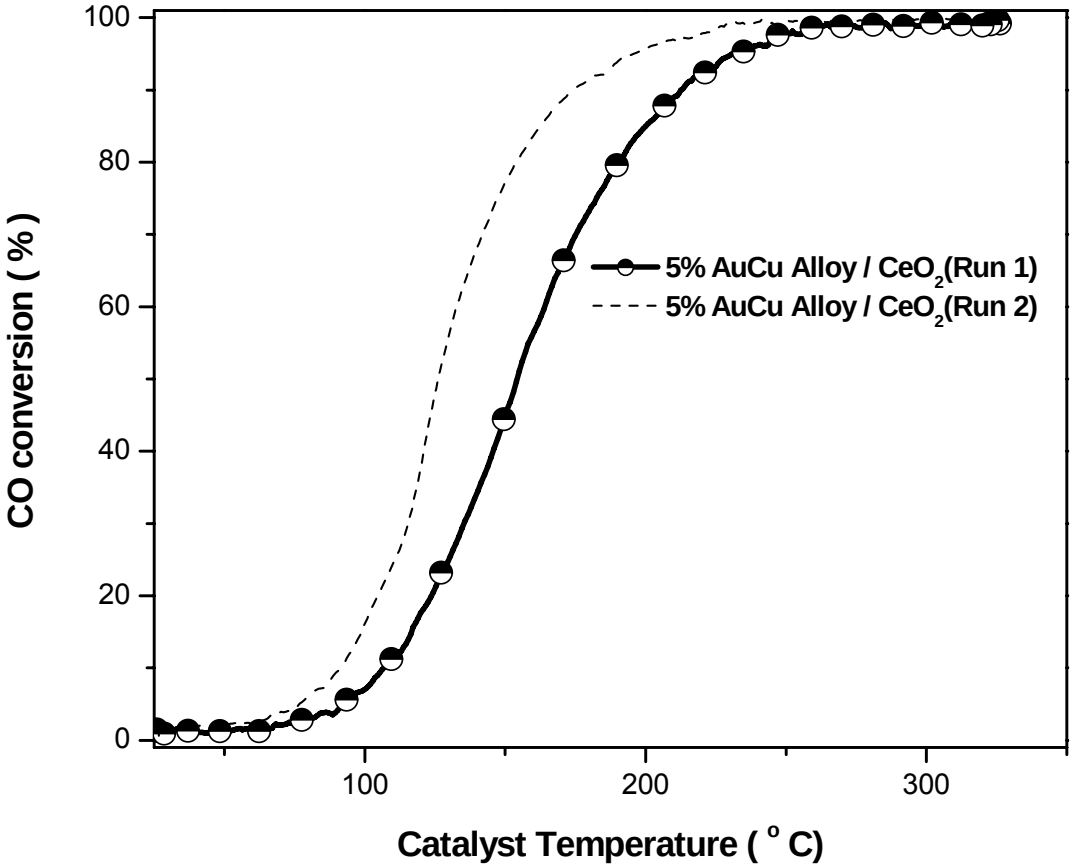

Figure 96: Comparison between the catalytic activities of the 5 % AuCu alloy before and after heat treatment.

Table 38 summarizes the catalytic activity of the 5 % AuCu alloy before and after heat treatment (run 1 and run 2).

Sample 5 % (Au, Cu mix.) / CeO_2	**3% Conversion Light-off Temp. (^{o} C)**	**50 % Conversion Temp. (^{o} C)**	**Maximum Conversion (%)**	
			Temp. (^{o} C)	**Conversion**
AuCu Alloy (Run 1)	82.4	154.0	290.2	99.1
AuCu Alloy (Run 2)	65.6	126.1	243.8	99.7

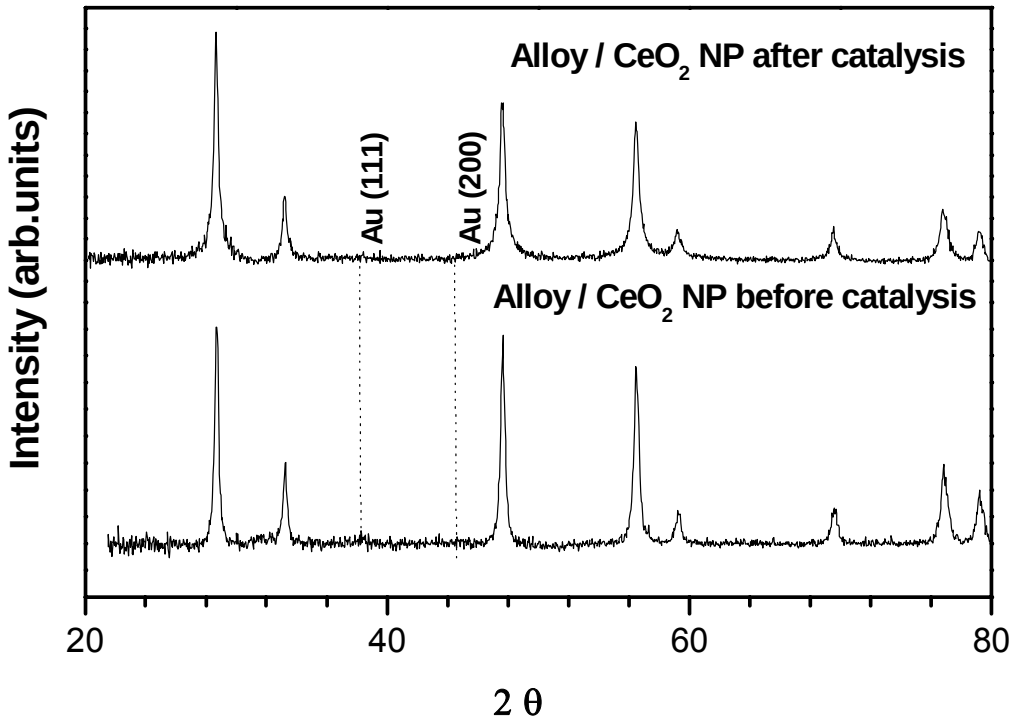

Figure 97: X-ray diffraction patterns of the 5 % AuCu alloy before and after catalysis

.

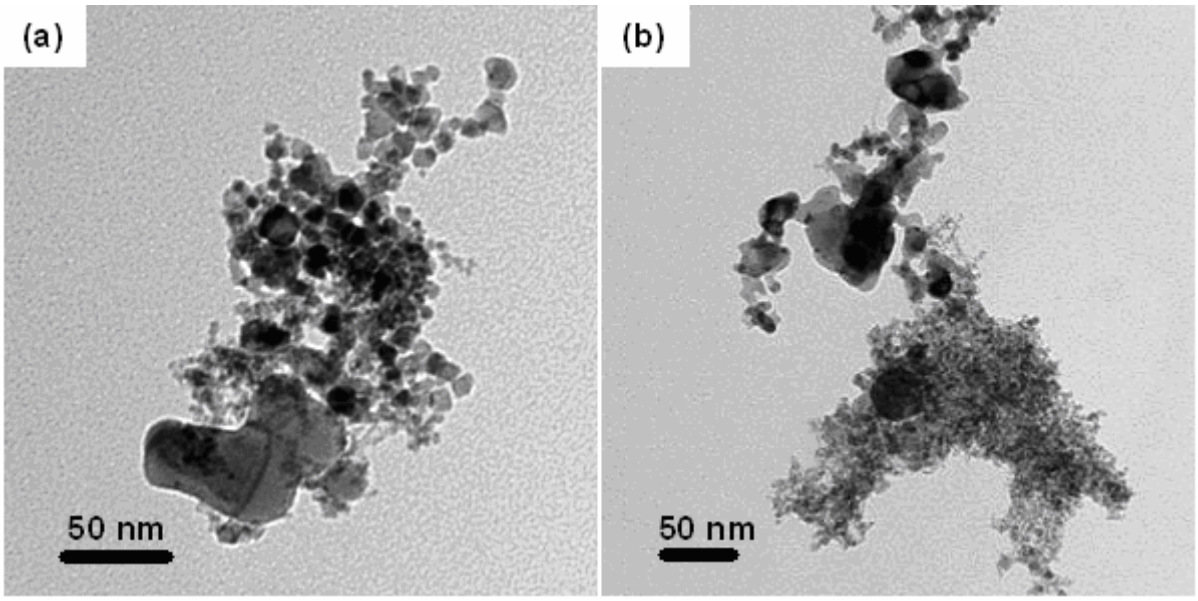

Figure 98: TEM micrographs of a) 5 % AuCu alloy/CeO_2 and b) 5 % AuCu physical mixture/CeO_2 as prepared by the LVCC method.

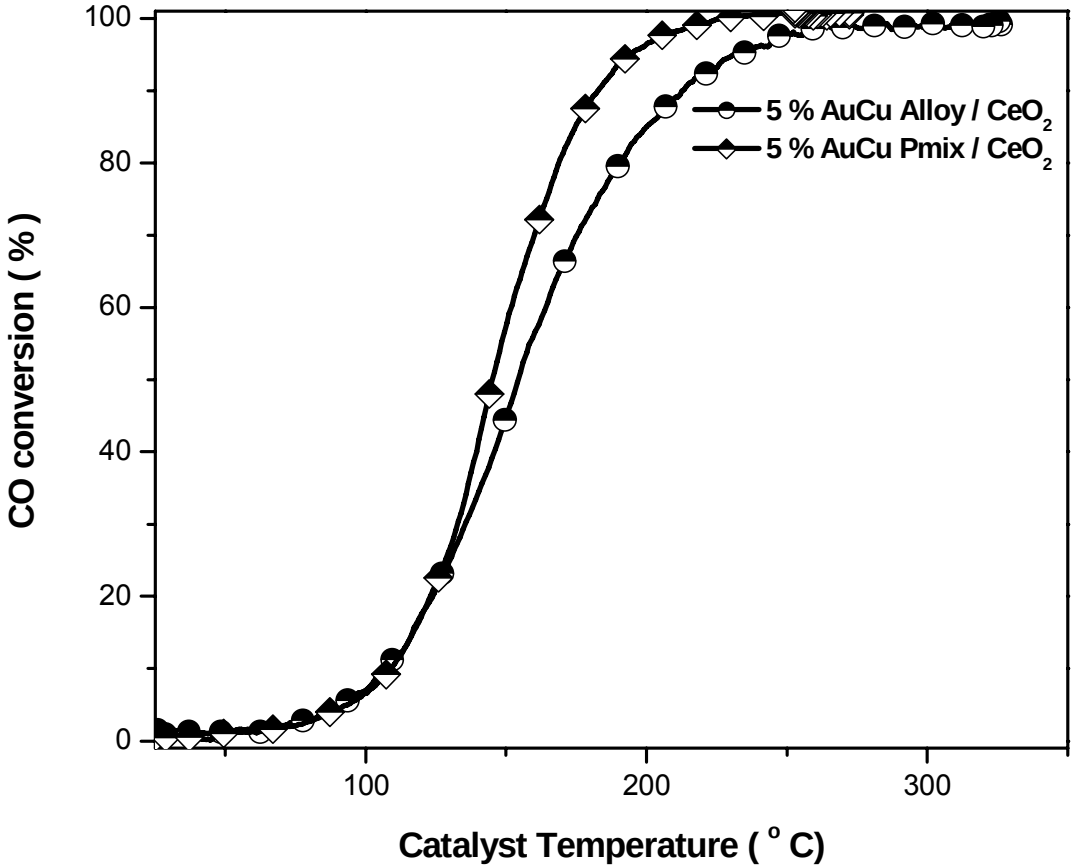

Figure 99: Comparison between the catalytic activities of 5 % AuCu alloy/CeO_2 and 5 % AuCu Physical mixture/CeO_2 as prepared by the LVCC method (run 1).

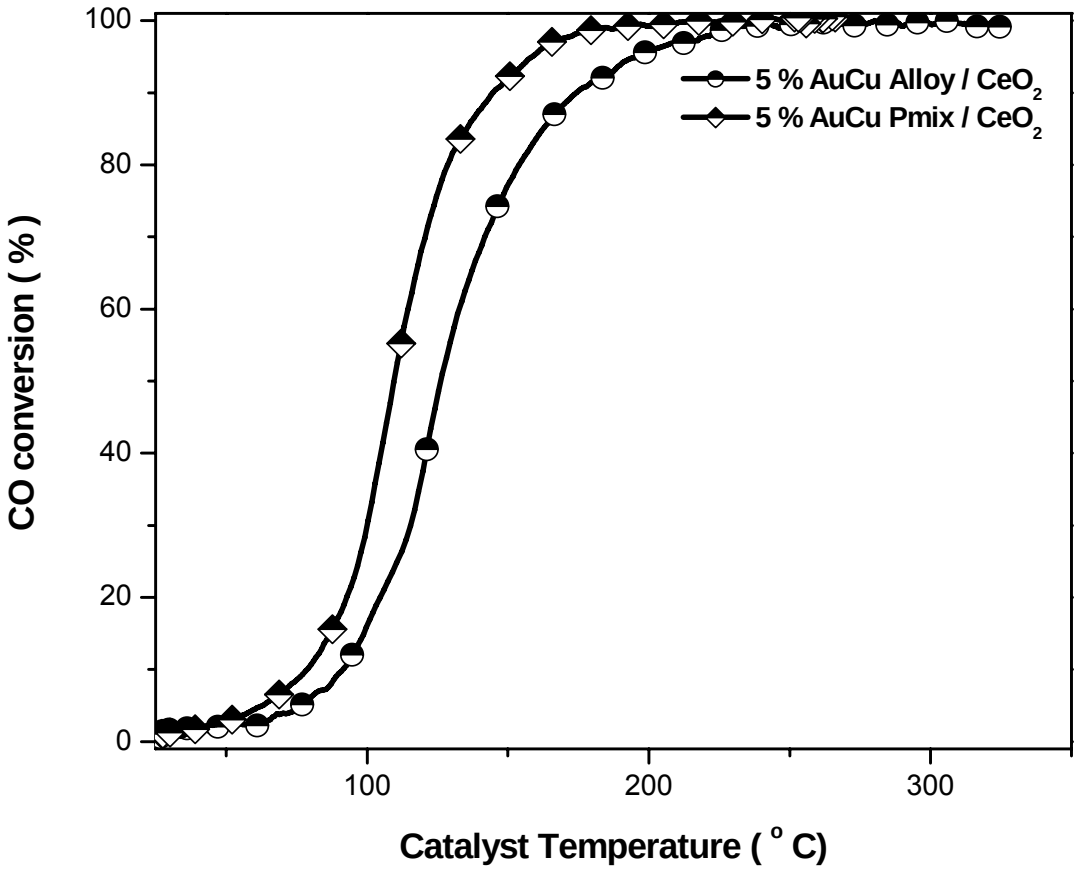

Figure 100: Comparison between the catalytic activities of 5 % AuCu alloy/CeO_2 and 5 % AuCu Physical mixture/CeO_2 prepared by the LVCC method after heat treatment (run 2).

Table 39 summarizes the catalytic activities of 5 % AuCu alloy/CeO_2 and 5 % AuCu Physical mixture/CeO_2 prepared by the LVCC method before and after heat treatment (run 1 and run 2)

Sample 5 % (Au, Cu mix.) / CeO_2	**3% Conversion Light-off Temp. (^{o} C)**	**50 % Conversion Temp. (^{o} C)**	**Maximum Conversion (%)**	
			Temp. (^{o} C)	**Conversion**
AuCu Alloy (Run 1)	82.4	154.0	290.2	99.1
AuCu Alloy (Run 2)	65.6	126.1	243.8	99.7
Alloy Phys. Mix. (Run 1)	82.4	144.8	226.4	100.0
Alloy Phys. Mix. (Run 2)	51.9	110.1	215.1	100.0

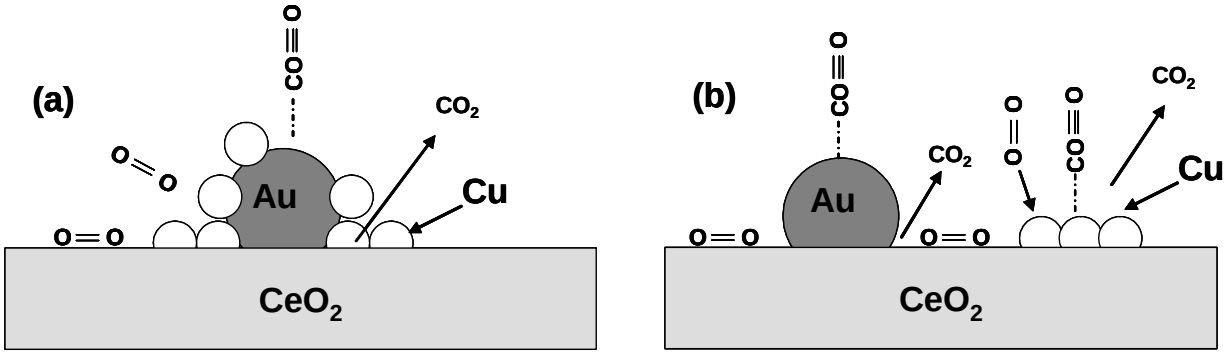

Figure 101: Schematic of proposed reaction mechanism of CO oxidation on (a) AuCu alloy/CeO_2 (b) AuCu physical mixture /CeO_2.

6 : Gas phase reactions of Au^+ and Cu^+ with small molecules

6.1 Introduction

The pressure gap between surface science and heterogeneous catalysis is a very important issue in catalysis. It is found that surface science experiments on well-defined surfaces in ultra-high vacuum (UHV) conditions yield results that are different from results obtained in high-pressure catalytic reactors. For example, catalytic CO oxidation on ruthenium at a total pressure **>** 10 torr, the rate of CO oxidation on Ru (001) is higher than on any other transition metal surface [151,152]. It was found that the oxidation rate is highest for a combination of high surface coverage of oxygen and extremely low coverage of CO. In contrast, Ru (001) is found to be among the poorest catalysts for CO oxidation under UHV conditions[153].

Gas phase reactions of metal ions with different molecules under typical reaction conditions can provide useful information about the intrinsic properties of metal ions and there reactivities. Valuable information such as reaction mechanisms, reaction rates, and thermochemestry can be obtained using this type of experiment. Understanding the crucial steps and characterizations of possible intermediates can improve the design of active catalyst systems [154]. The advantages of the gas phase reactions in catalysis arise from the elucidation of basic properties of isolated molecules and probing reactions under well defined conditions since they are not hampered by different disturbing factors in solution such as association by ion pairing, solvent–shell interactions, intra–and intermolecular

processes that lead to distraction, and / or modification of the catalytically active species (e.g. cyclometalation) [155]. There are many studies of the gas phase reactions of metal cations with molecules such as, H_2O, CO, etc [156,157]. Al^+ reacts with polar molecules such as water or ammonia [158] and alcohols such as methanol [159] or isobutylene [160]. Reactions of metal ions with methane, ethane, and linear Alkenes have been reported.

Although Au and Cu belong to the same group, and they have 1S electron outside a filled d shell, and they have similar oxidation states, the geometries of their complexes are different. This difference in the geometries is not explained well. One explanation is the difference in size where Cu^+ is smaller than Au^+ as a sequence; Cu having a higher coordination number, as shown in table 40 [161].

The gas phase reactions of Au^+ with small molecules, such as C_2H_4 and Propene, to form AuC_3H_6 and AuH [162], CO to form Au $(CO)^{+}$[163], Au $(CO)_2^{+}$ [163-165], and Au $(CO)_3^{+}$[166], have been investigated. However, some of these species are stable at room temperature [163-165]. Ozin *et al* studied gas phase interactions of gold neutral atoms with a CO/O_2 mixture using a matrix isolation experiment. He reported the formation of a Au $(CO)_2(O_2)$ stable complex and at very low temperatures (40 K), this complex is converted to CO_2 as shown in Figure 102 [55]. Hagen *et al* reported the formation of anionic complexes, such as $Au_2(CO)O_2^-$, $Au_3(CO)O_2^-$, and $Au_3(CO)(O_2)_2^-$, as intermediate in the catalytic CO oxidation over negatively charged Au clusters[167].

Gas phase reactions of Cu^+ with various molecules have been studied by many researchers[168-175]. Gas phase reactions of Cu^+ with methanol and ethanethiol clusters using

the laser ablation mol. beam (LAMB) technique is reported by Nui and Wang [170,171]. They reported the formation of $Cu^{+}(C_2H_5OH)_n$ and protonated ethanol $H^{+}(C_2H_5OH)n$ and $Cu^{+}(CH_3CH_2SH)_n$ clusters. Jarvis *et al* studied the gas phase reaction of Cu^{+} and Cu^{+} (pyrrole) $_2$ with CO and O_2 using inductively coupled plasma/selected-ion flow tube (ICP-SIFT) tandem mass spectrometer [168,172]. He reported that Cu^{+} interacts with O_2 and CO to form Cu^{+} $(O_2)_2$ and Cu^{+} $(CO)_2$ and the presence of one pyrrole molecule dramatically increases the reaction rate except in the case of Cu^{+} reaction with O_2.

Gas phase cationic polymerization is very important since the fundamental mechanism of this reaction can be probed. Metal cations act as initiator catalysts for cationic polymerization[176-183]. Catalytic polymerization in gas phase has been investigated. Fe^{+} was found to be catalytically active for a Diels-Alder reaction of dienes with alkenes and alkynes [184,185]. Also Fe^{+} can activate the C-H and C-C bonds [186].

As reported earlier, the XPS data of Au/CeO_2 of prepared by chemical and physical methods shows that the active species for CO oxidation are Au^{0} and Au^{+1}. However, Au/CeO_2, prepared by a chemical method shows higher catalytic activity for CO oxidation compared to Au/CeO_2 prepared by a physical method. The enhanced catalytic activity in the chemical method are attributed to the fact that it contains more of the Au^{+1} species, as shown in XPS data.

To understand the reaction mechanism of CO oxidation on Au and Cu based catalysts, it is important to study the gas phase reaction Au^{+1} and Cu^{+1} with CO, O_2, and their mixture. Furthermore, moisture and impurities such as hydrocarbons present on the

surface of a nanoparticle catalyst reduces the catalytic activity. Also, the catalytic activity of the Au/CeO_2 catalyst decreases significantly in the presence volatile organic compounds (VOC), such as butadiene and isoprene.

Gas phase polymerization is important not only for probing the mechanism of the catalytic process and the exact nature of the catalyst-cocatalyst interaction, but also for the elimination of various harmful organic vapors such as butadiene and isoprene by converting them into non volatile polymers [181,187,188]. Gas phase reactions of Au^+ and Cu^+ with butadiene and isoprene can provide valuable information on the reaction mechanism of the catalyst with these compounds and the possibility of cationic polymerization of VOC in the gas phase.

In this Chapter, Laser Vaporization ionization High Pressure Mass Spectrometry (LVI-HPMS), described in Figure 103, is used to study the interactions between singely charged metal ions and small molecules such as CO, O_2, CO/O_2 mixture, H_2O, Butadiene, and isoprene.

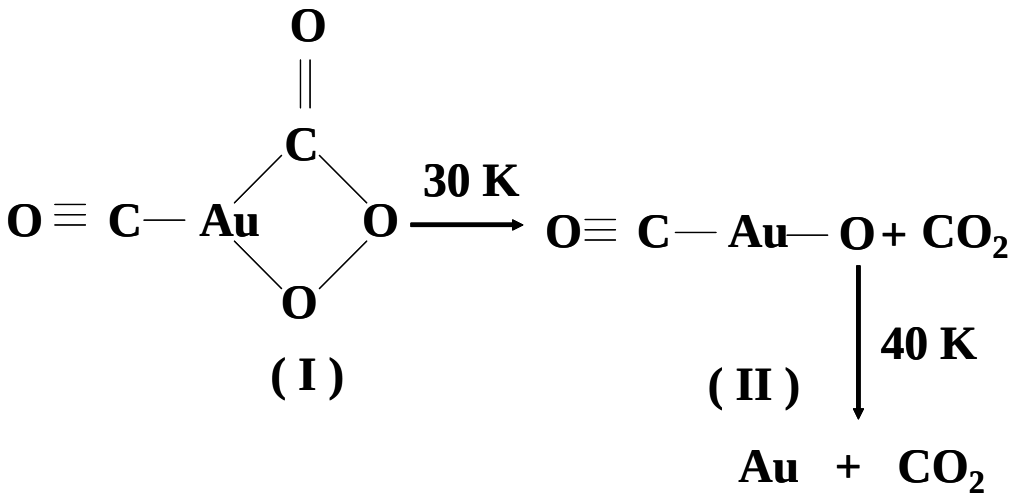

Figure 102: Proposed mechanism of CO oxidation reaction on gold neutral atoms using matrix isolation experiments as reported by Ozin *et a l* [55].

6.2 Experimental

The gas phase reactions of metal ions with several molecules have been studied using the Laser Vaporization Ionization High-Pressure Mass Spectrometry (LVI-HPMS) [177,182,183]. Metal cations are generated by focusing the output of the second harmonic of Nd: YAG laser (532 nm, energy of 22 mw pulsed at 10 Hz, laser spot 0.5 - 1 mm diameter and laser irradiance of ~ 7×10^7 W cm^{-2}) on a metal rod placed in a high pressure cell. The high-pressure cell is a 2.5 cm × 2.5 cm aluminum cube mounted inside a high vacuum chamber as shown in Figure 103. The HPMS cell has two S1-UV windows where the laser beam enters and exits. The gas is introduced to the cell via a needle valve, and is flowed behind the entrance window of the cell to prevent any metal particle deposition over the window during the laser vaporization of the metal. When the laser beam strikes the metal rod, it vaporizes the metal and forms a plasma consisting of neutral metal atoms, metal ions, and electrons. The metal ions react with the neutral molecules forming excited complexes of metal ion-neutral molecules. The excited complexes can get rid of their excess energy by colliding with the carrier gas (He) or by undergoing fragmentation (breaking bonds). The products can be addition products or they can be new products resulting from the chemical reaction[182,189]. The reaction products exit the cell through a pinhole, are focused by electrostatic lenses, analyzed by the quadrupole mass filter (Extrel C-50), and detected by the electron multiplier. The quadrupole mass spectrometer is manually controlled using an Extrel C-50 Controller with a mass range of 10-550 mass unites (amu). The resolution of the quadrupole is better than 1 amu. The ion current from

the electron multiplier is amplified and recorded. To collect the mass spectrum, the ion arrival time signal is gated using a boxcar integrator, averaged 5 times, and then recorded. To collect the arrival time of different species, the signal is recorded and averaged 200 times using a LeCroy 9450 oscilloscope.

Under typical experimental conditions the metal ions undergo several thousand collisions with the monomer molecules in the gas phase, thus resulting in ion-molecule reactions with product ions that could initiate further reactions leading to polymerization. the early stages of cationic polymerization of isoprene and butadiene using the metal cations Au^+ and Cu^+ act as initiators will be presented.

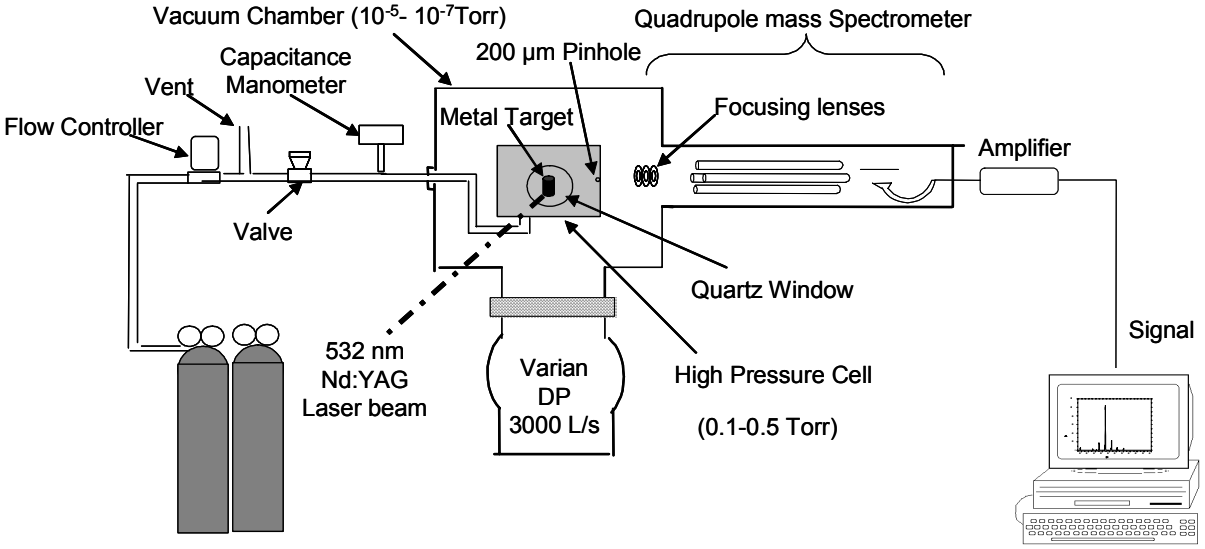

Figure 103: Schematic diagram of Laser Vaporization Ionization High Pressure Mass Spectrometry (LVI-HPMS) and relevant components.

6.3 Experimental Results

6.3.1 Gas phase reactions of Au^+ with small molecules

To understand the reaction mechanism of CO oxidation on gold, gas phase reaction of Au^+ with CO, O_2, (3.4 % CO, 20 % O_2/ He) mixture and CO oxidation in the presence of other compounds such as butadiene and isoprene. Au^+ interaction with these molecules has been studied as a function of pressure at room temperature using laser vaporization high pressure mass spectrometry. Au has one isotope at 197 amu. The gas phase reaction of Au with small molecules results in the addition of these molecules to Au^+.

6.3.1.1 Gas phase reactions of Au^+ with CO, O_2, and their mixtures

Collisional stabilization is a very important process in metal ion-molecule reactions. When the ion and molecules collide in the gas phase and attempt to combine chemically, the species formed in the excited state have excess vibrational energy. These species must loose this energy to stabilize. If no stabilization occurs, these species disassociate to the reactants. Low pressure stabilization is accomplished by collisions with another species, such as gases inside the cell or via a radiation process. However, at pressure collisional stabilization is dominant.

Gas phase reaction of Au^+ with pure CO

CO reaction of Au^+ ions results on the formation of Au^+ (CO), Au^+ $(CO)_2$, and Au^+ (CO) (O_2) at low pressure. At high pressure, there is an addition of H_2O to Au^+ (CO)

(O_2) and Au^+ $(CO)_2$. The addition of H_2O and O_2 is due to the presence of impurities in the CO tank as shown in Figure 104.

The proposed reaction scheme for Au^+ with CO is summarized as follow:

At low pressures of pure CO, the reaction of the Au^+ with CO is dominated by adduct formation where Au^+ reacts with pure CO to form $[Au^+ (CO)]^*$ excited complex which is stabilized by collision with CO to form Au^+ (CO) as shown in equation (6.1).

If no stabilization occurs, Au^+ (CO) either vanishes or can be stabilized by further collision with CO to form $Au^+ (CO)_2$, as shown in equation (6.2).

At high pressure, $[Au^+ (CO)]^*$ will be stabilized by either the reaction with CO to form $Au^+ (CO)_2$ or by the reaction with impurities such as O_2 to form $Au^+ (CO)(O_2)$, as shown in equation (6.3), which react with H_2O to form $Au^+ (CO)(O_2)(H_2O)$, as shown in equation (6.4). Also $Au^+ (CO)_2$ further react with H_2O to form $Au^+ (CO)(O_2)(H_2O)$ and $Au^+ (CO)_2(H_2O)$ as shown in (6.5).

$$Au^+ + CO \rightleftharpoons [Au^+(CO)]^* \longrightarrow Au^+(CO) \tag{6.1}$$

$$Au^+(CO) + CO \rightleftharpoons Au^+(CO)_2 \tag{6.2}$$

$$Au^+(CO) + O_2 \rightleftharpoons Au^+(CO)(O_2) \tag{6.3}$$

$$Au^+(CO)(O_2) + H_2O \rightleftharpoons Au^+(CO)(O_2)(H_2O) \tag{6.4}$$

$$Au^+(CO)_2 + H_2O \rightleftharpoons Au^+(CO)_2(H_2O) \tag{6.5}$$

Gas phase reaction of Au^+ with pure O_2

The reaction of Au^+ with O_2 at low pressure results in the formation of a Au^+ (O_2) complex. As the pressure increases, Au^+ (O_2) disappears and H_2O is adding to the Au^+ to form Au^+ $(H_2O)_n$, n = 1-5 cluster, as shown in Figure 105.

The reaction scheme can be summarized for Au^+ with O_2 as follow: At low pressures of pure O_2, Au^+ reacts with O_2 to form $[Au^+ (O_2)]^*$ and excited complexes which are stabilized by collision with O_2, as shown in equation (6.6). H_2O impurities also react with Au^+ to form Au^+ (H_2O).

At high pressure, Au^+ (O_2) vanishes and Au^+ (H_2O) reacts with H_2O to form Au^+ $(H_2O)_n$, n = 1-5 cluster, as shown in equation (6.7).

$$Au^+ + O_2 \rightleftharpoons [Au^+ + O_2]^* \longrightarrow Au^+(O_2) \tag{6.6}$$

$$Au^+ + nH_2O \rightleftharpoons Au^+(H_2O)_n, n = 1-5 \tag{6.7}$$

Gas phase reaction of Au^+ with 3.4 % CO, 20 % O_2 / He mixture

Mass spectrum of gas phase reaction of Au^+ with 3.4 % CO, 20 % O_2/ He mixture, shows the formation of Au^+ (CO), Au^+ $(CO)_2$, Au^+ $(CO)(H_2O)$, Au^+ (CO) $(H_2O)_2$ and Au^+ $(CO)(H_2O)_3$. However, the Au^+ $(CO)_2(O_2)$ complex is not observed as shown in Figure 106. Time profiles for ions obtained from the Au^+ reaction with CO/O_2 mixture in He at 298 K are shown in Figure 107. Time profiles of the products ions show that Au^+ is formed and decay followed by the formation of Au^+ (CO) and the addition of another CO molecule

to form $Au^+ (CO)_2$. At high pressures, H_2O is added to the $Au^+ (CO)$ complex. However, $Au^+ (CO)_2$ remains, which suggest a high stability of this complex

Based on the mass spectra and the time profiles of reactions of Au^+ with 3.4 % CO, 20 % O_2/ He mixture at different pressures at 298 K, the reaction scheme of Au^+ with CO/O_2 in He mixture can be explained as follows:

At low pressures of CO/O_2 in He mixture, the reaction of the Au^+ with CO/O_2 is dominated by adduct formation where Au^+ reacts with CO/O_2 to form $[Au^+ (CO/O_2)]^*$ excited complex which is stabilized by collision with CO, O_2, and He dissociates to form $Au^+ (CO)$, as shown in equation (6.8). At high pressure, $Au^+ (CO)$ is stabilized by collisions with CO/O_2 mixture to form a stable $Au^+ (CO)_2$ product according to the equation (6.9) or it reacts with H_2O to form $Au^+ (CO)(H_2O)_n$ where n=1-3 as shown in equation (6.10).

$$Au^+ + (CO/O_2 Mixture) \rightleftharpoons [Au^+ (CO/O_2)]^* \longrightarrow Au^+ (CO) \tag{6.8}$$

$$Au^+ (CO) + CO \rightleftharpoons Au^+ (CO)_2 \tag{6.9}$$

$$Au^+ (CO) + H_2O \rightleftharpoons Au^+ (CO)(H_2O)n, n = (1-3) \tag{6.10}$$

To investigate the formation of CO_2, electron impact of CO/O_2 mixture after the reaction of Au^+ with CO/O_2 and the electron impact and laser vaporization of Au^+ is performed at the same time. Figure 108 compares the mass spectra of CO/O_2 using electron impact, laser ionization, and both electron impact and laser ionization at the same time. As indicated from the mass spectra, there is no evidence of CO_2 formation. These

results can be explained based on the Ozin *et al* [55] results of CO oxidation on Au neutral atoms. According to Ozin *et al*, the precursor of CO oxidation reaction is the addition of two molecules of CO and one molecule of O_2 to form $Au^+ (CO)_2(O_2)$ complex which results in the conversion of CO to CO_2 at low temperatures (30-40 K). The presence of small traces of H_2O added to the $Au^+ (CO)_2$ and the replacing of the oxygen and prevention of the formation of $Au^+ (CO)_2(O_2)$ and CO oxidation reaction. In order for the reaction to proceed, it must occur at temperatures less than 100 K, where H_2O is frozen.

Gas phase reaction of Au^+ with Pure H_2O

The presence of a small amount of H_2O impurities prevents CO oxidation reaction where H_2O replaces O_2 and prevents CO oxidation reaction. Since the ionization potential of H_2O is much higher than the ionization potential of Au, there is no possibility of charge transfer from the gold to H_2O and the charge remains on the gold.

To investigate the water effect further, the reaction of Au^+ with pure H_2O is studied. Figure 109 shows the mass spectrum of Au^+ produced in pure H_2O at different pressures and at room temperature, Figure 110 shows the addition of seven H_2O to Au at room temperature which indicates that there is a strong bond. Time profiles for ions obtained from the Au^+ reaction with pure H_2O at 298 K are consistent with the mass spectrum as shown in Figure 111. The time profiles suggest that this system reached an equilibrium state. This can be seen from the flat curve of the product ions after a certain arrival time.

The proposed reaction scheme of Au^+ with H_2O molecules can be explained by the sequential addition of H_2O to Au^+. Au^+ reacts with H_2O to form $[Au^+(H_2O)]^*$. At a low pressure, $[Au^+(H_2O)]^*$ is stabilized by the collisions with H_2O molecules to produce $Au^+(H_2O)$ as shown in equation (6.11). At high pressure, $Au^+(H_2O)$ reacts with H_2O molecules to form higher $Au^+(H_2O)_n$ clusters as shown in equation (6.12)

$$Au^+ + H_2O \rightleftharpoons [Au^+(H_2O)]^* \longrightarrow Au^+(H_2O) \tag{6.11}$$

$$Au^+(H_2O) + nH_2O \rightleftharpoons Au^+(H_2O)_n, n = (1-5) \tag{6.12}$$

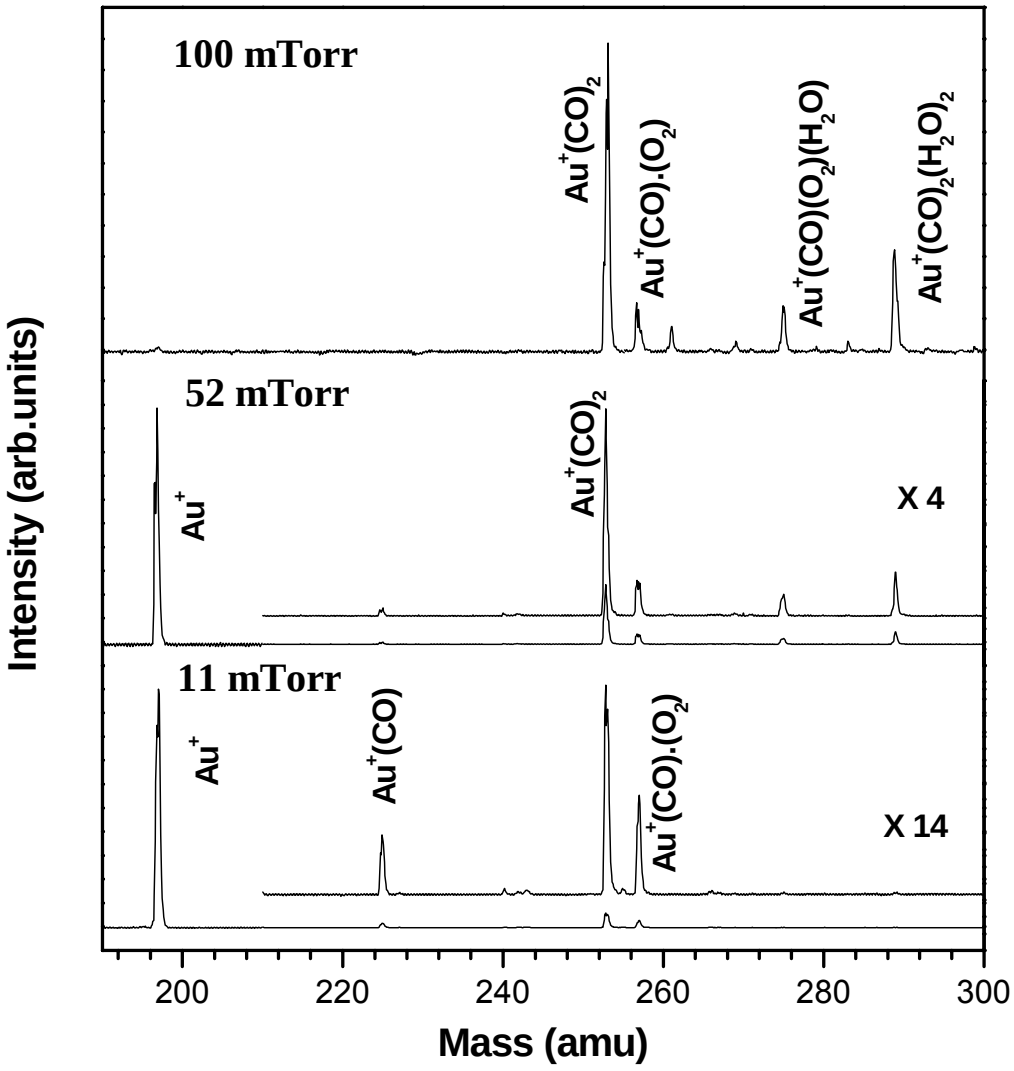

Figure 104: Mass spectrum of Gold (Au^+) ions produced in Pure CO at different pressures.

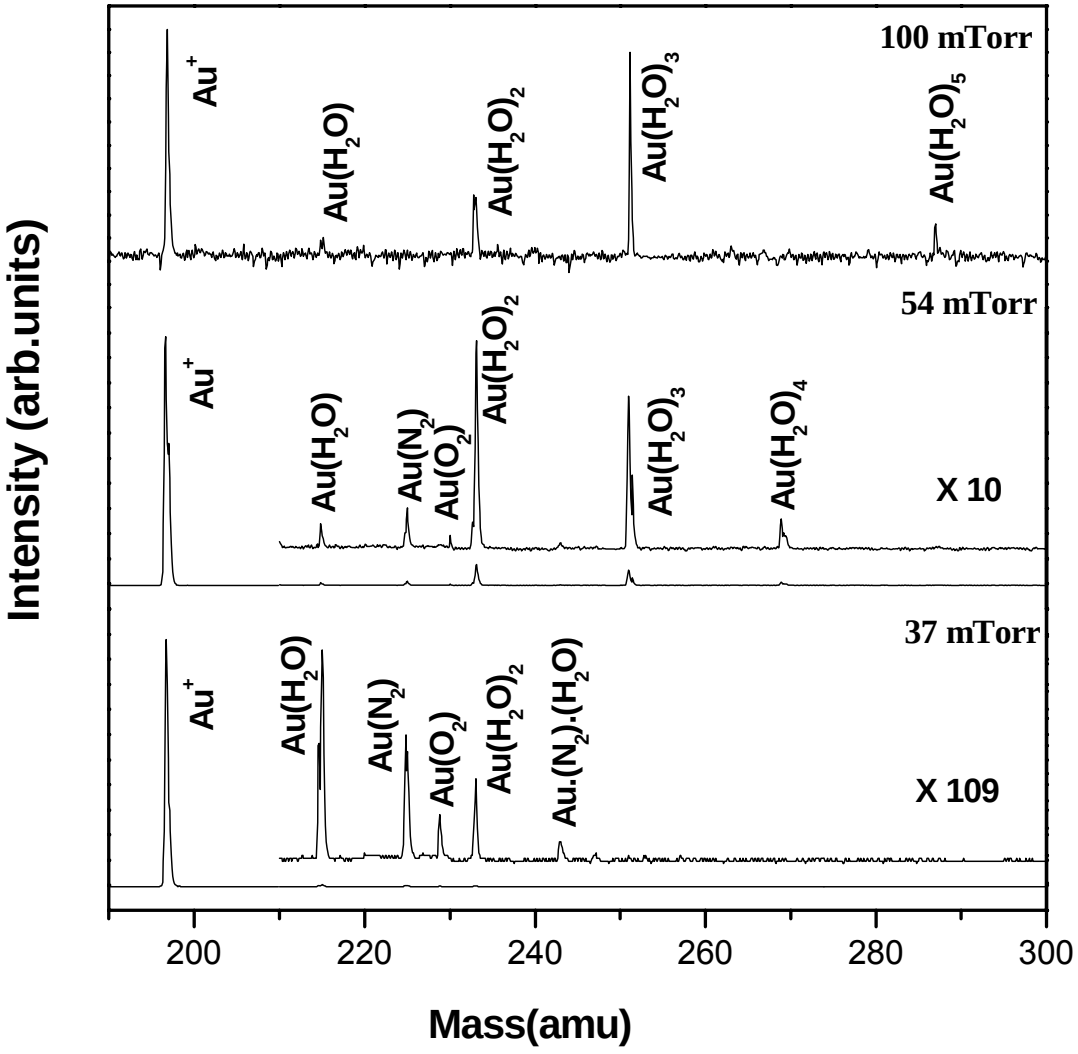

Figure 105: Mass spectrum of Gold (Au^+) ions produced in Pure O_2 at different pressure

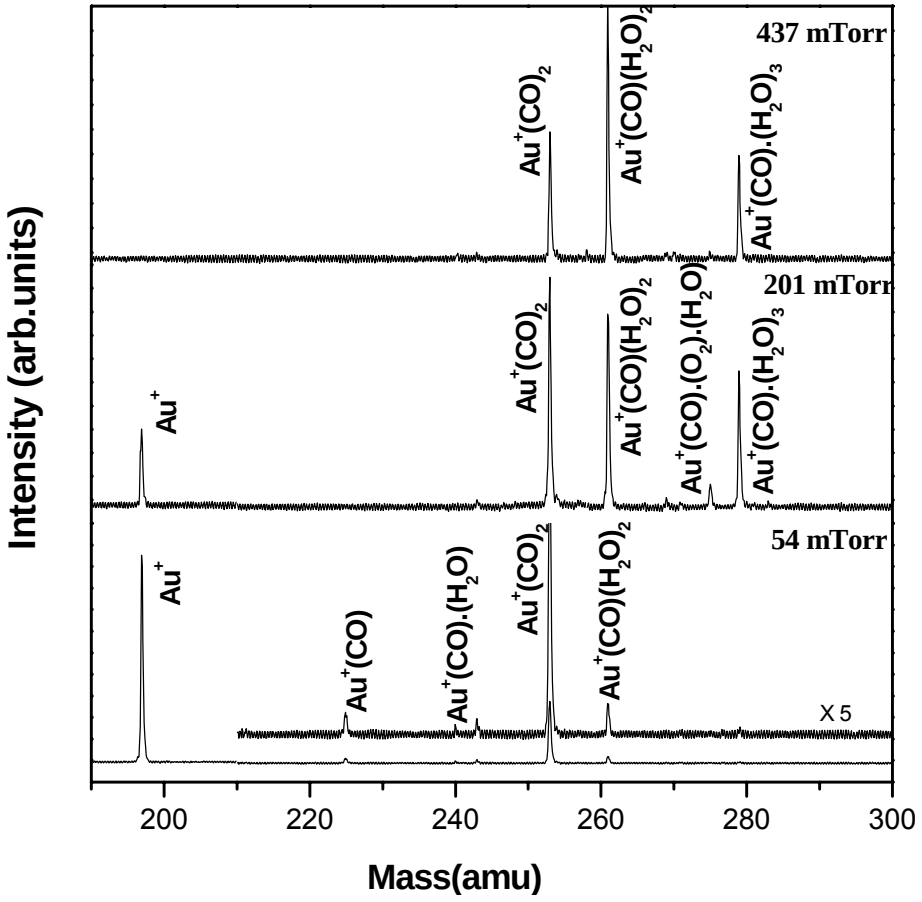

Figure 106: Mass spectrum of Gold (Au^+) ions produced in CO/O_2 mixture in He at different pressures.

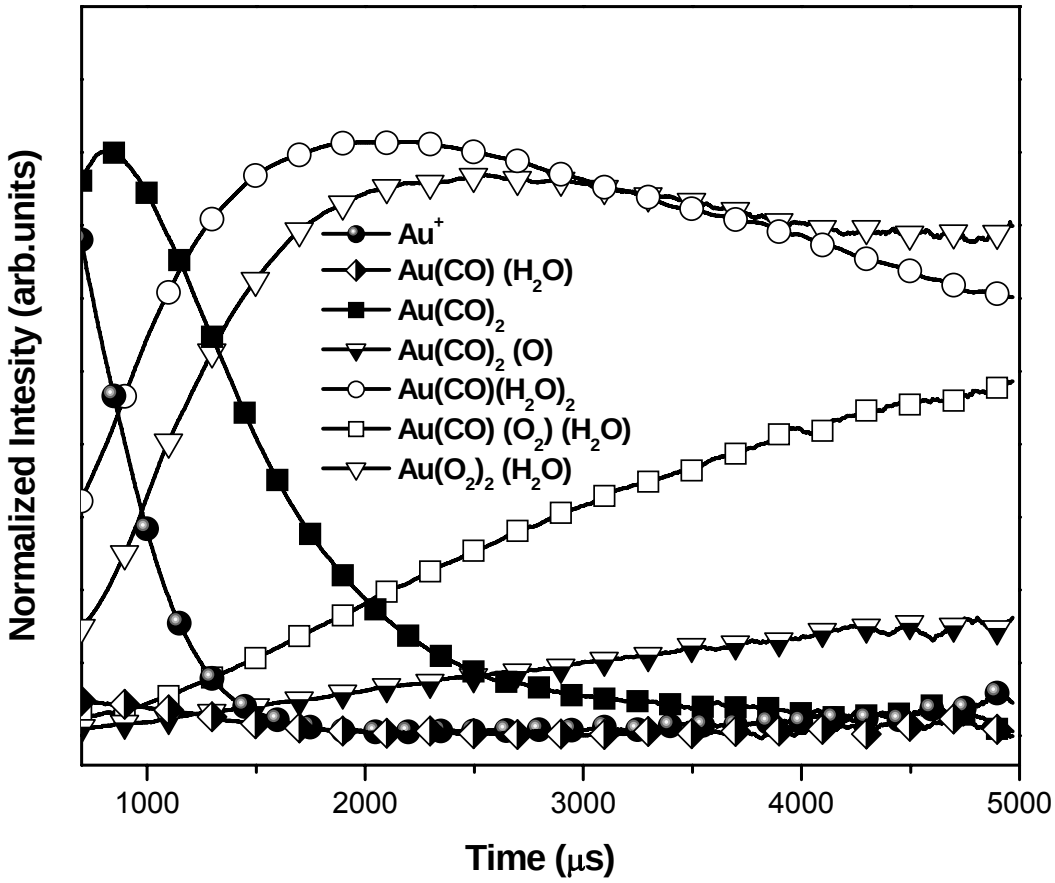

Figure 107: Normalized time profiles of major ions produced following the interaction of Au^+ ions with CO/O_2 mixture in He at 2001 mtorr and 298 K.

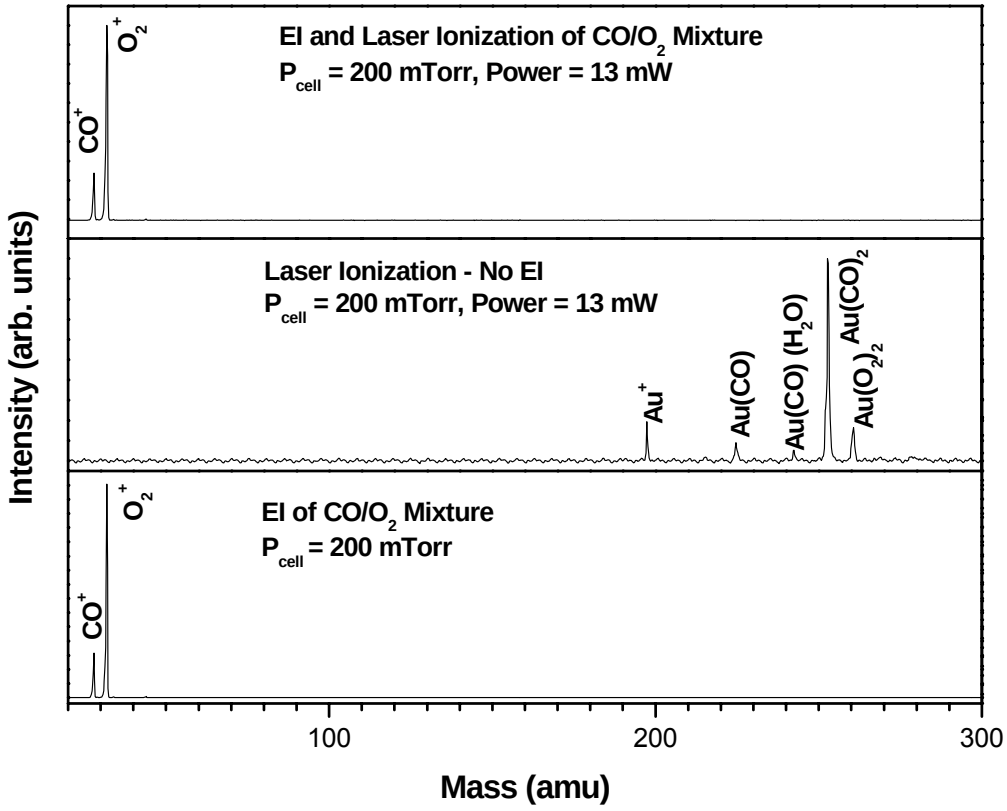

Figure 108: Electron impact ionization, Laser Ionization, and Electron impact with Laser Ionization of CO/O_2 mixture with 200 mTorr at 298 K.

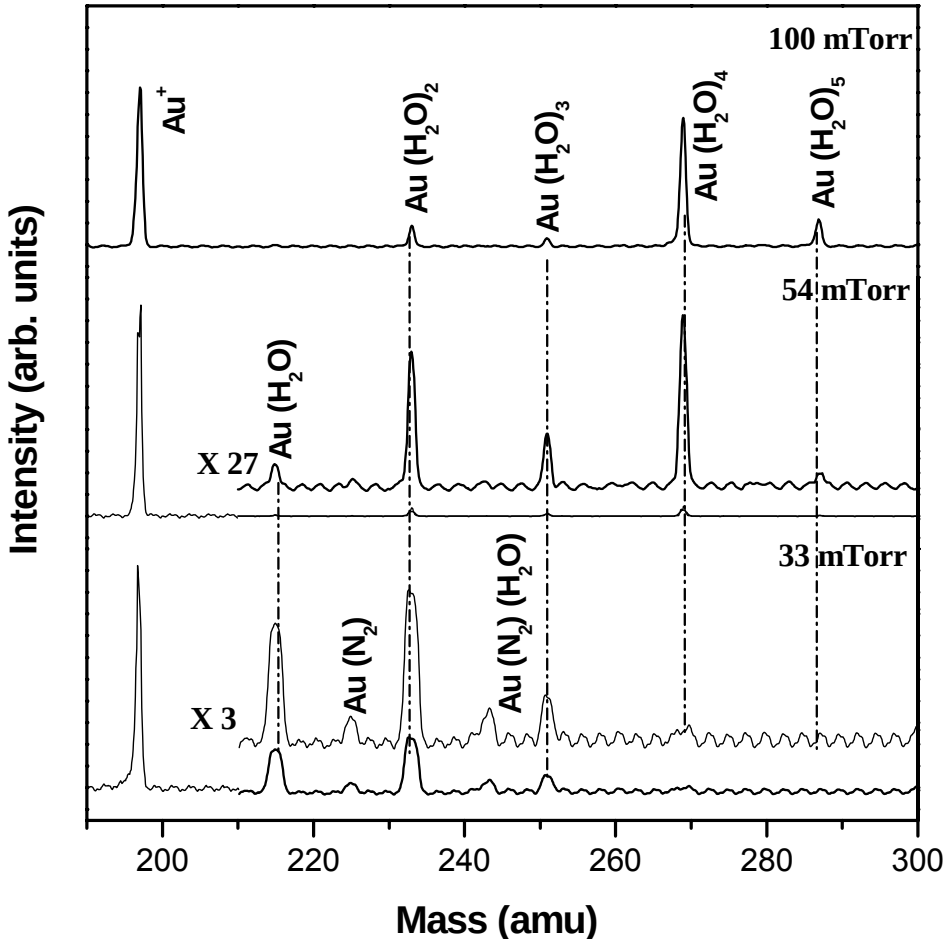

Figure 109: Mass spectrum of Gold (Au^+) ions produced in Pure H_2O at different pressure

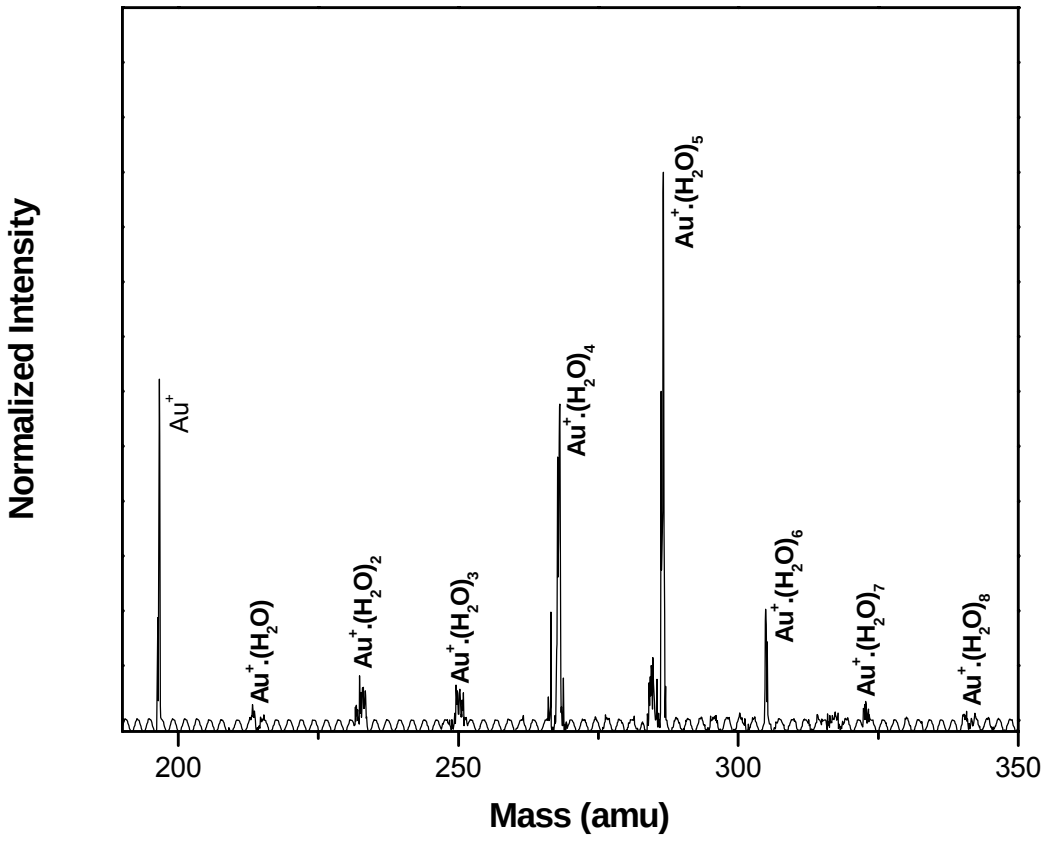

Figure 110: Mass spectrum of Gold (Au^+) ions produced in Pure H_2O at 150 mTorr and 298 K.

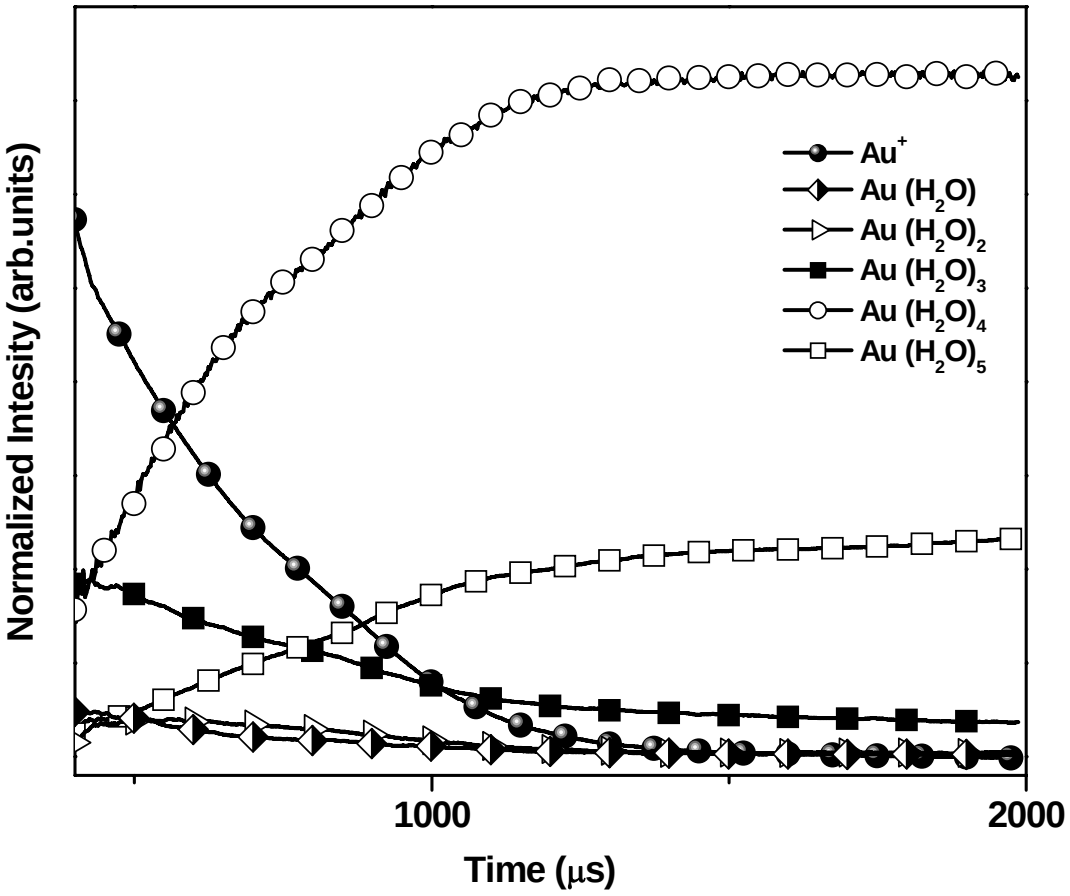

Figure 111: Normalized time profiles of major ions produced following the interaction of Au^+ ions with pure H_2O at 150 mTorr and 298 K.

6.3.1.2 Gas phase reactions of Au^+ with butadiene and isoprene

Gas phase reactions of Au^+ with butadiene

The gas phase reaction of Au^+ with butadiene results in the addition of butadiene molecules to the gold ion. As the pressure increases, these species start to disappear and a hydrocarbon chain are formed where the length of this chain increases as the pressure increases, as shown in Figure 112. To investigate these results further, the reaction of Au^+ with different concentration (1, 5, and 10 %) of butadiene at 50 mTorr cell pressure was studied. Figure 113 shows mass scans as a function of butadiene concentrations. As the concentration increases, the hydrocarbons chain increases. Additions of up to C_{24} were observed. The length of hydrocarbons is equivalent to 6 butadiene molecules, which is an indication of the early stages of butadiene polymerization. Au^+ ions react with butadiene and form a complex of Au^+ with butadiene which acts as a precursor to form a butadiene polymer. Au^+ acts as an initiator, or a catalyst, for gas phase polymerization of butadiene.

The proposed scheme for this reaction can be summarized by the following reactions: At a low pressure and concentration of butadiene, the reaction of the Au^+ with butadiene is dominated by adduct formation. Since adduct will be stabilized by releasing excess energy through collision with buffer gas.

There are different channels for this reaction to occur. The first channel involves the addition of C_4H_6 to Au^+ where $[Au^+(C_4H_6)]^*$ dissociates to $Au^+(C_4H_6)$ which reacts with C_4H_6 to form $Au^+(C_4H_6)_2$, as shown in equations (6.13) and (6.14).

At a high pressure and higher concentration of butadiene, the excited complex, $[Au^+(C_4H_6)]^*$, dissociates instead of being stabilized to adduct $Au^+(C_4H_6)$.

$$Au^+ + C_4H_6 \rightleftharpoons [Au^+(C_4H_6)]^* \longrightarrow Au^+(C_4H_6) \quad (6.13)$$

$$Au^+(C_4H_6) + C_4H_6 \rightleftharpoons Au^+(C_4H_6)_2 \quad (6.14)$$

The dissociation gives the hydrocarbon fragments that can be seen at higher pressures and concentrations of butadiene. The formation of these fragments can also be coming from the reaction of fast electrons (from plasma) with butadiene molecules which result in the ionization of butadiene to produce $C_4H_6^+$ ion.

Since the ionization potential of butadiene (9.07 eV) is less than the ionization potential of Au (9.22 eV), there is a possibility for direct charge transfer from Au to the butadiene molecules to produce $C_4H_6^+$. The presence of fast electrons associated with plasma ionizes isoprene molecules to produce $C_4H_6^+$. The reaction of the $C_4H_6^+$ ion with butadiene molecules to produce $[C_4H_6^+(C_4H_6)]^*$ excited complex as shown in equation (6.15). $[C_4H_6^+(C_4H_6)]^*$ dissociates instead of being stabilized to adduct $C_4H_6^+(C_4H_6)$. This dissociation gives the hydrocarbon fragments that can be seen in the electron impact of C_4H_6. These hydrocarbon fragments react with C_4H_6 molecules to produce higher hydrocarbon fragments via addition and elimination of H, CH_3, C_3H_3, and C_4H_5, as shown in equations (6.16) and (6.17).

$$C_4H_6^+ + C_4H_6 \rightleftharpoons [C_4H_6^+(C_4H_6)]^* \tag{6.15}$$

$$[C_4H_6^+(C_4H_6)]^* \begin{cases} \longrightarrow C_3H_3^+ + CH_3 \\ \longrightarrow C_4H_5^+ + H \\ \longrightarrow C_5H_7^+ + C_3H_3 \\ \longrightarrow C_4H_7^+ + C_4H_5 \end{cases} \tag{6.16}$$

$$\begin{aligned}
&C_4H_6^+ \xrightarrow{C_4H_6} C_8H_{12}^+ \xrightarrow{C_4H_6} C_{12}H_{18}^+ \xrightarrow{C_4H_6} C_{16}H_{24}^+ \xrightarrow{C_4H_6} C_{20}H_{30}^+ \\
&C_4H_7^+ \xrightarrow{C_4H_6} C_8H_{13}^+ \\
&C_5H_7^+ \xrightarrow{C_4H_6} C_9H_{13}^+ \xrightarrow{C_4H_6} C_{13}H_{18}^+ + H \xrightarrow{C_4H_6} C_{17}H_{24}^+ \xrightarrow{C_4H_6} C_{21}H_{30}^+ \\
&C_4H_5^+ \xrightarrow{C_4H_6} C_6H_9^+ + C_2H_2 \xrightarrow{C_4H_6} C_{10}H_{14}^+ + H \xrightarrow{C_4H_6} C_{14}H_{20}^+ \xrightarrow{C_4H_6} C_{18}H_{26}^+ \\
&C_3H_3^+ \xrightarrow{C_4H_6} C_7H_9^+ \xrightarrow{C_4H_6} C_{11}H_{15}^+ \xrightarrow{C_4H_6} C_{11}H_{13}^+ + H_2
\end{aligned} \tag{6.17}$$

Gas phase reactions of Au^+ with isoprene

The gas phase interaction of Au^+ with isoprene shows a different behavior than Au^+ with butadiene, as shown in Figure 114. The interaction Au^+ with isoprene results in the addition of isoprene molecules to the gold ion and the formation of Au^+ isoprene complexes and two isoprene units simultaneously. However, at high pressure, the Au^+ (C_5H_8) complex disappears while Au^+ $(C_5H_8)_2$ remains and a hydrocarbon chain is formed, where the length of this chain increases as the pressure increases. At 500 mTorr, addition up to C_{15} was observed. This length of hydrocarbons is the equivalent of 3 isoprene molecules, which is an indication of the early stages of isoprene polymerization.

The proposed reaction mechanism can be explained as follows: At a low pressure of the isoprene/He mixture, the reaction of the Au^+ with butadiene is dominated by adduct

formation. These adducts will be stabilized by releasing excess energy through collisions with He.

There are different channels for Au^+ with C_5H_8 reaction to occur. The first channel involves the addition of C_5H_8 to Au^+ where $[Au^+(C_5H_8)]^*$ dissociates to $Au^+(C_5H_8)$ as shown in equation (6.18). However, at high pressures of isoprene, the excited complex, $[Au^+(C_5H_8)]^*$, dissociates instead of being stabilized to adduct $Au^+(C_5H_8)$ which reacts with C_5H_8 to form which reacts with C_5H_8 to form $Au^+(C_5H_8)_n$, n=1-2 clusters as shown equation (6.19).

$$Au^+ + C_5H_8 \rightleftharpoons [Au^+(C_5H_8)]^* \longrightarrow Au^+(C_5H_8) \tag{6.18}$$

$$Au^+(C_5H_6) + C_5H_8 \rightleftharpoons Au^+(C_5H_8)_2 \tag{6.19}$$

Since the ionization potential of isoprene (8.86 eV) is less than the ionization potential of Au (9.22 eV), there is a possibility of direct charge transfer from Au to the isoprene which results in the formation of $C_5H_8^+$. The $C_5H_8^+$is also can be formed as a result of the presence of fast electrons associated with plasma ionizes isoprene molecules to produce $C_5H_8^+$ which reacts with isoprene molecules to produce $[C_5H_8^+(C_5H_8)]^*$ excited complex as indicated in equation (6.20).

This excited complex disassociates at high pressures to produce hydrocarbons fragments which are similar to fragments of isoprene ion-molecule products that are observed in electron impact ionization, as shown in equation (6.21). Several channels for this reaction can be distinguished. The first channel involves the reaction of the $C_5H_8^+$ and $C_{10}H_{16}^+$ with isoprene neutral molecules and the elimination of H as shown in equation

(6.22). Second channel is the condensation channel, where isoprene molecules are added to the hydrocarbon fragments to produce higher fragments as shown in equation (6.23).

$$C_5H_8^+ + C_5H_8 \rightleftharpoons [C_5H_8^+(C_5H_8)]^* \tag{6.20}$$

$$\begin{aligned} &C_5H_8^+ \xrightarrow{C_5H_8} C_4H_5^+ + CH_3 \xrightarrow{C_5H_8} C_3H_3^+ + CH_3 \\ &C_5H_8^+ \xrightarrow{C_5H_8} C_6H_9^+ + C_5H_7 \xrightarrow{C_5H_8} C_7H_{10}^+ + C_3H_6 \\ &\xrightarrow{C_5H_8} C_7H_{10}^+ + C_2H_5 \xrightarrow{C_5H_8} C_9H_{13}^+ + CH_3 \end{aligned} \tag{6.21}$$

$$\begin{aligned} C_5H_8^+ &\xrightarrow{C_5H_8} C_5H_7^+ + H \\ C_{10}H_{16}^+ &\xrightarrow{C_5H_8} C_{10}H_{15}^+ + H \end{aligned} \tag{6.22}$$

$$\begin{aligned} &C_5H_8^+ \xrightarrow{C_5H_8} C_{10}H_{16}^+ \xrightarrow{C_5H_8} C_{15}H_{24}^+ \\ &C_6H_9^+ \xrightarrow{C_5H_8} C_{11}H_{17}^+ \\ &C_7H_{10}^+ \xrightarrow{C_5H_8} C_{12}H_{18}^+ \\ &C_8H_{11}^+ \xrightarrow{C_5H_8} C_{13}H_{19}^+ \end{aligned} \tag{6.23}$$

When comparing the gas phase interaction of Au^+ with butadiene and isoprene, it is clear that butadiene polymerization starts with small hydrocarbon chains and the length of the chain increases, as the pressure increases while in the case of isoprene the polymerization starts with one unit of isoprene and at high pressures fragments of hydrocarbons starts to appear. Au^+ and butadiene complexes disappears totally at high pressures, which results in an increase in the hydrocarbon chain length to form up to 6 butadiene units while in the case of isoprene, Au^+ and isoprene complexes remain and the hydrocarbon chain length increases to form up to 3 isoprene units. These results suggest

that the butadiene polymerization is faster than the isoprene polymerization due to a larger number of C-H bonds in the isoprene molecules.

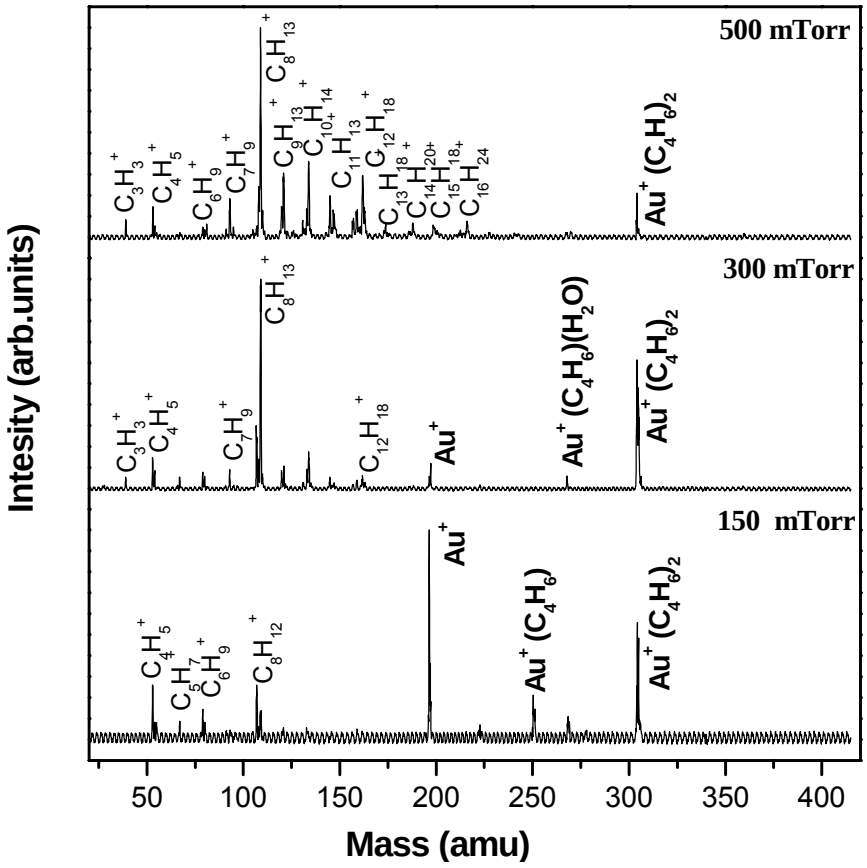

Figure 112: Mass spectrum of Gold (Au^+) ions produced in 1% butadiene in He at different pressures and at 298 K.

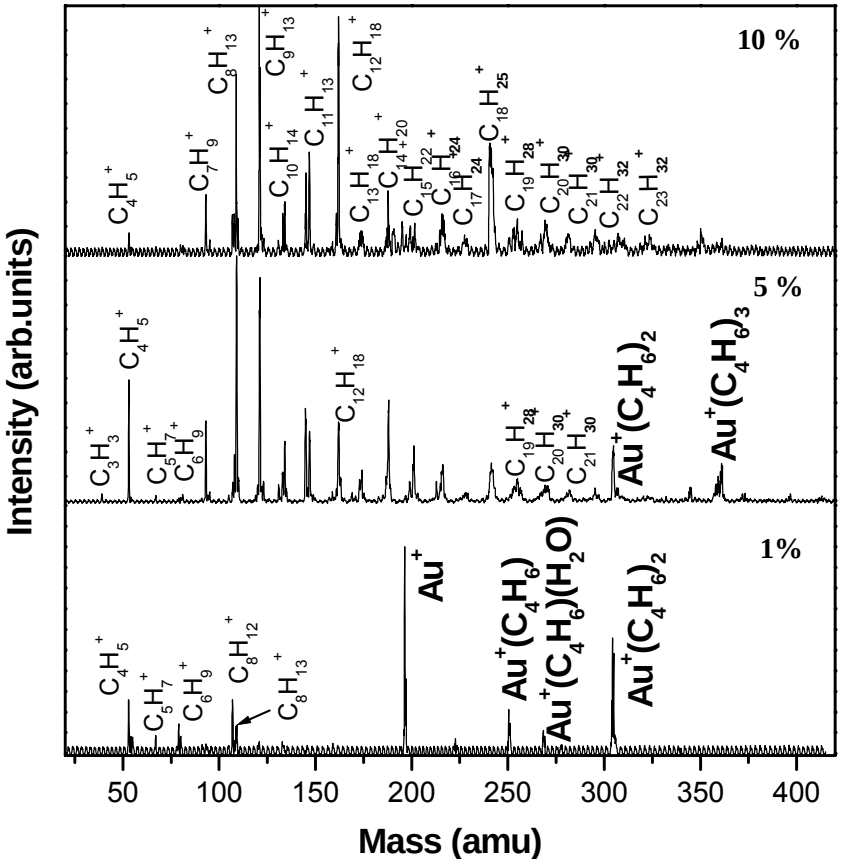

Figure 113: Mass spectrum of Gold (Au^+) ions produced in 1, 5, 10 % butadiene in He at 150 mTorr and 298 K.

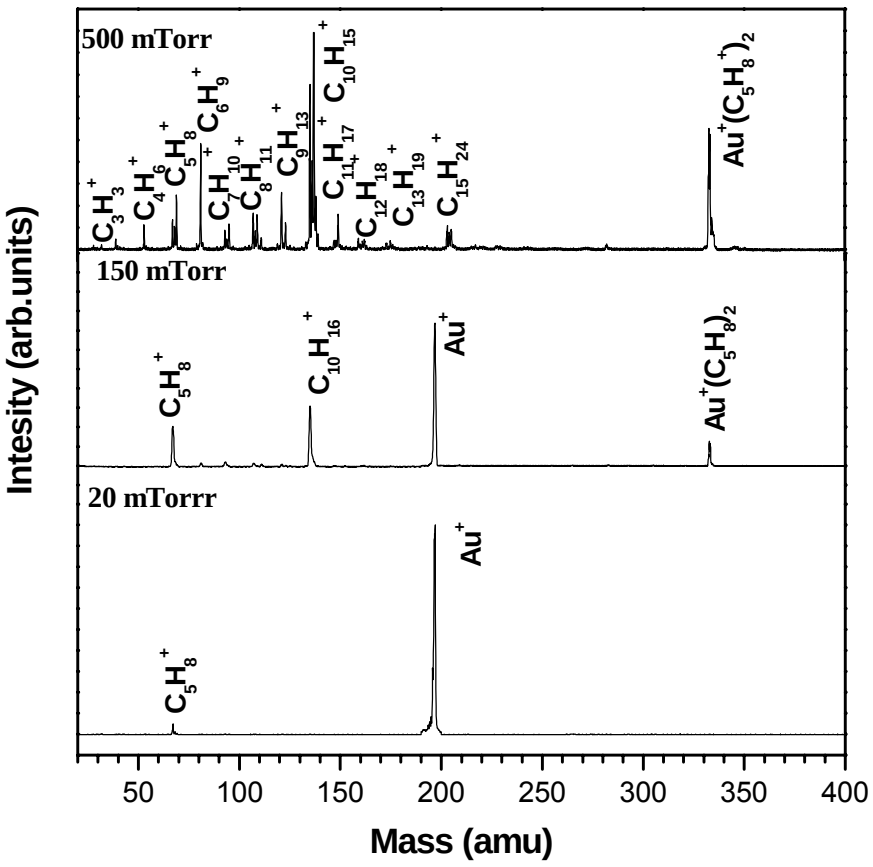

Figure 114: Mass spectrum of Gold (Au^+) ions produced in 5% butadiene in He at different pressures and at 298 K.

6.3.2 Gas phase reactions of Cu^+ with small molecules

Unlike Au, Cu has two isotopes. One isotope has a mass of 63 amu with high abundance and the second isotope has a mass of 65 amu. In the gas phase reaction of Cu^+ with small molecules, these molecules addition to both isotopes is expected.

6.3.2.1 Gas phase reactions of Cu^+ with CO, O_2, and their mixtures

Gas phase reactions of Cu^+ with CO

Gas phase reactions of Cu^+ with CO at low pressures and 298 K result in the addition of CO molecules to the copper ions, and the formation of Cu^+ (CO), and the addition of O_2 to form Cu^+ (O_2) and Cu^+ $(O_2)_2$ complexes. At moderate pressures, CO starts adding to form Cu^+ (CO) and Cu^+ $(CO)_2$ complexes. On the other hand, H_2O starts adding to Cu^+ (CO) and Cu^+ $(CO)_2$ to form Cu^+ (CO)(H_2O), Cu^+ $(CO)_2$(H_2O), and Cu^+ $(CO)_2$($H_2O)_2$ complexes. However, at high pressures, these complexes disappear and only Cu^+ $(CO)_n$ with n = 1-4 are observed as shown in Figure 115. The addition of H_2O and O_2 at low pressures is due to the presence of impurities in the CO tank as mentioned earlier.

The proposed reaction scheme for Cu^+ with CO is summarized as follow:

At low pressure of pure CO, the reaction of the Cu^+ with CO is dominated by adduct formation, where Cu^+ reacts with pure CO to form $[Cu^+ (CO)]^*$ excited complex, which is stabilized by collisions with CO to form Cu^+ (CO), as shown in equation (6.24).

If no stabilization occurs, Cu^+ (CO) either vanishes or stabilizes by further collisions with CO.

At high pressure, $[Au^+ (CO)]^*$ stabilizes by the reaction with CO to form $Cu^+ (CO)_n$, n=1-4 as shown in equation (6.25).

$$Cu^+ + CO \rightleftharpoons [Cu^+(CO)]^* \longrightarrow Cu^+(CO) \quad (6.24)$$

$$Cu^+(CO) + CO \rightleftharpoons Cu^+(CO)_2 \overset{CO}{\rightleftharpoons} Cu^+(CO)_3 \overset{CO}{\rightleftharpoons} Cu^+(CO)_4 \quad (6.25)$$

Gas phase reactions of Cu^+ with O_2

O_2 reaction of Cu^+ ions results on the formation of $Cu^+ (O_2)_2$, $Cu^+ (N_2)$, and $Cu^+ (H_2O)$ at low pressures. As the pressure increases, $Cu^+ (O_2)$ disappears and $Cu^+ (O)$ is formed. Also, H_2O and N_2 is added to $Cu^+ (H_2O)$ and $Cu^+ (N_2)$ to form $Cu^+ (H_2O)_2$, and $Cu^+ (N_2)_2$, as shown in Figure 116.

The reaction scheme of Cu^+ with pure O_2 is different than that of Au^+ with O_2, where in the case of Au^+; H_2O replaces O_2 at high pressure. Cu^+ reacts with O_2 to form the excited complex $[Cu^+(O_2)]^*$ which dissociate to form $Cu^+ (O_2)$ as shown in equation (6.26). $Cu^+ (O_2)$ stabilizes by further collision with O_2, were $Cu^+ (O_2)$ dissociates to form $Cu^+(O)$ and O, as shown in equation (6.27).

$$Cu^+ + O_2 \rightleftharpoons [Cu^+(O_2)]^* \longrightarrow Cu^+(O_2) \quad (6.26)$$

$$Cu^+(O_2) + O_2 \rightleftharpoons Cu^+(O) + O \quad (6.27)$$

Gas phase reactions of Cu^+ with CO/O_2

After the gas phase reaction of Cu^+ with the individual components (i.e. CO and O_2) were studied, the reaction of Cu^+ with CO/O_2 mixture in He at 298 K could be studied.

Figure 117 shows the reaction products after Cu^+ interacts with the CO/O_2 mixture in He. At a low pressures, both atomic oxygen and molecular oxygen are added to Cu^+ to form Cu^+ (O) and Cu^+ $(O)_2$. Also, CO is added to Cu^+ $(O)_2$ to form Cu^+ $(O)_2(CO)$. As the pressure increases, Cu^+ (O), Cu^+ $(O)_2$, Cu^+ $(O)_2(CO)$, and CO is added to Cu^+ to form Cu^+ (CO), Cu^+ $(CO)_2$, and Cu^+ $(CO)_3$. Furthermore, H_2O is added to Cu^+ to form Cu^+ (H_2O) and to Cu^+ (CO), Cu^+ $(CO)_2$, and Cu^+ $(CO)_3$ to form Cu^+ (CO) $(H_2O)_2$, Cu^+ (CO) $(H_2O)_3$, Cu^+ $(CO)_2$ (H_2O), Cu^+ $(CO)_2$ $(H_2O)_2$, and Cu^+ $(CO)_3$ (H_2O). At high pressure, Cu^+ (CO) $(H_2O)_2$, Cu^+ (CO) $(H_2O)_3$ are observed with high intensities.

The proposed reaction scheme of Cu^+ with CO/O_2 mixture in He at 298 K is can be explained based on the mass spectrum as follows: At low pressures, Cu^+ reacts with CO/O_2 mixture to form $[Cu^+(CO/O_2)]^*$, which is stabilized by the collisions with CO/O_2 mixture and He. As result, $[Cu^+(CO/O_2)]^*$ dissociates to form $Cu^+(O)$, $Cu^+(O_2)$, and $Cu^+(CO)$, as shown in equation (6.28).

At high pressures, these products react with CO/O_2 mixture which result in the formation of $Cu^+(CO)_3$ (6.30) and impurities that present in the cell to form products as shown in equations(6.30-6.33) .

$$Cu^+ + CO/O_2 \rightleftharpoons [Cu^+(CO/O_2)]^* \begin{cases} \longrightarrow Cu^+(CO) \\ \longrightarrow Cu^+(O) \\ \longrightarrow Cu^+(O_2) \end{cases} \quad (6.28)$$

$$Cu^+(CO) + CO \rightleftharpoons Cu^+(CO)_2 \overset{CO}{\rightleftharpoons} Cu^+(CO)_3 \quad (6.29)$$

$$Cu^+(CO) + O_2 \rightleftharpoons Cu^+(CO)(O_2) \quad (6.30)$$

$$Cu^+(CO)_2 + H_2O \rightleftharpoons Cu^+(CO)_2(H_2O) \overset{H_2O}{\rightleftharpoons} Cu^+(CO)_2(H_2O)_2 \quad (6.31)$$

$$Cu^+(CO)_2(H_2O) + CO \rightleftharpoons Cu^+(CO)_3(H_2O) \quad (6.32)$$

$$Cu^+(CO) + H_2O \rightleftharpoons Cu^+(CO)(H_2O) \overset{H_2O}{\rightleftharpoons} Cu^+(CO)(H_2O)_2 \overset{H_2O}{\rightleftharpoons} Cu^+(CO)(H_2O)_3 \quad (6.33)$$

6.3.2.2 Gas phase reactions of Cu^+ with butadiene and isoprene

Gas phase reactions of Cu^+ with butadiene

As mentioned in the previous sections, the gas phase reaction of Au^+ with butadiene and isoprene result in the addition of butadiene and isoprene molecules to the Au^+. As the pressure increases, these species start to disappear and a hydrocarbon chain are formed where the length of this chain increases. These results indicate that Au^+ acts like an initiator for the early stages of polymerization of these molecules.

The same behavior is observed for the gas phase reactions of Cu^+ with butadiene and isoprene. Figure 118 shows the mass spectra of the gas phase reaction of Cu^+ with 1 % butadiene at 298 K as a function of pressures. At low pressure, Cu^+ reacts with butadiene to form Cu^+ (C_4H_6), Cu^+ $(C_4H_6)_2$, and Cu^+ (C_4H_6) (H_2O) complex which results from the

presence of small impurities of H_2O, which is typical in any vacuum system. Also, $C_2H_3^+$ hydrocarbon is observed. However, at high pressure $Cu^+ (C_4H_6)_2$, and $Cu^+ (C_4H_6) (H_2O)$ disappear, while $Cu^+ (C_4H_6)_2$ along with a long chain (up to C_{11}) of hydrocarbons are observed.

The proposed scheme for this reaction can be summarized as follows: At low pressures of butadiene, the reaction of the Cu^+ with butadiene is dominated by $[Cu^+ (C_4H_6)]^*$ adduct formation. Since adduct will be stabilized by releasing excess energy through collisions with He. There different channels for this reaction to occur. First channel involves the addition of C_4H_6 to Cu^+ at low pressures, where $[Cu^+(C_4H_6)]^*$ dissociates to $Cu^+ (C_4H_6)$, which reacts with C_4H_6 to form $Cu^+(C_4H_6)_2$, as shown in equation (6.34). However, at high pressures and concentrations, the $[Cu^+(C_4H_6)]^*$, dissociates instead of being stabilized to adduct $Cu^+.(C_4H_6)$.

Since the ionization potential of the butadiene (9.07 eV), which is less than that of Cu (7.8 eV), there is no possibility for direct charge transfer from Cu to the butadiene molecules to produce $C_4H_6^+$. The presence of fast electrons associated with plasma could be responsible for ionizing the isoprene molecules to produce the $C_4H_6^+$. The $C_4H_6^+$ reacts with C_4H_6 molecules to produce $[C_4H_6^+(C_4H_6)]^*$ excited complex, as shown in equation (6.35). This complex dissociates instead of being stabilized to adduct $C_4H_6^+(C_4H_6)$.as a result, hydrocarbon fragments are formed as result of the addition of $C_4H_6^+$. Addition of C_4H_6 and elimination of H, CH_2, C_3 H_3 and C_4H_5 can produce higher hydrocarbons fragments, as shown in equations (6.35-6.38).

$$Cu^{+} + C_4H_6 \rightleftharpoons [Cu^{+}(C_4H_6)]^{*} \longrightarrow Cu^{+}(C_4H_6) \tag{6.34}$$

$$Cu^{+}(C_4H_6) + C_4H_6 \rightleftharpoons Cu^{+}(C_8H_{12}) \overset{C_4H_6}{\rightleftharpoons} Cu^{+}(C_{12}H_{18}) \tag{6.35}$$

$$\begin{aligned} &C_4H_6^{+} + C_4H_6 \rightleftharpoons C_8H_{12}^{+} \overset{C_4H_6}{\rightleftharpoons} C_{12}H_{18}^{+} \\ &C_4H_6^{+} + C_4H_6 \longrightarrow C_5H_7^{+} + C_3H_5 \xrightarrow{C_4H_6} C_9H_{13}^{+} \\ &C_3H_3 + C_4H_6 \longrightarrow C_7H_9^{+} \longrightarrow C_{11}H_{15}^{+} \end{aligned} \tag{6.36}$$

$$\begin{aligned} &C_4H_6^{+} \xrightarrow{C_4H_6} C_6H_9^{+} \xrightarrow{C_4H_6} C_{10}H_{14}^{+} + H \\ &\text{or} \qquad C_6H_9^{+} \xrightarrow{C_4H_6} C_9H_{15}^{+} + CH_2 \end{aligned} \tag{6.37}$$

$$\begin{aligned} &C_4H_6^{+} \xrightarrow{C_4H_6} C_4H_5^{+} + H \\ &C_8H_{12}^{+} \xrightarrow{C_4H_6} C_8H_{13}^{+} + C_4H_5^{+} \end{aligned} \tag{6.38}$$

Gas phase reactions of Cu^{+} with Isoprene

The gas phase reaction of Cu^{+} with isoprene at low pressures result in the addition of isoprene and H_2O to the Cu^{+} ions in a similar fashion as the reaction with butadiene. The formation of Cu^{+} (C_5H_8), Cu^{+} $(C_5H_8)_2$, and Cu^{+} (C_5H_8) (H_2O) at low pressures was observed. As the pressure increases, Cu^{+} (C_5H_8) and Cu^{+} (C_5H_8) (H_2O) disappear while Cu^{+} $(C_5H_8)_2$ remains. Also, a long chain (up to C_{11}) of hydrocarbons is observed, as shown in Figure 119.

The proposed reaction scheme of Cu^{+} with C_5H_8 can be summarized as follow:
At low pressures, Cu^{+} reacts with C_5H_8 to form $[Cu^{+}$ $(C_5H_8)]^{*}$ excited complex. This exited complex stabilizes by collisions with C_5H_8 and He. If no stabilization occur, $[Cu^{+}$ $(C_5H_8)]^{*}$ disassociates to Cu^{+} (C_5H_8) adduct as explained in equation (6.39). At high pressures, Cu^{+} (C_5H_8) reacts with C_5H_8 to form Cu^{+} $(C_5H_8)_2$, as shown in equation (6.40).

Since ionization potential of butadiene (8.86 eV) is less than the ionization potential of Cu (7.8 eV), there is no possibility for direct charge transfer from Cu^+ to the C_5H_8 molecules to produce $C_5H_8^+$. The presence of fast electrons associated with plasma for the C5H8 being ionized. The $C_4H_6^+$ reacts with C_5H_8 to form $[C_5H_8^+(C_5H_8)]^*$ excited complex, as shown in equation (6.41). This complex dissociates at high pressures to produce hydrocarbon fragments, which react with C_5H_8 and by elimination of CH_2 and CH_3 groups to form higher fragments, as expressed in equation (6.42).

$$Cu^+ + C_5H_8 \rightleftharpoons [Cu^+(C_5H_8)]^* \longrightarrow Cu^+(C_5H_8) \tag{6.39}$$

$$Cu^+(C_5H_8) + C_5H_8 \rightleftharpoons Cu^+(C_{10}H_{16})_2 \tag{6.40}$$

$$C_5H_8^+ + (C_5H_8) \rightleftharpoons [C_5H_8^+(C_5H_8)]^* \tag{6.41}$$

$$[C_5H_8^+(C_5H_8)]^* \begin{cases} \longrightarrow C_4H_5^+ + CH_3 \\ \longrightarrow C_3H_3^+ + CH_3 \\ \longrightarrow C_{10}H_{16}^+ \xrightarrow{C_5H_8} C_{15}H_{24}^+ \\ \longrightarrow C_{10}H_{16}^+ \xrightarrow{C_5H_8} C_9H_{13}^+ + CH_3 \\ \qquad\qquad \xrightarrow{C_5H_8} C_8H_{11}^+ + CH_2 \xrightarrow{C_5H_8} C_7H_9^+ + CH_2 \end{cases} \tag{6.42}$$

These results suggest that Cu^+ acts as an initiator for the early stages of gas phase cationic butadiene and isoprene polymerization, as observed for Au^+ with these molecules.

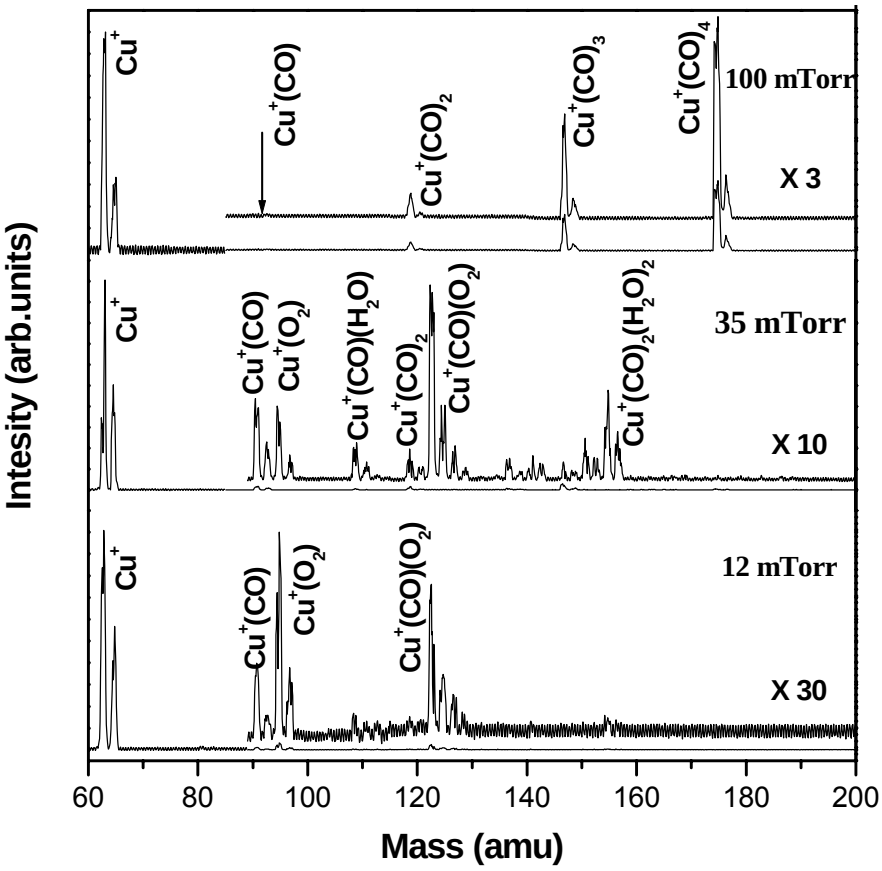

Figure 115: Mass spectrum of copper (Cu^+) ions produced in pure CO at different pressure and at 298 K.

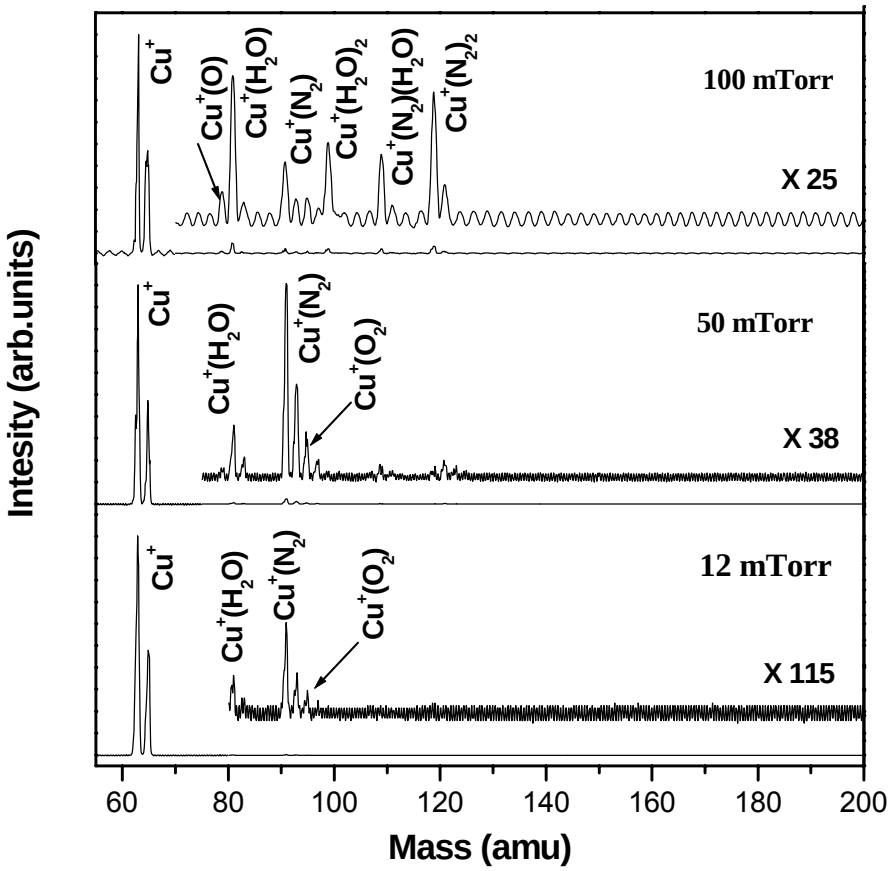

Figure 116: Mass spectrum of copper (Cu^+) ions produced in pure O_2 at different pressures and at 298 K.

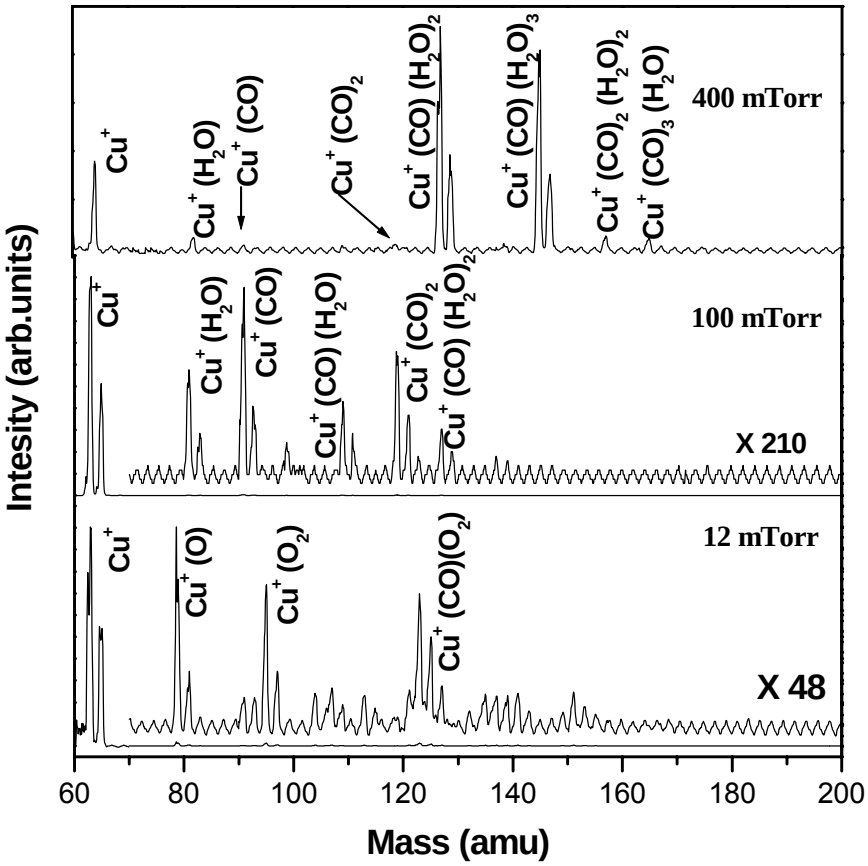

Figure 117: Mass spectrum of copper (Cu^+) ions produced in CO/O_2 mixture in He at different pressures and at 298 K.

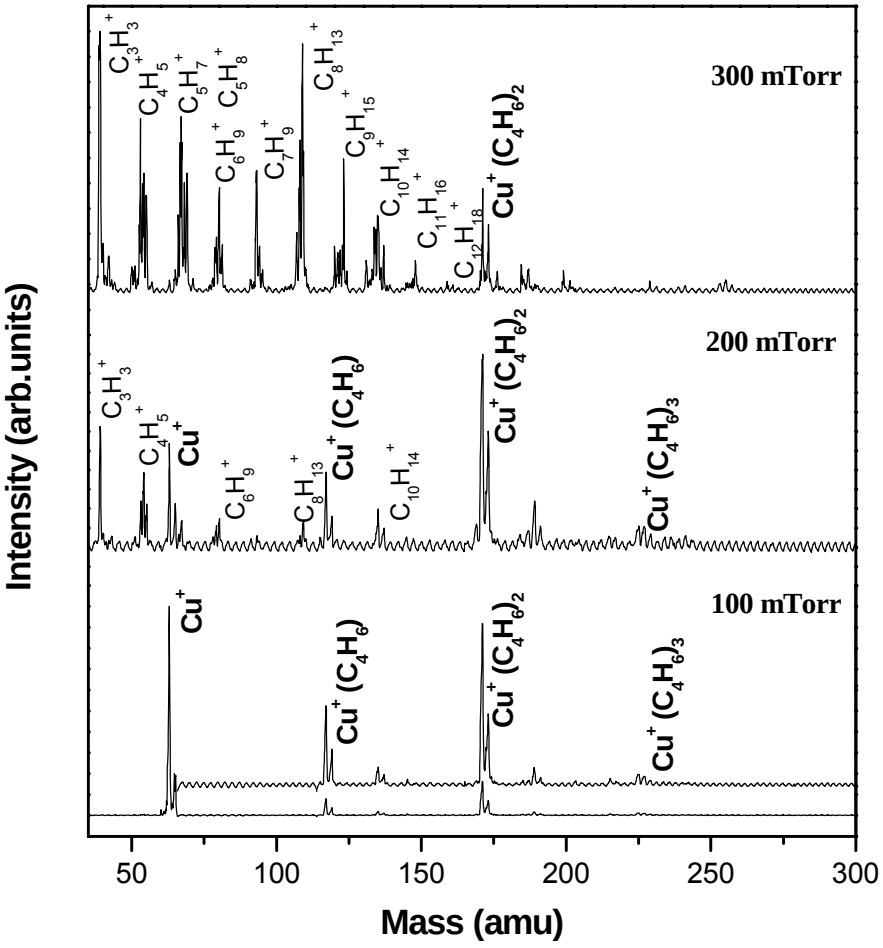

Figure 118: Mass spectrum of copper (Cu^+) ions produced in pure butadiene at different pressures and at 298 K (B = Butadiene).

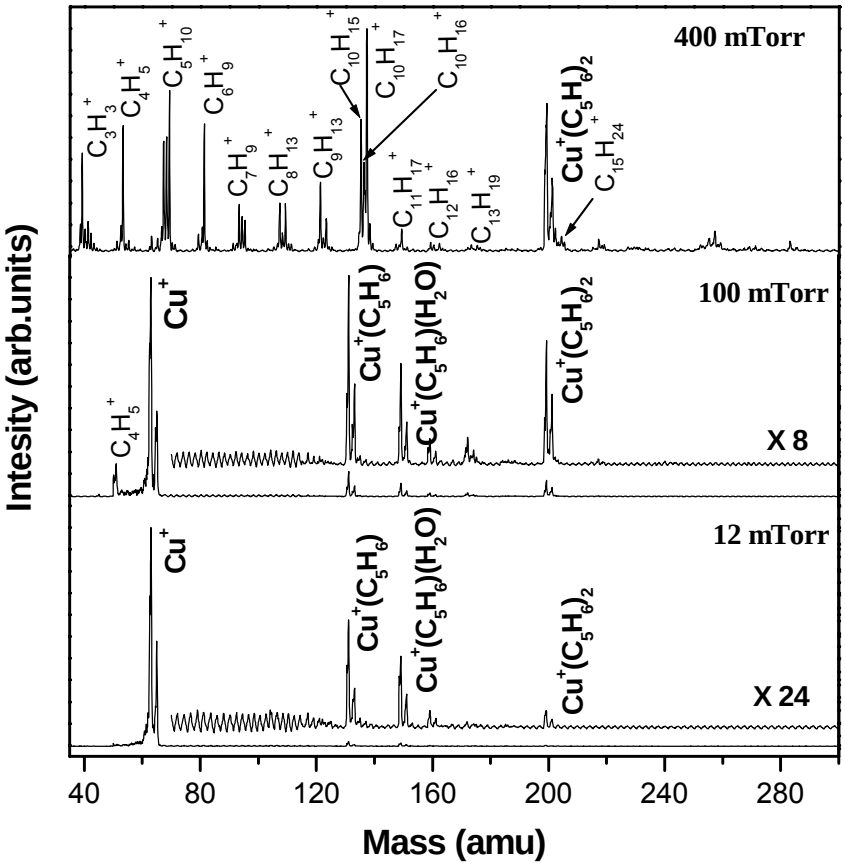

Figure 119: Mass spectrum of copper (Cu^+) ions produced in 1% isoprene at different pressures and at 298 K (I = Isoprene).

7 : Summary and Conclusions

Vapor phase method was used to synthesize supported and unsupported nanoparticle catalysts for CO oxidation. The Laser Vaporization/Controlled Condensation (LVCC) technique combines the features of pulsed laser vaporization and the controlled condensation process from the vapor phase, where vapor phase synthesis yields contamination-free products (as compared to Chemical reductions in solutions), the elimination of chemical precursors and solvents, and in most cases, the production of highly crystalline nanoparticles.

Gold nanoparticles supported on a variety of oxide supports such as CeO_2, TiO_2, CuO and MgO were synthesize using the LVCC method. Au nanoparticles supported on CeO_2 exhibit higher catalytic activity than Au supported on other oxides. Characterizations of these particles confirm that the resulting Au nanoparticles are highly dispersed on the surface of the large support CeO_2 nanoparticles. The high activity of the Au/CeO_2 catalyst is attributed to the strong interaction of Au with CeO_2, where Au can promote the reduction of Ce^{+4} to Ce^{+3} and thus facilitate the charge transfer from Au to Ce, which results in a higher oxidation state of Au and hence increases the oxygen storage capacity of CeO_2. Our results indicate that 5 % Au loading on CeO_2 has higher activity than 2% Au or 10% Au. When comparing the catalytic activity of Au/CeO_2 prepared by physical (LVCC) and chemical (Deposition-precipitation) methods, it was found that the catalytic activity is higher for Au/CeO_2 prepared by Deposition-precipitation method. This was attributed these results to the small particle size and the strong metal-support interaction (SMSI).

The effect of alloying Au and Cu nanoparticles on the catalytic activity for low temperature CO oxidation was also investigated. The first vapor phase synthesis of unsupported bimetallic Au/Cu alloy nanoparticles was demonstrated. The unsupported Au-Cu alloy nanoparticle catalyst exhibits higher catalytic activity than the activities of the individual components and their physical mixtures. Another important finding was obtained from the XRD data taken after the catalysis test which indicates the formation of CuO within the bimetallic nanoparticles. Therefore, the improved conversion efficiencies of these nanoparticles after the catalysis test are attributed to the formation of CuO, which is known to have a higher catalytic activity than Cu for CO oxidation [177,190,191]

The high activity and stability of the nanoparticle catalysts prepared using the LVCC method are remarkable and imply that a variety of efficient catalysts can be designed and tested using this approach. The significance of the current method lies mainly in its simplicity, flexibility, and the control of the different factors that determine the activity of the nanoparticle catalysts. For example, control exerted on the composition of the active metal (Pd, Au, and Cu) and the oxide support (CeO_2, ZrO_2, TiO_2, Al_2O_3, and SiO_2) can be achieved by controlling the compositions of the initial targets. Nonstoichiometric oxide supports can be prepared by using metal powders such as Ce, Zr, Ti, Al, CuO, MgO and Si in the selected targets and carrying out the LVCC process in the presence of varying concentrations of oxygen/helium carrier gas mixtures. Control of the size distribution of the nanoparticle catalysts can be accomplished by controlling the pressure of the carrier gas and the temperature gradients during the LVCC synthesis.

The gas phase reactions of Au^+ and Cu^+ with CO, O_2 and H_2O molecules using the Laser Vaporization ionization, High-Pressure Mass Spectrometry (LVI-HPMS) technique were investigated. The gas phase reactions resulting from the interactions of Au^+ with CO and O_2 molecules were also investigated. Although, multiple additions of CO and O_2 molecules have been observed on Au^+ at room temperature, no evidence was found of the production of CO_2. This is attributed to the presence of water molecules which effectively replace the oxygen molecules on Au^+ at room temperature. The results show, for the first time, that extensive numbers of water molecules (up to 8) can be added on the Au^+ at room temperature. The experimental observation of the unusual stability of the $Au^+(H_2O)_n$ clusters is confirmed by theoretical calculations.

Finally, the role of the metal cations Au^+ and Cu^+ in initiating the gas phase polymerization of butadiene and isoprene vapors was investigated. Under typical experimental conditions the metal ions undergo several thousand collisions with the monomer molecules in the gas phase thus resulting in ion-molecule reactions with product ions that could initiate further reactions leading to polymerization. Gas phase polymerization is important not only for probing the mechanism of the catalytic process and the exact nature of the catalyst-cocatalyst interaction, but also for the elimination of various harmful organic vapors, such as butadiene and isoprene, by converting them into non volatile polymers. The early stages of cationic polymerization of isoprene and butadiene using the metal cations Au^+ and Cu^+ act as initiators is presented.

It is worth noting that the laser vaporization/polymerization method provides the ability to encapsulate several different metals or metal oxides which will undoubtedly play

a significant role in tuning the various properties of the polymer composites. Systematic experimentation on a range of important monomers that can be polymerized by laser plasma mechanisms and matched metal nanoparticles would make available a base of results upon which the properties of future nanocomposite materials could be reliably assessed.

List of References

(1) Swinnerton, J. W., Lamontagne, R. A., Linnenbom, V. J.. *Science* **1971**, *172*, 942-945.

(2) Seiler, W., Jungle, C. E. *J. Geophys. Res.* **1970**, *75*, 2217-2226.

(3) Guenther, A.; Geron, C.; Pierce, T.; Lamb, B.; Harley, P.; Fall, R. *Atmospheric Environment* **2000**, *34*, 2205-2230.

(4) Seinfeld, J. H.; Pandis, S. N. *Atmospheric Chemistry and Physics: From Air Pollution to Climate Change*, 1998.

(5) Organization, W. H. "Carbon Monoxide. Environmental Health Criteria," World Health Organization, 1999.

(6) Varon J, M. P., Fromm RE, Gueler A. :; A Review for Clinicians. *J. Emerg. Med.* **1999**, *17*, 87-93.

(7) Aronow WS, H. C., Isbel MW, Rojaw SN, Imparato, B . *Ann Intern Med* **1972**, *79*, 392-395.

(8) Von Burg, R. *J Applied Toxicol.* **1999**, *19*, 379-386.

(9) McCrea, K. R.; Parker, J. S.; Somorjai, G. A. *Journal of Physical Chemistry B* **2002**, *106*, 10854-10863.

(10) Valden, M.; Lai, X.; Goodman, D. W. *Science (Washington, D. C.)* **1998**, *281*, 1647-1650.

(11) Xu, X.; Goodman, D. W. *Journal of Physical Chemistry* **1993**, *97*, 683-9.

(12) Moser, W. R.; Editor *Advanced Catalysts and Nanostructured Materials: Modern Synthetic Methods*, 1996.

(13) Haruta, M.; Yamada, N.; Kobayashi, T.; Iijima, S. *Journal of Catalysis* **1989**, *115*, 301-9.

(14) Blyholder, G. *J. of Chem. Phys.* **1964**, *68*, 2772.

(15) Doyen, G., Ertl, G. *Surf. Sci.* **1974**, *43*, 197.

(16) Zaki, M. I., Knozinger, H. 2nd Int. Conf. on Chemical Reaction Engineering, New Delhi, 1987; p 19-30.

(17) Zaki, M. I., Hasan, M. A., Pasupulety, L. *App. Catal. A: Gen.* **2000**, *198*, 247-259.

(18) Flytzani-Stephanopoulos, M. *MRS Bulletin* **2001**, 885-889.

(19) Kung, H. H. In *Studies in Surface Science and Catalysis*; Elsevier: Amesterdam, 1989; Vol. 45.

(20) Sinfelt, J. H. *J. Catal.* **1973**, *29*, 308.

(21) Sinfelt, H., Via, G.H., Lytle, F.W. *J. Chem. Phys.* **1980**, *72*, 4832.

(22) Howitt, C., Pitchon, V., and Maire, G. *J. Catal.* **1995**, *154*, 47.

(23) Kortshagen, U. R., Bhandarkar,U. V., Swihart, M. T., Girshick, S. L. *Pure Appl. Chem.* **1999**, *71*, 1871.

(24) Sun, C. B., Murray, D., Weller, L., Folks, Moser, A. *Science* **1989**, *287*, 2000.

(25) Chandrasekharan, N., Kamat, P. V. *Nano Letters* **2001**, *1*, 67.

(26) El-Shall, M. S. L., S., , , . *Adv. Metal and Semiconductor Clusters* **1998**, *4*, 115.

(27) Edelstein, A. S. C., R. C.; Editors , . *Nanomaterials: Synthesis, Properties, and Applications*, 1996.

(28) Somorjai, G. A. *Pure & Appl. Chem.* **1978**, *50*, 963-969.

(29) Li, S. S., S. J.; El-Shall, M. S. *Journal of Physical Chemistry B* **1997**, *101*, 1794.

(30) Li, S. G., I. N.; El-Shall, M. S. *Journal of Physical Chemistry B* **1998**, *102*, 7319.

(31) Kruis F. E, F., H., Peled, A. *J. Aerosol Sci.* **1998**, *29*, 511-35.

(32) El-Shall, M. S.; Slack, W.; Vann, W.; Kane, D.; Hanley, D. *Journal of Physical Chemistry* **1994**, *98*, 3067-70.

(33) El-Shall, M. S.; Li, S.; Graiver, D.; Pernisz, U. *ACS Symposium Series* **1996**, *622*, 79-99.

(34) Li, S.; Silvers, S. J.; El-Shall, M. S. *Journal of Physical Chemistry B* **1997**, *101*, 1794-1802.

(35) Pithawalla, Y. B.; El-Shall, M. S.; Deevi, S. C.; Stroem, V.; Rao, K. V. *Journal of Physical Chemistry B* **2001**, *105*, 2085-2090.

(36) El-Shall, M. S.; Abdelsayed, V.; Pithawalla, Y. B.; Alsharaeh, E.; Deevi, S. C. *Journal of Physical Chemistry B* **2003**, *107*, 2882-2886.

(37) Abdelsayed, V.; Saoud, K. M.; El-Shall, M. S. *J. Nanoparticle Research* **in press (2005)**.

(38) Yang, Y.; Saoud, K. M.; Abdelsayed, V.; Glaspell, G.; Deevi, S.; El-Shall, M. S. *J. Phys. Chem. B* **Submitted (2005)**.

(39) Li, s., Germanenko, I. N., El-Shall, M. S. *J. of Cluster Science* **1999**, *10*, 4.

(40) Hahn H. *Mater* **1997**, *9*, 3 -12.

(41) Iizuka, Y., Tode,T., Takao,T., Yatsu, K., Takeuchi,T., Tsubota, S., Haruta, M. *J.Catal* **1999**, *187*, 50.

(42) Bond, G. C.; Thompson, D. T. *Catalysis Reviews - Science and Engineering* **1999**, *41*, 319-388.

(43) Bond, G. C. *Catal. Today* **2002**, *72*, 5.

(44) Burke, L. D.; Buckley, D. T.; Morrissey, J. A. *Analyst (Cambridge, United Kingdom)* **1994**, *119*, 841-5.

(45) Burke, L. D.; Nugent, P. F. *Gold Bulletin (London)* **1997**, *30*, 43-53.

(46) Haruta, M. *J. Catal* **1989**, *115*, 301.

(47) Haruta, M.; Tsubota, S.; Kobayashi, T.; Ueda, A.; Sakurai, H.; Ando, M. *Studies in Surface Science and Catalysis* **1993**, *75*, 2657-60.

(48) Haruta, M. *Chemical record (New York, N.Y.) FIELD Publication Date:2003*, *3*, 75-87.

(49) Haruta, M. *Cattech* **2002**, *6*, 102-115.

(50) Haruta, M.; Date, M. *Applied Catalysis, A: General* **2001**, *222*, 427-437.

(51) Soares, J. M. C., Morrall, et al. *Jornal of Catalysis* **2003**, *219*, 17-24.

(52) Valden, M., Lai, X. and Goodman, D.W. *Science* **1998**, *281*, 1647-1650.

(53) Bond, G. C. *Catalysis Today* **2002**, *72*, 5-9.

(54) Bond, G. C. *Gold Bulletin (Geneva)* **1972**, *5*, 11-13.

(55) Huber, H.; McIntosh, D.; Ozin, G. A. *Inorganic Chemistry* **1977**, *16*, 975-9.

(56) McIntosh, D.; Ozin, G. A. *Journal of Organometallic Chemistry* **1976**, *121*, 127-36.

(57) Hatching, J. G. *Catalysis Today* **2002**, *72*, 11-17.

(58) Haruta, M. *Chem. Record,* **2003**, *75*, 3.

(59) Haruta, M., Sano, H. *Studies in Surface Science and Catalysis* **1982**, *16*, 225.

(60) Jaksic, M. M. *Solid State Ionics* **2000**, *136-137*, 733-746.

(61) Jaksic, M. M. *Electrochimica Acta* **2000**, *45*, 4085-4099.

(62) Jaksic, M. M. *Hemijska Industrija* **1999**, *53*, 441-453.

(63) Haruta, M. *Journal of New Materials for Electrochemical Systems* **2004**, *7*, 163-172.

(64) Goodman, D. W., Choudary, T. V. *Top. Catal.* **2002**, *21*, 25.

(65) Haruta, M. *J. New Mat. for Elechem. systems.* **2004**, *7*, 163-172.

(66) Guczi, L.; Horvath, D.; Paszti, Z.; Peto, G. *Catalysis Today* **2002**, *72*, 101-105.

(67) Maciejewski, M.; Fabrizioli, P.; Grunwaldt, J.-D.; Sven Becker, O.; Baiker, A. *Physical Chemistry Chemical Physics* **2001**, *3*, 3846-3855.

(68) Castro, T., Reifenberger, R., Choi, E., Andrew, R. P. *Phys. Rev. B* **1990**, *13*, 8548.

(69) Park, E. D.; Lee, J. S. *Journal of Catalysis* **1999**, *186*, 1-11.

(70) Pantelouris, A., Kuper, G., Hormes, J., Feldmann, C., and Jansen, M. *J. Am. Chem. Soc.* **1995**, *117*, 749.

(71) Bassi, I. W., Lytle, F. W., and Parravano, G. *J. Phys. Chem.* **1968**, *72*, 3563.

(72) Cocco, G., Enzo, S., Fagherazzi, G., Schiffini, L., Bassi, I.W., Vlaic, G.,; Galvagno, S., and Parravano, G. *J. Phys. Chem.* **1979**, *83*, 2527.

(73) Haruta, M. *Catalysis Today* **1997**, *36*, 153-166.

(74) Dobrosz, I.; Jiratova, K.; Pitchon, V.; Rynkowski, J. M. *Journal of Molecular Catalysis A: Chemical* **2005**, *234*, 187-197.

(75) Schubert, M. M.; Hackenberg, S.; van Veen, A. C.; Muhler, M.; Plzak, V.; Behm, R. J. *Journal of Catalysis* **2001**, *197*, 113-122.

(76) Molina, L. M.; Hammer, B. *Physical review letters FIELD Publication Date:2003 May 23*, *90*, 206102.

(77) Bond, G. C.; Burch, R. *Catalysis* **1983**, *6*, 27-60.

(78) Le, V. T.; Ho, S. T.; Che, M.; Djega-Mariadassou, G.; Bugli, G.; Bureau-Tardy, M.; Bond, G. C. *Tap Chi Hoa Hoc* **1986**, *24*, 1-4.

(79) Haruta, M.; Tsubota, S. *Catalysis and Electrocatalysis at Nanoparticle Surfaces* **2003**, 645-665.

(80) Travarelli, A. *Catal. Rev.-Sci.Eng.* **1996**, *38*, 439.

(81) Travarelli, A. *J. Catal* **1995**, *151*, 111-124.

(82) Bunluesin, T., Cordatos, H., Gorte, R. J. *J. Catal* **1995**, *157*, 222.

(83) Rocchini, E., Vicario, M., Llorca, J., Leitenburg, C., Dolcetti, G. and Trovarelli. A *J. Catal.* **2002**, *211*, 407-421.

(84) Travarelli, A., Leitenburg, C., Dolcetti, G., Boaro, M. *Catal. T.* **1999**, *50*, 353-367.

(85) Li, Y., Fu, Q., Flytzani-Stephanopoulos, M. *App. Catal. B: Environ* **2000**, *27*, 179.

(86) Bera, P., Patil, K. C., Jayaram, V., Subbanna, G. N., Hegde, M. S. *J. Catal* **2000**, *196*, 293-301.

(87) Fu, Q., Weber A., Flytzani-Stephanopoulos, M. *Catal. Lett* **2001**, *77*, 1-3.

(88) Luengnaruemitchai, A., Ouswan, S., Gulari, E. *Cat. Comm.* **2003**, *4*, 215-221.

(89) Gardner, S. D., Hoflund, G.B., Schryer, D.R., Schryer,J., Upchurch,B.T., Kielin,E.J. *Langmuir* **1991**, *7*, 2135.

(90) Liu, W., Flytzani-Stephanopoulos, M. *J. Catal.* **1995**, *153*, 304.

(91) Dekkers, M. A. P., Lippits, M.J., Nieuwenhuis, B.E. *Cat. Today* **1999**, *54*, 381.

(92) Bera, P., Hegde, M.S. *Cat. Lett.* **2002**, *79*, 75.

(93) Han, Y. F., Plzak, V., Kinne, M., Behm, R.J., in: F.N. Buchi, G.G.; Scherer A. Wokam (Eds.), Proceedings of the 1st European PEFC Forum,, Lucerne, 2–6 July 2001; p 393.

(94) Scire, S., Minico, S., Crisafulli, C., Satriano, C., Pistone, A. *App. Catal. B: Environ.* **2003**, *40*, 43-49.

(95) Kittel, C. *Introduction to solid state physics*; 6 ed., 1988.

(96) Ashcroft, N. W., Mermin, N. D. *Solid state Physics*, 1976.

(97) Remediakis, I. N.; Lopez, N.; Norskov, J. K. *Angewandte Chemie, International Edition* **2005**, *44*, 1824-1826.

(98) Okumura, M.; Tsubota, S.; Iwamoto, M.; Haruta, M. *Chemistry Letters* **1998**, 315-316.

(99) Palmqvist, A. E. C. *Nano-structured materials*, 1999.

(100) Lopez, N.; Janssens, T. V. W.; Clausen, B. S.; Xu, Y.; Mavrikakis, M.; Bligaard, T.; Norskov, J. K. *Journal of Catalysis* **2004**, *223*, 232-235.

(101) Grunwaldt, J.-D.; Baiker, A. *Journal of Physical Chemistry B* **1999**, *103*, 1002-1012.

(102) Johansson, S., Wong, K., Zhdanov, V. P., Kasemo, B. *J. Vac. Sci. Technol. A* **1999**, *17*, 1.

(103) Andreeva, D., Idakiev, V., Tabakova, T., Ilieva, L., Falaras, P., Bourlinos, A., Travlos, A. *catal. Today* **2002**, *72*, 51.

(104) Tsubota, M.; Haruta, M.; Nakahara, Y.; Tsubota, M.; Kobayashi, T.; Ueda, A. In *Elsevier Science B. V.*:; Poncelet, G., et al.,, Ed. New York, 1991.

(105) Wolf, A., Schuth, F. *Applied Catalysis, A* **2002**, *226*, 1.

(106) Yuan, Y. Z., Asukura, Wan, H. L., Tsai, K., Iwasawa, Y. *Catal. Lett.* **1996**, *42 (1-2)*, 15-20.

(107) Springer Verlag: New York, 1979.

(108) Wagner F. E., G., S., Milone, C. Visco, A. M., Steivano, L., Calogero, S. *J. Chem. Soc. Faraday Trans.* **1997**, *93*, 3404.

(109) Khoudiakov, M., Gupta, M. C., Deevi, S. *Nanotechnology* **2004**, *15*, 987-990.

(110) Liu, W.; Flytzani-Stephanopoulos, M. *Chemical Engineering Journal (Lausanne)* **1996**, *64*, 283-294.

(111) Zhang, S.-M.; Huang, W.-P.; Qiu, X.-H.; Li, B.-Q.; Zheng, X.-C.; Wu, S.-H. *Catalysis Letters* **2002**, *80*, 41-46.

(112) Guzman, J.; Gates Bruce, C. *Journal of the American Chemical Society*, *126*, 2672-3.

(113) Haruta, M. *Chemical record (New York, N.Y.)* **2003**, *3*, 75-87.

(114) Gallagher, P. K., Johnson, D. W., Vogel, E. M. *J. Am. Ceram. Soc.* **1977**, *60*, 28.

(115) Sueyoshi, T.; Sasaki, T.; Iwasawa, Y. *Journal of Physical Chemistry B* **1997**, *101*, 4648-4655.

(116) Du, F., Cui, Z., Zhang, Z., Chen, S. *Natural Gas Chemistry* **1997**, *6*, 135-141.

(117) Jernigan, G. G. S., J. *J. Catal.* **1994**, *147*, 567.

(118) Sasaki, T. S., T.; Iwasawa, Y. *Surf. Sci.* **1994**, *316*, L1081.

(119) Huang, T., Tsai, D. *Catalysis Letters* **2003**, *87*, 173-178.

(120) Ma, Z.-Y.; Yang, C.; Wei, W.; Li, W.-H.; Sun, Y.-H. *Journal of Molecular Catalysis A: Chemical* **2005**, *231*, 75-81.

(121) Stone, F. S.; Waller, D. *Topics in Catalysis* **2003**, *22*, 305-318.

(122) Lindstrom, B.; Pettersson, L. J.; Govind Menon, P. *Applied Catalysis, A: General* **2002**, *234*, 111-125.

(123) Ma, J.; Park, C.; Rodriguez, N. M.; Baker, R. T. K. *Journal of Physical Chemistry B* **2001**, *105*, 11994-12002.

(124) Yang, R.; Zhong, B.; Hu, T.; Liu, T. *Fenzi Cuihua* **1998**, *12*, 241-245.

(125) Rainer, D. R.; Xu, C.; Holmblad, P. M.; Goodman, D. W. *Journal of Vacuum Science & Technology, A: Vacuum, Surfaces, and Films* **1997**, *15*, 1653-1662.

(126) Boccuzzi, F.; Chiorino, A.; Gargano, M.; Ravasio, N. *Journal of Catalysis* **1997**, *165*, 140-149.

(127) Avgouropoulos, G.; Ioannides, T. *Applied Catalysis, A: General* **2003**, *244*, 155-167.

(128) Martinez-Arias, A.; Fernandez-Garcia, M.; Hungria, A. B.; Iglesias-Juez, A.; Galvez, O.; Anderson, J. A.; Conesa, J. C.; Soria, J.; Munuera, G. *Journal of Catalysis* **2003**, *214*, 261-272.

(129) Tschoepe, A.; Ying, J. Y.; Chiang, Y.-M. *Materials Science & Engineering, A: Structural Materials: Properties, Microstructure and Processing* **1995**, *A204*, 267-71.

(130) Du, F.-L.; Cui, Z.-L.; Zhang, Z.-K.; Chen, S.-Y. *Journal of Natural Gas Chemistry* **1997**, *6*, 135-141.

(131) Sinfelt, J. H. *Bimetallic Catalysts, DiscoVeries, Concepts and Applications*: New York, 1983.

(132) Roucoux, A. S., J.; Patin, H. . *Chem. ReV.* **2002**, *102*, 3757-3778.

(133) Scott, R. W. J. D., A. K.; Crooks, R. M. *J. Am. Chem. Soc.* **2003**, *125*, 3708-3709.

(134) Chung, Y. M. R., H. K. *Catal. Lett.* **2003**, *85*, 159-164.

(135) Haruta, M.; Sakurai, H.; Tsubota, M.; Kobayashi, T.; Ueda, A. In *Jpn. Kokai Tokkyo Koho*; (Kogyo Gijutsuin, Japan). Jp, 1993.

(136) Häkkinen, H., Abbet, S., Sanchez, A., Heiz, U., Landman, U. *Angew. Chem. Int. Ed.* **2004**, *42*, 1297.

(137) Wang, Q. A., Liu a, G. H, Linb,S.D., Lin, T. S., Mou,C.Y. *J. of Catal.* **2005**, *233*, 186–197.

(138) Venezia, A. M., Liotta, L.F. Pantaleo, G., La Parola,V. Deganello, G., Beck,A., Koppany, Zs., Frey,K., Horvath,D., Guczi,L. *Appl. Catal. A* **2003**, *251*, 359.

(139) Nakatsuji, H., Nakai, H. *Chem. Phys. Lett.* **1990**, *174*, 283.

(140) Nakatsuji, H., Hu, Z.M., Nakai, H., Ikeda, K. *Surf. Sci.* **1997**, *387*, 328.

(141) Sandell, A., Bennich, P., Nilsson, A., Hernnäs, B., Björneholm, O., Mårtensson, N. *Surf. Sci.* **1994**, *310*, 16.

(142) Sra, A. K., Ewers,T. D., Schaak, R.E **2005**, *17*, 758-766.

(143) Liu, W., Sarofim, A. F., Flytzani-Stephanopoulos, M. *Chem. Eng. Sci.* **1994**, *49*, 4871.

(144) Luo, M. F., Zhong, Y. J., Yuan, X. X., Zheng, X. M. *Appl. Catal. A* **1997**, *162*, 121.

(145) Xu, Y.; Mavrikakis, M. *Journal of Physical Chemistry B* **2003**, *107*, 9298-9307.

(146) Mills, G.; Gordon, M. S.; Metiu, H. *Journal of Chemical Physics* **2003**, *118*, 4198-4205.

(147) Kim, T. S.; Stiehl, J. D.; Reeves, C. T.; Meyer, R. J.; Mullins, C. B. *Journal of the American Chemical Society* **2003**, *125*, 2018-2019.

(148) Stiehl, J. D.; Kim, T. S.; McClure, S. M.; Mullins, C. B. *Journal of the American Chemical Society* **2004**, *126*, 1606-1607.

(149) Wang , A. Q., Liu, J., Linb,S.D., Lin, T., Mou, C. *Journal of Catalysis* **2005**, *233*, 186–197.

(150) Kondarides, D. I., Verykios, X.E. *J. Catal.* **1996**, *158*, 363.

(151) Peden, C. H. F., Goodman, D. W., *J. Phys. Chem.* **1986**, *90*, 4839-4843.

(152) Peden, C. H. F., Goodman, D. W., Weisel, M. D., Hoffmann, F. M. *Surf. Sci.* **1991**, *253*, 44-58.

(153) Engel, T., Ertl, G. *Adv. Catal.* **1979**, *28*, 1-78.

(154) Somorjai, G. A. *Chem. Soc. Rev* **1984**, *13*, 321.

(155) Ryabov, A. D. *Chem..Rev.* **1990**, *90*, 403.

(156) Holland, P. M., Castleman, A. W., Jr. *J. Chem. phys.* **1982**, *76*, 4195.

(157) Marinelli, P. J., Squires, R. R. *J. Am. Chem. Soc.* **1989**, *111*, 4101.

(158) Sato, H. H., Y. and Osamu, I. *J. Photochem. Photobio. A: Chemistry* **1995**, *92*.

(159) Uppal, J. S. a. S., R. H. *J. Am. Chem. Soc.* **1982**, *104*, 1229.

(160) Daly, M. G. a. E.-S., M. S. *J. Phys. Chem.* **1995**, *99*, 5283.

(161) Cotton, A. F., Wilkinson, G. *Advanced Inorganic Chemistry*; 4th Edition ed.; John Wiley & Sons: New York, 1980.

(162) Schwarz. H , E. K. *Chem. Rev.* **1991**, *91*, 1121-1177.

(163) Willner, H., Aubke, F. *Inorganic Chemistry* **1990**, *29*, 2195.

(164) Kuster, R., Seppelt, K., Allgem, Z. *Allgem.Chem.* **2000**, *626*, 236.

(165) Willner, H., Schaebs, J., Hwang, J., Mistry, F., Jones, R., Trotter, J., Aubke, F. *J. Am. Chem. Soc.* **1992**, *114*, 8972.

(166) Lupinetti, A. J., Jonas, V., Thiel, W., Strauss, S. H., Frenking, G., *Chem. Europ. J.* **1999**, *5*, 2573.

(167) Hagen, J., Socaciu, L. D., Elijazyfer, M., Hiez, U., Bernhardt, T. M., Woste, L. *Phys. Chem. Chem. Phys.* **2002**, *4*, 1707.

(168) Jarvis, M. J. Y.; Blagojevic, V.; Koyanagi, G. K.; Bohme, D. K. *European Journal of Mass Spectrometry* **2004**, *10*, 949-961.

(169) Taylor, W. S.; Matthews, C. C.; Parkhill, K. S. *Journal of Physical Chemistry A* **2005**, *109*, 356-365.

(170) Niu, D.-M.; Zhang, S.-D.; Zhang, X.-Y.; Li, H.-Y. *Wuli Huaxue Xuebao* **2003**, *19*, 1114-1118.

(171) Wang, J.; Wang, J.; Zhang, Y.-W.; Sheng, L.-S. *Yuanzi Yu Fenzi Wuli Xuebao* **2003**, *20*, 127-131.

(172) Jarvis, M. J. Y.; Pisterzi, L. F.; Blagojevic, V.; Koyanagi, G. K.; Bohme, D. K. *International Journal of Mass Spectrometry* **2003**, *227*, 161-173.

(173) Hinako, H.; Watanabe, M. In *Jpn. Kokai Tokkyo Koho*; (Asahi Kasei Corporation, Japan). Jp, 2002.

(174) Taylor, W. S.; May, J. C. *Book of Abstracts, 219th ACS National Meeting, San Francisco, CA, March 26-30, 2000* **2000**, CHED-781.

(175) Gibson, J. K. *Journal of Organometallic Chemistry* **1998**, *558*, 51-60.

(176) Daly, G. M.; El-Shall, M. S. *Zeitschrift fuer Physik D: Atoms, Molecules and Clusters* **1993**, *26*, 186-8.

(177) Daly, G. M.; El-Shall, M. S. *Journal of Physical Chemistry* **1994**, *98*, 696-701.

(178) Daly, G. M.; El-Shall, M. S. *Journal of Physical Chemistry* **1995**, *99*, 5283-90.

(179) El-Shall, M. S.; Marks, C. *Journal of Physical Chemistry* **1991**, *95*, 4932-5.

(180) El-Shall, M. S. *Polymer Preprints (American Chemical Society, Division of Polymer Chemistry)* **1996**, *37*, 367-8.

(181) Pithawalla, Y. B.; El-Shall, M. S. *ACS Symposium Series* **1998**, *713*, 232-245.

(182) Daly, G. M.; Pithawalla, Y. B.; Yu, Z.; El-Shall, M. S. *Chemical Physics Letters* **1995**, *237*, 97-105.

(183) Pithawalla, Y. B.; McPherson, J.; El-Shall, M. S. *Chemical Physics Letters* **1999**, *309*, 215-220.

(184) Chen, Q. S., C.; Kan, S. Z. and Freiser. B. S. *Int. J. Mass Spectrom.* **1998**, *179*, 231.

(185) Bakhtiar, R. D., J. J. and Jacobson, D. B. *J. Am. Chem. Soc.* **1992**, *114*, 8304.

(186) Tjelta, B. L. a. A., P. B. *J. Am. Chem. Soc.* **1996**, *118*, 9652.

(187) El-Shall, M. S.; Slack, W. *Macromolecules* **1995**, *28*, 8456-8.

(188) Vann, W.; El-Shall, M. S. *Journal of the American Chemical Society* **1993**, *115*, 4385-6.

(189) El-Shall, M. S. *NASA Conference Publication* **1999**, *209092*, 187-192.

(190) Skarman, B.; Grandjean, D.; Benfield, R. E.; Hinz, A.; Andersson, A.; Wallenberg, L. R. *Journal of Catalysis* **2002**, *211*, 119-133.

(191) Wang, J. B.; Tsai, D.-H.; Huang, T.-J. *Journal of Catalysis* **2002**, *208*, 370-380.

APPENDIX A

The initial results of Au nanoparticle catalyst obtained using flow reactor mass spectrometry system.

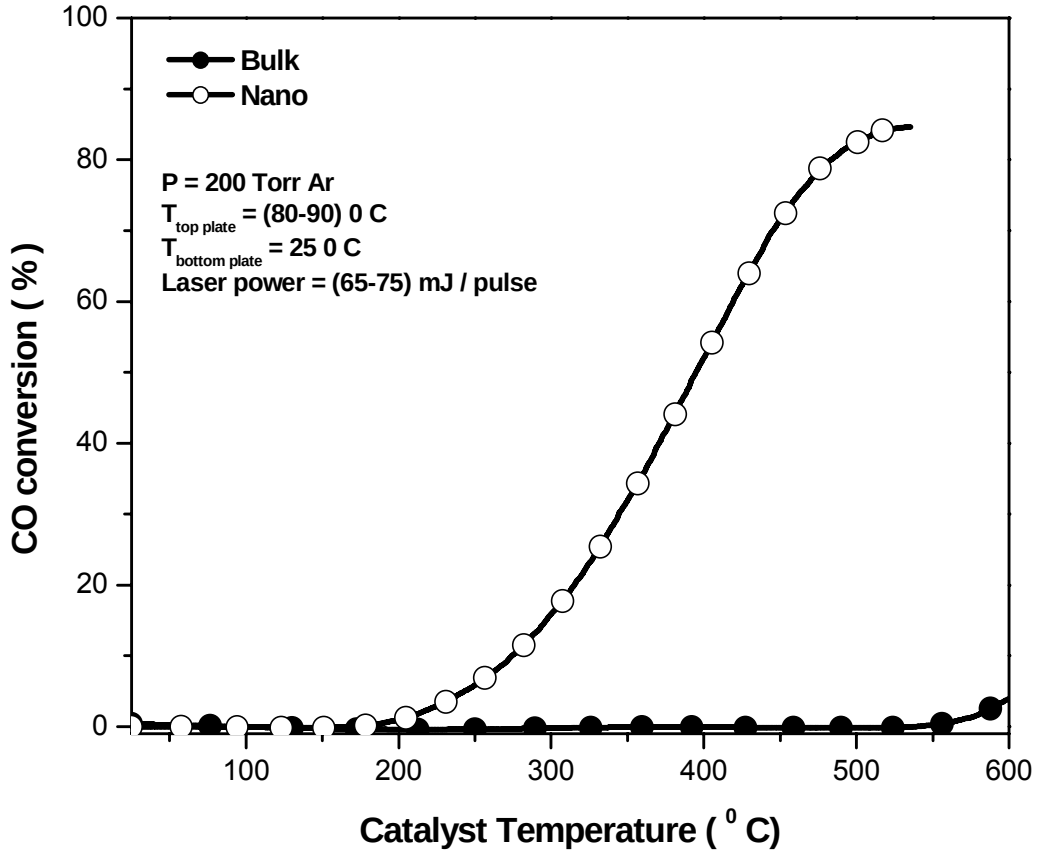

Figure A 1: Comparison between the catalytic activities of both Au micron-sized powder and fresh Au nanoparticle prepared by the LVCC method (run 1).

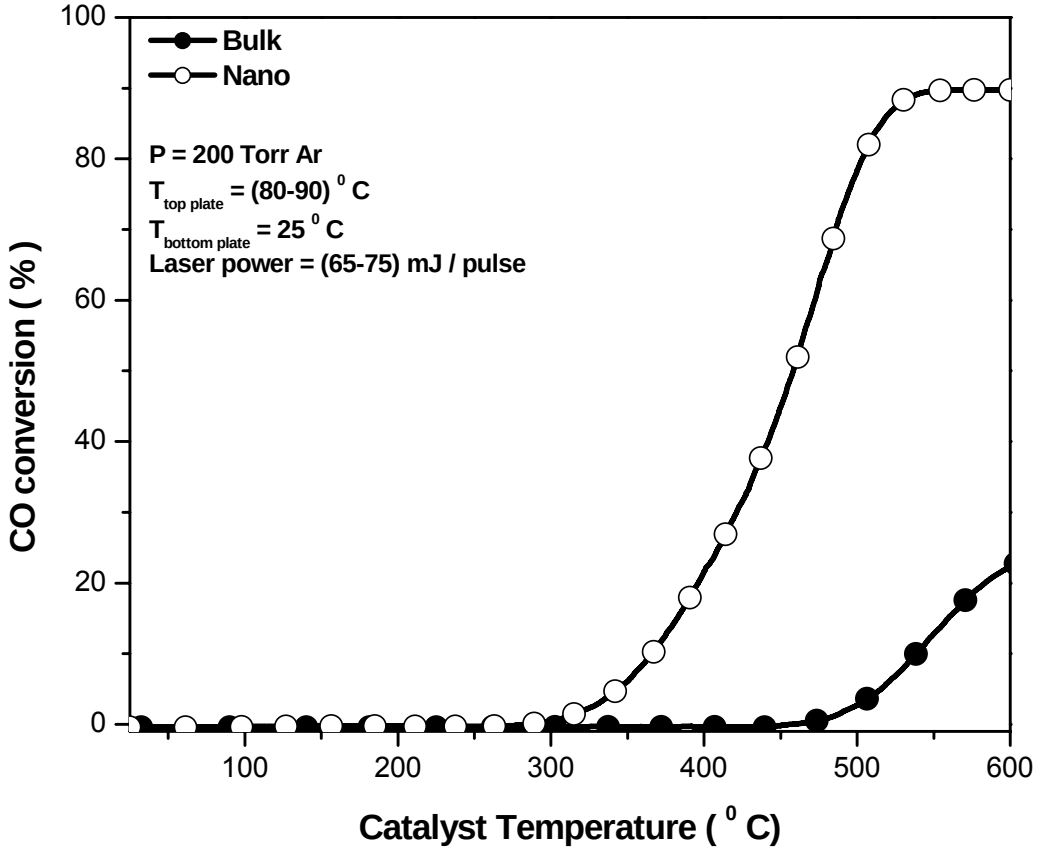

Figure A 2: Catalytic activities of both Au micron-sized powder and fresh Au nanoparticle prepared by the LVCC method (run 2).

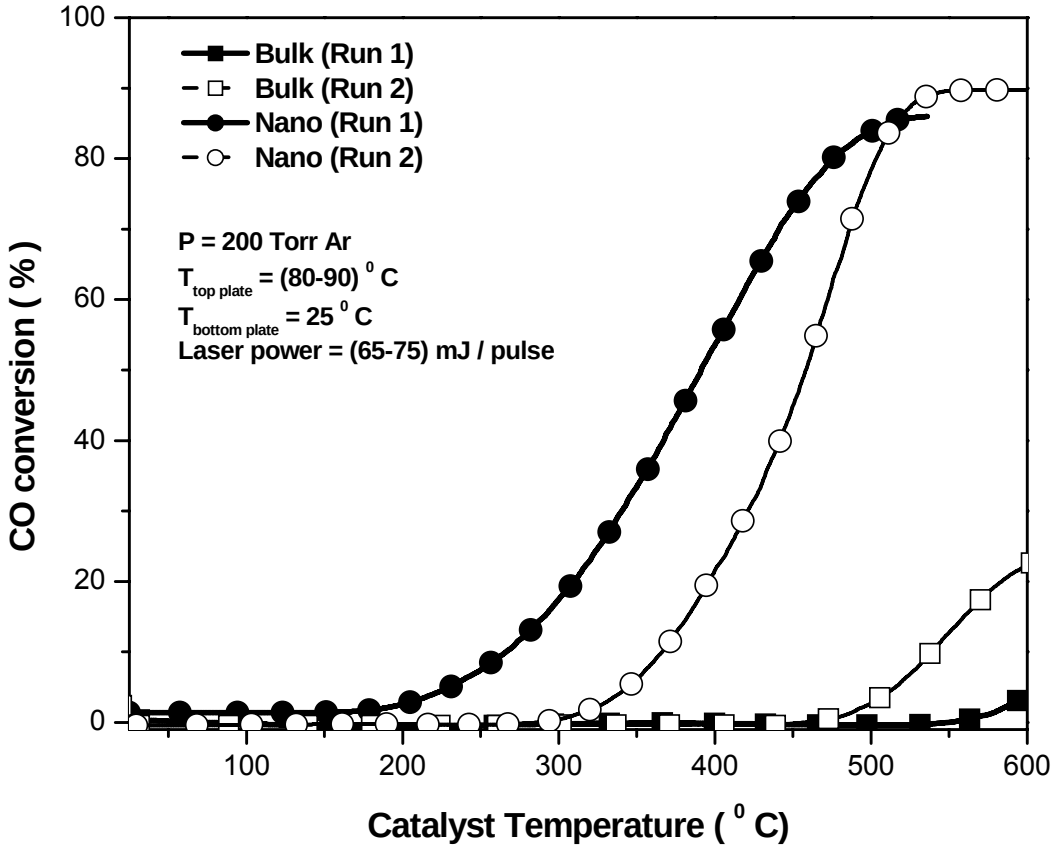

Figure A 3: Comparison between the catalytic activities of Au micron size and Au nanoparticle catalyst (run 1 and run 2).

Table A 1 Comparison between the catalytic activities of Au micron size and Au nanoparticle catalyst (run 1 and run 2).

Sample Au	**3% Conversion Light-off Temp. (^{o} C)**	**50 % Conversion Temp. (^{o} C)**	**Maximum Conversion (%)**	
			Temp. (^{o} C)	**Conversion**
Bulk-Run 1	592.4	-	600.3	4.0
Bulk-Run 2	503.5	-	600.0	22.4
Nano-Run 1	226.4	394.6	535.6	84.7
Nano-Run 2	331.3	458.2	600.0	89.8

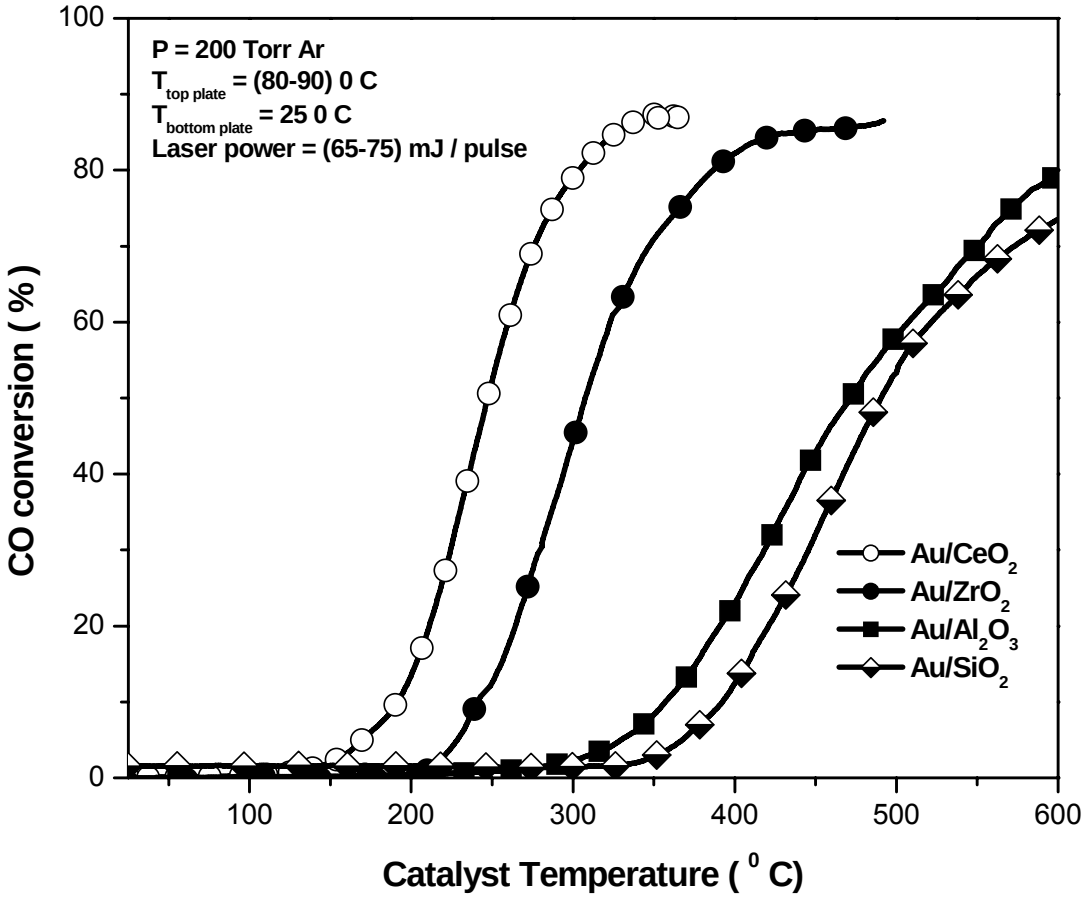

Figure A 4: Catalytic activities of nanoparticle catalysts containing 5% Au on the nanoparticle supports (run 1) by the LVCC method in 200 Torr Ar using the flow reactor mass spectrometry system.

Table A 2: Summary of catalytic activities of the nanoparticle catalysts consisting of 5% Au on different supports as prepared by LVCC (run 1) using the flow reactor mass spectrometry system.

Sample	**3% Conversion Light-off Temp. (^{o} C)**	**50 % Conversion Temp. (^{o} C)**	**Maximum Conversion (%)**	
			Temp. (^{o} C)	**Conversion**
Au/CeO_2	159.1	247.3	351.4	87.3
Au/ZrO_2	221.2	307.6	492.1	86.5
Au/Al_2O_3	314.4	470.9	600.0	79.6
Au/SiO_2	360.2	490.8	600.0	73.6

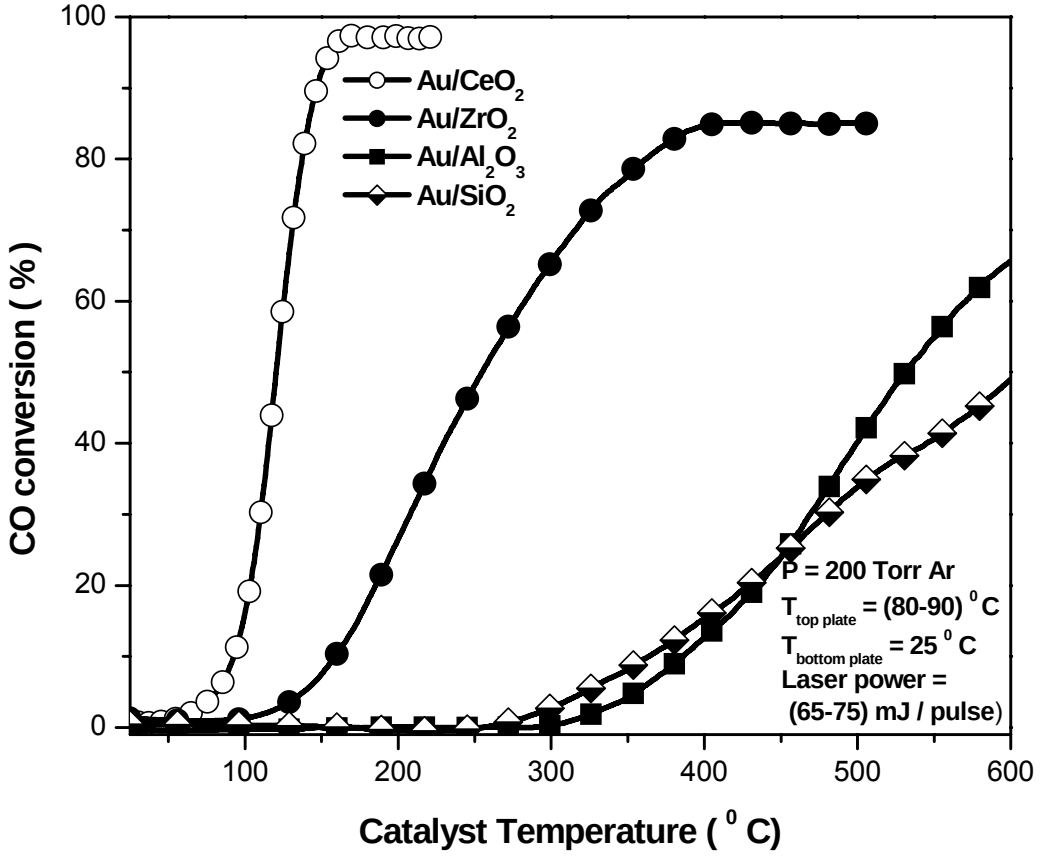

Figure A 5: Catalytic activities of nanoparticle catalysts containing 5% Au on different metal oxide supports (run 2) prepared by the LVCC method in 200 Torr Ar using the flow reactor mass spectrometry system.

Table A 3 summary of catalytic activities of nanoparticle catalysts containing 5% Au on different metal oxide supports (run 2) prepared by the LVCC method in 200 Torr Ar using the flow reactor mass spectrometry system.

Sample	**3% Conversion Light-off Temp.(^{o} C)**	**50 % Conversion Temp. (^{o} C)**	**Maximum Conversion (%)**	
			Temp. (^{o} C)	**Conversion**
Au/CeO_2	72.2	120.3	183.3	97.2
Au/ZrO_2	124.6	255.5	431.0	85.1
Au/Al_2O_3	339.1	531.5	600.0	65.7
Au/SiO_2	302.5	-	600.0	49.0

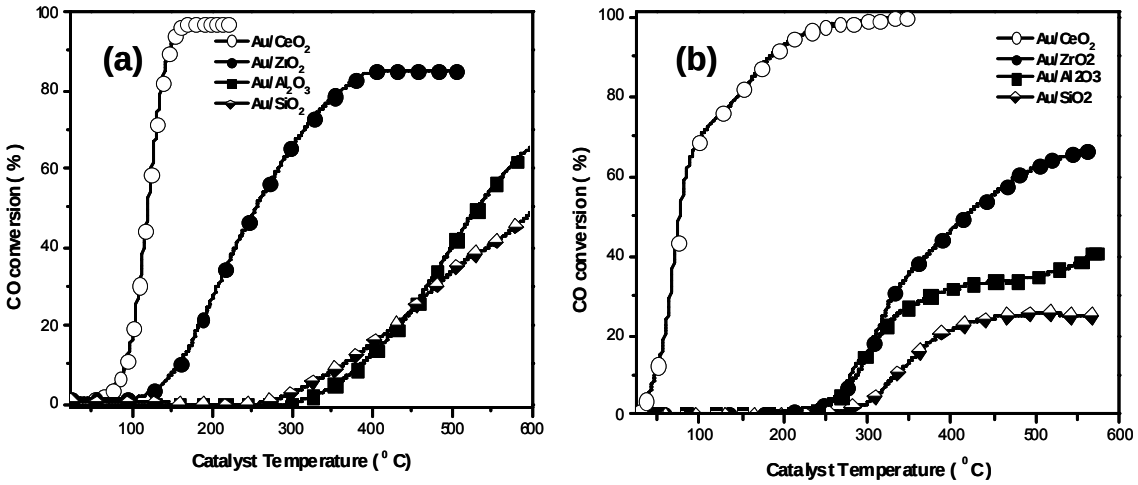

Figure A 6: Comparison between catalytic activities of 5 % Au in different oxide support obtained using a) Flow reactor mass spectroscopy. b) Flow reactor IR spectrometry system.

Table A 4 compares the catalytic activities of 5 % Au on metal oxide support using both flow reactor mass spectroscopy and flow reactor IR spectroscopy.

Sample	3% Conversion Light-off Temp. (^{o} C)	50 % Conversion Temp. (^{o} C)	Maximum Conversion (%)	
			Temp. (^{o} C)	Conversion
Au/CeO_2 (Mass spec)	72.2	120.3	183.3	97.2
Au/CeO_2 (IR)	33.5	76.4	330.2	99.8
Au/ZrO_2 (Mass spec)	124.6	255.5	431.0	85.1
Au/ZrO_2 (IR)	249.0	416.4	561.2	66.5
Au/Al_2O_3 (Mass spec)	339.1	531.5	600.0	65.7
Au/Al_2O_3 (IR)	256.8	-	565.9	40.3
Au/SiO_2 (Mass spec)	302.5	-	600.0	49.0
Au/SiO_2 (IR)	298.4	-	494.9	25.6

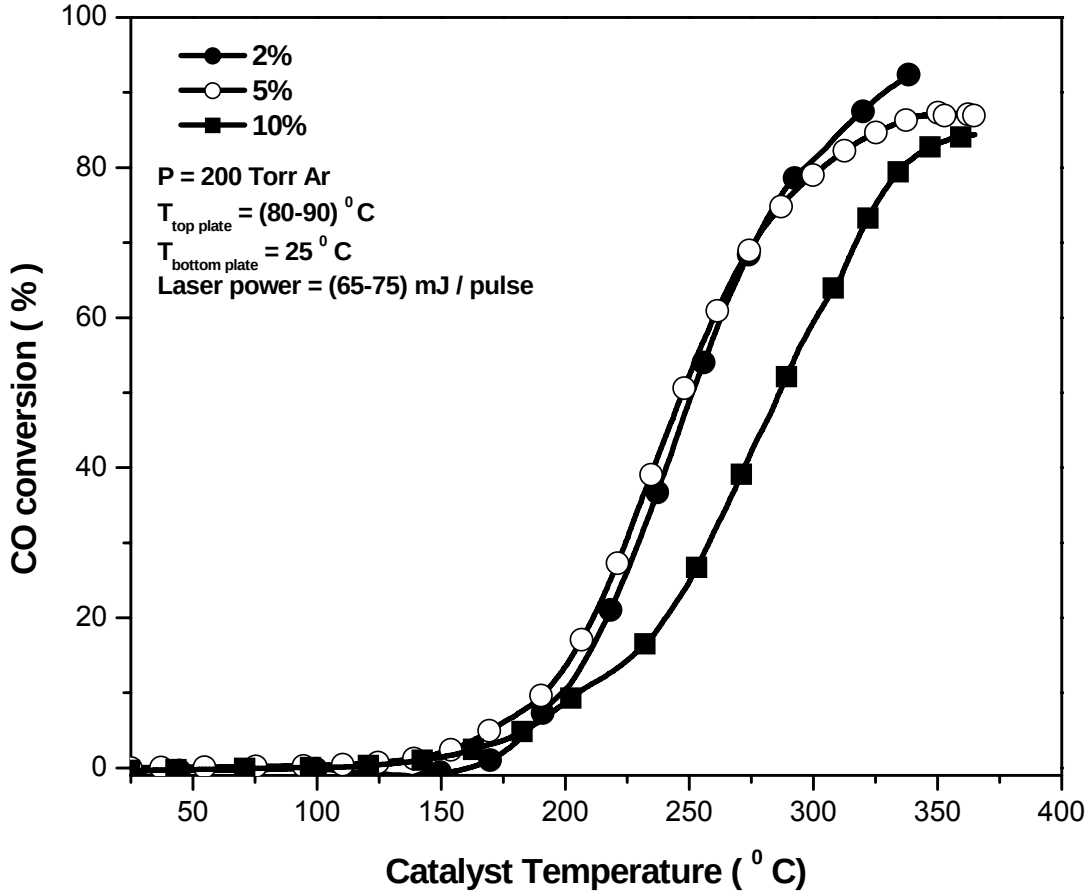

Figure A 7: Comparison of activities of different loadings of Au on CeO_2 support as prepared by the LVCC method (run 1) using flow reactor mass spectrometry.

Table A 5 summarizes the catalytic activities of Au/CeO_2 system with 2, 5, and 10 % Au loading supported on CeO_2 as prepared by the LVCC method (run 1) using flow reactor mass spectrometry.

Sample Au/CeO_2	**3% Conversion Light-off Temp. (^{o} C)**	**50 % Conversion Temp. (^{o} C)**	**Maximum Conversion (%)**	
			Temp. (^{o} C)	**Conversion**
2% Au	178.8	251.0	340.5	93.0
5% Au	159.1	247.3	351.4	87.3
10% Au	168.9	286.5	364.4	84.4

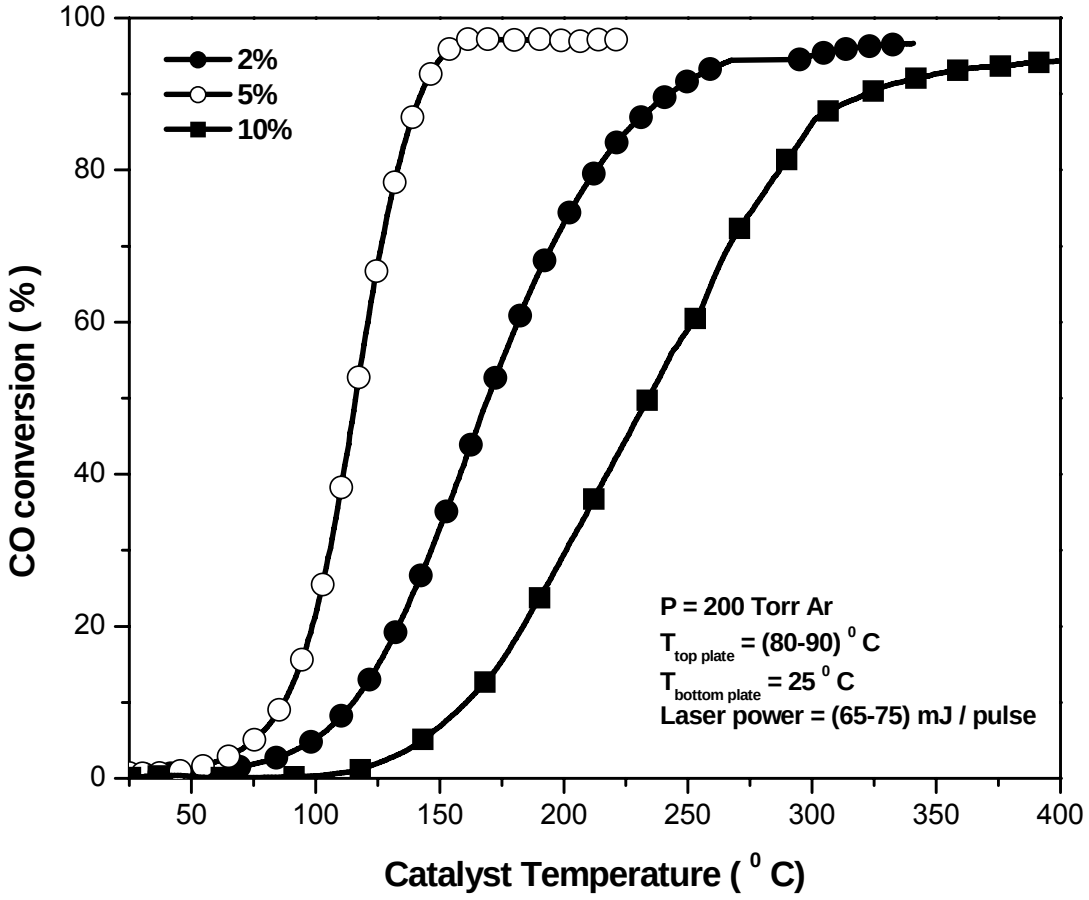

Figure A 8: Comparison between the activities of Au/CeO_2 system with 2, 5, and 10 % Au loading supported on CeO_2 as prepared by the LVCC method (run 2) using flow reactor mass spectrometry .

Table A 6 summarizes the catalytic activities of Au/CeO_2 system with 2, 5, and 10 % Au loading supported on CeO_2 as prepared by the LVCC method (run 1) using flow reactor mass spectrometry.

Sample Au/CeO2	**3% Conversion Light-off Temp. (^{o} C)**	**50 % Conversion Temp. (^{o} C)**	**Maximum Conversion (%)**	
			Temp. (^{o} C)	**Conversion**
2% Au	81.7	170.1	341.1	96.9
5% Au	72.2	120.3	183.3	97.2
10% Au	133.7	233.4	400.0	94.6

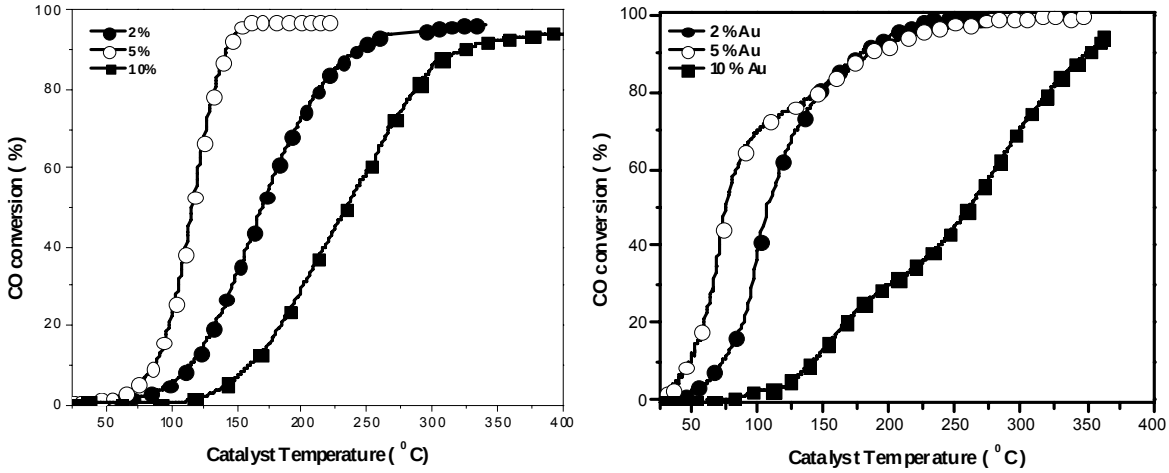

Figure A 9: Comparison between the catalytic activities of Au/CeO_2 system with 2, 5, and 10 % Au loading supported on CeO_2 as prepared by the LVCC method (run 2) using flow reactor mass spectroscopy and flow reactor IR spectroscopy.

Table A 7 summarizes the catalytic activities of Au/CeO_2 system with 2, 5, and 10 % Au loading supported on CeO_2 as prepared by the LVCC method (run 2) using flow reactor mass spectroscopy and flow reactor IR spectroscopy.

Sample Au/CeO_2	**3% Conversion Light-off Temp. (^{o} C)**	**50 % Conversion Temp. (^{o} C)**	**Maximum Conversion (%)**	
			Temp. (^{o} C)	**Conversion**
2 % Au (Mass spec)	81.7	170.1	341.1	96.9
2 % Au (IR)	53.2	107.5	258.2	99.9
5 % Au (Mass spec)	72.2	120.3	183.3	97.2
5 % Au (IR)	33.5	76.4	330.2	99.8
10 % Au (Mass spec)	133.7	233.4	400.0	94.6
10 % Au (IR)	117.6	260.1	361.0	94.1

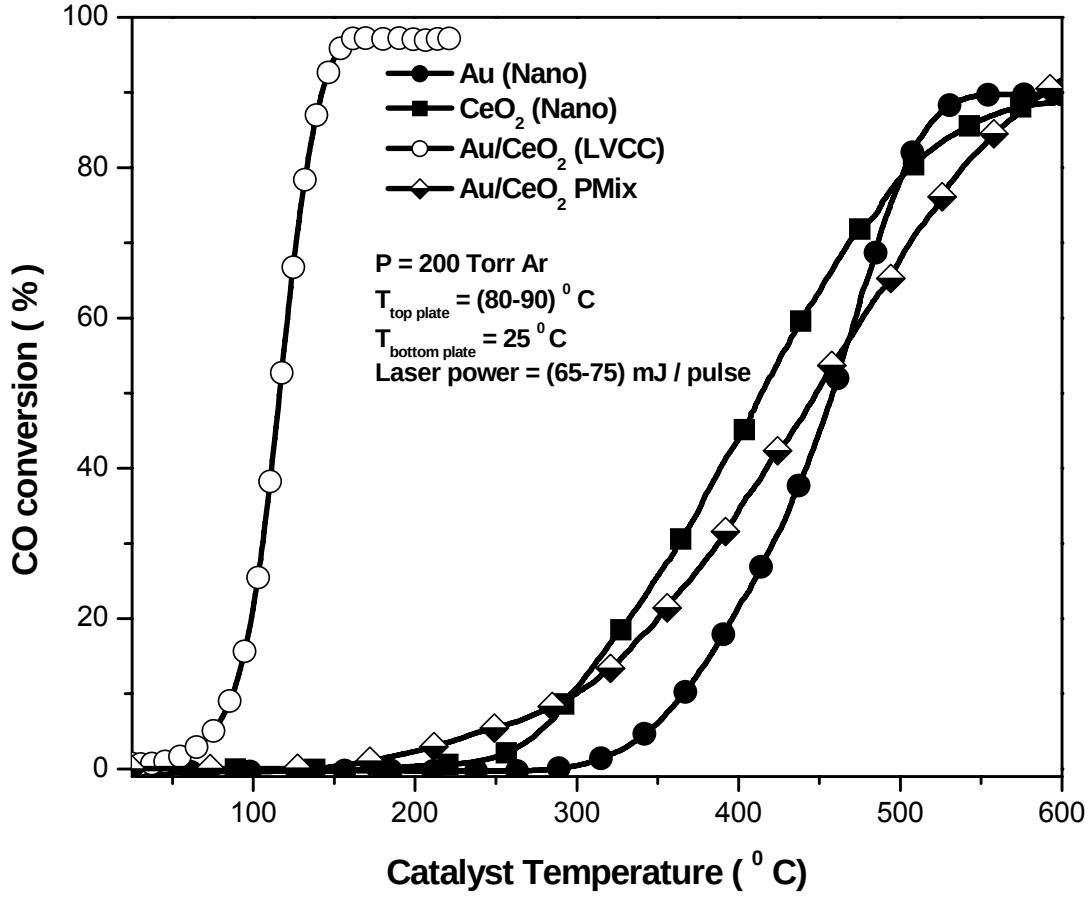

Figure A 10: Comparison between the catalytic activity of the supported Au/CeO_2 nanoparticles prepared by the LVCC method (run 2) with the activities of individual Au nanoparticles, CeO_2 nanoparticles, and the 5% Au nanoparticles in a 95 % CeO_2 nanoparticles mixture.

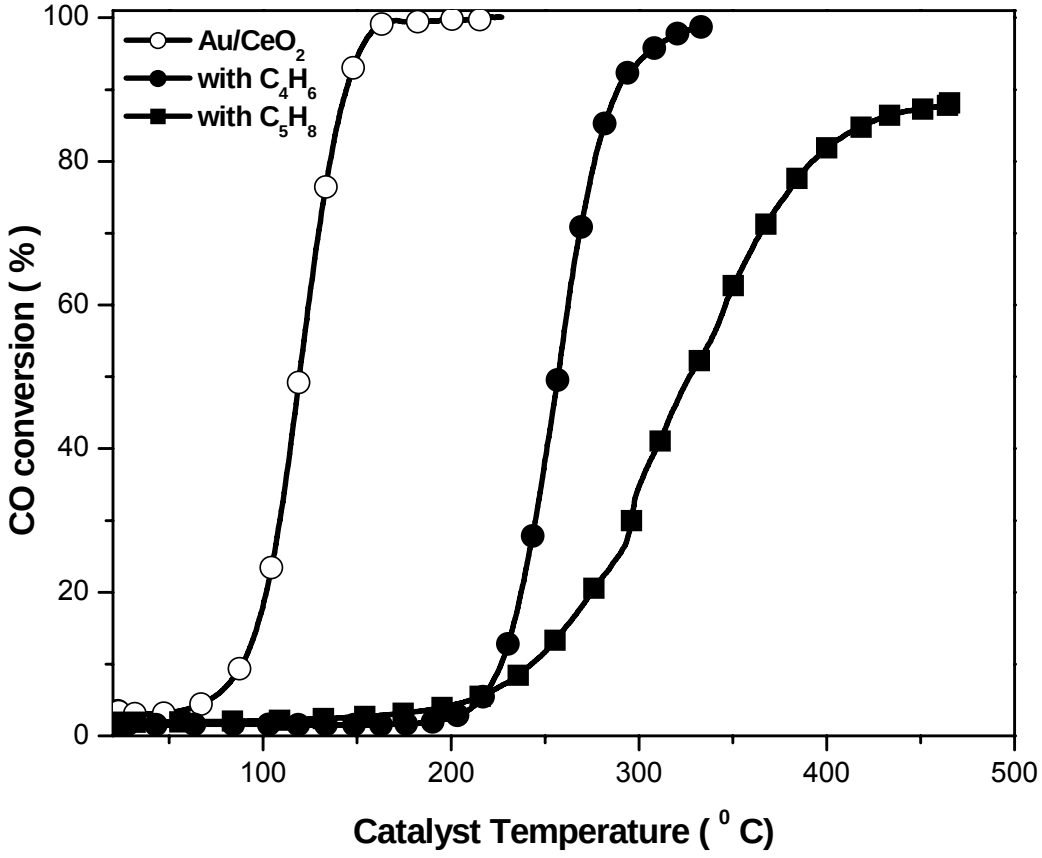

Figure A 11: Comparison between the catalytic activities of 5 % Au/CeO_2 with and without the presence of 1000 ppm butadiene and 1000 ppm isoprene.

Table A 8 summarizes the catalytic activities of Au/CeO_2 system with 2, 5, and 10 % Au loading supported on CeO_2 as prepared by the LVCC method (run 2) using flow reactor mass spectroscopy and flow reactor IR spectroscopy.

Sample Au/CeO2	**3% Conversion Light-off Temp. (^{o} C)**	**50 % Conversion Temp. (^{o} C)**	**Maximum Conversion (%)**	
			Temp. (^{o} C)	**Conversion**
Au/CeO2	72.2	120.3	183.3	97.2
With butadiene	206.0	255.0	334.0	99.0
With isoprene	170.0	327.0	466	88.0

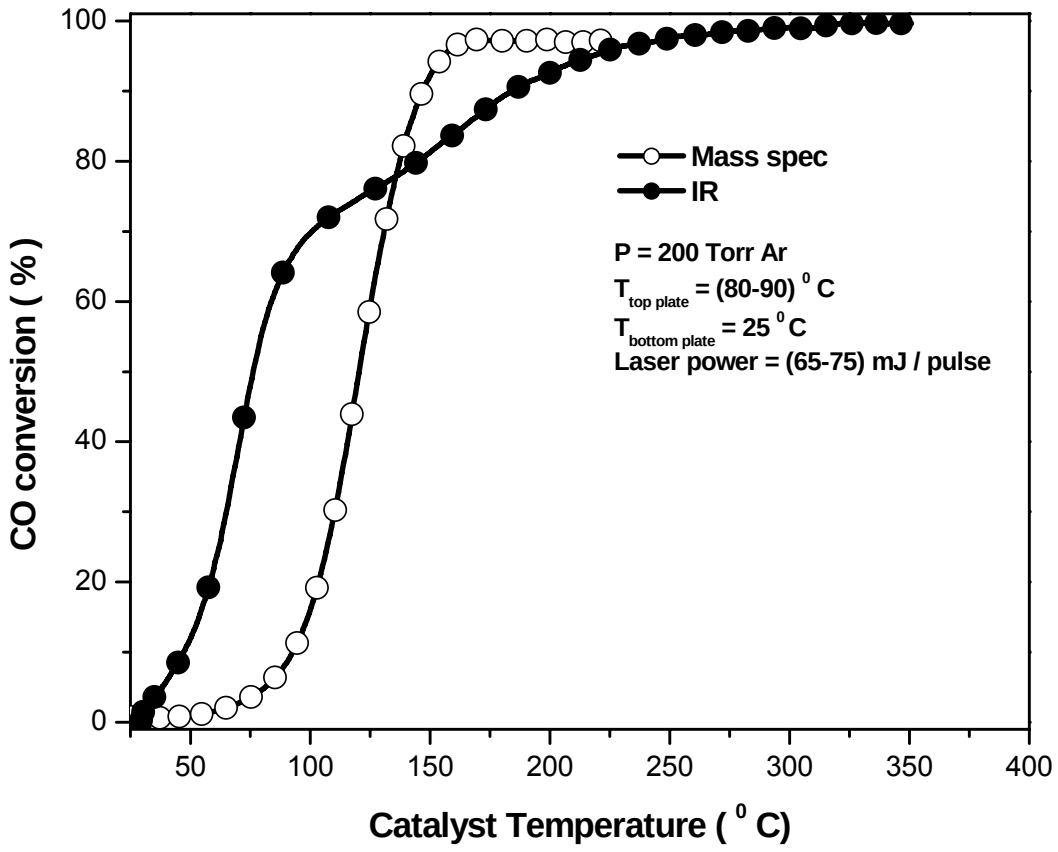

Figure A 12: Catalytic activities of 5 % Au/CeO_2 prepared by LVCC in 200 Torr Ar (run 2) by using flow reactor mass spectroscopy and flow reactor IR spectroscopy.

Table A 9 summarizes the catalytic activities of 5 % Au/CeO_2 prepared by LVCC in 200 Torr Ar (run 2) by using flow reactor mass spectroscopy and flow reactor IR spectroscopy.

Sample 5%Au/CeO_2 (Run 2)	**3% Conversion Light-off Temp. (^{o}C)**	**50 % Conversion Temp. (^{o}C)**	**Maximum Conversion (%)**	
			Temp. (^{o}C)	**Conversion**
Mass spec	72.2	120.3	183.3	97.2
IR	33.5	76.4	330.2	99.8

Table A 10 compares the catalytic activity of the supported Au/CeO_2 nanoparticles prepared by the LVCC method (run 2) with the activities of individual Au nanoparticles, CeO_2 nanoparticles, and the 5% Au nanoparticles in a 95 % CeO_2 nanoparticles mixture.

Sample	**3% Conversion Light-off Temp. (^{o} C)**	**50 % Conversion Temp. (^{o} C)**	**Maximum Conversion (%)**	
			Temp. (^{o} C)	**Conversion**
Au (Nano)	331.3	458.2	600.0	89.8
CeO_2 (Nano)	264.6	415.2	600.0	88.7
Physical Mixture	212.6	448.5	600.0	91.8
Au/CeO_2 (LVCC)	72.2	120.3	183.3	97.2

VITA

Khaled Mohammad Saoud was born on August 30, 1968 in Irbid, Jordan. He earned his B. Sc. in Physics/Math from Yarmouk University in 1990, and his M. Sc. in Applied Physics from Virginia Commonwealth University in 2000. Since 2001, he is pursuing his Ph. D. degree in Chemical Physics at Virginia Commonwealth University.

Employment Experience:

(2001-present) **Research Assistance (co-op) R&D**, Philip Morris USA Richmond, VA

(2000-2001) **Application Engineer**, Nova Measuring Instruments Inc., Phoenix, AZ.

(2000-2001). **Physics instructor**, Science Museum, Richmond, VA

(1998-2000). Teacher assistance, Virginia commonwealth university

(1992-1998) Owner and Manager of a business, Richmond, VA

(1990-1991).**Physics teacher**, ministry of education, Jordan

Honors and Awards:

- Elected member of Organizing Committee of Jordan International Conference of Material Science engineering, and Nanotechnology. (2005)
- Philip Morris USA Research Fund Grant (2001-2004)
- Virginia Commonwealth University research Award (2000, 2003)
- Ultramicroscopy Cover, *STM Image of Clean Si (5512) surface,* 2001.
- Elected member of Sigma Pi Sigma, American Physics Honor Society, (1999).
- Virginia Commonwealth University Research Assistance (1999-2000)
- Virginia Commonwealth University Teaching Assistance (1998-1999)
- King Hussein undergraduate Scholarship (1986-1990)

Professional Society Memberships:

- Sigma Pi Sigma, American Physics Honor Society, (1999-present).
- American Physical Society (1999-present).
- American Vacuum Society (1998-present).
- Society of Physics students (1998-present).

Referred publications:

1. Saoud, K.M. et al., *Cigarettes and cigarette components containing nanostructured fibril materials*, in *PCT Int. Appl.* 2005, (Philip Morris Products S.A., Switz.). Wo. p. 43 pp.
2. Yadav, R., Saoud, K. M., Hajaligol, M., *Study of cigarette smoke aerosol using time of flight mass spectrometry.* Journal of Analytical and Applied Pyrolysis, 2004. 72(1): p. 17-25.
3. Baski, A.A., K.M. Saoud, and K.M. Jones, *1-D nanostructures grown on the Si (5 5 12) surface.* Applied Surface Science, 2001. 182(3-4): p. 216-222.
4. Baski, A.A. and K.M. Saoud, *Au-induced faceting of Si (5 5 12).* Journal of Cluster Science, 2001. 12(3): p. 527-535.

5. Jones, K.M., K.M. Saoud, and A.A. Baski, *Noble metal row growth on Si (5 5 12).* Clusters and Nanostructure Interfaces, [Proceedings of the International Symposium on Clusters and Nanostructure Interfaces], Richmond, VA, United States, Oct. 25-28, 1999, 2000: p. 49-54.
6. Baski, A.A., K.M. Jones, and K.M. Saoud, *STM studies of 1-D noble metal growth on silicon.* Ultramicroscopy, 2001. 86(1/2): p. 23-30.
7. Baski, A.A., K.M. Jones, and K.M. Saoud, *STM studies of 1-D noble metal growth on silicon.* Ultramicroscopy FIELD Publication Date: 2001 Jan. 86(1-2):

Papers under submission

1. Hajaligol, M., Rasouli, F., Saoud, K. M., Yadav, R., *Formation and Deposition of nanoscale particles in cigarette manufacture*, US. Patent. Application. # 10/972205 (2004) (Pending).
2. Rabiei, S., Miser, D. E., Lipscomb, J. A., Saoud, K. M., Gedevanishvili, S., Rasouli, F., *Conversion of hausmanite (Mn_3O_4) particles to nano-fibrous manganite (MnOOH) at ambient conditions*, Material Science Journal (accepted for publication 2005).
3. Vapor Phase Synthesis and Characterization of Bimetallic Alloy and Supported Nanoparticle Catalysts, Victor Abdelsayed, Khaled Saoud and M. Samy El-Shall

Presentations:

1. Saoud, K. M., M.; El-Shall, M. Samy, *Gold nanoparticle Catalysts for Low Temperature CO Oxidation*, First Jordanian International Conference of Material Science, Engineering, and Nanotechnology, Al-salt, Jordan. May (2005).
2. Saoud, K. M., M.; El-Shall, M. Samy. Vapor Phase Synthesis of Gold Nanoparticle Catalysts for Low Temperature CO Oxidation. Abstracts of Papers, 229th ACS National Meeting, San Diego, CA, United States, March 13-17, 2005 (2005).
3. Saoud, K. M.; El-Shall, M. Samy. Vapor phase synthesis of Au nanoparticle catalysts. Abstracts, 56th Southeast Regional Meeting of the American Chemical Society, Research Triangle Park, NC, United States, November 10-13 (2004).
4. Saoud, K. M.; El-Shall, *M. Samy. Au/CeO_2 Nanoparticle Catalysts prepared by chemical and Physical Methods. for Low Temperature CO Oxidation*, Philip Morris Basic Science Research Symposium, Richmond, VA 2004.
5. Saoud, K. M.; El-Shall, M. Samy. *Synthesis and Characterization of Au Nanoparticle Catalysts. for Low Temperature CO Oxidation*, Clusters and Nano Conference, Richmond, VA 2003.
6. Saoud, K. M., Baski, A. A., *STM studies of 1-D noble metal growth on silicon,* Clusters and Nano Conference, Richmond, VA (1999)
7. Saoud, K. M., Baski, A. A., *Growth of Au nanowires on Si (5512) surface*, 46th International Symposium of the American Vacuum Society Seattle, Washington October 25th, (1999).